Transport in Weakly Coupled Vertical Double Quantum Dots: Single-Particle Energy Level Spectroscopy and Hyperfine Interaction Effects

Christopher Payette

Doctor of Philosophy

Department of Physics

Montreal, Quebec

August 2010

A thesis submitted to McGill University in partial fulfillment of the requirements of the degree of Doctor of Philosophy

Acknowledgements

Many people contributed to this project and deserve my thanks. First, my supervisor at NRC-IMS, Guy Austing, who has kindly and patiently guided me over the last five years. Second, my co-supervisor at McGill, Michael Hilke, who got me started on the project and has enthusiastically supported me during its course. Third, Piotr Zawadzki deserves special mention for the excellent technical support he provides at NRC-IMS. Furthermore, the other members of the quantum physics group at NRC-IMS, Andy, Sergei, Sylvain, Ghislain, Louis, Simon, Will and Joe have made it a pleasure to come into the lab everyday.

I would also like to acknowledge my many experimental and theoretical collaborators whose hard work and dedication has contributed to the success of this project. Many thanks to Goulin Yu, James Gupta, Selva Nair, Bart Partoens, Geof Aers, Shinichi Amaha, and Seigo Tarucha.

Finally, I would like to thank my family for their unstinting support and, of course, Sandra for her love and faith in me.

Abstract

Performing transport measurements on weakly coupled vertical double quantum dots, we study by magneto-resonant-tunneling spectroscopy, single-particle energy spectra of the constituent dots over a wide energy window. The measured energy spectra are well modeled overall by ideal spectra calculated for elliptical and parabolic in-dot-plane confinement potentials. However, in regions where single-particle energy levels are naively expected to cross, we observe pronounced level anti-crossing behaviour and strong resonant current variations (both enhancement and suppression). Within a coherent tunneling picture, these effects can be attributed to coherent level mixing induced by weak perturbations in the nearly ideal dot confinement potentials. We analyze the energy spectra in detail, and focus on examples of two-, three- and four-level crossings where we observe the suppression of an otherwise strong current resonance, a signature of dark state formation due to destructive interference. The mixing we measure and model at two three-level crossings represents an all-electrical analogue of coherent population trapping. We also explore the limitations of the applicability of the coherent level mixing model and demonstrate in-situ alteration of the coupling between levels.

We further examine the electron spin-nuclear spin (hyperfine) interaction. In the familiar two-electron spin blockade regime, on application of an out-of-dot-plane magnetic field, we observe current switching and hysteresis, and a funnel-like structure in the leakage current, all hallmarks of the hyperfine interaction. The measurements bring to light a strong gate voltage dependence, significant device-to-device variations, and an intricate bias voltage history dependence not accounted for in any existing model. Unexpectedly, we also observe signatures of the hyperfine interaction at high bias, well

outside the spin blockade regime. We characterize these features and suggest how the hyperfine interaction may play a role at high bias, although the electronic states involved generally can not easily be identified. As a first step toward understanding this new regime, we describe another hysteretic funnel-like structure observed at high bias where the electronic states involved can be identified as two-electron states, so allowing us to postulate a specific mechanism for this funnel.

Abrégé

En effectuant des mesures de transport sur des boîtes quantiques doubles faiblement couplées, nous étudions, par la spectroscopie par effet tunnel magnetorésonant, les spectres d'énergie de particule simple dans une grande fenêtre d'énergie. Les spectres d'énergie mesurés sont modélisés par les spectres calculés pour des potentiels de confinement elliptique et parabolique. Cependant, dans les régions où les niveaux d'énergie de particule simple doivent se croiser, nous observons des comportements de croisements évités et des variations du courant résonnant. Dans le cadre de l'effet tunnel cohérent, ces effets peuvent être attribués au mélange cohérent des niveaux induit par les faibles perturbations du confinement. Nous analysons les spectres d'énergie et focalisons sur des exemples de croisements de deux à quatre niveaux où nous observons la suppression d'une résonance de courant qui est une signature de la formation d'un état sombre dû à de l'interférence destructive. Le mélange que nous mesurons et modélisons à deux croisements de trois niveaux représente un piégeage cohérent de population.

Nous examinons plus en détail l'interaction hyperfine entre les spins des électrons et des noyaux. Dans le régime du blocage de spin avec deux électrons, lors de l'application d'un champ magnétique hors plan, nous observons un courant intermittent avec de l'hystérèse et une structure en entonnoir dans le courant de fuite, qui sont des aspects marquants de l'interaction hyperfine. Les mesures dévoilent une dépendance sur la tension de grille, des variations d'un dispositif à l'autre et une dépendance sur l'histoire de la tension de biais qui apparaît dans aucun modèle existant. Nous observons également des signatures de l'interaction hyperfine à biais élevé, au-delà du régime du blocage de spin. Nous caractérisons ces aspects et suggérons comment l'interaction

hyperfine peut jouer un rôle à biais élevé, quoique les états électroniques impliqués ne puissent pas être identifiés facilement. Comme première étape vers la compréhension de ce nouveau régime, nous décrivons une autre structure hystérétique en entonnoir observée à biais élevé où les états électroniques impliqués peuvent être identifiés comme des états à deux électrons, ce qui nous permet de postuler un mécanisme spécifique pour cet entonnoir.

List of Publications

1. D. G. Austing, C. Payette, G. Yu, J. A. Gupta, G. C. Aers, S. V. Nair, B. Partoens, S. Amaha, and S. Tarucha, *Characterization and modeling of single-particle energy levels and resonant currents in a coherent quantum dot mixer*, AIP Conference Proceedings, submitted (2010).

2. D. G. Austing, C. Payette, G. Yu, and J. A. Gupta, *Fine structure in the high bias current of vertical quantum dot molecules*, AIP Conference Proceedings, submitted (2010).

3. C. Payette, S. Amaha, T. Hatano, K. Ono, J. A. Gupta, G. C. Aers, D. G. Austing, S. V. Nair, and S. Tarucha, Gate adjustable coherent three and four level mixing in a vertical quantum dot molecule, Physica E, **42**, 2588 (2010).

4. C. Payette, S. Amaha, G. Yu, J. A. Gupta, D. G. Austing, S. V. Nair, B. Partoens, and S. Tarucha, *Coherent level mixing in dot energy spectra measured by magneto-resonant-tunneling spectroscopy of vertical quantum dot molecules*, Phys. Rev. B, **81,** 245310 (2010).

5. D. G. Austing, C. Payette, G. Yu, J. A. Gupta, G. C. Aers, S. V. Nair, S. Amaha, and S. Tarucha, *Slow and fast electron channels in a coherent quantum dot mixer*, Jpn. J. Appl. Phys., **49,** 04DJ03 (2010).

6. D. G. Austing, C. Payette, G. Yu, and J. A. Gupta, *Hysteretic funnel structures in vertical quantum dot molecules*, Physica E, **42,** 891 (2010).

7. C. Payette, D. G. Austing, G. Yu, J. A. Gupta, S. V. Nair, B. Partoens, S. Amaha, and S. Tarucha, *Branch current behavior at two level anti-crossings in vertical quantum dot single-particle spectra*, AIP Conference Proceedings, **1199,** 271 (2010).

8. C. Payette, D. G. Austing, G. Yu, and J. A. Gupta, *Hyperfine coupling effects induced by out-of-plane magnetic field throughout the two-electron spin blockade regime in a vertical quantum dot molecule*, AIP Conference Proceedings, **1199,** 437 (2010).

9. D. G. Austing, C. Payette, G. Yu, and J. A. Gupta, *Hyperfine-coupling-programming of current through coupled quantum dots with multiple-sweep bias voltage waveforms*, Jpn. J. Appl. Phys., **48,** 04C143 (2009).

10. C. Payette, B. Partoens, G. Yu, J. A. Gupta, D. G. Austing, S. V. Nair, S. Amaha, and S. Tarucha, *Modeling single-particle energy levels and resonance currents in a coherent electronic quantum dot mixer*, Appl. Phys. Lett., **94,** 222101 (2009).

11. C. Payette, G. Yu, J. A. Gupta, D. G. Austing, S. V. Nair, B. Partoens, S. Amaha, and S. Tarucha, *Coherent three-level mixing in an electronic quantum dot*, Phys. Rev. Lett., **102,** 026808 (2009).

12. D. G. Austing, C. Payette, S. V. Nair, G. Yu, J. A. Gupta, B. Partoens, S. Amaha, and S. Tarucha, *Scheme for coherently quenching resonant current in a three-level quantum dot energy level mixer*, Phys. Stat. Sol. (c), **6,** 940 (2009).

13. S. Amaha, C. Payette, J. A. Gupta, T. Hatano, K. Ono, T. Kodera, Y. Tokura, D. G. Austing, and S. Tarucha, *Two level mixing effects probed by resonant tunnelling through vertically coupled quantum dots*, Phys. Stat. Sol. (c), **5,** 174 (2008).

14. C. Payette, G. Yu, J. A. Gupta, D. G. Austing, S. V. Nair, B. Partoens, S. Amaha, and S. Tarucha, *Two-level anti-crossings high up in the single-particle energy spectrum of a quantum dot*, Physica E, **40,** 1807 (2007).

15. D. G. Austing, C. Payette, G. Yu, and J. A. Gupta, *Magnetic field-induced effects in the high source–drain bias current of weakly coupled vertical quantum dot molecules*, Physica E, **40,** 1118 (2007).

16. D. G. Austing, G. Yu, C. Payette, J. A. Gupta, C. Dharma-Wardana, and G. C. Aers, *High bias magneto-transport through two weakly coupled vertical quantum dots and quantum wells*, AIP Conference Proceedings, **893,** 789 (2007).

17. D. G. Austing, G. Yu, C. Payette, J. A. Gupta, and M. Korkusinski, *Probing by transport the single-particle energy spectrum up to high energy of one quantum dot with the ground state of an adjacent weakly coupled quantum dot*, Phys. Stat. Sol. (a), **204,** 508 (2007).

Statement of Contributions

The majority of the experiments described in this thesis (specifically all those on Devices I-V) were carried out by myself and D. G. Austing (my supervisor). Additionally, I also performed the data analysis on all of the experiments described with guidance from D. G. Austing.

However, many other researchers contributed to the work presented here. In terms of the growth and processing, the hetero-structure starting material for all the measured devices was grown by J. A. Gupta (NRC), while the processing for Devices I-V was executed by D. G. Austing (with assistance from members of the Nano-fabrication group at NRC), and for Device VI by S. Amaha (ICORP, Japan). All experiments on Device VI, as well as those on the four-gated device discussed in Sec. 5.4, were carried out by S. Amaha. In terms of theory, the self-consistent conduction band profile for the double-well triple-barrier hetero-structure presented in Chap. 3 was calculated by G. C. Aers (NRC). Model calculations exploring the inclusion of higher order terms to the dot confinement potential presented in Chaps. 4 and 5 were performed B. Partoens (Antwerp, Belgium). The matrix Hamiltonian model used in Chap. 5 was developed by S. V. Nair (Toronto) and fitting the experimental data to the model was done by either by S. V. Nair or G. C. Aers.

Table of Contents

List of Figures

List of Tables

List of Abbreviations, Symbols and Fundamental Constants

Abbreviations:

DAC	Digital-to-Analog Converter
DC	Direct Current
DET	Double Electron Tunneling
DNP	Dynamical Nuclear Polarization
FD	Fock-Darwin
NMR	Nuclear Magnetic Resonance
PECVD	Plasma-Enhanced Chemical Vapour Deposition
QD	Quantum Dot
QPC	Quantum Point Contact
SET	Single Electron Tunneling
SEM	Scanning Electron Microscope
TET	Triple Electron Tunneling

Symbols:

E_{add}	Addition energy
E_C	Charging energy
N	Total number of electrons in a quantum dot system
N_1	Number of electrons on quantum dot 1 in double dot system
N_2	Number of electrons on quantum dot 2 in double dot system
V_{SD}	Source-drain voltage
V_G	Gate voltage
I	Current
μ	Electrochemical potential
T	Temperature
R_T	Tunneling resistance
B-field	Magnetic field
B_n	Effective nuclear magnetic field
$B_{n,max}$	Effective nuclear magnetic field for fully polarized nuclear spins
n	Radial quantum number
ℓ	Orbital angular momentum quantum number
V_{eff}	Effective confinement potential in the x-y plane
$\hbar\omega_0$	Confinement energy for circular, parabolic confinement potential
n_x , n_y	Quantum numbers appropriate for two dimensional elliptical, parabolic confinement
$\hbar\omega_x$, $\hbar\omega_y$	Confinement energies along the x and y axes for elliptical, parabolic confinement potential
δ	Ellipticity
m^*	Effective mass of the electron
E_{C1}, E_{C2}	Intra-dot charging energies of dots 1 and 2 in a double dot
E_{CM}	Inter-dot electrostatic coupling energy between the dots in a double dot

E_{off}	Energy offset between the dots in a double dot at zero bias
ε	Detuning between the ground states of two coupled quantum dots
S	Singlet
T	Triplet
Γ	Inter-dot tunneling rate
Γ_U	Tunneling rate from source contact to upstream dot
Γ_D	Tunneling rate from downstream dot to drain contact
Δ_{SAS}	Bare inter-dot tunnel coupling energy
Ω_j	Inter-dot tunnel coupling between the upstream dot's 1s-like state and the downstream dot's *j*th state, where *j* labels the state's lateral component

Fundamental Constants:

e	1.602×10^{-19} C	Elementary unit of electric charge
k_B	8.617×10^{-5} eV/K	Boltzmann constant
h	4.135×10^{-15} eV·s	Planck's constant
$\hbar$	6.582×10^{-16} eV·s	Planck's constant divided by 2π
μ_B	5.788×10^{-15} eV/T	Bohr magneton

Chapter 1

Introduction

1.1 Quantum Dots

A quantum dot (QD) is a small region (or 'island') in a solid structure, typically a few tens to several hundreds of nanometers in size and consisting of roughly one thousand to one million atoms, in which electrons can be trapped [1-8]. The most identifiable characteristic of a QD is that the energy required to overcome Coulomb repulsion and add an extra electron to the dot, known as the charging energy, can not be neglected. Provided the charging energy exceeds the thermal energy, k_BT, where T is the temperature, the discrete nature of the charging will be resolvable. In practice, the number of electrons on a dot, *N*, may be large (several thousand) or small (even reaching the single electron limit). If the dot is sufficiently small, not only will the charging energy generally be larger, but quantum confinement can also become significant revealing the discrete energy spectrum of the dot. In this regime, the addition energy, which reflects both charging and quantum confinement, becomes strongly dependent on *N*, closely analogous to the ionization energy of a real atom. For this reason, few-electron QDs are often referred to as artificial atoms [9,10], although addition energies for dots (generally 1-10 meV) are typically three to four orders of magnitude less than ionization energies for atoms. QDs provide excellent opportunities not only for accessing atomic-like physics in the laboratory, but also for probing new physics or regimes not attainable in real atoms (see for example Ref. [11]).

Since single QDs can be regarded as artificial atoms, it is natural to think of systems of coupled QDs as artificial molecules. Systems of coupled QDs offer extra degrees of freedom providing access to new physics and new opportunities for applications (a particularly interesting example is quantum information processing).

In this thesis we will be interested in transport properties of QDs. Figure 1.1 shows cartoons of a typical set-up for transport measurements on a single QD, and a double QD system where the dots are connected in series. Tunnel barriers connect the dots to source and drain contacts. A tunneling current, *I*, flows through the dots in response to an applied bias voltage, V_{SD}. In the majority of realizations of QD systems, the dots are capacitively coupled to one or more gates. When voltages are applied to the gates the electrochemical potential of the dots can be tuned.

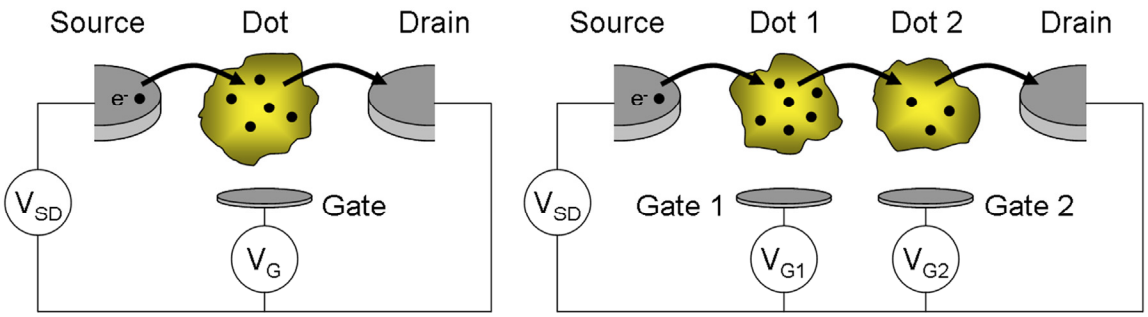

Fig. 1.1. Cartoons of a generic transport measurement set-up for a single QD with a single gate (left) and a system of two coupled QDs with two gates (right) (cartoon adapted from Ref. [4]).

1.2 Quantum Dot Structures for Transport

Much early work was performed with small metal grains located between source and drain contacts (see for instance Refs. [12-14]). This work focused primarily on electron charging and largely quantum confinement played no role. In order to observe

strong quantum confinement of electrons, techniques were developed in the late 1980s and early 1990s to fabricate semiconductor QDs (see for example Refs. [9,10,15-18]). In the twenty years since these pioneering works, single and coupled semiconductor QDs have been fabricated in many different geometries and material systems.

Semiconductor QDs intended for transport measurements can be conveniently divided into two categories according to how they are fabricated. The first category, namely 'top-down,' includes GaAs based lateral and vertical QDs [see Figs. 1.2(a)-(d)]. These dots are generally fabricated by combining conventional (uniform) layer growth techniques, such as molecular beam epitaxy, and standard processing techniques. On the other hand, the second category, namely 'bottom-up,' includes self-assembled QDs, and QDs defined in semiconducting nanowires, carbon nanotubes and graphene [see Figs. 1.2(e)-(h)]. Fabrication of these dots commonly involves unconventional growth techniques involving templates or catalysts, or lattice strain, and possibly unusual processing techniques (like scotch tape for graphene). Overall, the 'top-down' dots are more established having been around longer, while the 'bottom-up' dots offer some unique opportunities and advantages.

From a transport perspective, the most familiar type of QD is the GaAs-based lateral QD [see Figs. 1.2(a) and (b)]. These structures are fabricated by depositing metallic gates on top of a two-dimensional electron gas. Their major advantage is that operation of the metallic gates allows the tunnel barriers to be tuned in-situ (see reviews in Refs. [4,7,8]). The design of lateral QD devices is highly flexible and components for additional functionality, such as a quantum point contact (QPC) (see Ref. [19]), an on-chip microcoil (see Ref. [20]), or a micromagnet (see Ref. [21]), can be easily integrated.

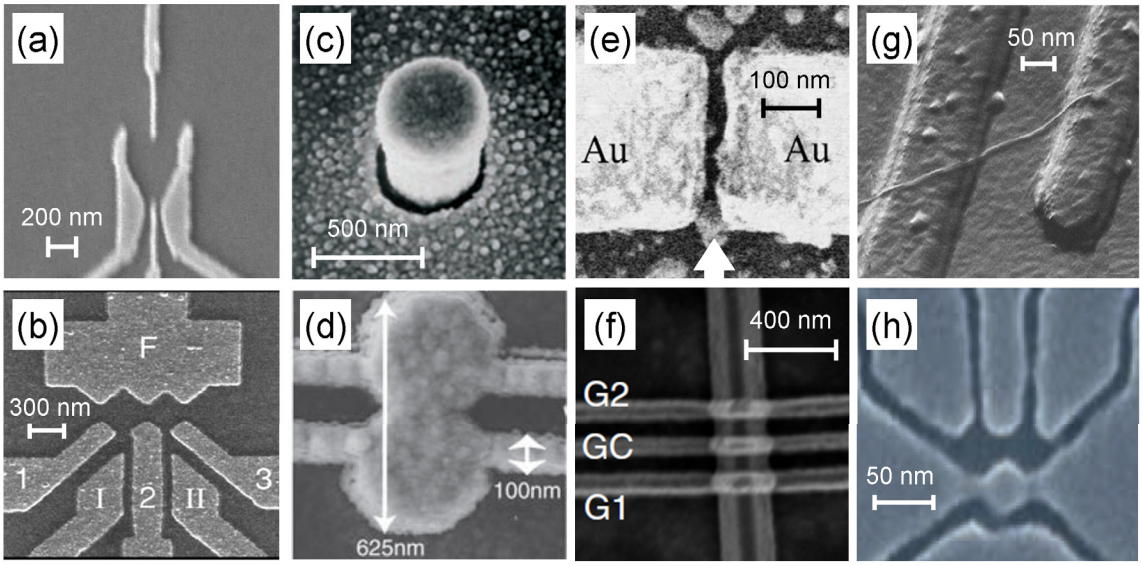

Fig. 1.2. Various examples of single and double QD structures for transport measurements. (a) Single GaAs-based lateral QD (image adapted from Ref. [22]). (b) Double lateral QD (image adapted from Ref. [23]). (c) GaAs-based vertical QD mesa (image adapted from Ref. [5]). (d) Double QD formed by coupling two vertical QD mesas laterally (image adapted from Ref. [24]). (e) Self assembled InAs QD, marked by the white arrow, located between two contacts (image adapted from Ref. [25]). (f) Double QD defined by metal gates deposited on top of an InAs nanowire (image adapted from Ref. [26]). (g) QD formed by a carbon nanotube lain on top of two contacts (image adapted from Ref. [27]). (h) QD defined in graphene (image adapted from Ref. [28]).

Another type of QD studied by transport is the vertical QD (see Refs. [29,30] as well as a review in Ref. [5]). These QDs, which are fabricated by etching a resonant tunneling structure into small mesas [see Fig. 1.2(c)], are known to be highly symmetric with a well defined confinement potential. In addition, it is possible for vertical QDs to be coupled together in either the vertical or lateral direction [see for instance Fig. 1.2(d)]. Single vertical QDs have been used to demonstrate an electronic shell structure [31], while vertically coupled double QD devices were employed for the original demonstration of the two-electron Pauli spin blockade [32] and for pioneering transport

measurements demonstrating the influence of electron spin-nuclear spin (hyperfine) coupling [33]. Weakly coupled vertical double QDs will be the experimental system we focus on in this thesis and many of the aforementioned topics will be expanded on in later chapters.

Compared to the more traditional 'top-down' GaAs based QDs, 'bottom-up' QDs collectively offer opportunities such as higher confinement energies, access to optical measurement techniques, and different coupling geometries and material properties. For instance, self-assembled QDs [see Fig. 1.2(e)], which are formed due to strain between two materials with different lattice constants (commonly InAs and GaAs), can have confinement energies greater than 20 meV (compared to ~5 meV for typical lateral and vertical QDs). These structures are most commonly studied by optical means, although they can also be contacted electrically. Meanwhile, transport measurements on QDs defined in nanowires, either by metallic gates [see Fig. 1.2(f)] or by hetero-structure barriers, are currently performed most commonly in InAs and InAs/InP (see review in Ref. [34]). These materials offer the advantage of inherently stronger spin-orbit coupling, while the cylindrical geometry of a nanowire provides a well defined lateral confinement potential. Finally, QDs in both carbon nanotubes [see Fig. 1.2(g)] and graphene [see Fig. 1.2(h)] offer the attractive possibility of studying electron spins in an environment where the hyperfine interaction can be minimized (for a recent review of QDs in graphene, see Ref. [35]).

1.3 Quantum Dot Applications

QDs continue to attract intense interest because they offer not only many possibilities for exploring basic physics on the nano-scale, but also new electronic and optical applications. In modern electronic devices, components, such as transistors, continue to decrease in size, a trend well described by Moore's law [36]. As this trend continues, the operation of such devices will increasingly be influenced by quantum mechanics. Not only does this present challenges, but it also offers many exciting opportunities for exploring new applications. One example, which has the potential to revolutionize the electronics and communications industries, is quantum information processing, which includes both quantum computing and quantum cryptography. In quantum computation, the basic building block is a two-level quantum system, known as a quantum bit (qubit), rather than the more familiar binary bit. With two (or more) coupled qubits, it is possible to implement quantum logic gates and by performing multiple quantum gates, quantum computation algorithms can be implemented.

The theory behind quantum computation, including the quantum gates and algorithms necessary to potentially solve computationally demanding NP-complete problems, such as, for example, integer factorization [37], and to perform simulations of quantum systems [38], is now quite well developed (see Ref. [39]). However, the physical implementation of quantum computation continues to lag behind. At the present time, several competing approaches for realizing quantum computation are being actively investigated from different fields of physics, including nuclear magnetic resonance, ion and atom traps, cavity quantum electro-dynamics, optics, solid state, and superconductors (see Ref. [40]). While experiments in these fields have explored much basic quantum

physics, they remain largely at the proof of principle stage in terms of performing actual quantum computation. A robust few-qubit test-bed which could execute useful basic quantum algorithms remains a modest goal (5-10 years) and significant innovation will be necessary before a full-scale (~100 or more qubits) quantum computer can be realized which outperforms conventional Si-based computers.

In 1998 Loss and DiVincenzo [41] proposed to use the spin of an electron trapped on a semiconductor QD as a qubit to carry out quantum computation algorithms. Since then, research in this field has exploded with a large number of groups pursuing this goal. While spins trapped on QDs may not be the most technologically advanced of the approaches to quantum computation currently being investigated, it is believed that this system offers several long term advantages. Firstly, solid state qubit fabrication processes are compatible with those of the semiconducting computing industry, offering high potential for integrated on-chip devices. Secondly, it is hoped that if one can make a single well-behaved semiconductor QD based qubit, then one could couple several essentially identical qubits together in order to perform useful quantum computation, i.e., semiconductor qubits are thought to be an inherently scalable system.

In fact, progress has been rapid and many of the steps necessary to demonstrate one and two qubit operations by coherent control and readout of electron spins confined in QDs have successfully been demonstrated. Some recent highlights include the implementation of QPCs as sensitive charge sensors [42] which can also be used for efficient spin readout via Pauli spin blockade, an effect originally demonstrated in a vertical double QD device [32]. Furthermore, high frequency techniques were developed to measure the spin relaxation time, T_1, in a single vertical QD [11]. Subsequently these

techniques were adapted for a lateral double QD system in order to measure the spin dephasing time, T_2^*, by separating and recombining a spin singlet state [43]. Later, coherent single electron spin rotation was demonstrated with the technique of electron spin resonance, using an oscillating B-field generated by an on-chip coil [20]. Subsequently, coherent control of the electron spin mediated by the spin orbit interaction was achieved electrically using an oscillating electric field applied to a local gate [44] and coherent spin rotations using micromagnets were recently realised [21].

While much progress has been made, many basic questions remain about QDs which must be answered before a useful quantum computer could ever be constructed with QDs as the building blocks.

1.4 Thesis Topics

Using weakly coupled vertical QDs, the experimental work described in this thesis will attempt to shed light on some particular topics which are of interest from the point of view of basic physics and may also be relevant for new applications in nano-electronics such as quantum information processing.

The familiar single-particle Fock-Darwin (FD) states, which arise from a strictly two-dimensional circular parabolic confinement potential under the influence of an out-of-dot-plane magnetic (B-) field, are widely used for the characterization and calculation of confined states in QD structures [1-4,6-8]. In Chap. 4, we will describe measurements of single-particle energy spectra of the constituent QDs in the QD devices. The QDs are demonstrated to be highly symmetric and so they are ideal vehicles for assessing to what degree the single-particle spectra of QD structures are in practice FD-like in character.

An initially unexpected, although positive, observation from the measured QD energy spectra is widespread anti-crossing and level mixing behaviour at B-field induced crossings of the single-particle states. Such anti-crossings are attributed to natural anharmonicity and anisotropy in the QD confinement potentials. Hence, the measurements can potentially shed valuable light on the microscopic form of the confinement potential in realistic QDs, often assumed to be perfectly symmetric in form, as well as addressing issues related to coherent tunneling.

The coupling and consequent coherent mixing between quantum levels, which leads to level anti-crossing and coherent quantum superposition phenomena, are of broad interest in many different types of low dimensional semiconductor nano-systems (diversely exemplified for two-level-systems in Refs. [45-53]). Many advanced quantum information protocols envisage coherent mixing between three (or more) levels in systems of three (or more) coupled QDs (see for example Refs. [54-59]). However, highly controllable devices with three (or more) coupled QDs are in their infancy (see for example Refs. [60,61]). In Chap. 5, we will focus on essentially the same physics but accessed by an alternative approach, namely multiple levels mixing within a single QD, i.e., we exploit *intra*-dot level mixing as opposed to *inter*-dot mixing. We will study coherent multi-level mixing at crossings between two, three and even four single-particle levels in the measured QD energy spectra introduced in Chap. 4. Suppression of an otherwise strong resonance due to coherent mixing (‘dark state formation’) at three-level crossings, an all-electrical analogue of coherent population trapping from the realm of quantum and atom optics [62,63], will figure prominently. These observations are

potentially useful for quantum coherent phenomena in transport involving multiple quantum levels.

It has become apparent only comparatively recently that in QD transport measurements one needs to consider how confined electrons can couple to nuclei in the host material (see the pioneering work of Ref. [33]). Indeed, it is now realized that in any III-V semiconductor QD based qubit the main source of electron decoherence is hyperfine coupling to nuclear spins (see for example Refs. [26,43,64-69]), although many basic questions about the hyperfine interaction in QDs remain. In Chap. 6, we will describe measurements that probe the hyperfine interaction, focusing on two different electronic regimes. In the first regime, namely the familiar two-electron spin blockade region, we will perform experiments which bring to light a strong gate voltage dependence, considerable device-to-device variations and a bias voltage history dependence emphasizing the many unanswered questions about the hyperfine induced fine features observed in this regime. Nonetheless, by using multiple-sweep mHz bias voltage waveforms we will demonstrate that we can program the total current response in this regime via the hyperfine interaction. The second regime is at high bias, well outside the spin blockade region, and in this regime we will probe features which are consistent with a hyperfine interaction origin. However, the electronic states and the tunneling processes involved in this regime are too numerous and too complicated to identify hindering the development of any detailed models. As an initial attempt to understand the features observed at high bias, we will finish by focusing on a particular high bias region where the electronic states can be identified as two-electron states and spin-blockade-like physics can play a role.

This thesis is arranged as follows. We begin in Chap. 2 by providing the relevant background information in preparation for the experimental work to follow. In particular, to motivate the work described in Chaps. 4 and 5, we will discuss possible techniques for acquiring information about the single-particle states of single and double QDs. Furthermore, we will introduce the concept of spin blockade which, as discussed in Chap. 6, can provide a convenient mechanism to probe the hyperfine interaction in double QDs. In Chap. 3 we begin by explaining the device geometry, hetero-structure layer details and device processing before proceeding to discuss some basic transport measurements which characterize the devices. This will enable us to identify devices appropriate for performing the desired experiments. In Chap. 4, we describe how we can measure the single-particle energy spectra of the constituent QDs in the devices and then we compare these spectra to spectra calculated for ideal elliptical and parabolic confinement. In Chap. 5, we investigate coherent mixing at specific two-, three- and four-level crossings from the measured single-particle dot energy spectra, focusing on those where destructive interference leads to the suppression of an otherwise strong resonance. In Chap. 6, we describe observations of current switching, hysteresis, funnel-like structures and slow oscillations, which we attribute to the hyperfine interaction, in two distinct electronic regimes. Finally, Chap. 7 contains the conclusions and a discussion of possible directions for future work.

Chapter 2

Introduction to Quantum and Spin Effects in Double Quantum Dots

In this chapter we provide some background information necessary to understand Chaps. 3-6 of this thesis.

The first major goal of this thesis is to study the energy spectra of single-particle states arising from quantum confinement in vertical QDs. As such, in this chapter, we will describe available techniques to obtain the desired information about such states from transport measurements. We begin with the simplest technique which comes to mind, namely measuring Coulomb oscillations in a single QD. Although information about single-particle (ground) states can be obtained using this technique, it is ultimately limited because the quantum effects of interest are obscured by charging effects. The next logical approach involves measuring a single QD at finite bias. This technique allows single-particle excited states to be accessed directly however, the information it can provide is also restricted because the energy window over which such states can be easily observed is limited to about the dot confinement energy (typically a few meV). Subsequently, we will introduce the technique of Ref. [70] which overcomes these limitations so that the single particle states of one of the constituent dots in a double QD device can be probed directly over a wide energy window by using the ground state of the other dot as an 'energy filter'.

The second major goal of this thesis is to probe electron spin-nuclear spin (hyperfine) interactions. In this chapter, we will introduce the concept of spin blockade, which has proven instrumental in previous experiments which probe the hyperfine interaction in double dots.

2.1 Probing Quantum Effects in Single Quantum Dots

In this section we will consider standard transport measurements that can be performed on a single QD (recall Fig. 1.1). Although the ultimate goal is to gain access to information about the single-particle states, we begin in Sec. 2.1.1 by ignoring quantum effects entirely in order to introduce orthodox Coulomb blockade theory as a starting point. Subsequently, in Sec. 2.1.2 we will introduce the Fock-Darwin (single-particle) states which are widely employed to model the single-particle states of a QD. In Sec. 2.1.3, we will turn to a few-electron QD and explain how information about the single-particle states can be extracted from the Coulomb oscillations. Subsequently, Sec. 2.1.4 will describe how when a finite bias is applied the Coulomb oscillation peaks change into current 'stripes'. This will prepare the way for a discussion in Sec 2.1.5 of how single-particle excited states appear in current 'stripes.'

2.1.1 Orthodox Coulomb Blockade

Before we outline orthodox Coulomb blockade theory, we recall under what conditions charging effects are important. As described in Ref. [4], there are two conditions which must be satisfied for single electron charging to have a measureable effect. First, the charging energy, E_C, expressed as $E_C = e^2/C$, where C is the total

capacitance of the dot, must be larger than the thermal energy, $k_B T$. Second, the resistance of the tunnel barriers, R_T, must be sufficiently large that the electrons can be regarded as localized either in one of the contacts, or on the dot. To quantify this, the characteristic timescale for single electron charging is $\Delta t = R_T C$ and the corresponding change in energy is $\Delta E = E_C$. Thus, by the Heinsenberg uncertainty relation, $\Delta E \Delta t = (e^2/C)(R_T C) > h$, so R_T must be larger than $h/e^2 \approx 26$ KΩ, the resistance quantum.

Provided that the two preceding conditions can be satisfied, orthodox Coulomb blockade theory can be applied (we will demonstrate that these two conditions are met for the measurements we perform on weakly coupled double QD devices in Chap. 3). We now define several important quantities. i. The energy window which opens when a bias is applied, $eV_{SD,}$, is defined as μ_S - μ_D where μ_S and μ_D are the chemical potentials (Fermi levels) of the source and drain contacts. We will initially consider the case of $V_{SD} \approx 0$ and defer finite bias until Sec. 2.1.3. ii. The electrochemical potential of a dot, $\mu_{dot}(N)$, is defined as $U(N) - U(N-1)$, where $U(N)$ is the energy of the N-electron (ground) state. iii. The addition energy, $E_{add}(N)$, is defined as $\mu_{dot}(N+1) - \mu_{dot}(N)$. Within a constant interaction picture, the charging energy, effectively the Coulomb interaction energy for each distinct pair of electrons trapped on the dot, is a constant, and so, in the absence of quantum effects, $E_{add}(N)$ is given by Eq. 2.1,

$$E_{add}(N) = \mu_{dot}(N+1) - \mu_{dot}(N) = E_C \qquad (2.1).$$

Suppose that initially N electrons are trapped on the dot, meaning that $\mu_D \geq \mu_{dot}(N)$ and $\mu_{dot}(N+1) \geq \mu_S$, so that no state lies within the energy window [see Fig. 2.1(a)]. In this situation, the number of electrons on the dot is fixed and no current flows

through the system. This condition is referred to as Coulomb blockade (see Refs. [71-73]). In this classical picture, adding another electron to the dot requires energy $E_{add}(N) = E_C$.

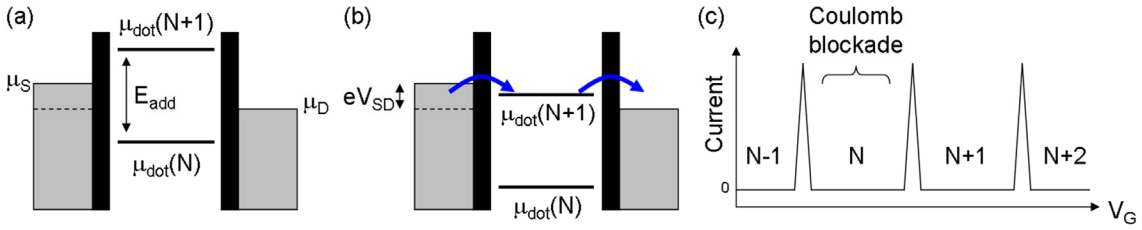

Fig. 2.1. (a) and (b) Potential diagram for a QD. The states in the source and drain contacts are filled up to μ_S and μ_D respectively, while electrons in the QD occupy the energy levels up to $\mu_{dot}(N)$. In (a) [(b)] electron transport through the system is blocked (allowed). (c) Schematic diagram of Coulomb oscillation peaks measured for $V_{SD} \approx 0$.

The Coulomb blockade can be lifted by applying a voltage, V_G, to the gate (recall Fig. 1.1), which moves the ladder of electrochemical potentials up (negative V_G) or down (positive V_G). For example, when V_G is made more positive the condition $\mu_S \geq \mu_{dot}(N + 1) \geq \mu_D$ can be satisfied in which case electrons can tunnel onto and off of the dot [see Fig. 2.1(b)]. Due to Coulomb blockade, only one additional electron can occupy the dot at a time meaning that the number of electrons on the dot will fluctuate between $N \leftrightarrow N + 1$. As V_G is swept continuously towards more positive values, each time the condition $\mu_S \geq \mu_{dot} \geq \mu_D$ is satisfied current can flow, leading to a series of current peaks, known as Coulomb oscillation peaks, separated by regions of Coulomb blockade (where the dot occupancy is fixed) [see Fig. 2.1(c)]. The separation between the current peaks is proportional to E_{add} (see Eq. 2.1), and so in this classical regime, under the assumption of a constant interaction, the peaks are evenly spaced.

Until now, we have neglected quantum effects. However, if we include them, $E_{add}(N)$ from Eq. 2.1 is modified as given in Eq. 2.2,

$$E_{add}(N) = \mu_{dot}(N+1) - \mu_{dot}(N) = E_C + \Delta E \qquad (2.2),$$

where ΔE is the energy difference between the single-particle states occupied by the N and $N + 1$ electrons. This suggests that the spacings between Coulomb oscillation peaks can reveal information about the single-particle states, although it will be 'tied up' with Coulomb interactions. We will explore this further in Sec. 2.1.3, but first we must introduce an appropriate confinement potential in order to determine ΔE for the single-particle states of the QDs of interest.

2.1.2 Single-Particle States of a Two Dimensional Harmonic Oscillator

We now picture a QD disc where electrons are strongly confined in the z-direction (out-of-dot-plane) and weakly confined in the x- and y-directions (in-dot-plane or lateral direction). For such a dot, the lateral confinement is commonly assumed to be well approximated by a circular parabolic confinement potential [4,5,10,31]. Explicitly, the lateral confinement potential is taken to be $V(r) = \frac{1}{2}m^*\omega_0^2 r^2$, where $r = \sqrt{x^2 + y^2}$ is the distance from the dot center, ω_0 is the oscillator frequency and m^* is the effective mass of the electron.

Considering such a circular parabolic confinement potential, the non-interacting Schrödinger equation can be solved exactly, resulting in eigenenergies $E_{n,\ell} = \hbar\omega_0(2n + |\ell| + 1)$ at zero B-field, where n (= 0, 1, 2, …) and ℓ (= 0, ±1, ±2, …) are respectively the

radial and orbital angular momentum quantum numbers [74,75]. This solution reveals quantized single-particle energy states organized into groups of degenerate states which are separated by the confinement energy, $\hbar\omega_0$. This arrangement of states is known as a shell structure, where the M^{th} shell contains M degenerate states [the first shell contains only the ground $(n,\ell) = (0,0)$ state, while the second shell contains the degenerate (0,1) and (0,-1) states and so on].

If we additionally consider a B-field applied in the z-direction, the non-interacting Schrödinger equation remains exactly solvable for a circular parabolic confinement potential [74,75]. The eigenenergies are now given by Eq. 2.3,

$$E_{n,\ell}(B) = (2n + |\ell| + 1)\hbar\sqrt{\tfrac{1}{4}\omega_c^{\,2} + \omega_0^{\,2}} - \tfrac{1}{2}\ell\hbar\omega_c \qquad (2.3),$$

where $\hbar\omega_C = \hbar eB/m^*$ is the cyclotron energy. States with these eigenenergies are known as Fock-Darwin (FD) states (note that each state is doubly spin degenerate). The FD spectrum shown in Fig. 2.2 displays the evolution of the energies of these states as a function of B-field. This ideal calculated spectrum will feature prominently in Chap. 4 as the starting point for modeling the single-particle dot energy spectra we measure.

The shell structure of the FD states is apparent at B = 0 T, but as one moves to finite B-field the degeneracies are lifted. In particular, for very weak B-fields, states with $\ell > 0$ ($\ell < 0$) move towards lower (higher) energy. As the B-field is increased, there are many points where degeneracies occur as two or more single-particle states are brought into alignment. The ability to access such level crossings will be critical for the investigation in Chap. 5. Note that at very high B-fields the states which have the same value of $n + \frac{1}{2}|\ell| - \frac{1}{2}\ell$ merge into the same Landau level, but for the selected confinement energy, this occurs well beyond 6 T and so is not visible in Fig. 2.2.

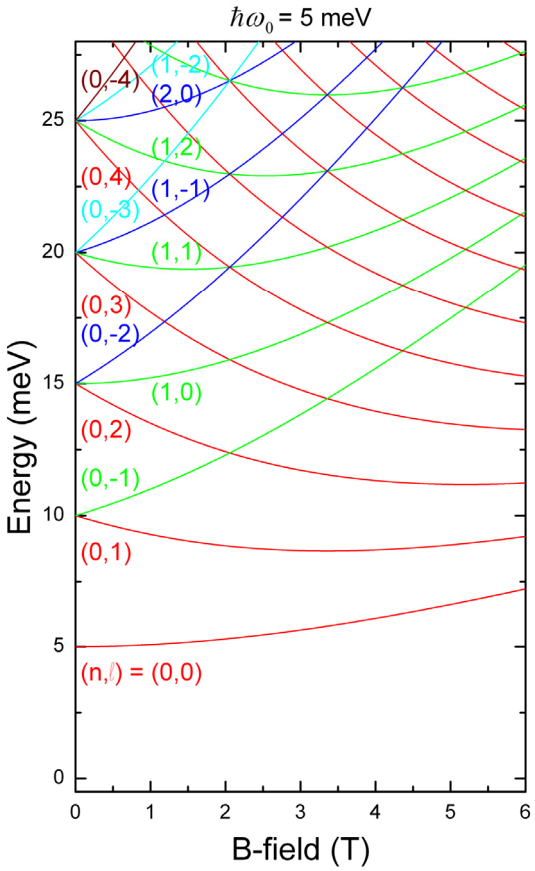

Fig. 2.2. FD spectrum calculated with confinement energy $\hbar\omega_0$ = 5 meV. States from the first five shells are labelled by their quantum numbers (n,ℓ) and states which merge to the same Landau level at high B-field are coloured the same.

The wavefunctions for the FD states are given by Eq. 2.4,

$$\psi_{n,\ell}(r,\phi) = \frac{e^{i\ell\phi}}{\sqrt{2\pi}l_B}\sqrt{\frac{n!}{(n+|\ell|)!}}e^{-r^2/4l_B{}^2}\left(\frac{r}{\sqrt{2}l_B}\right)^{|\ell|}L_n{}^{|\ell|}\left(\frac{r^2}{2l_B{}^2}\right) \tag{2.4}$$

where $L_n{}^{|\ell|}$ are the generalized Laguerre polynomials and $l_B = \sqrt{\hbar/m^*\sqrt{\frac{1}{4}\omega_c{}^2+\omega_0{}^2}}$ is the effective magnetic length. Figure 2.3 plots the square of the wavefunctions, $\left|\psi_{n,\ell}(r,\phi)\right|^2$, for some of the lower energy states with different values of n and ℓ. Note that for two states which differ only by the sign of ℓ, $\left|\psi_{n,\ell}(r,\phi)\right|^2$ is the same for both as the

wavefunctions differ only by a phase factor (see Eq. 2.4). Additionally, note that the (0,0) wavefunction is the most spatially compact and that the wavefunctions with higher values of n and ℓ spread out radially (this point will be relevant in Chap. 5).

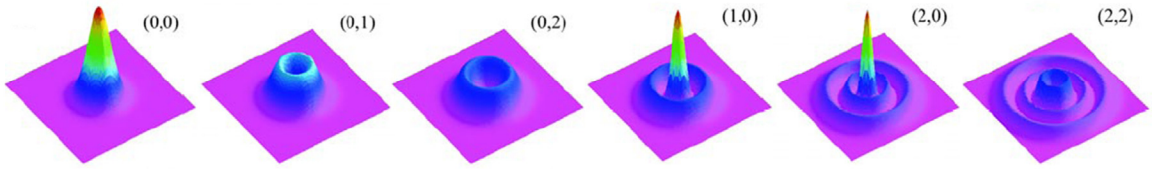

Fig. 2.3. Plots of the squared FD wavefunctions (given by Eq. 2.4) for several different values of (n, ℓ) (figure adapted from Ref. [5]).

In this introductory section the FD states are labelled by their quantum numbers n and ℓ. However, throughout this thesis, we will interchangeably use an equivalent, more intuitive, notation, namely that of atomic orbitals, i.e., 1s for the ground state in the first shell; $2p^+$ and $2p^-$ for the two states in the second shell and so on. In this notation, the number $M = 2n + |\ell| + 1$ indexes the shell [the M^{th} shell has M states (degenerate at 0 T)], while the letter relates to $|\ell|$ with $|\ell| = 0, 1, 2, 3, 4, 5, \ldots$ corresponding to s, p, d, f, g, h, …, and the + or – superscript refers to the sign of ℓ.

2.1.3 Coulomb Oscillations in a Few-Electron Circular Parabolic Quantum Dot

Now that the FD spectrum has been introduced, we pick up from Sec. 2.1.1 and discuss the Coulomb oscillation peak spacings for a few-electron circular parabolic QD where the quantum confinement of electrons on the dot now plays an important role.

Figure 2.4(a) shows a measurement of Coulomb oscillations performed with a single vertical QD [31]. Everywhere to the left of the first peak, the current is zero, indicating that the dot is empty ($N = 0$) and each successive peak marks the addition of a single electron to the dot [recall Fig. 2.1(c)]. The spacing between adjacent peaks, which is proportional to E_{add}, varies significantly as a function of N, a hallmark of quantum effects [recall that in the classical regime, under the assumption of a constant interaction, E_{add} is fixed (see Eq. 2.1)]. In particular, E_{add} is significantly larger when the dot contains 2, 6 or 12 electrons [see inset to Fig. 2.4(a)]. If we assume that the N^{th} electron entering the dot occupies the N-electron ground state, then this dependence can be simply explained in terms of the FD spectrum's shell structure. Since E_{add} consists of a purely electrostatic part, E_C, and a purely quantum part, ΔE (recall Eq. 2.2), it is immediately apparent that when an electron is added to an empty shell, the energy cost will be greater by an amount $\Delta E = \hbar\omega_0$. Recalling Fig. 2.2, the first shell, which consists of only the (0,0) state, can contain two electrons (with anti-parallel spin), while the second shell, which consists of the degenerate (0,1) and (0,-1) states, can contain four electrons. To see how this impacts the filling, consider the following. If we begin with one electron on the dot in the (0,0) state, when the second electron is added it also goes into the (0,0) state with anti-parallel spin, at a cost of E_C, under the assumption of a constant interaction (see Sec. 2.1.1). However, when the third electron is added, it must go into one of the two degenerate states in the second shell, as the (0,0) state is full, and so $E_{add} = E_C + \hbar\omega_0$. In a similar fashion, adding electrons four through six only requires energy E_C as they all enter into degenerate states in the second shell, but when adding the seventh electron, it must enter one of the states in the third shell and again $E_{add} = E_C + \hbar\omega_0$ [see Fig. 2.4(b)].

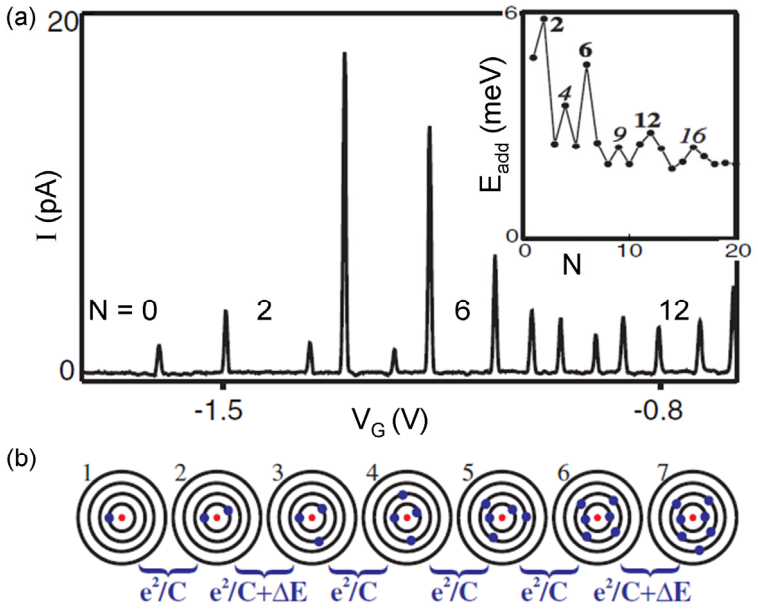

Fig. 2.4. (a) Coulomb oscillations as a function of V_G measured with $B = 0$ T and a small applied bias (V_{SD} = 150 μV) [31]. The inset shows the spacing between adjacent peaks. (b) Schematic representation of the shell structure of a QD, with E_{add} shown (figure adapted from Ref. [5]).

The underlying shell structure of a FD spectrum is readily apparent from the increased peak spacings observed when the states in a shell are full (see the large addition energies for N = 2, 6 and 12 in the inset to Fig. 2.4). *However*, for the simple picture described we would expect $E_{add} = E_C$ for all values of N except when shells are full (N = 2, 6, 12, …) in which case $E_{add} = E_C + \hbar\omega_0$. Evidently, this is not the case for the measured addition energies, which tend generally to increase as N is decreased. The reason for this is that in order to reduce N, a more negative V_G is required and hence the dot is 'squeezed' more (see Ref. [76]). This results in increases of both the Coulomb interactions and the confinement energy. Consequently, E_{add} also increases. Additionally, note that the unusually large E_{add} for half filled shells [see for example N = 4, 9, and 16]

can be attributed to exchange interactions and Hund's first rule [31] indicating further that the constant interaction picture is only an approximation.

As discussed in Sec. 2.1.2, the single-particle states in a circular parabolic QD are expected to evolve according to the FD spectrum as a function of B-field. Figure 2.5(a) shows the evolution of the Coulomb oscillation peaks from Fig. 2.4(a) as a function of B-field for a vertical QD. The first thing to note in Fig. 2.5(a) is that the peaks evolve in pairs, which is due to the fact that two electrons with opposite spin can occupy each single-particle state, and the two peaks in each pair are separated by E_C. Also evident from Fig. 2.5(a) is the fact that as N increases (for $N \geq 5$) the positions of the peaks begin to display an increasing number of 'wiggles.' These 'wiggles' can be understood in terms of the B-field evolution of the FD states. For example, consider the seventh and eighth Coulomb oscillation peaks which correspond to adding respectively the seventh and eighth electrons to the dot. These two peaks both show two 'wiggles,' labelled α and β in Fig. 2.5(a). Given that each FD state can hold up to two electrons, the seventh and eighth electrons must enter into the fourth lowest energy state as the lower energy states will be filled by the first six electrons already on the dot. Correspondingly, the relevant ground state for seven and eight electrons is highlighted in red in Fig. 2.5(b). Clearly, electrons which occupy this state undergo transitions in their quantum numbers as the B-field is increased. Explicitly, these electrons, which begin in the (0,2) single-particle state transition to the (0,-1) state at ~1.3 T and then to the (0,3) state at ~2.0 T. Correspondingly, two 'wiggles' are observed for the seventh and eighth peaks at ~1.3 T and ~2.0 T in 2.5(a).

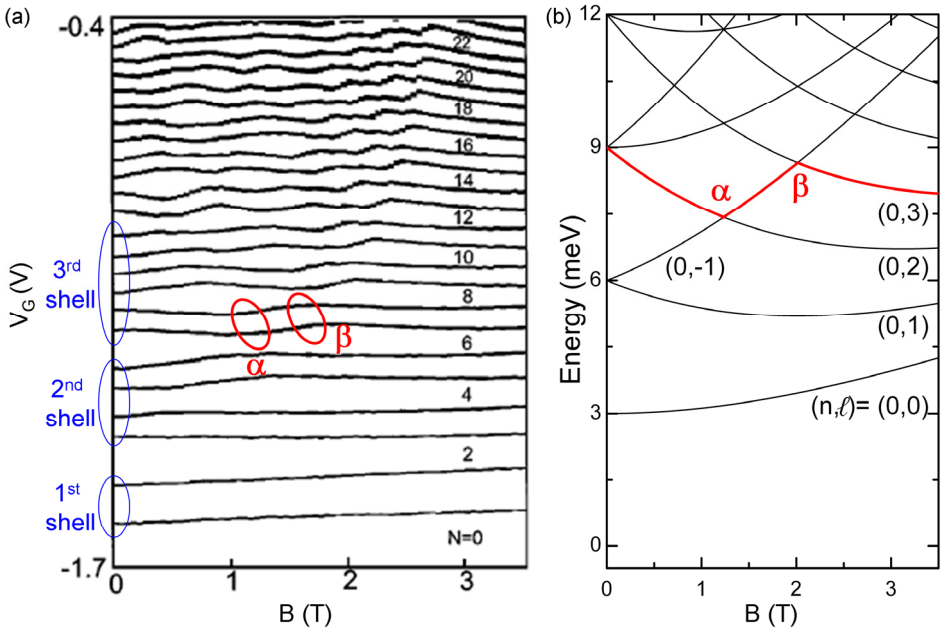

Fig. 2.5. (a) Position of Coulomb oscillation peaks as a function of B-field. The FD shell structure is apparent at 0 T (figure adapted from Ref. [31]). (b) FD spectrum calculated with confinement energy $\hbar\omega_0 = 3$ meV [appropriate for discussing the data in (a)].

It is important to note that while the data described in Figs. 2.4(a) and 2.5(a) reveal clear evidence for a FD shell structure, there are nonetheless several important limitations to the information we can easily acquire about single-particle states from Coulomb oscillation measurements which will motivate us to look for other methods of probing the quantum effects of interest. Firstly, these experiments generally involve many electrons trapped on the dot. Consequently, except for the first Coulomb oscillation peak, Coulomb interactions must be accounted for. If these interactions could easily be accounted for by a constant interaction, the quantum effects of interest could be trivially separated from the charging effects (see Ref. [77]). However, as N increases we see evidence that the Coulomb interaction is not constant. Specifically, in addition to the fact that E_C generally decreases as N increases [recall the inset to Fig. 2.4(a)], small deviations in the peak spacings occur throughout Fig. 2.5(a) (see for example the second

shell for B < 0.5 T). These deviations can be attributed to exchange effects [77]. As a consequence, it is challenging to extract information about the single-particle states from the Coulomb oscillation peak spacing as N becomes large. Secondly, as V_G is made more positive, the dots are squeezed less, and, not only does E_C decrease, but so does $\hbar\omega_0$. This ultimately means that confinement effects of interest become washed out as N becomes larger. Thirdly, although most 'wiggles' in Fig. 2.5 are due to two-level crossings in the FD spectrum, crossings involving more levels are harder to discern. This is because such crossings occur at higher energy (recall Fig. 2.2) and hence require a more positive V_G to access. However, the V_G range in Fig. 2.5 exceeds 1 V, which is already a large portion of the available range (see discussion in Sec. 3.3.2).

Due to these complications, we examine other techniques for probing quantum effects in QDs. While Coulomb oscillation measurements are limited to probing the ground single-particle state directly, it is possible to access excited single-particle states and avoid Coulomb interactions entirely by other means. Such measurements must be performed at finite bias and so in the next section, as a starting point, we first explore what happens to the Coulomb oscillations as the bias across the dot is increased.

2.1.4 Coulomb Blockade Diamonds

Turning to transport through a few-electron QD at finite bias, we enter the realm of non-linear transport. The primary goal of discussing this regime here is to explain how to measure single-particle excited states in a single QD. However, the general description of the transport processes at high bias will also lay the groundwork for understanding high bias transport in double QD devices (see also Sec. 2.2.2). This will be of particular

importance in Chap. 6. Furthermore, identification of the single-electron tunneling (SET) regime in double QD devices will be critical to the measurements described in Chaps. 4 and 5.

Figure 2.6(a) plots the differential conductance (dI/dV_{SD}) measured in the V_{SD}-V_G plane for a single vertical QD. The most prominent feature in Fig. 2.6(a) is the series of diamond shaped regions near zero bias inside which the current is essentially zero. With an I-V_G trace measured at zero bias in mind (recall Fig. 2.4), it is clear that the diamond shaped regions correspond to regions of Coulomb blockade (widely referred to as Coulomb diamonds) and the points where they touch at zero bias mark the location of the Coulomb oscillation peaks. The region at the bottom of Fig. 2.6(a) (labelled $N = 0$) indicates where the dot is empty ('pinched off') while moving towards more positive V_G, the number of electrons trapped on the dot increases by one in each Coulomb diamond. Lines running parallel to the edges of the Coulomb diamonds are also visible. Many of those with negative (positive) slopes in forward (reverse) bias correspond to transport through N-electron excited states. We will discuss excited states in Sec. 2.1.5, but for the moment we focus only on ground states.

To understand how a finite bias can lift Coulomb blockade, consider the $N = 2$ Coulomb blockade diamond as an example, and specifically the two values of V_G indicated by dotted lines in Fig. 2.6(a). In both cases, at zero bias no current flows because of Coulomb blockade. As V_{SD} is increased, no current flows until we reach a point on either the upper or lower edge of the diamond. At the point on the upper (lower) edge the condition $\mu_S = \mu_{dot}(3)$ [$\mu_{dot}(2) = \mu_D$] is satisfied, i.e., an energy level enters the energy window and current can flow [see Figs. 2.6(b) and (c)].

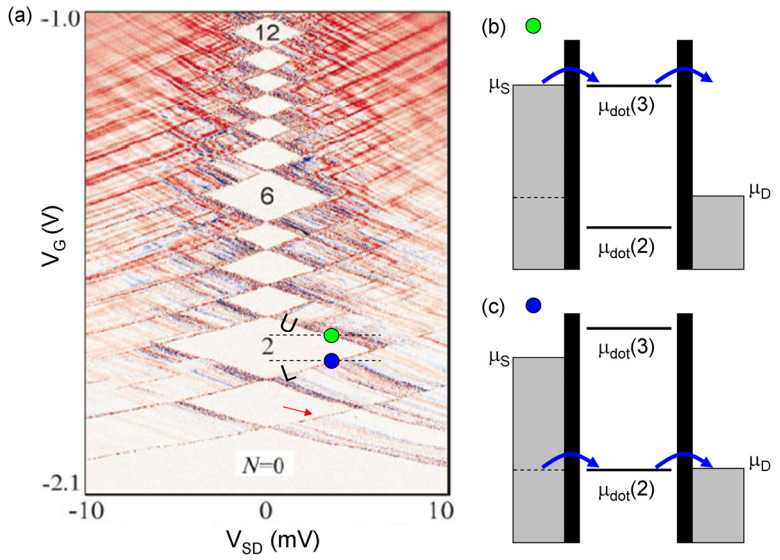

Fig. 2.6. (a) Numerically derived dI/dV_{SD} plot showing the first few Coulomb diamonds measured in a single vertical QD close to zero bias. Red, white and blue correspond to positive, zero and negative dI/dV_{SD}. The red arrow indicates tunneling through an $N = 1$ excited state (figure adapted from Ref. [78]). (b) and (c) Potential diagrams for a QD with a finite V_{SD} applied at two different values of V_G. The diagrams are drawn for V_{SD} and V_G conditions corresponding to points on the upper and lower edges of the $N = 2$ Coulomb diamond [labelled U and L in (a)].

More generally, at finite bias there are two sets of conditions for the onset of transport, namely $\mu_S \geq \mu_{dot}(N + 1)$ and $\mu_{dot}(N) \geq \mu_D$ related to the addition and removal of electrons respectively. These two conditions give rise to two families of lines in the V_{SD}-V_G plane [see black lines in Fig. 2.7(a)] which map out the Coulomb diamonds close to zero bias. While the discussion so far has been limited to the case when a maximum of one state is available for tunneling at a time [referred to as SET], extending these lines to higher bias allows us to identify regions of the V_{SD}-V_G plane where multi-electron tunneling is possible (see Ref. [8]). We highlight two specific points in the V_{SD}-V_G plane as illustrative examples. At the point labelled by a red circle in Fig. 2.7(a), the conditions $\mu_S = \mu_{dot}(2)$ and $\mu_{dot}(1) = \mu_D$ are both satisfied [see Fig. 2.7(b)]. This means that both the

single-electron ground state and the two-electron ground state are energetically available for tunneling and consequently the number of electrons on the dot can fluctuate between $0 \leftrightarrow 1 \leftrightarrow 2$, a situation referred to as double-electron tunneling (DET). Meanwhile, at the point labelled by the pink circle in Fig. 2.7(a), the conditions $\mu_S = \mu_{dot}(3)$ and $\mu_{dot}(1) = \mu_D$ are satisfied. In this case, triple-electron tunneling (TET) is possible, i.e., the number of electrons on the dot can fluctuate between $0 \leftrightarrow 1 \leftrightarrow 2 \leftrightarrow 3$ [see Fig. 2.7(c)].

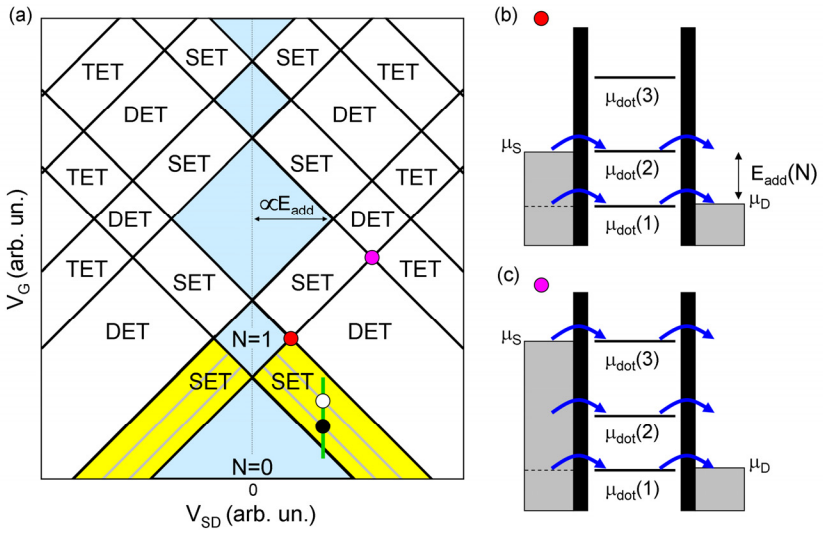

Fig. 2.7. (a) Schematic charging diagram showing the location the first few Coulomb blockade diamonds (shaded in blue) for a single vertical QD [the width of each diamond is proportional to $E_{add}(N)$]. The region where the dot is empty is labelled $N = 0$ and the first Coulomb diamond is labelled $N = 1$. The grey lines indicate where transport is possible through the first and second $N = 1$ excited states (see Sec. 2.1.5). (b) [(c)] Potential diagram for a QD corresponding to the V_{SD} and V_G condition indicated by the red [pink] point in (a). For the situation pictured in (b) [(c)] DET (TET) is possible.

Although tunneling involving fluctuations between more than three configurations is also possible at higher bias, for simplicity, we label only regions where SET, DET and TET can occur in Fig. 2.7(a). Unless otherwise specified, from this point onward whenever we use the term 'SET region,' we will be referring to the two SET regions

adjacent to the $N = 0$ region [highlighted in yellow Fig. 2.7(a)]. In the next section, we turn to these regions, where transport through single-particle excited states is possible [recall the feature indicated by the red arrow in Fig. 2.6(a)]. The measurements we describe in Chaps. 4 and 5 will be performed in the corresponding SET regions of a double dot (see also Sec. 2.2.2).

2.1.5 Excited State Spectroscopy of Single Quantum Dots

Having discussed the N-electron ground states of a QD at finite bias in Sec. 2.1.4, we are now prepared to describe how to acquire the desired information about single-particle states by accessing the $N = 1$ excited states directly. In particular, we now summarize the results of Ref. [78] which demonstrate to what extent these states evolve according to the FD spectrum when an out-of-dot-plane B-field is applied. For clarity, in this section we use the notation $\mu_{dot}^{gs}(N)$ [$\mu_{dot}^{esM}(N)$] to identify the electrochemical potential of the N-electron ground (M^{th} excited) state.

To demonstrate how $N = 1$ excited states can be seen in a single dot, suppose that we initially fix V_{SD} and V_G at a point just below the lower edge of the forward bias SET region and then make V_G more positive [see for example the green line in Fig. 2.7(a)]. At the point labelled by a black circle in Fig. 2.7(a), the first $N = 1$ excited state enters the energy window [see Fig. 2.8(a)]. As V_G is made even more positive, additional $N = 1$ excited states can enter the energy window [see for example Fig. 2.8(b) which corresponds to the point labelled by a white circle in Fig. 2.7(a)]. Each additional channel which is made available for tunneling can potentially lead to a change in current [see for example the feature highlighted by the red arrow in Fig. 2.6(a)]. It is important to note

that if $\mu_{dot}^{esM}(1) > \mu_{dot}^{gs}(2)$, a change in current attributable to the M^{th} $N = 1$ excited state can still be observed, but it will not be located in the SET region and so the presence of two-electron states will complicate its identification. We stress that when the $N = 1$ ground state and one or more $N = 1$ excited states are within the energy window, transport is only possible through one of these states at a time due to Coulomb blockade, meaning that the situations depicted in Fig. 2.8 still correspond to SET.

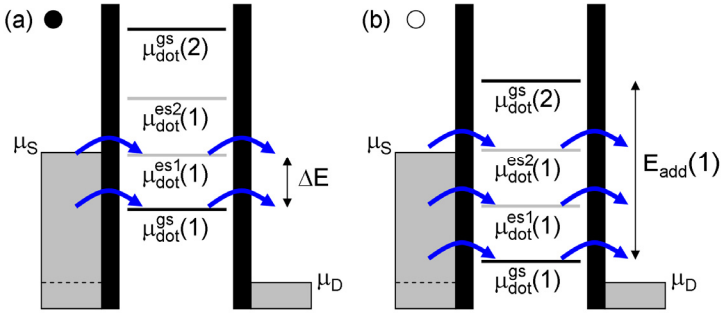

Fig. 2.8. (a) and (b) Potential diagrams for a QD with a finite V_{SD} applied. In (a) for the situation depicted where $\Delta E < E_{add}$, transport is possible through the $N = 1$ ground state [black line labelled $\mu_{dot}^{gs}(1)$] or the first $N = 1$ excited state [grey line labelled $\mu_{dot}^{es1}(1)$]. In (b) V_G has been adjusted so that additionally the second $N = 1$ excited state lies within the energy window. The V_{SD}-V_G conditions depicted in (a) [(b)] correspond to the black (white) circle in Fig. 2.7(a).

In an experiment to access single-particle excited states, V_G is swept at finite bias precisely as described above. As a result, the sharp Coulomb oscillation peaks broaden and change into current 'stripes.' Figure 2.9(a) shows the B-field evolution of the first ($N = 1$) 'stripe' in a measurement on a single vertical QD. The lower edge of the 'stripe' [highlighted in green and labelled $(n,\ell) = (0,0)$] follows the evolution of the $N = 1$ ground state. That this edge moves to higher V_G as the B-field is increased reflects the increase in energy of the $N = 1$ ground state with B-field. This shift is known as the diamagnetic shift.

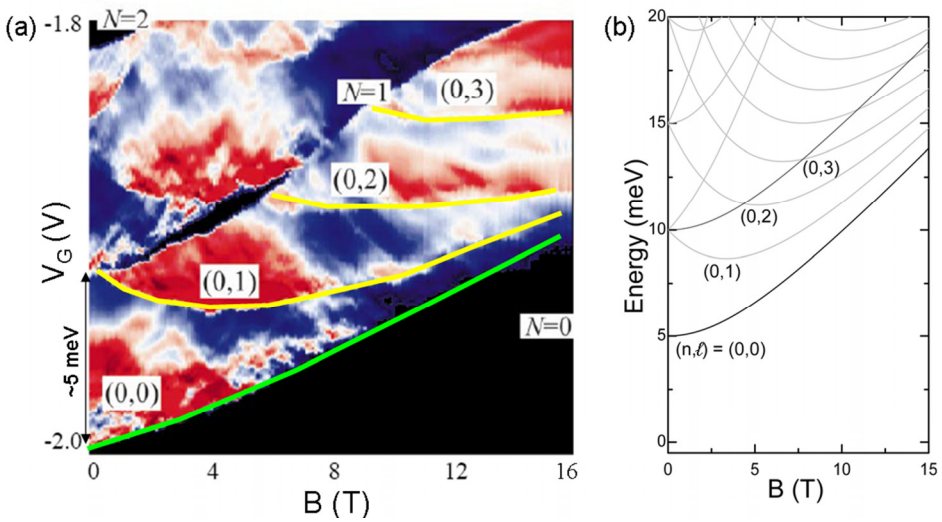

Fig 2.9. (a) The first current stripe measured in a single vertical QD at V_{SD} = 5 mV. The colour scale indicates the strength of the measured current, with I < 0.1 pA in the black regions and varying between 0.1 pA (blue) and 10 pA (red) in current 'stripes' (figure adapted from Ref. [78]). (b) FD spectrum where the ground state (n,ℓ) = (0,0) energy and a copy of it shifted up by 5 meV are both highlighted in black. Only states which lie between the two black curves, i.e., within the energy window, are observed in (a).

Three smoothly evolving boundaries (identifying current steps) are clearly visible within the first current 'stripe' [highlighted by yellow lines in Fig. 2.9(a)]. Each of these steps indicates when an additional N = 1 excited state has entered the energy window. The properties of the B-field evolution of these current steps are consistent with the FD spectrum. As the B-field is increased, the separation between the (0,0) and (0,1) states decreases, as does the separation between the other two states [labelled (0,2) and (0,3)] and the ground state, all of which is consistent with the FD spectrum. Finally, none of the three excited states cross each other or cross the ground state as is expected for the FD spectrum.

The measurement shown in Fig 2.9(a) is a marked improvement over a measurement of Coulomb oscillations in terms of providing direct information about the

single-particle states. In particular, Coulomb interactions are not relevant for the $N = 1$ current 'stripe.' Furthermore, the V_G range over which the first three single-particle excited states in the $N = 1$ current 'stripe' are observed is only ~0.2 V. This is in contrast to the ~0.6 V range required to observe the first eight Coulomb oscillation peaks (corresponding to electrons occupying the $N = 1$ ground state and first three $N = 1$ excited states) in Fig. 2.5(a).

Despite the improvement there is still an important limitation inherent to the measurement of single-particle excited states in a single QD with this finite bias technique. This is because for $eV_{SD} > E_{add}(1)$ the first current 'stripe' overlaps with the second, and so measurements of the high energy single-particle excited states would be complicated by the presence of two-electron states. For the data shown in Fig. 2.9(a) the first and second current stripes 'just touch' meaning $eV_{SD} \approx E_{add}(1)$. As this measurement was performed at V_{SD} = 5 mV, the width of the first current stripe is ~5 meV. Consequently, only states which lie within 5 meV from the (0,0) state can be observed [see Fig. 2.9(b)]. Noting that the (0,1) state just appears in the first 'stripe' at 0 T we infer that $\hbar\omega_0$ is also ~5 meV. Thus, the energy window over which the single-particle excited states can be accessed is typically limited to about the dot confinement energy in vertical QDs. As a consequence, no states with negative values of ℓ (or non-zero values of n) are visible in the first current 'stripe' in Fig. 2.9(a). This means that high energy crossings between two (or more) $N = 1$ excited states induced by the applied B-field as expected for the FD spectrum can not be studied. However, the ability to see these crossing is crucial for the physics of interest in Chaps. 4 and 5.

This motivates us to study the single-particle spectrum by an alternative strategy. Having exhausted the simplest strategy of using a single QD, to achieve our goal we shift to a weakly coupled double QD system.

2.2 Double Quantum Dots

In this section we introduce several important properties of double QDs as background for the experimental work presented in Chaps. 4-6. In particular, we will describe a technique to measure the single-particle spectrum of one of the constituent dots in a double dot device using the (N = 1) ground state of the other as a probe (or 'energy filter'). Subsequently, we will explain the concept of spin blockade which will provide a starting point to explore the hyperfine interaction in double QDs. However, before proceeding to discuss these topics, we will first provide a brief introduction to some relevant transport characteristics of double QDs.

2.2.1 Double Quantum Dot Stability Diagram

We begin by considering a generic double QD system in which two dots are coupled together in series between the source and drain contacts (recall Fig. 1.1). In addition, we will assume that the electrochemical potentials of the dots can be controlled by applying voltages V_{G1} and V_{G2} to two gates. We define E_{C1} and E_{C2} as the intra-dot charging energies of dot 1 (the upstream dot) and dot 2 (the downstream dot) and E_{CM} as the inter-dot electrostatic coupling energy, effectively the Coulomb interaction energy between each distinct pair of electrons with the two electrons located on different dots.

Figure 2.10(a) shows a schematic charge stability diagram for a coupled double QD [7,8] which identifies the regions in the V_{G1}-V_{G2} plane where, for $V_{SD} \approx 0$, the numbers of electrons in the two dots (N_1 and N_2) are fixed. Specifically, for given values of V_{G1} and V_{G2}, N_1 and N_2 are the largest integers such that $\mu_{dot1}(N_1, N_2)$ and $\mu_{dot2}(N_1, N_2)$ are less than $\mu_S \approx \mu_D$. The characteristic honeycomb structure arises essentially because the dots are electrostatically coupled. The vertices of the honeycomb structure are known as triple points because at these points three charge states are degenerate. Consequently, at the triple points elastic tunneling through the system is possible [see Figure 2.10(b)].

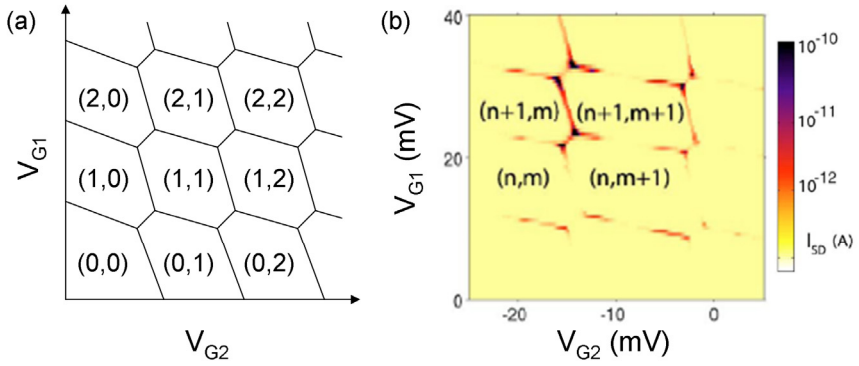

Fig. 2.10. (a) One example of a schematic stability diagram for a coupled double QD with two gates which assumes that E_{C1} and E_{C2}, as well as E_{CM}, are independent of N_1 and N_2. (b) A measured double QD stability diagram reflecting well the honeycomb structure in (a) (figure adapted from Ref. [79]). In (a) and (b) regions are labelled by the number of electrons occupying each dot (N_1, N_2).

2.2.2 Coulomb Blockade in Vertical Double Quantum Dots

Instead of a double QD system with *two gates*, we now consider a double QD system with only a *single gate* coupled (equally) to both dots. This is motivated by the fact that in this thesis we principally study weakly coupled vertical double QD devices which have a single gate. For such a singly gated double dot structure, the energy offset

between the two dots, which we refer to as detuning, can only be altered by changing the bias. This is in contrast to a double dot with two gates where the energy offset can also be adjusted at fixed bias by altering V_{G1} and V_{G2}.

Even with a double QD structure that has only a single gate, we can still employ the stability diagram for a double QD with two gates as a starting point to understand the appearance of the charging diagram in the V_{SD}-V_G plane (see Fig. 2.11). In particular, by considering sections along which $V_G = V_{G1} = V_{G2}$ (as appropriate for a gate which is equally coupled to both dots) we can understand the $V_{SD} = 0$ section through the V_{SD}-V_G plane. In constructing the honeycomb structure shown in Fig. 2.11(a), we take the condition $E_{C1} = E_{C2} = 2E_{CM}$ and assume these energies are independent of N_1 and N_2. These conditions are appropriate for model calculations relevant to the experimental results both of Ref. [32] in Sec. 2.2.4 and for the devices we measure (see Sec. 3.3). Furthermore, we assume that V_{SD} is dropped evenly across the two dots.

We can now compute the shape of the Coulomb blockade regions in the V_{SD}-V_G plane. If we initially assume that energy offset between the two dots at zero bias, E_{off}, is zero, which corresponds to the blue section in Fig. 2.11(a), the result, shown in Fig. 2.11(b), reveals well formed Coulomb diamonds (regions where $N = N_1 + N_2$ is fixed) of alternating sizes. When $E_{off} = 0$, all the triple points are traversed [see blue section in Fig. 2.11(a)] and so the Coulomb diamonds are all well formed in Fig. 2.11(b). In contrast, for $E_{off} > 0$, a situation which can arise if the two dots are not identical (as is always the case in practice), the first few Coulomb diamonds become ‘unzipped’ near pinch-off. For a specific example, suppose that at zero bias the potential of the downstream dot is lower than that of the upstream dot by an amount equal to E_{CM} [see red section in Fig. 2.11(a)].

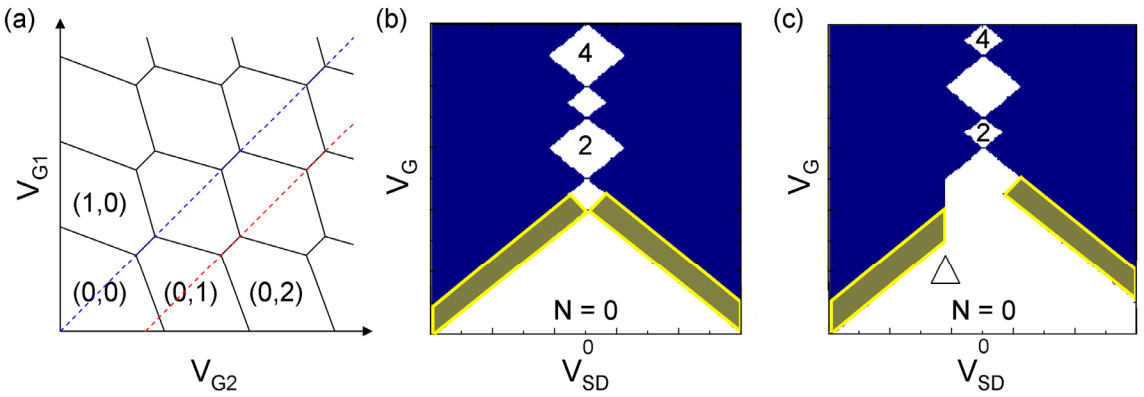

Fig. 2.11. (a) Schematic stability diagram of a coupled double QD with two gates constructed for the condition $E_{C1} = E_{C2} = 2E_{CM}$. (b) and (c) Model calculations in the V_{SD}-V_G plane showing the few-electron Coulomb blockade diamonds [80]. In (b) [(c)] $E_{off} = 0$ ($E_{off} = E_{CM}$) corresponding to the dotted blue (red) section in (a). In both (b) and (c) white indicates zero current, while blue indicates where sequential electron tunneling through the double dot is possible. The region highlighted in yellow corresponds to the single-electron tunneling (SET) regime where sequential tunneling in the absence of electrons being trapped on either dot is possible, i.e., transport occurs via the (0,0) → (1,0) → (0,1) → (0,0) sequential tunneling cycle, where (N_1,N_2) denotes the number of electrons on the upstream and downstream dots. No other distinction is made between regions of SET and many-electron tunneling (unlike in Fig. 2.7 for a single dot). Note that the upper border of the SET region also identifies the onset of an additional sequential tunneling cycle for which one electron is permanently trapped in the downstream dot, i.e., the (0,1) → (1,1) → (0,2) → (0,1) cycle (see also Sec. 4.3.1). Weaker features due to co-tunneling processes are not included. The calculation in (b) [(c)] is most appropriate for rough comparison with two (three) of the devices we measure, namely Devices I and II (III, IV and V) (see Sec. 3.3).

This results in the plot shown in Fig. 2.11(c). In this case, the $N = 1$ Coulomb diamond is 'unzipped' because when the $N = 1$ ground state of the downstream dot is aligned with μ_S and μ_D at zero bias the $N = 1$ ground state of the upstream dot is at higher energy and can not be occupied. The energy offset can be removed by applying an appropriate bias

leading to, in particular, the vertical line marked by the white triangle in Fig. 2.11(c). This line corresponds to the situation of resonant transport through the system when the N = 1 ground states of the upstream and downstream dots are aligned, explicitly $\mu_{dot1}(1,0) = \mu_{dot2}(0,1)$. Note that in later sections, when we explicitly include quantum effects, we will identify the ground state of each dot as a 1s state and hence this line will be referred to as the 1s-1s resonance.

The model discussed so far successfully reproduces the main features of the differential conductance plot in the V_{SD}-V_G plane of the measured devices reasonably well (see Fig. 3.11). However, it neglects several important factors including the two most relevant to this thesis, namely quantum confinement and excited states, and electron spin. The remainder of this chapter will serve to introduce these two important components. In particular, although the discussion of double dot transport has thus far neglected all mention of excited states, single-electron transport can also proceed through these states. In fact, as we will introduce in Sec. 2.2.3 and discuss extensively in Chaps. 4 and 5, double QD devices will provide us with an excellent opportunity to achieve our goal of probing single-particle states over a wide energy range. Furthermore, introducing electron spin, leads to a particularly interesting many-body effect, known as spin blockade, which will be the focus of Sec. 2.2.4. The hallmark of the spin blockade mechanism is that transport through the system is suppressed due to Pauli exclusion. Spin blockade will also ultimately provide a means to observe the influence of the hyperfine interaction in coupled QDs (see Chap. 6).

2.2.3 Single Electron Tunneling Spectroscopy in Double Quantum Dots

Moving beyond the simple picture described in the previous section, we now consider transport through excited states in a double dot. Recall that Sec. 2.1.5 discussed how single-particle excited states could be investigated in a single dot by applying a finite bias to measure the $N = 1$ current 'stripe' as a function of B-field. However, a limitation to this approach is that the states of interest can only be probed within a small energy window (limited to $\sim\hbar\omega_0$ due to overlapping current 'stripes'). We now introduce the technique developed by Ono et. al. [70] for probing the single-particle excited states of one of the constituent dots in a double QD device in the single-electron tunneling (SET) regime. This technique will be employed extensively in Chaps. 4 and 5 to probe the single-particle spectra of the constituent dots in the vertical double QD devices we study and to investigate coherent mixing at single-particle energy level crossings.

The goal of the technique is to map out the single-particle energy spectrum of the downstream dot using the single-particle ground (1s) state of the upstream dot as a probe (a well defined 'energy filter'). With reference to the idealized situation shown in Fig. 2.12, by co-varying the bias across the dots and the gate voltage(s), the 1s level of the upstream dot and a single-particle level from the downstream dot can be energetically aligned with each other such that they lie between the Fermi levels of the source and drain contacts. In such configurations, we would anticipate a single-electron resonant current to flow through the two dots. An important point about the situations shown in Fig. 2.12 is that in order to remain within the SET region and to avoid permanently trapping electrons in the system an increasingly large V_{SD} must be applied (when probing

higher energy states in the downstream dot). Due to this necessity, a vertical double dot is an ideal device with which to apply the measurement technique because of its robustness (see Chap. 3).

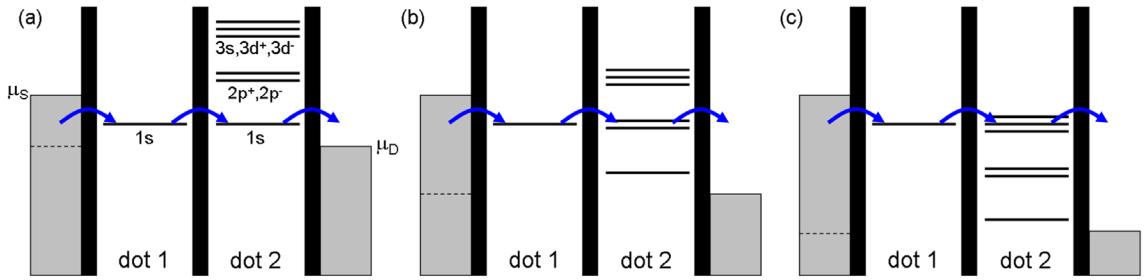

Fig. 2.12. Potential diagram for a circular parabolic weakly coupled double QD at B = 0 T showing resonant tunneling through the 1s state of the upstream dot (dot 1) and (a) the 1s ground state, (b) one of the two degenerate excited states in the second shell and (c) one of the three degenerate excited states in the third shell of the downstream dot (dot 2). In (a) the states are labelled using the atomic-orbital-like notation (recall Sec. 2.1.2). Higher energy states in both dots are omitted.

We now discuss the results of Ref. [70]. Figure 2.13(a) shows the differential conductance in the V_{SD}-V_G plane measured for different out-of-dot-plane B-fields in a singly gated vertical double QD device very similar to those described in this thesis (see Chap. 3). The simple model discussed in the previous section reproduces some key features of the data shown in Fig 2.13(a) [recall Fig. 2.11(c)]. In particular, the black line identified by the two red circles in the 0 T panel marks an increase in the measured current due to the onset of (non-resonant) sequential tunneling through the double QD system (see also Sec. 3.3 and Refs. [70,81]). Furthermore, this line forms the lower edge of the easily identifiable SET region (the shape of the SET region will be discussed in detail in Sec. 4.3.1). Within the SET region, by suitably adjusting V_{SD} and V_G simultaneously, resonant tunneling can occur (see Fig. 2.12). Each time a resonant

tunneling condition is satisfied a current peak is observed, indicated by a black-white stripe in Fig. 2.13(a) (see arrows in the 0 T panel). The panels in Fig. 2.13(a) show clearly that the positions of these resonances are strongly influenced by the applied B-field. In order to explore this further, the positions of the points where the resonances intersect the lower edge of the SET region are plotted in Fig. 2.13(b) as a function of B-field. The dispersion of the resonance positions appear to reflect part of a FD spectrum (recall Sec. 2.1.2).

Notably, the spectrum mapped out in Fig. 2.13(b) clearly covers a wider energy range (~$2\hbar\omega_0$) compared to the current 'stripe' measurements [78] discussed in Sec. 2.1.5 (where the range was limited to ~$\hbar\omega_0$). Although both techniques probe the single-electron excited states within the SET region, a wider energy range is available with a double dot because there is a fundamental difference in the appearance of the excited single-particle states in the V_{SD}-V_G plots. For a single dot, excited single-particle states appear as lines within the SET region which run *parallel* to its lower edge. Consequently, while lines due to lower energy single-particle excited states may be visible *within* the SET region, those due to higher energy single-particle excited states occur at progressively more positive V_G and eventually will be located *outside* the SET region. If this occurs, the lines related to N-electron ($N > 1$) excited states now present make it challenging to extract information about the single-particle excited states of interest. However, for a double dot, the single-particle resonances appear as (almost) vertical lines that intersect the edges of the SET region. As a result, the higher energy single-particle resonances are still located *within* the SET region just at higher bias. Consequently, the single-particle states can be probed over a wide energy range which, as

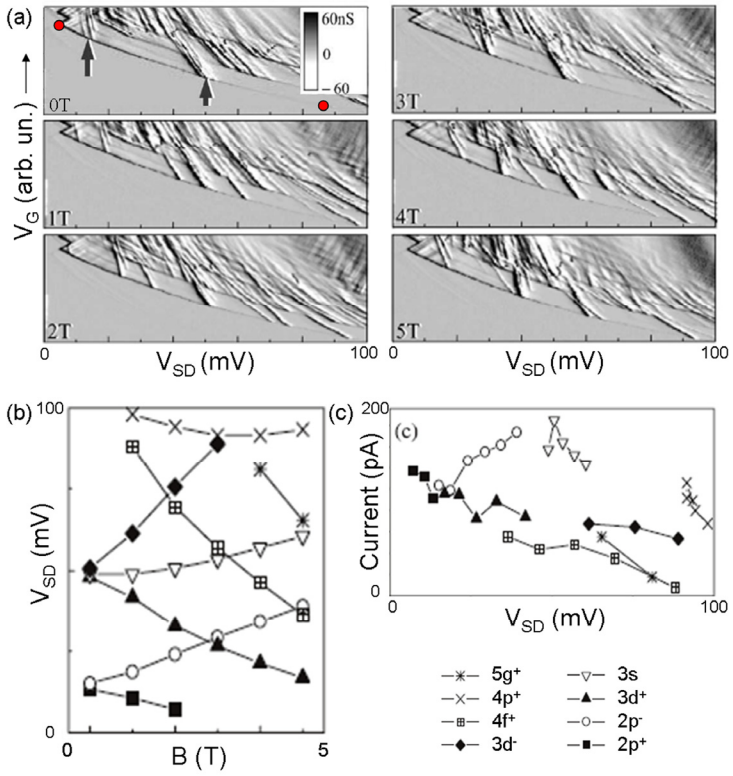

Fig 2.13. (a) Differential conductance, d*I*/dV_{SD}, in the V_{SD}-V_G plane, measured in a weakly coupled vertical double dot for B-fields of 0-5 T (steps of 1 T). The edges of the first Coulomb diamond are just visible in the top left corner of each panel and in the grey region at the bottom of each panel there are no electrons trapped in either dot. For values of V_{SD} and V_G along the black line indicating the lower edge of the SET region (marked by red circles in the 0 T panel for example), the 1s state of the upstream dot is aligned with the Fermi energy of the source contact, while the 1s state of the downstream dot is below the Fermi energy of the source contact, but above that of the drain contact. In this situation, only SET is permitted and no electrons are permanently trapped in either dot. In the 0 T panel, the resonances between the 1s state of the upstream dot and states in the second (third) shell of the downstream dot are indicated by the arrow on the left (right). (b) V_{SD} position of the point where the resonances intersect the lower edge of the SET region as a function of B-field. Note that the 1s state is not visible in the spectrum because in this device (as a result of a finite offset between the two dots at zero bias) the 1s-1s resonance occurs in the opposite bias direction (not shown). (c) Resonant current for each state (figure adapted from Ref. [70]).

will be discussed in Chap. 4, is ultimately limited only by the onset of longitudinal-optical phonon emission (at ~37 meV).

We have now identified a technique which has the potential to access the single-particle states of interest over a wide energy range. However, taking the original data in Fig 2.13(b) at face value, several aspects of this spectrum motivate further investigation. i. The B-field resolution of the data points in Fig 2.13(b) is extremely limited and as a result it is not possible to determine if when two single-particle resonances are brought into alignment they cross exactly as predicted by the FD spectrum (recall Fig. 2.2) or not. This ultimately addresses the issue of how ideal the confinement potentials are in real QDs. ii. The energy range probed is not large enough to investigate level crossings between more than two single-particle states. Level crossings between more than two levels are relatively rare and so studying them could lead to interesting new physics. iii. While the spectrum is clearly FD-like, it was the only one reported in Ref. [70]. A natural question to ask is how typical is this spectrum, i.e., was this particular dot unusually symmetric and can all dots well modelled by the FD spectrum? iv. Resonant current data [see Fig. 2.13(c)] was also presented and, clearly, these currents vary as a function of both V_{SD} and B-field. It was argued in Ref. [70] based on this data that the resonant currents could likely be explained in a sequential (incoherent) tunneling picture (as opposed to a coherent tunneling one). However, the resonant currents shown in Fig 2.13(c) include a significant (as large as ~100 pA) non-resonant background component which was not accounted for.

Addressing these points is the primary motivation for the spectral measurements we introduce in Chap. 4. By implementing the measurement principle of Ref. [70] over a

larger energy range and with an increased B-field resolution, we will aim to determine how well the FD spectrum can account for vertical QD energy spectra. As a direct result of the improved spectral measurements we will also be able to examine two-, three- and four-level crossings in detail. At such crossings we observe initially unexpected pronounced level mixing effects and this will be the focus of Chap. 5.

2.2.4 Pauli Spin Blockade in Double Quantum Dots

The fact that electrons have spin has thus far been neglected and, in particular, it plays no role in the preceding discussion of single-particle states. However, spin effects can strongly influence the transport characteristics of QDs in other regimes. One of the most striking examples in a double dot is the many-body effect known as the Pauli spin blockade [32] which we now introduce. This effect will be particularly relevant in Chap. 6 when we will consider the influence of the hyperfine interaction.

While a detailed understanding of spin blockade physics requires a full discussion of the two-electron energy versus detuning diagram in a double QD system (see Sec. 2.2.5), the cartoon model we now describe provides a clear, intuitive starting point. In the cartoon model, we picture two dots, each with a single energy level available for electrons to occupy. Supposing that an electron is permanently trapped on dot 2 (see Fig. 2.14), we consider sequential tunneling of a second electron through such a system in both bias directions. Initially, neglecting spin, we assume that it is energetically possible for transport to proceed in forward (reverse) bias via the $(0,1) \rightarrow (1,1) \rightarrow (0,2) \rightarrow (0,1)$ [$(0,1) \rightarrow (0,2) \rightarrow (1,1) \rightarrow (0,1)$] sequential tunneling cycle, where (N_1,N_2), denotes a charge configuration with the number of electrons on dot 1 and dot 2 given by N_1 and N_2

respectively. However, when spin is included, we must account for the fact that the two-electron states of the system are either spin singlet (S) or triplet (T) states.

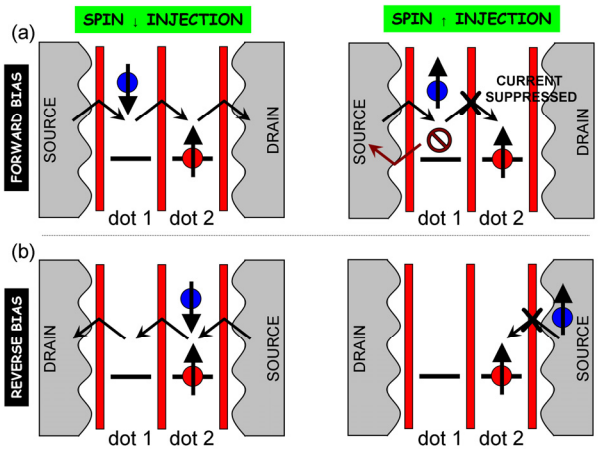

Fig. 2.14: Cartoon model illustrating spin blockade. (a) Forward bias. (b) Reverse bias.

We now suppose that the electron trapped on dot 2 has spin up (as shown in Fig. 2.14). In forward bias [see Fig. 2.14(a)], an electron entering dot 1 from the source contact can have spin up or down with roughly equal probability, meaning that either the S(1,1) or T(1,1) state can be occupied. If the S(1,1) state is occupied, transport can proceed through the S(0,2) state [see left side of Fig. 2.14(a)] as both electrons can occupy the single energy level available in dot 2. However, once the T(1,1) state is occupied, and provided the electron on dot 1 can not return to the source contact, transport can not proceed as two electrons with the same spin can not occupy dot 2 due to the Pauli exclusion principle [see right side of Fig. 2.14(a)]. In this situation, provided there is no available mechanism for flipping a spin, we should expect the current through the system to be suppressed. This is the hallmark of the spin blockade effect. On the other hand, in reverse bias [see Fig. 2.14(b)], no spin blockade is expected. Again due to the Pauli exclusion principle, only an electron which has down spin can be injected onto dot

2 from the source contact, i.e., the S(0,2) state can be occupied [see left side of Fig. 2.14(b)], while the T(0,2) state is never occupied [see right side of Fig. 2.14(b)].

We now describe the original experimental work of Ono et. al. [32] which introduced the concept of spin blockade. The I-V_{SD} trace in Fig. 2.15(a) demonstrates the bias dependent current suppression (consistent with Fig. 2.14). In particular, a region of reduced current (circled in pink and labelled SB) is visible at positive bias, while at negative bias, no such current suppression is observed, i.e., current rectification is exhibited. The differential conductance, dI/dV_{SD}, plot shown in Fig. 2.15(b) reveals that current suppression due to spin blockade is present throughout a chevron shaped region (highlighted in pink) to the right of the $N = 2$ Coulomb blockade diamond. Note that the spin blockade can be lifted when a sufficiently large bias is applied that either the electron trapped on dot 2 tunnels to the drain contact or two electrons can occupy dot 1. These conditions correspond respectively to the lower and upper right boundaries of the spin blockade chevron [labelled L and U in Fig. 2.15(c)]. Furthermore, the spin blockade can also be lifted by the application of an out-of-dot-plane B-field (see Sec. 2.2.5).

The simple model discussed in Sec. 2.2.2 reproduces some of the key features of Fig. 2.15(b), i.e., the 'unzipped' first Coulomb diamond [recall Fig. 2.11(c)]. Additionally, by considering the conditions for spin blockade, the position of the chevron shaped region of suppressed current can also be identified [see Fig. 2.15(c)]. The model calculation which well reproduces the data uses the condition $E_{C1} = E_{C2} = 2E_{CM} = 2E_{off}$ (recall Sec. 2.2.2). In particular, the finite energy offset between the dots at zero bias is necessary to trap an electron in one of the two dots as required to observe spin blockade.

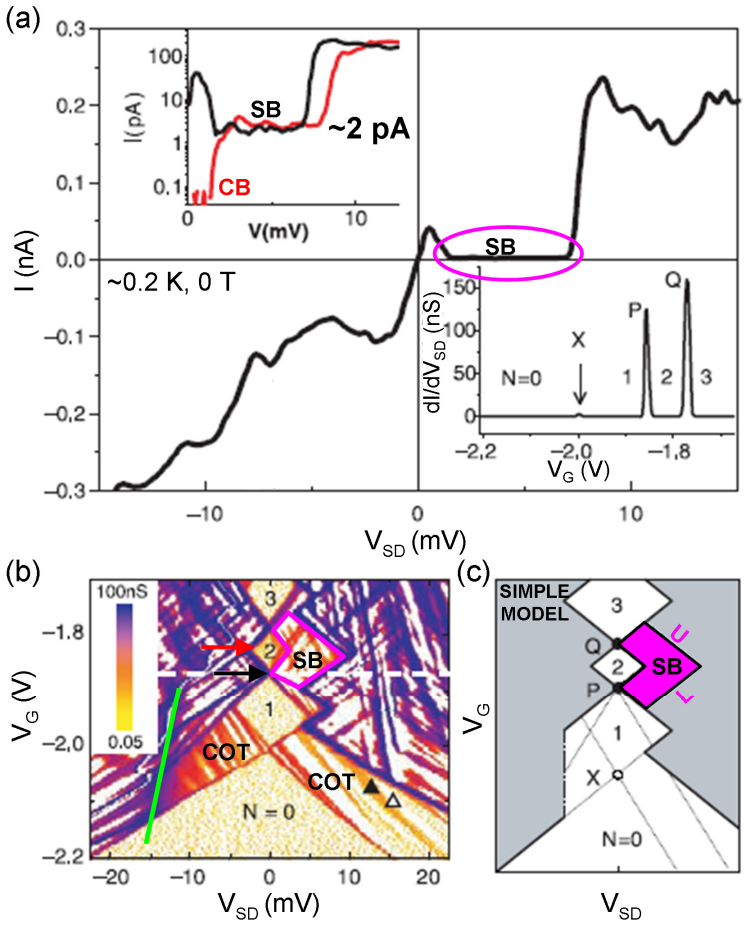

Fig. 2.15. (a) I-V_{SD} trace demonstrating the spin blockade (SB) effect in a weakly coupled vertical double dot. The lower right inset shows the first, second and third Coulomb oscillation peaks (labelled X, P and Q) measured with $V_{SD} \approx 0$ mV. At peaks P and Q, the current is large due to elastic tunneling through the system, while at peak X, due to the finite offset between the two dots at zero bias, the weaker current is the result an electron being added to dot 2 by a cotunneling process. The I-V_{SD} trace is recorded at a V_G corresponding to peak P. The upper left inset is discussed in the main text. (b) Colour scale plot (log scale) of dI/dV_{SD} in the V_{SD}-V_G plane. Regions where co-tunneling (COT) occurs are indicated. The nearly vertical green line at negative bias identifies the 1s-1s resonance (recall discussion in Sec. 2.2.2), while the black (white) triangle in forward bias indicates the resonance between the 1s state of dot 1 and the $2p^+$ ($2p^-$) state of dot 2 (recall Sec. 2.2.3). (c) Simple model calculation which reproduces some of the key features of the data in (b). Dotted lines indicate where the $N = 1$ Coulomb blockade can be lifted by cotunneling processes (figure adapted from Ref. [32]).

Figure 2.15(a) initially suggests that the current has been completely suppressed in the spin blockade region. However, although the current is small in the spin blockade region, *it is not zero* as would be naively expected from the simple mechanism described in this section. Consider the upper left inset of Fig. 2.15(a) which shows a close up of two I-V_{SD} traces (plotted on a log scale) measured at two different gate voltages. The black (red) trace was measured at a V_G corresponding to peak P (a point approximately midway between peaks P and Q) [see coloured arrows in Fig. 2.15(b)]. The black trace shows finite current near zero bias, before the current is suppressed due to spin blockade. Meanwhile, the red trace cuts through the $N = 2$ Coulomb diamond first before entering the spin blockade region. A small but finite change in current at the transition from the Coulomb blockade region to the spin blockade region is clearly visible. In fact, while the current in the region of Coulomb blockade is ~0.1 pA (roughly equal to the level of noise in the measurement), the current in the spin blockade region is ~2 pA. This non-zero leakage current was originally attributed solely to cotunneling or spin-orbit interaction processes [32]. Subsequently, in the pioneering work of Ono et. al. [33] it was determined that the hyperfine interaction can also provide a mechanism to lift the spin blockade leading to current switching and hysteresis. In preparation for a full discussion of the hyperfine interaction in Chap. 6, we now discuss a more complete model of the two-electron spin blockade which will lay the groundwork for understanding how, under appropriate conditions, the hyperfine interaction is implicated in lifting the spin blockade. Explicitly, this model will consider the details of the energetics of the two-electron singlet and triplet states which were neglected in the cartoon picture presented in this section.

2.2.5 Two-Electron Physics in a Double Quantum Dot

While the cartoon picture presented in Sec. 2.2.4 is easy to understand, we ultimately need a more sophisticated model which explicitly includes the energies of the singlet (S) and triplet (T) states. In the model, an important parameter is the detuning, ε, which we define as the energy difference between the uncoupled ground (1s) states of the two dots. When ε = 0, these two states are aligned in energy. For ε > 0 the ground state in the upstream dot (dot 1) shifts to higher energy, while the ground state of the downstream dot (dot 2) shifts to lower energy and the opposite occurs for ε < 0. In this section, we are considering principally a vertical double dot with a single gate, meaning the detuning can only be adjusted by changing the bias voltage. Next, we must identify all the relevant two-electron spin states. There are four possible spin states, namely a spin singlet $|S\rangle = {}^{1}\!/_{\sqrt{2}}(|\uparrow\downarrow\rangle - |\downarrow\uparrow\rangle)$ with total spin quantum number $S = 0$ (which is always the ground state at zero B-field) and three triplet states $|T_0\rangle = {}^{1}\!/_{\sqrt{2}}(|\uparrow\downarrow\rangle + |\downarrow\uparrow\rangle)$, $|T_+\rangle = |\uparrow\uparrow\rangle$ and $|T_-\rangle = |\downarrow\downarrow\rangle$ all with $S = 1$ where the subscripts 0, +, and - label the z-component of the spin, explicitly $S_z = 0, +1, -1$. Now we have all the ingredients necessary to understand the schematic diagram in Fig. 2.16 which shows the energies of all the relevant two-electron states at B = 0 T as a function of ε for two cases.

We first consider the case where there is no tunnel coupling between the two dots [Fig. 2.16(a)] and make several observations. i. There are four relevant two-electron states (specifically two singlet states and two triplet states). In all of these states both electrons occupy 1s levels, *except* for the (0,2) triplet state. In this state one electron *must* occupy a higher (2p) level due to the Pauli exclusion principle. To emphasize this

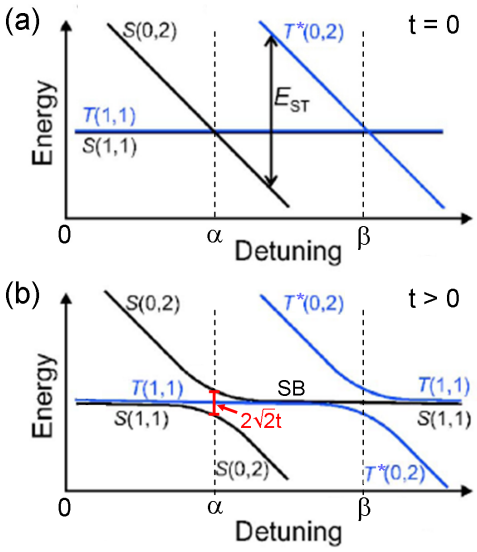

Fig. 2.16. Schematic energy diagrams showing the two-electron singlet and triplet states as a function of detuning, ε, at B = 0 T, for (a) zero tunnel coupling (t = 0) and (b) finite tunnel coupling (t > 0). Spin blockade (SB) can be observed in the region where $\alpha > \varepsilon > \beta$. The splitting between the two singlet branches is given by $2\sqrt{2}$ t. The splitting between the two triplet branches need not be the same, as was recently demonstrated experimentally [82] (figure adapted from Ref. [8]).

important point, this state is denoted $T^*(0,2)$. As a consequence, the S(0,2) state is always at lower energy than the $T^*(0,2)$ state and their energy separation is labelled E_{ST} (note that $E_{ST} < \hbar\omega_0$ [5,8]). ii. Reflecting the movement of the energies of the ground states of the two dots, the energy of the S(1,1) and T(1,1) states are constant as a function of ε while the S(0,2) and $T^*(0,2)$ states decrease in energy for ε > 0. iii. As a function of ε, for zero tunnel coupling, there is a point where the S(1,1) and S(0,2) [T(1,1) and $T^*(0,2)$] states are degenerate, which we label $\varepsilon = \alpha$ ($\varepsilon = \beta$).

Next, we consider the case where there is finite tunnel coupling between the two dots [Fig. 2.16(b)]. Since inter-dot tunneling preserves spin only states with the same

total spin can couple. Hence, in Fig. 2.16, we see that at $\varepsilon = \alpha$ (β) the S(0,2) and S(1,1) [T^*(0,2) and T(1,1)] states have hybridized forming bonding and anti-bonding branches.

We can now provide a more complete picture of how transport is suppressed due to the Pauli spin blockade using the potential diagrams shown in Fig. 2.17 for which a spin up electron is permanently trapped on the downstream dot (dot 2). In the following we explicitly discuss the effect of changing the detuning (V_{SD}) while keeping V_G fixed at an appropriate value where spin blockade can be observed. In fact we will describe the situation encountered in the original spin blockade measurements summarized in Fig. 2.15, namely for V_G corresponding to where the $N = 1$ and $N = 2$ Coulomb diamonds touch at zero bias.

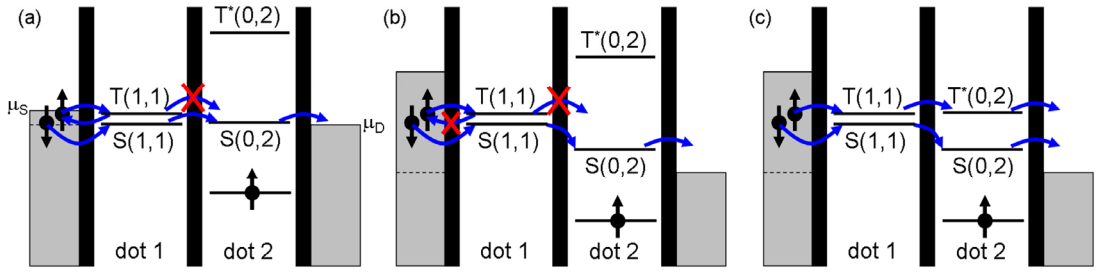

Fig. 2.17: Potential diagrams which schematically illustrate single-electron transport through two weakly coupled dots with a spin up electron permanently trapped on dot 2. The tunnel coupling between the dots is taken to be arbitrarily weak. In (a) $\varepsilon \approx \alpha$ close to zero bias, B = 0 T, while in (b) $\alpha < \varepsilon < \beta$, B = 0 T and in (c) ε is the same as in (b), but a finite out-of-dot-plane B-field has been applied. Blue arrows indicate energetically allowed transfer of electrons while in (a) and (b) the red crosses indicates transitions from the T(1,1) state which are not allowed. Note that non-resonant transitions, where an electron needs to lose energy in order to tunnel from the upstream dot to the downstream dot, are always possible via phonon emission processes. However, when an electron would need to gain energy to tunnel from an upstream dot state to an available downstream dot state at higher energy, phonon absorption is strongly suppressed at low temperature [83].

First consider the potential diagram shown in Fig. 2.17(a) which corresponds to $\varepsilon \approx \alpha$ close to zero bias. Here, assuming the dots are weakly coupled, the S(1,1), T(1,1) and S(0,2) states are practically degenerate. In this situation if the S(1,1) state is occupied transport can proceed via the (0,1) → S(1,1) → S(0,2) → (0,1) cycle. However, if the T(1,1) state is occupied, transport can not proceed via the (0,1) → T(1,1) → T^*(0,2) → (0,1) cycle because the transition T(1,1) → T^*(0,2) is energetically forbidden. Critically, however, as the T(1,1) state is aligned with the Fermi level of the source contact, the electron on the upstream dot (dot 1) can easily return to the contact, allowing a new electron to take its place. If this new electron populates the S(1,1) state then transport can proceed. In this way, transport through the system is always possible and no blockade is observed.

Increasing the detuning such that $\alpha < \varepsilon < \beta$, we now consider the potential diagram shown in Fig. 2.17(b). Here the S(0,2) state is at lower energy than the practically degenerate S(1,1) and T(1,1) states. In this situation, once again if the S(1,1) state is occupied transport can proceed. However, crucially, if the T(1,1) state is occupied, as it is not aligned with the Fermi level of the source contact, the electron on the upstream dot can not easily return to the source contact (as the hole state it left behind in the contact is quickly filled). As a result, further transport is not possible in the absence of a spin-flip mechanism. This situation corresponds to spin blockade.

As already discussed in terms of the cartoon model in Sec. 2.2.4, there are several possibilities for lifting the spin blockade at 0 T. For the situation considered in Figs. 2.17(a) and (b), increasing the detuning further will eventually result in the spin blockade being lifted as the electron on the downstream dot will be able to tunnel to the drain

contact. However, another possibility for lifting the spin blockade involves applying an out-of-dot-plane B-field. Recall that for an electron to occupy the $T^*(0,2)$ state it must enter into a higher energy (2p) single-particle state of the downstream dot. As the B-field is applied, the $2p^+$ state decreases in energy (recall Fig. 2.2) and so it is possible to energetically align the T(1,1) and $T^*(0,2)$ states [see Fig. 2.17(c)]. When this occurs transport is allowed via the $(0,1) \rightarrow T(1,1) \rightarrow T^*(0,2) \rightarrow (0,1)$ cycle and so the spin blockade is lifted. Note that we will show data which demonstrates this explicitly in Chap. 6 (see also Ref. [32]).

2.3 Summary

In this chapter we have laid the groundwork for Chaps. 4-6. Although measurements on single QDs can provide some information about the single-particle states, the information is either indirect or limited. We have argued that the technique of Ref. [70], which employs double QDs, is a more promising approach. In Chaps. 4 and 5 we will investigate single-particle energy spectra and the consequences of almost but not perfectly symmetric confinement potentials. We also described the concept of the two-electron spin blockade. In the original work of Ref. [32] it was noted that in the spin blockade region the suppressed current was not zero. As we will see, subsequent examination of this leakage current provided key evidence for the influence of electron spin-nuclear spin (hyperfine) interactions in QDs [33,66,84]. In Chap. 6 we will investigate features which we attribute to the hyperfine interaction in different electronic regimes.

Chapter 3

Experimental Details

In this chapter, we introduce the weakly coupled double vertical QD devices which will be used for the experimental work described in this thesis. In Sec. 3.1, we discuss the device geometry, the hetero-structure growth and the device processing. Subsequently, in Sec. 3.2, we describe the measurement setup for performing low-temperature electronic measurements on the devices. Section 3.3 presents some basic measurements which demonstrate that the five devices to be studied in detail work as intended. We will also use these measurements to explain how to interpret common features in the measured current-voltage traces and the corresponding numerically derived differential conductance greyscale plots, i.e., the two forms in which we typically present experimental data. Furthermore, we will identify the electronic regimes where each of the five devices will be studied in detail in the later chapters. By the end of this chapter we will have discussed all the experimental details necessary as a precursor for understanding the work described in Chaps. 4, 5 and 6.

3.1 Weakly Coupled Vertical Quantum Dots

3.1.1 Device Geometry

In this thesis, we study vertical double QD devices (see schematic diagram in Fig. 3.1 and Ref. [85] where such devices were first described). The two weakly and vertically coupled QDs are located in a sub-micron circular mesa. An $Al_{0.22}Ga_{0.78}As/In_{0.05}Ga_{0.95}As$

triple-barrier double-quantum-well hetero-structure (described fully in Sec. 3.1.2) leads to strong confinement in the vertical (*z*-) direction. The tunnel coupling in the *z*-direction between the two dots will be discussed in Sec. 3.1.3. The weaker confinement of the electrons in the lateral (*x*- and *y*-) direction is provided by mesa side-wall depletion [grey regions in Fig. 3.1] and can be tuned by applying a voltage, V_G, to a single metal gate wrapped around the mesa. In order to drive a tunneling current, *I*, through the two dots in series, we apply a bias voltage, V_{SD}, between the top contact and the substrate contact. We can induce current to flow through the device in either direction by applying positive or negative V_{SD}. Taking dot 1 (dot 2) to be the QD nearest (furthest) from the top contact, we define the bias convention such that in forward (reverse) bias electrons flow from the source contact through dot 2 (dot 1) first and then to dot 1 (dot 2) next before exiting to the drain contact. Furthermore, when we apply a B-field, it is in the *z*-direction, parallel to the tunneling current, i.e., in the out-of-dot-plane direction.

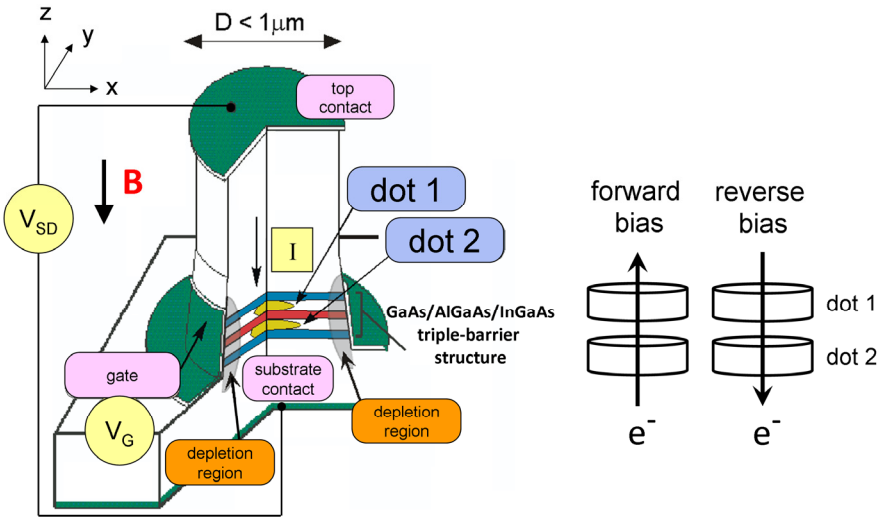

Fig. 3.1. Schematic section of a vertical double QD mesa structure. The outer hetero-structure barriers are blue and the inner barrier is red. The direction of electron flow for the bias convention we use is shown on the right.

3.1.2 Resonant Tunneling Structure Growth

The devices are fabricated from a triple-barrier double-quantum-well resonant-tunneling hetero-structure grown on a heavily Si-doped GaAs substrate by molecular beam epitaxy. The structure can be divided into several key regions, namely the substrate, the lower doped contact region, the triple-barrier double-well resonant tunneling structure, the upper doped contact region and the surface layer. The nominal details of the growth of each of these regions are presented in Table 3.1.

Material	Doping Concentration (cm^{-3})	Thickness (nm)	Layer Description
n^+-GaAs	$2.0x10^{18}$	7.0	Surface Layer
Si-delta doping	$1.5x10^{13}cm^{-2}$		Delta Doping Layers (x10)
n^+-GaAs	$2.0x10^{18}$	2.5	
n^+-GaAs	$2.0x10^{18}$	17.5	Upper Doped Contact Region
n-GaAs	$2.0x10^{17}$	180.0	
n-GaAs	$1.4x10^{17}$	150.0	
n-GaAs	$1.2x10^{17}$	70.0	
i-GaAs	-	3.0	Spacer
i-$Al_{0.22}Ga_{0.78}As$	-	8.5	Outer Barrier
i-$In_{0.05}Ga_{0.95}As$	-	12.0	Upper Well (dot 1)
i-$Al_{0.22}Ga_{0.78}As$	-	8.5	Center Barrier
i-$In_{0.05}Ga_{0.95}As$	-	12.0	Lower Well (dot 2)
i-$Al_{0.22}Ga_{0.78}As$	-	8.5	Outer Barrier
i-GaAs	-	3.0	Spacer
n-GaAs	$1.2x10^{17}$	70.0	Lower Doped Contact Region
n-GaAs	$1.4x10^{17}$	150.0	
n-GaAs	$2.0x10^{17}$	180.0	
n^+-GaAs	$2.0x10^{18}$	500.0	
n^+-GaAs			Substrate

Table 3.1: Nominal hetero-structure growth parameters.

The hetero-structure is grown as follows. First, four n-doped GaAs layers, designed to 'step-down' the doping concentration, are deposited on top of the substrate and form the lower doped contact region. These layers are followed by an undoped GaAs spacer layer. Next are the $Al_{0.22}Ga_{0.78}As$ and $In_{0.05}Ga_{0.95}As$ layers which form the undoped central region of the triple-barrier double-well structure. These layers are

followed by another undoped GaAs spacer layer and then the doping concentration is 'stepped-up' through four more doped GaAs layers which form the upper doped contact region. In order to facilitate a non-alloyed Ohmic contact to the top of the device mesa, ten delta-doping layers of Si each separated by n-doped GaAs layers are then inserted. Finally, another n-doped GaAs layer is deposited to form the surface of the structure.

3.1.3 Vertical Confinement and Tunnel Coupling

Figure 3.2 presents a one dimensional self-consistent calculation of the triple-barrier double-well conduction band profile for the hetero-structure described in Sec. 3.1.2. Several key points can be made. Firstly, this resonant tunneling structure is quite atypical in the sense that the presence of the In lowers the conduction band edge of the quantum wells relative to the n-doped GaAs contact regions. Consequently, the electronic ground state in the wells (lowest energy blue line in Fig. 3.2) is below the Fermi level of the contacts and hence, as intended, with no applied bias, electrons are already accumulated in the wells. The equilibration processes leading to the accumulation of electrons in the wells results in band bending including partial depletion in the contacts adjacent to the outer barriers (as shown in Fig. 3.2). Secondly, noting that the tunnel coupling in the *z*-direction between the two wells (or the two dots once formed) is exponentially dependant on the barrier thickness [85,86], for this hetero-structure, with a comparatively thick 8.5 nm center barrier, the self-consistent calculation reveals that the splitting between the lowest energy symmetric and anti-symmetric states, Δ_{SAS}, is <0.1 meV. This is sufficiently weak that Δ_{SAS} can essentially be neglected in the experiments we perform, i.e., we will take the states of interest to be the separate well (dot) states and

not symmetric and anti-symmetric states (see also Sec. 4.4). Thirdly, an electron incident on the hetero-structure from the source contact encounters a potential barrier ~200 meV high. This indicates that the structure will be robust even when we apply a bias of several hundred mV. Finally, the spacing between the ground state and the first excited state in each well (dot), i.e., the confinement energy along the *z*-axis, $\hbar\omega_z$, is large, ~70 meV. This value is 10-15 times larger then the confinement energy in the lateral (*x*-*y*) direction to be discussed in Chap. 4 and so we will be able to neglect states with higher energy *z*-components when we probe dot single-particle energy spectra.

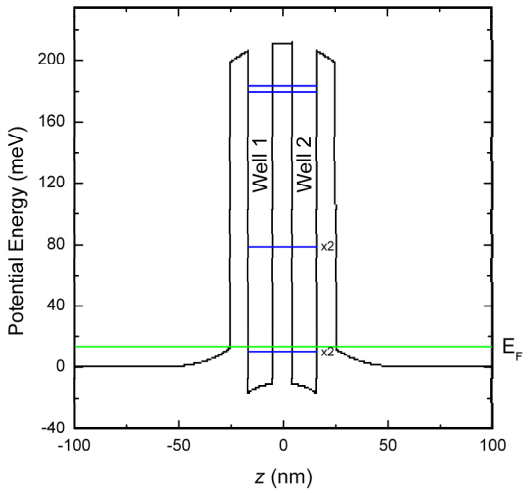

Fig. 3.2. Calculated conduction band profile in the *z*-direction for the triple-barrier double-well hetero-structure at zero bias. The green line indicates the Fermi energy, E_F, while the blue lines are the allowed energy states in the system. Each of the lower two blue lines represent a pair of almost degenerate symmetric and anti-symmetric states [87].

3.1.4 Device Processing

After the triple-barrier double-well hetero-structure is grown, several processing steps must be performed in order to obtain working QD devices (full details can be found in Refs. [29,85]). Before proceeding with the *main* processing steps summarized in Fig.

3.3, we evaporate Au/Ge/Ni onto the backside of the heavily Si-doped GaAs substrate (represented by the dotted region at the bottom of each panel in Fig. 3.3) and anneal it in order to form the substrate Ohmic contact.

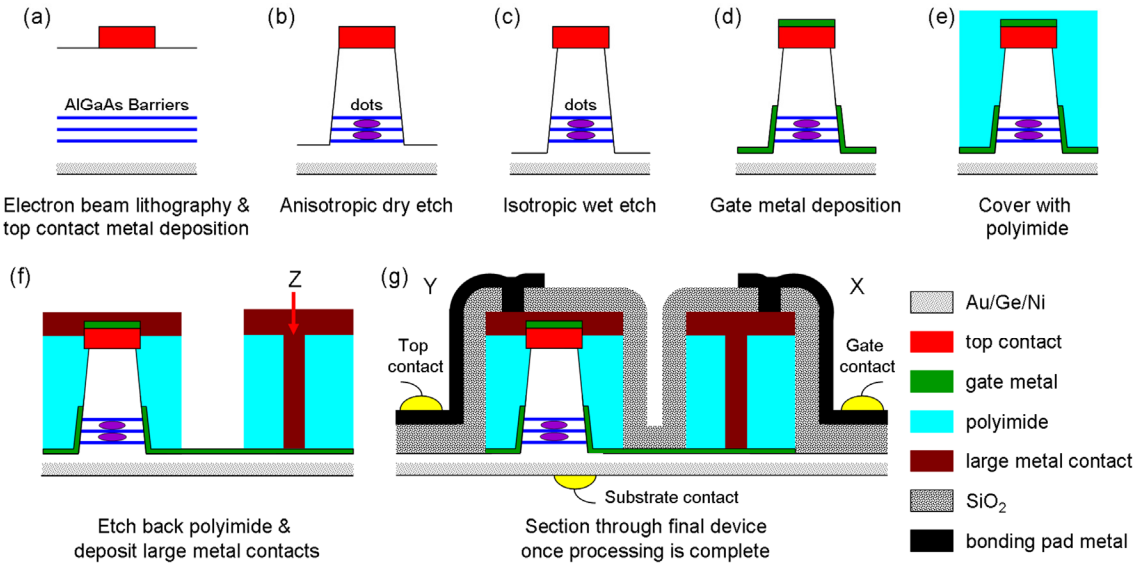

Fig. 3.3. Schematic diagrams illustrating the *main* device processing steps. Panels (f) and (g) show a wider cross section than panels (a)-(e)

The first main processing step [see Fig. 3.3(a)] is to use electron beam lithography in order to define the submicron circular top contact (the diameter of each measured mesa is given in Table 3.2 in Sec. 3.3). The non-alloyed Ohmic top contact is formed by depositing a thin Ti sticking layer and a thicker Au layer. The next step is to perform a dry etch in a BCl_3 plasma using the top contact metal as an etch mask in order to form the circular mesa containing the coupled QDs [see Fig. 3.3(b)]. The dry etching is done to a depth just below the triple-barrier double-well hetero-structure (~500 nm). Thus, the lateral confinement of the QDs will be determined by depletion from the mesa side wall (recall Fig. 3.1). This etching procedure results in a mesa side wall which is almost but not exactly vertical, i.e., it is slightly tapered in practice. After the dry etch, a shallow

(<50 nm) wet etch is performed in a standard H_2SO_4:H_2O_2:H_2O solution (1:8:160 at 25^oC) [see Fig. 3.3(c)]. Crucially, the wet etch creates a slight undercut beneath the top contact, which, combined with the fact that the side wall is slightly tapered, usually ensures that when more metal (Ti/Au) is deposited in a self-aligned process to form the Schottky gate [see Fig. 3.3(d)] the metal does not adhere to the entire mesa side wall [although additional metal does accumulate on the existing top contact. Hence, a short between the gate and the top contact is avoided. Note also that the area of the gate metal on the etched surface is generally kept as small as possible to minimize gate leakage.

A scanning electron microscope (SEM) image of a test mesa is shown in Fig. 3.4(a). The undercut caused by the wet etch is readily apparent. However, it would be difficult to view the gate metallization on a sub-micron circular mesa. Figure 3.4(b) demonstrates on a cleaved line mesa test sample how the undercut ensures that the metal forming the gate remains separate from the top contact [30].

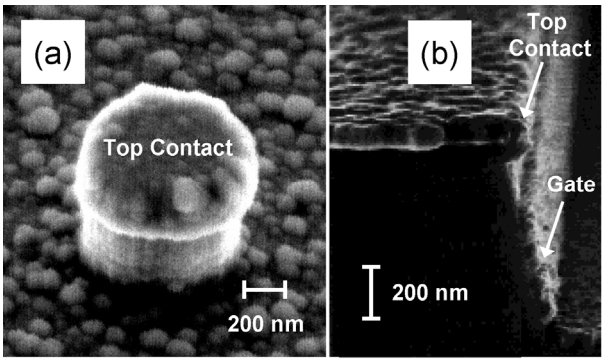

Fig. 3.4. (a) SEM image of a test mesa similar to those measured. The granular features are SiO_2 deposited by PECVD during subsequent processing. (b) SEM image of a section through a line mesa test structure [image in (b) adapted from Ref. [30]].

At this point in the processing, the confinement potentials of the QDs are defined and so from this point of view the QD structure is complete. However in order to perform

transport measurements, it is necessary to make electrical connections to both the top contact and the gate. Since it is impossible to wire bond to a sub-micron mesa, further processing is required. This additional processing begins by covering the mesa with polyimide [see Fig. 3.3(e)], which will eventually support two large metal contacts (one for the top contact and another for the gate). Photoresist is then deposited on the polyimide and a via hole pattern transferred to it by photolithography. Subsequently, an oxygen plasma etch is used to expose the gate metal and the top contact. The etch is stopped at a point where the top contact just 'sticks up' from the polyimide. Next, more metal (Cr/Au) is deposited to form two large metal contacts [see Fig. 3.3(f)]. At this stage, one might expect to be able to wire bond to the large metal contacts, however the polyimide supporting them can not easily withstand the ultrasonic pulse applied when wire bonding. We therefore deposit SiO_2 by plasma-enhanced chemical vapour deposition (PECVD) [see Fig. 3.3(g)] and pattern it using a buffered oxide etch in order to open up two more via holes, one for access to each of the large metal contacts. Finally, more metal (Cr/Au) is deposited in order to form large bonding pads resting directly on the SiO_2, and not on the polyimide, so wire bonding can easily be performed. Figure 3.5 shows an SEM image of a mesa covered by a large metal contact (highlighted by a solid white box). Also visible in Fig. 3.5 is a via hole [see point Z in Fig. 3.3(f)] which allows the gate metal (identified by a dotted white line) to be connected to the second large metal contact.

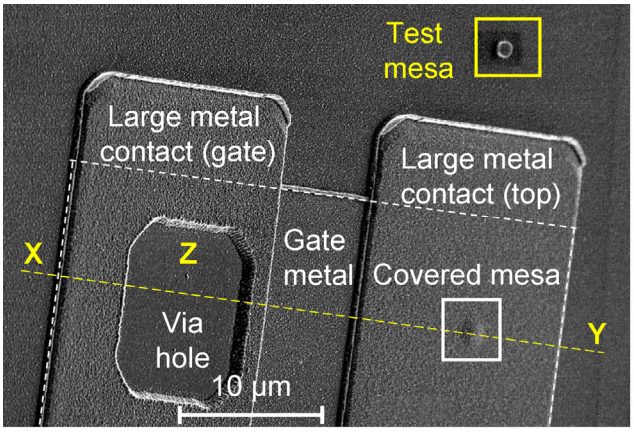

Fig. 3.5. SEM image of a completed device. The SEM image in Fig. 3.4(a) is of the test mesa highlighted by the yellow box which is covered by SiO_2, but not metal. The dotted yellow line X-Y identifies the cross section shown schematically in Fig. 3.3(g).

In order to increase the likelihood of finding a working double QD device, ~300 mesas are fabricated on a ~10 mm^2 sample of hetero-structure starting material. Specifically, a sample contains a six by seven array of ~1 mm^2 'chips' which each consist of eight double QD devices (and their sixteen associated bonding pads) as shown in Fig. 3.6(a). Once the processing is completed, the sample is cleaved into small pieces typically containing a few (up to six) chips. Each of these pieces may then be glued into an eight pin dual-in-line chip carrier [see Fig. 3.6(b)] using a conducting silver epoxy. After the piece is secure, gold wires are bonded from the chip carrier to the bonding pads on the chips. One of the chip carrier's eight pins is used for the common substrate contact, and as each double QD needs two additional pins (one each for the top contact and the gate) it is possible to connect three double QD devices on each chip carrier. Once the wire bonding is complete, the chip carrier is then mounted on a sample probe, which enables electrical connection to the measurement equipment described next.

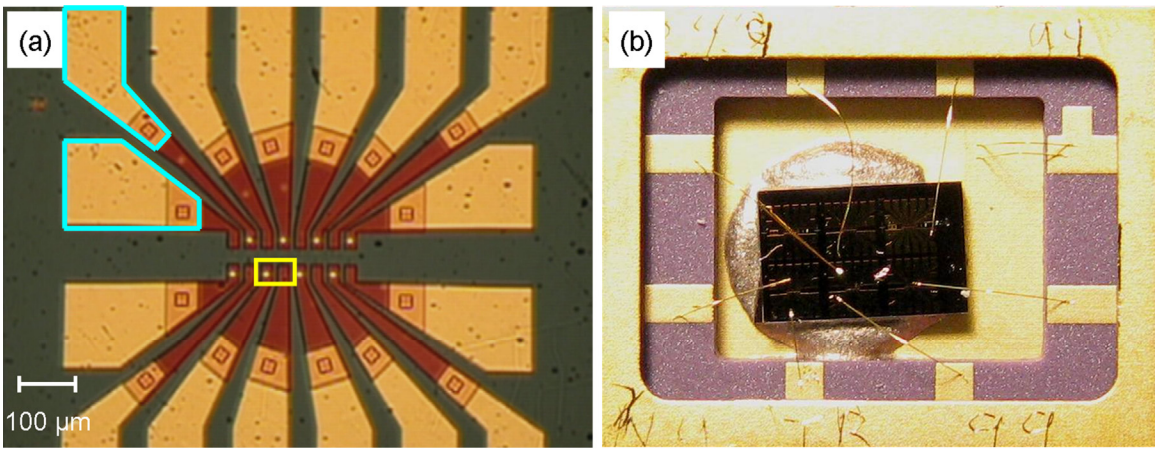

Fig. 3.6. (a) Optical image of a single 1 mm^2 chip after processing is completed. The large gold coloured regions are the metal bonding pads (one pair, belonging to a single QD device, is highlighted in blue). The yellow box highlights the region shown in Fig. 3.5. (b) Top view of an eight pin dual-in-line chip carrier with a sample piece containing six chips mounted and wire bonded. The area of the chip carrier is ~80 mm^2.

3.2 Measurement Setup

Most of the measurements described in Chaps. 4, 5 and 6 were carried out with a Janus top-loading He-3 cryostat [see Fig. 3.7]. A superconducting magnet which can attain a maximum B-field of 9 T is located in the cryostat (11 T is attainable by pumping on the lambda plate). We now describe some relevant characteristics of the system.

The cryostat's base temperature is ~0.3 K, corresponding to a thermal energy, k_BT, of ~0.025 meV, and it can be maintained for ~24 hours. Thus, for the QDs studied, where the charging energy, E_C, is typically a few meV, the condition, $E_C \gg k_BT$ is easily satisfied, as required for observing single-electron tunneling (recall Sec. 2.1.1). Furthermore, we note that the cryostat can remain 'cold' for several months without being warmed up to room temperature. When the cryostat is 'cold', the devices are warmed up (typically once a day) to a maximum of ~10 K during the He-3 condensation cycle. The devices we

measure are quite stable and warming them (to ~10 K or even to room temperature) and subsequently cooling them back down to ~0.3 K results in very little change, if any, in their electronic characteristics.

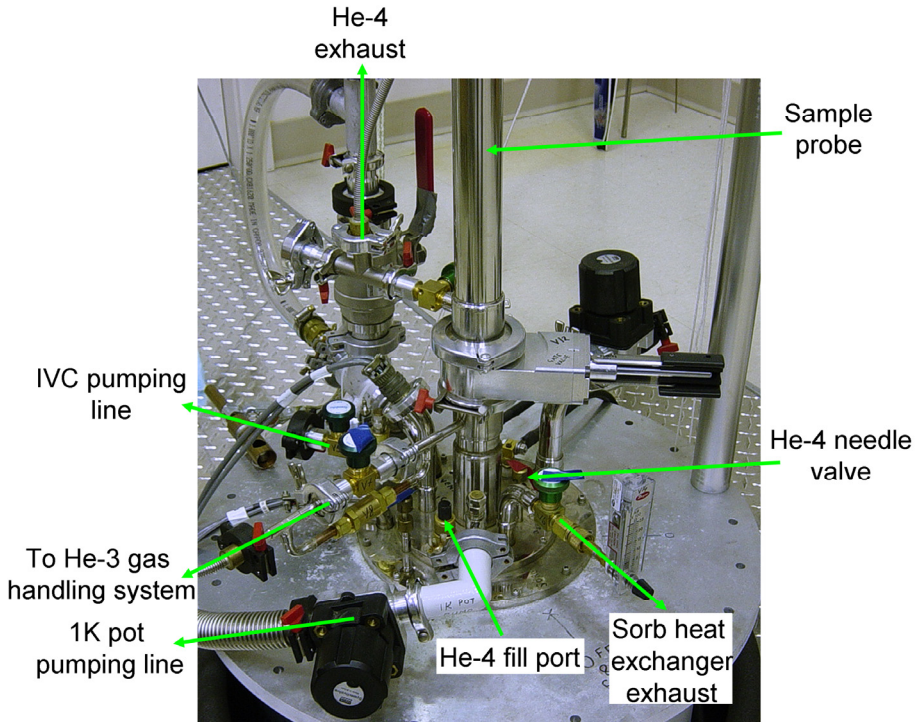

Fig. 3.7. Photograph of the top plate of the Janus top-loading He-3 cryostat.

In order to perform electrical measurements on the double QD devices, a Keithley electrometer (model no. 6517A) and an IOtech four channel digital-to-analog converter (DAC) (model no. 488HR/4) are used (see Fig. 3.8). The choice of these specific units is largely historical. They have been found to be sufficient for performing low noise, low current (~pA) measurements and are conveniently controlled by National Instruments Labview software via general purpose interface bus (GPIB) cables.

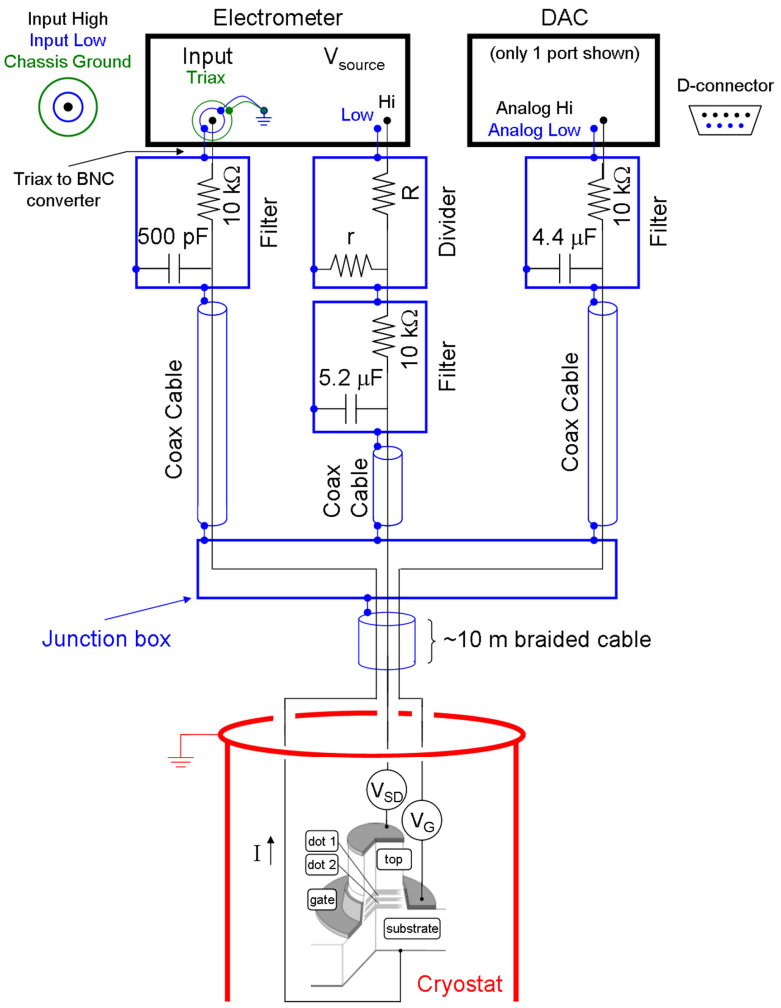

Fig. 3.8. Schematic of the measurement electronics. The electrometer is connected to the top and substrate contacts of the device while the DAC is connected to the gate. The long (~10 m) shielded miniature cables connecting the junction box to the sample probe are braided together to minimize pick-up.

The electrometer serves two purposes. Firstly, it acts as a voltage source to provide V_{SD}. The internal voltage source of the electrometer can provide a maximum output voltage of ±100 V with a minimum step size of 5 mV. However, voltages of ±100 V are too large for the QD devices and the step size of 5 mV is not fine enough. Therefore, we use a simple voltage divider circuit to reduce the output voltage and provide a suitable V_{SD}. Simple circuit analysis shows that the divider reduces the voltage

from the electrometer voltage output by a factor of r/(r+R) (typically we use R ≈ 1 MΩ and take r such that a 100 V output from the electrometer results in ~50 mV to ~500 mV across the device). Secondly, the electrometer measures *I* by means of a high-resistance internal circuit which converts the input current to a voltage and compares it to a reference voltage (typically we limit *I* to be in the range of ±200 pA). The electrical measurements we are performing are essentially DC measurements where data points are acquired at a rate of up to ~5 data points per second.

The DAC, which provides V_G, has a maximum voltage output range of ±10 V with a step size of 305 μV, although we often limit the output range to ±2 V which increases the resolution to 61 μV. Note that the voltage on the Schottky gate is kept roughly in the range of -2/-3 V to +0.5 V, since outside this range leakage current becomes significant (this range avoids breakdown in reverse bias and the flat-band condition in forward bias). As this range corresponds closely to the output range of the DAC, sufficient resolution is available without using a voltage divider.

In order to avoid ground loops in the electronic setup, several precautions are taken. For instance, the outer shell of all the coaxial cables are connected together via the junction box and connected to the internal ground of the electrometer through its input connection (see Fig. 3.8). Furthermore the cryostat sits on a rubber mat, and all pumping and exhaust lines include a non-conducting connection. This means we can ground the cryostat at a single point. Crucially, there is a break between the cryostat ground and the electronics ground near where the braided cable is connected to the sample probe.

As we are performing high-sensitivity DC electrical measurements, further steps are taken to minimize high frequency noise emanating from the internal electronics of the

electrometer and DAC. Hence, all electrical connections to the device include resistor-capacitor (RC) low pass filters (see Fig. 3.8). The values of the resistances and capacitances in the filters, originally determined by researchers at NTT in Japan, result in a noise floor in the measured current of ~25 fA. Explicitly, the filters connected to the electrometer output and the DAC both have a cut-off frequency of ~3 Hz, while the filter connected to the electrometer input has a cut-off frequency of ~30 kHz. The ~3 Hz cut-off frequency also limits how fast voltages can be changed and, consequently, influences how fast data can be captured.

3.3 Characterization of Double Quantum Dot Devices

3.3.1 Device Details

Six weakly coupled vertical double QD devices (recall Sec. 3.1), all fabricated from the same GaAs/$Al_{0.22}Ga_{0.78}As$/$In_{0.05}Ga_{0.95}As$ triple-barrier double-well hetero-structure (recall Table 3.1), will be discussed at various points in this thesis. Henceforth, they will be referred to as Devices I-VI. Devices I-V were processed according to the steps described in Sec. 3.1.4 and measured at NRC-IMS. Device VI was processed and measured by S. Amaha at ICORP in Japan. Unless otherwise noted, all experiments on Devices I-V (VI) presented in this thesis were performed at ~0.3 K (~1.6 K). The main difference between Device VI and Devices I-V is that Device VI has a thin (~0.15 μm) line mesa attached to the circular mesa containing the coupled dots [see Fig. 5.21(a) which shows a SEM image of a device mesa with four such line mesas attached to it and also Ref. [81]]. Metal deposited on top of this line mesa allows the top contact of the device to be electrically contacted directly to a bonding pad. Note that current only flows

vertically through the larger circular mesa containing the dots and not through the narrow line mesa as the semiconducting material within it is pinched-off [88]. Thus, the measured transport characteristics of the device are unaffected by the presence of the line mesa. The details of the six devices are summarized in Table 3.2.

Device	Fabricated and Measured at	Mesa Diameter (μm)
I	NRC-IMS	0.55
II	NRC-IMS	0.55
III	NRC-IMS	0.55
IV	NRC-IMS	0.65
V	NRC-IMS	0.65
VI	ICORP	0.43

Table 3.2. Device mesa details.

3.3.2 Demonstration of Basic Device Operation

In order to verify that we have successfully obtained the desired QDs from the quantum well hetero-structure, we take a device and record a series of I-V_{SD} traces over a wide V_{SD} range (typically ~±0.5 V) for different values of V_G (typically -2 V or -3 V to +0.5 V) at 0 T. Such measurements serve to determine whether the gate can successfully reduce the effective size of the QDs and that there is minimal gate leakage current.

Using Device I as a typical example of a successful device, Fig. 3.9 shows I-V_{SD} traces measured over a ±425 mV bias range. That the traces can be measured over such a wide V_{SD} range demonstrates the robustness of the device. Examining the I-V_{SD} trace measured for V_G = 0.5 V, we make two key observations indicating the hetero-structure material is of good quality and has been properly designed. Firstly, two clear resonances are visible (a primary one at ~±50 mV and a secondary one at higher bias) and, secondly, the device is conducting at zero bias as expected due to the In present in the quantum wells (recall Table 3.1). The primary resonance is essentially due to resonant tunneling

through the ground states of the two quantum wells (recall Fig. 3.2) as, for this V_G, the QDs are so weakly 'squeezed' that the measurement is in the quasi-two-dimensional regime (the origin of the secondary resonance is beyond the scope of this thesis).

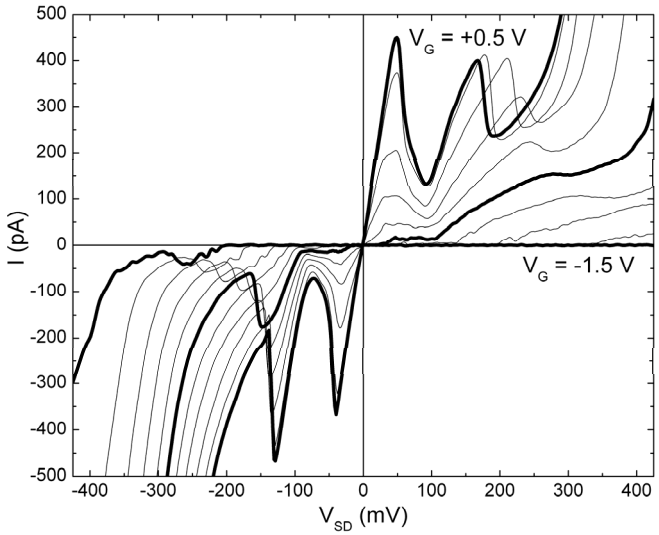

Fig. 3.9. *I*-V_{SD} traces measured in Device I for V_G = -1.5 V to 0.5 V (steps of 0.2 V). The V_G = 0.5, -0.5 and -1.5 V traces are bold. The resistance near zero bias extracted from the V_G = 0.5 V trace is ~100 MΩ » h/e^2 ≈ 26 KΩ. This satisfies a necessary condition for observing SET (see Sec. 2.1.1) although features due to SET are not apparent at this V_G.

As V_G is made progressively more negative, the QDs are steadily 'squeezed' and their zero-dimensional character strengthens. Specifically, as the conducting channel is 'squeezed' towards pinch-off, the primary resonance initially weakens and breaks up into numerous sharp resonances and steps. In particular, the V_G = -0.5 V trace starts to reveal extra features for $|V_{SD}| <$ ~100 mV, however the two main resonances are still identifiable. Meanwhile, the V_G = -1.5 V trace is flat near zero bias, indicating that the device has been pinched-off, i.e., there are no electrons trapped on the two dots. That pinch-off can be achieved demonstrates that the mesa diameter is appropriate, and that the gate is working as intended (with no leakage current for the V_G range shown).

3.3.3 Correspondence of Current Traces and Conductance Plots

Once we have demonstrated that a device is working as intended, we can perform detailed measurements in the zero-dimensional regime close to pinch-off. Again using Device I as an example, the main goal of this section is to identify and locate potential features of interest. However, the measurement we discuss here will also serve as a helpful example to explain how to interpret corresponding features in the same data set presented in the two forms commonly encountered in this thesis: a series of measured I-V_{SD} traces and a numerically derived differential conductance, dI/dV_{SD}, greyscale plot.

We begin by showing a series of I-V_{SD} traces in Fig. 3.10 which demonstrate clearly that we can measure features characteristic of a coupled QD system including, for instance, Coulomb diamonds and strong current resonances (recall Chap. 2). In particular, the V-shaped region near the top of the figure inside which $I \approx 0$ pA indentifies the region where the device is pinched-off and there are no electrons trapped on the dots ($N = 0$). The pinch-off gate voltage (corresponding to the bottom of the V-shaped $N = 0$ region) is ~-0.25 V in this device. Remaining near zero bias, but moving towards more positive V_G we can see additional diamond shaped regions of zero current (highlighted in green). These are the first few Coulomb diamonds (recall Sec. 2.2.2) and the points where they touch (at zero bias) would correspond to the location of the Coulomb oscillations were the current measured as a function of V_G for $V_{SD} \approx 0$ mV. We also note that at finite bias, as we move towards more positive V_G (starting from pinch-off) the current generally increases. This reflects the opening of the conducting channel and consequent increase in size of the QDs leading to a reduction of the confinement energy. Hence, more energy levels are available in a given energy window and a larger current can flow.

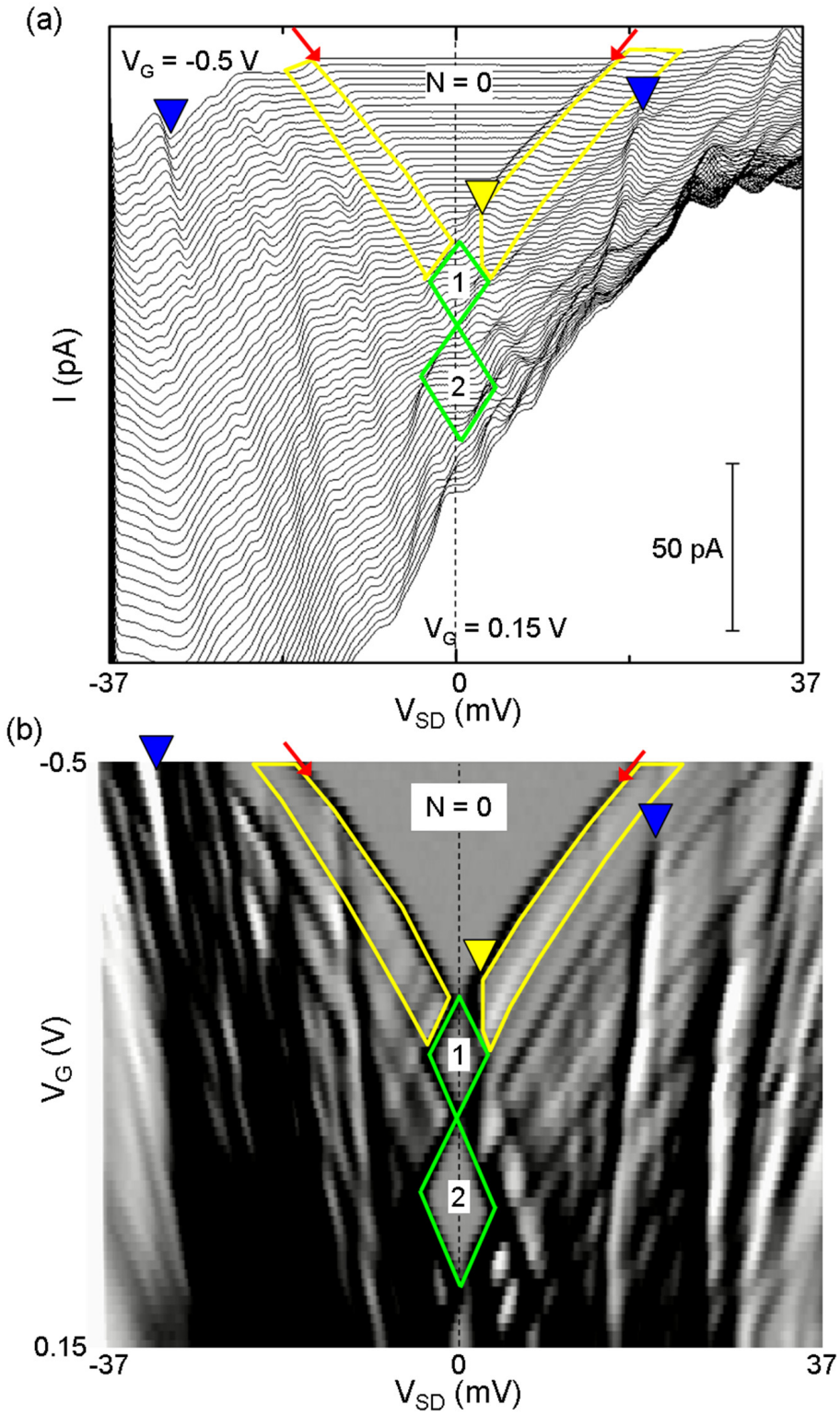

Fig. 3.10. (a) I-V_{SD} traces measured in Device I for V_G = 0.15 to -0.5 V (steps of 0.01 V). Traces are vertically offset by 2 pA. (b) Numerically derived dI/dV_{SD} greyscale plot of the data in (a). Highlighted features in both (a) and (b) are discussed in the text.

There are many features beyond the obvious ones just identified in Fig. 3.10(a), but they are so numerous it is hard to identify them or their behaviour. In order to make features in the I-V_{SD} traces easier to identify and track, it is useful to take the numerical derivative of the data and examine the resulting differential conductance, dI/dV_{SD}, greyscale plot shown in Fig. 3.10(b). We will employ such greyscale plots throughout this thesis and the convention we use is that black, grey, and white respectively represent positive, zero, and negative conductance. In this representation, step-like increases in the current appear as black lines in either bias direction (see the examples highlighted by red arrows in Fig. 3.10), while resonances appear as black and white stripes. Notably, in forward (reverse) bias where we measure positive (negative) current the resonances which are 'peaks' ('dips') appear as black-white (white-black) stripes (see for example the two resonances identified by blue triangles). Furthermore, the grey regions near zero bias are easily identifiable as the regions where N is fixed.

Now that we have explained the correspondence between a sequence of I-V_{SD} traces and a dI/dV_{SD} greyscale plot, we can identify several other features of interest in Fig. 3.10. Firstly, the step-like features identified by the red arrows mark the onset of sequential tunneling in either bias direction. Secondly, in each bias direction an arc-shaped region [outlined in yellow] in which single-electron tunneling (SET) occurs is visible just below the V-shaped $N = 0$ region [recall Fig. 2.11(b)]. Thirdly, within these arc-shaped regions, a few single-particle resonances are visible (recall Sec. 2.2.3 and Fig. 2.13). In particular, the 1s-1s resonance is visible just the right of zero bias [highlighted by a yellow triangle].

3.3.4 Identification of Regions of Interest in the Measured Devices

We begin this section by examining the collective properties of Devices I-V, noting in particular some relevant similarities and differences between them.

Figures 3.11(a)-(e) show dI/dV_{SD} plots for the five devices [note Fig. 3.11(a) shows the same greyscale plot as Fig. 3.10(b)] and several observations can be made. i. Each panel corresponds to a single ~24 hour measurement and clearly all the devices are stable throughout an entire measurement, i.e., we observe no abrupt switching (due to charge traps for example). ii. All the devices can be pinched-off and the first few Coulomb diamonds are visible in each device. iii. While the pinch-off gate voltage is similar for Devices I-III (~-0.3 V), it is significantly more negative for Devices IV and V (~-1.5 V). The reason for this is that the nominal mesa diameter of Devices I-III is 0.55 μm compared to 0.65 μm for Devices IV and V. As a consequence of their increased size, a more negative V_G is required to remove all the electrons from the QDs in Devices IV and V (see Refs. [76,89]). iv. No two devices have identical transport characteristics. This device-to-device variation is ultimately due to natural perturbations in the confinement potentials of vertical QDs caused by local randomness (in, for example, dopant distribution) and imperfections (in, for example, processing). v. The distinctive $N = 2$ spin blockade chevron (recall Sec. 2.2.4) is only visible in Devices III-V which have an appropriate energy offset at zero bias (E_{off}). The position of the 1s-1s resonance line (marked by a yellow triangle in each panel of Fig. 3.11) relative to zero bias provides a measure of E_{off}. For Devices I and II the 1s-1s resonance occurs very close to zero bias [just to the left (right) in Device I (II)] indicating E_{off} is small. This also explains why the Coulomb diamonds are well formed in these devices [86,90,91]. In contrast, for Devices

III-V, the 1s-1s resonance is at higher (forward) bias. By comparing 3.11(c)-(e) with the calculation presented in Fig. 2.11(c), we surmise that E_{off} is comparable to the inter-dot electrostatic coupling energy, E_{CM}, and half the dot charging energies, E_{C1} and E_{C2}. As a consequence, the first few Coulomb diamonds in these devices appear 'unzipped.'

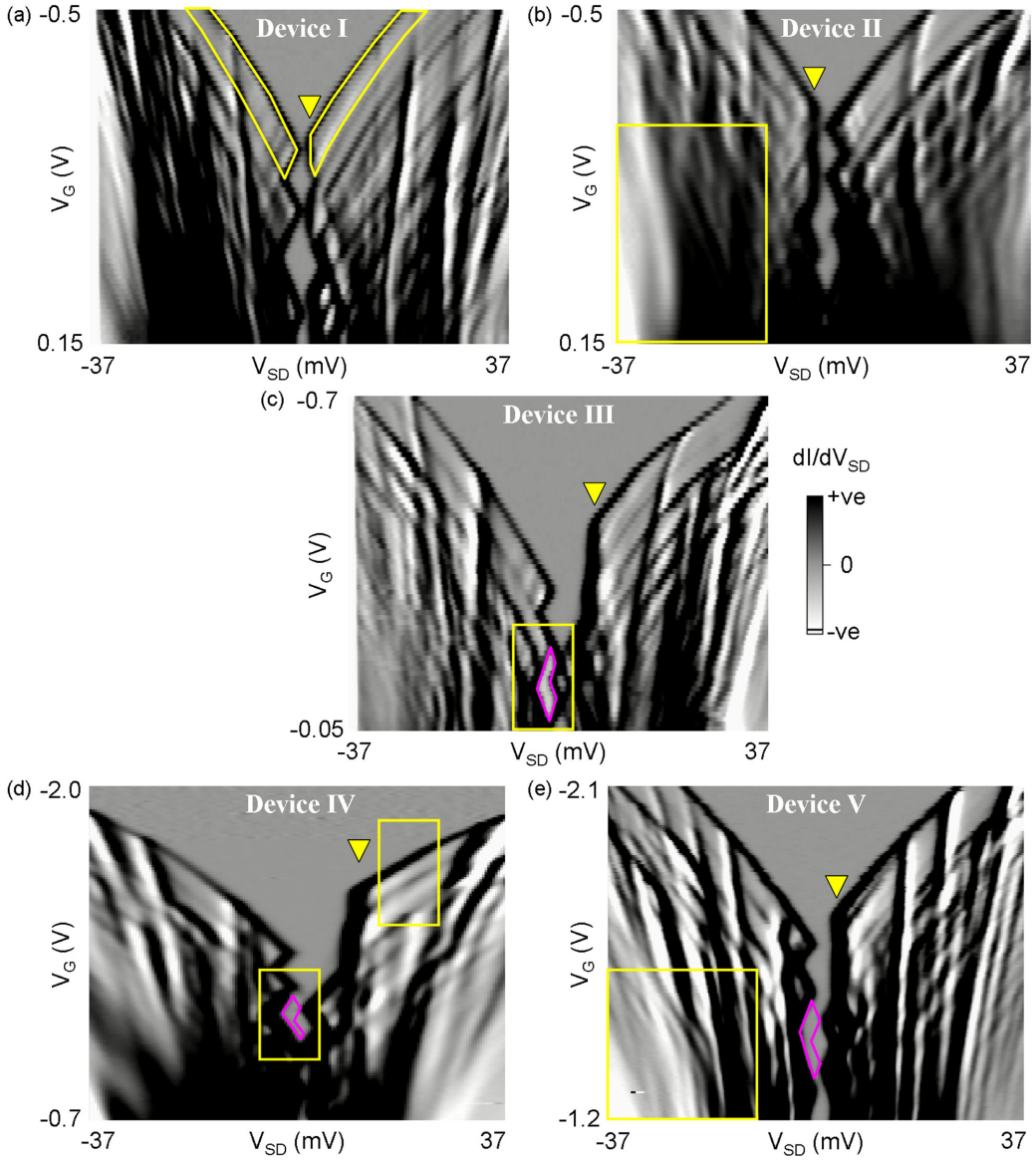

Fig. 3.11. (a)-(e) Numerically derived differential conductance, dI/dV_{SD}, in the V_{SD}-V_G plane for the five devices fabricated and measured at NRC-IMS (Devices I-V). In panels (c)-(e) the chevron-shaped $N = 2$ spin blockade region is outlined in pink. Yellow boxes highlight regions of interest which will be discussed in Chaps. 4, 5 and 6.

Having introduced Devices I-V, we conclude this chapter by identifying regions from specific devices on which we will focus in Chaps. 4, 5 and 6.

In Chap. 4, employing the measurement principle described in Sec. 2.2.3, we use the 1s-like state of the upstream dot to probe the single-particle states of the downstream dot in the SET region just below the V-shaped $N = 0$ region. In principle, such measurements could be performed on any of the measured devices, although the majority were performed on Devices I [Fig. 3.11(a)] and VI (not shown in Fig. 3.11). As will become clear in Chap. 4, we selected these two devices because the constituent dots in Device VI (I) show clear evidence for circular (elliptical) parabolic confinement. Additionally, in Chap. 5 we will use these two devices to focus on B-field induced energy level crossings between two, three, or four single-particle energy levels where we observe coherent mixing and quantum superposition phenomena.

In Chap. 6, we will examine the electron spin-nuclear spin (hyperfine) interaction. The $N = 2$ spin blockade is known to provide a means to observe the hyperfine interaction in double QDs (see for example Refs. [33,84]) and so we will begin by investigating this regime. To do so, we select Devices III and IV which show clear spin blockade chevrons [see Figs. 3.11(d) and (e)]. Subsequently, we will explore whether the hyperfine interaction can influence the electronic properties of the devices at high bias well beyond the $N = 2$ spin blockade regime. For reasons which will become clear in Chap. 6, we focus on results obtained using Devices II, IV and V. In particular, we will investigate a large portion of V_{SD}-V_G plane at negative bias in Devices II and V [see Figs. 3.11(b) and (e)], while we focus on a region close to pinch-off at positive bias in Device IV [see Fig. 3.11(d)].

Chapter 4

Global Properties of Quantum Dot Energy Spectra

As discussed in Chap. 1, QDs are potentially useful for new electronic and optical applications, such as quantum information processing, as well as for exploring basic nano-scale physics [1-4,6-8,41]. Towards these goals, a concrete understanding of the basic properties of realistic QDs is actively being sought.

The Fock-Darwin (FD) spectrum, discussed in Sec. 2.1.2, shows the evolution of the energy of single-particle states for a strictly two-dimensional circular parabolic confinement potential under the influence of an out-of-dot-plane B-field [74,75]. The FD states are widely used for the characterization and calculation of confined states in QD structures realized in a number of different ways [1-4,6-8]. Indeed, spectra with clear and dominant FD-like characteristics have been observed in transport measurements of vertical QDs [31,78], and recently, for example, by magneto-optical spectroscopy of self-assembled InAs QDs [92], and by magneto-tunneling spectroscopy of QDs induced in GaAs quantum wells by interstitial Mn ions [93].

However, the information these measurements can provide on single-particle states is limited. In particular, as described in Chap. 2, in Ref. [31] information about the single-particle states had to be extracted from many-electron states, while Ref. [78] could only access the single-particle states over a narrow energy range limited by the dot confinement energy (~5 meV). Furthermore, although a clear FD-like spectrum was observed in Ref. [92], the measurements involved an exciton so Coulomb interactions could not be neglected, and, in addition, the confinement energies of the ensemble of dots

studied were quite large (~30 meV) meaning that the range over which the spectrum could be measured was limited by the height of the confinement potential. Meanwhile, although a large portion of a FD-like spectrum was revealed by the measurements of Ref. [93], the spectrum was not sufficiently clear to resolve the many-level crossings, perhaps due to the fact that the measured QD arose randomly.

Although the measurements on single vertical QDs in Refs. [31,78] could only provide limited information about the single-particle states, they did demonstrate that vertical dots possess a strong and well defined confinement potential with a high degree of symmetry (see also Ref. [11]). As we shall see, vertical double QDs are an ideal vehicle for looking at single-particle states and assessing to what degree in practice these states are FD-like in character over a wide energy window.

In this chapter, we describe detailed magneto-resonant-tunneling spectroscopy measurements performed on vertical double QD devices by extending the measurement technique of Ref. [70]. The main goal of this chapter is to discuss the global properties of measured single-particle energy spectra [see for example Fig. 4.1(a) which shows a typical spectrum]. We focus on the B-field evolution of both the energies of the single-particle states and the strength of the spectral features. In particular, we will show that the measured energy spectra of the dots are well modeled overall by calculated spectra for dots with in-plane (lateral) confinement potentials which are close to *elliptical* and parabolic in form [see for example Fig. 4.1(b). By comparison with the ideal calculated spectra, we will determine global properties of the measured spectra such as the confinement energies and ellipticities. Another notable feature of the measured dot energy spectra is widespread anti-crossing behaviour and strong variation in the resonant

currents whenever two or more single-particle states are brought close together in energy by the B-field [for example, see the three-level crossing labelled γ in Fig. 4.1(a) and note the suppression of the otherwise strong center branch near the center of the crossing region]. We will also describe model calculations, based on a coherent tunneling picture, which reproduce these general properties of the observed spectra (detailed discussion of the coherent mixing at *specific* level crossings, such as the γ crossing, will be delayed until Chap. 5). An essential ingredient of the model is the inclusion of higher degree terms in the confinement potentials to account for deviations from ideal elliptical parabolic confinement and induce the coherent mixing. Therefore, an attractive aspect of the measurements is that they can shed light on the microscopic form of the confinement potential in realistic QDs.

The structure of this chapter is as follows. In Sec. 4.1 we introduce the ideal calculated spectrum for an *elliptical* parabolic lateral confinement potential and compare and contrast it with the limiting case of the FD spectrum for *circular* parabolic confinement (recall Sec. 2.1.2). In Sec. 4.2, focusing on two dots (from two different devices), we will show how the measured dot energy spectra can be well modelled overall by ideal spectra allowing us to extract confinement energies and ellipticities. Section 4.3 will describe explicitly how the spectral measurements are performed. Subsequently, in Sec. 4.4 we will argue that in order for the measurements of single-particle energy spectra to be possible at all in a simple coherent tunneling picture, finite inter-dot tunnel coupling, which we attribute to natural anharmonicity and anisotropy (unrelated to the bare tunnel coupling, Δ_{SAS}), is necessary. Section 4.5 will introduce a simple coherent tunneling model which attempts to explain in general terms the

widespread anti-crossing (intra-dot level mixing) behaviour observed in the dot energy spectra. A key component of the model is the inclusion of higher degree terms in the dot confinement potentials in order to induce the necessary inter-dot tunnel coupling, which accounts for the strength of the spectral features, and the intra-dot mixing. Additionally, we will discuss what would need to be done, both experimentally and theoretically, to go beyond this simple coherent tunneling picture.

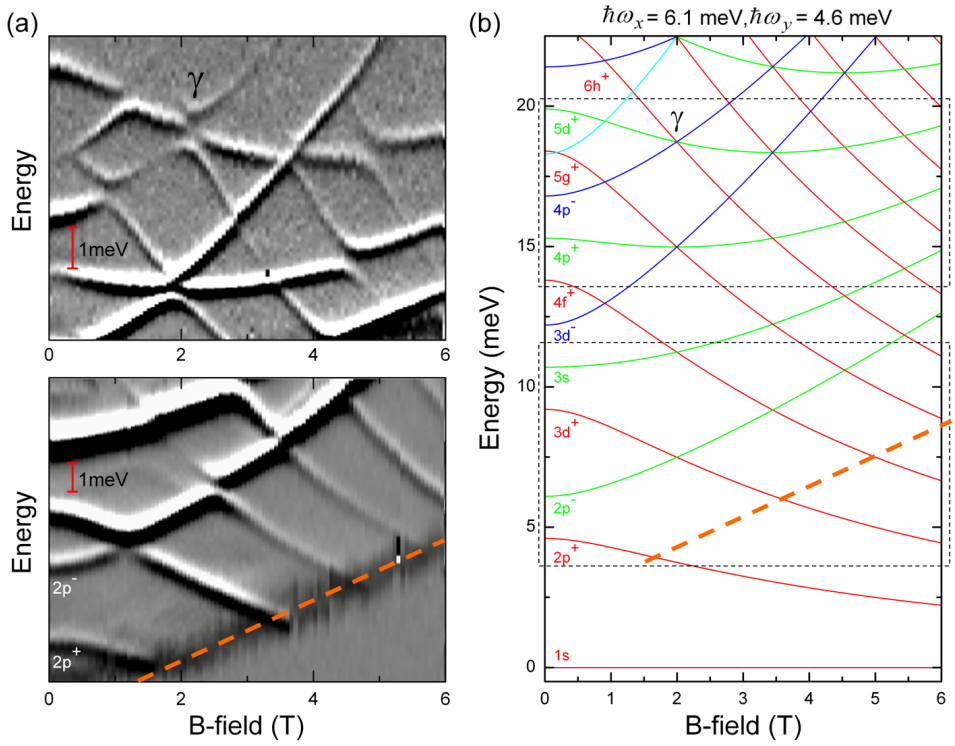

Fig. 4.1. (a) Energy spectrum of dot 2 from Device I. The orange dashed line indicates the edge of the measurement window (see Sec. 4.3). (b) Calculated elliptical parabolic spectrum which reproduces well the measured spectrum *overall*. Dotted black lines approximately identify the portions of the spectrum visible in (a). Some relevant states are labelled using the atomic orbital-like notation.

4.1 Ideal Calculated Quantum Dot Energy Spectra

The confined states in QD structures are commonly assumed to be those

appropriate for a two-dimensional confinement potential that is strictly *elliptical* and parabolic in the *x*-*y* plane, which is a reasonable starting point if the confinement in the *z*-direction is much stronger. Explicitly, the effective in-plane confinement potential is taken to be $V_{eff}(x,y) \propto (\delta x^2 + \delta^{-1} y^2)$, with ellipticity $\delta = \hbar\omega_x / \hbar\omega_y \geq 1$, where $\hbar\omega_x$ and $\hbar\omega_y$ are the confinement energies along the *x* and *y* axes respectively [6,94-97]. If we consider only single-particle states and apply a B-field along the *z*-direction, setting $\delta = 1$, we recover the familiar FD spectrum for a *circular* parabolic dot (recall Sec. 2.1.2) with confinement energy $\hbar\omega_0 = \hbar\omega_x = \hbar\omega_y$. Meanwhile, allowing $\delta > 1$ results in a spectrum which is quite similar to the FD spectrum in some respects, but exhibits several differences due to the reduction in symmetry of the confinement potential. Note that both these ideal spectra are strictly for *infinitely* high two-dimensional confinement potentials (here, in the lateral direction) and so the energy levels in either spectrum can, in principle, be computed for arbitrarily high energies.

Two important features of the vertical QD devices justify the employment of the FD spectrum and the elliptical parabolic spectrum as a starting point for modelling the measured dot spectra. First, recalling the 1D self-consistent calculation for the triple-barrier double-quantum-well resonant-tunneling structure discussed in Sec. 3.1.3 (see Fig. 3.2), the confinement energy in each well along the *z*-axis, $\hbar\omega_z$, is ~70 meV. As we shall see shortly, this value is significantly larger than the energy range over which we can access single-particle states of the probed QD. Consequently, as the states of interest all have the same (ground state) *z*-component and this allows us to focus solely on the properties of the lateral confinement potential (see also discussion in Sec. 4.4). Therefore we can justifiably think of the dots as two-dimensional discs for which the ideal FD and

elliptical, parabolic spectra are appropriate if the dot is sufficiently symmetric. Second, the lateral confinement potentials of vertical QDs, though not *infinitely* high, are certainly sufficiently high that the employment of the FD spectrum and the elliptical parabolic spectrum is quite justified provided one does not go too high up in energy (or equivalently let x and y get too large). This certainly holds for the single-particle states in the accessible energy range.

Figure 4.2 shows two calculated single-particle energy spectra, one for a circular parabolic confinement potential [Fig. 4.2(a)] and the other for an elliptical parabolic confinement potential [Fig. 4.2(b)]. The selected confinement energies are appropriate to compare these spectra with the measured energy spectra to be discussed in Sec. 4.2. Furthermore, the spectra are plotted with the energy of the ground state subtracted from the energy of all states, which eliminates the influence of the diamagnetic shift of the ground state, as this is appropriate for the measurement principle we employ (recall Sec. 2.2.3 and see Sec. 4.3), and hence for comparison with the measured spectra. Throughout both the calculated spectra shown in Fig. 4.2, many level crossings occur. In particular, two-level crossings are visible even starting from quite low down in energy, provided the B-field is not too large, and as one moves progressively up in energy, one encounters level crossings between three or more energy levels at finite B-field. For instance, several three-level crossings and even a couple of four-level crossings are visible in the top half of the spectra in Fig. 4.2 for the energy range shown. Chapter 5 will focus on these crossing points in the measured dot spectra where we observe pronounced level anti-crossing behaviour and strong variations in the resonant currents as a consequence of coherent mixing.

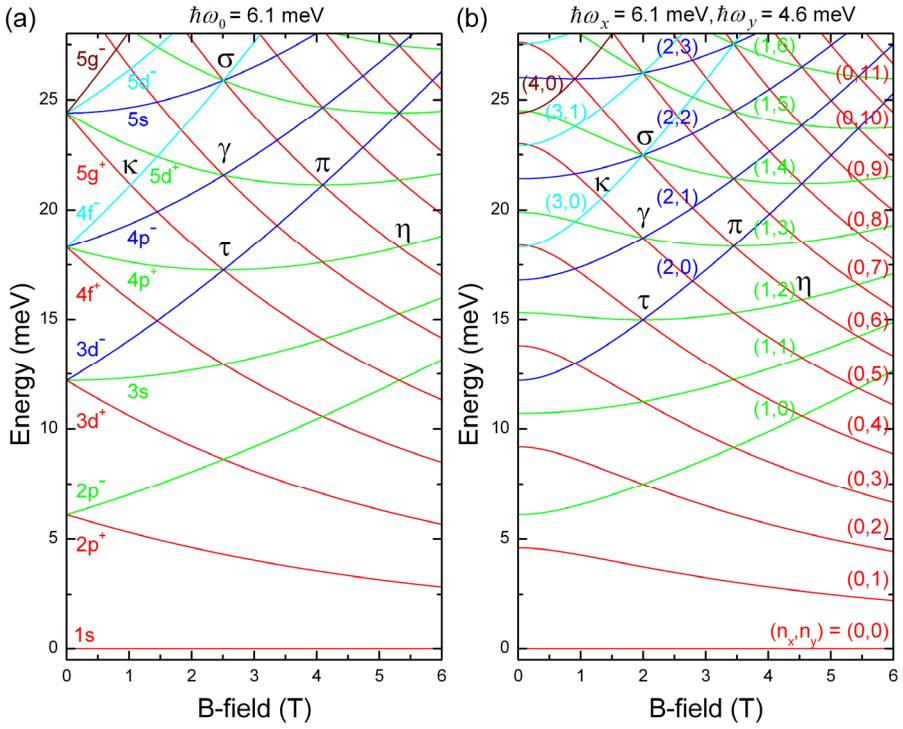

Fig. 4.2. (a) FD spectrum calculated with $\hbar\omega_0$ = 6.1 meV. The states originating from the first five shells at 0 T are labelled using the atomic-orbital-like notation (recall Sec. 2.1.2). (b) Energy spectrum calculated for elliptical parabolic confinement with $\hbar\omega_x$ = 6.1 meV and $\hbar\omega_y$ = 4.6 meV. Here, the states are labelled using the n_x and n_y quantum numbers. In both (a) and (b) energy levels which merge into the same Landau level at high B-field are coloured the same and several crossings to be studied in detail in Chap. 5 are identified by Greek symbols.

Before discussing the properties of the two spectra shown in Fig. 4.2, the notation used to label the single-particle states deserves comment. Recall that in Sec. 2.1.2, the single-particle states in the FD spectrum were labelled by two quantum numbers (n,ℓ) where n and ℓ are respectively the radial quantum number and the orbital angular momentum quantum number. Furthermore, we introduced an equivalent atomic-orbital-like notation, i.e., 1s for the ground state in the first shell; $2p^+$ and $2p^-$ for the two states in the second shell and so on. In the case of an ideal elliptical parabolic confinement

potential, since the orbital angular momentum quantum number is no longer appropriate, quantum numbers n_x and n_y are used instead of n and ℓ [see Fig. 4.2(b)]. We note that for $\delta = 1$, (n,ℓ) can be conveniently converted to (n_x,n_y) by the following relations: $n_x = n + \frac{1}{2}|\ell| - \frac{1}{2}\ell$ and $n_y = n + \frac{1}{2}|\ell| + \frac{1}{2}\ell$ [95], and the shell to which a state belongs, M, is given by $M = n_x + n_y + 1$ [recall from Sec. 2.1.2 that for the (n,ℓ) notation $M = 2n + |\ell| + 1$]. However, even when the ellipticity is not unity, it is often less cumbersome and more transparent to label the states as if $\delta = 1$, i.e., with the atomic-orbital-like notation.

The two ideal calculated spectra shown in Fig. 4.2 exhibit many similarities, but also one striking difference and a second more subtle one. The most important similarity is that *all* the level crossings in both the ideal spectra are *exact* crossings, i.e., there is no anti-crossing behaviour between crossing single-particle energy levels. This is in contrast to the measured spectra to be discussed in Sec. 4.2, where anti-crossing behaviour, attributed to anharmonicity and anisotropy, is prevalent. Another similarity is that the level crossings occur in 'families' at certain distinct B-fields in these ideal spectra because the confinement energy is a constant for an entire spectrum. As an example, the three-level crossings labelled τ and γ occur at the same B-field, along with many other level crossings, in both of the spectra. This too is different from what is observed in the measured spectra and will provide information about how the confinement energy itself changes with energy in practice. A further similarity between the two ideal spectra is that at very high B-field, well beyond 6 T, the energy levels with the same n_x quantum number merge into the same Landau level. At such B-fields, the influence of an ellipticity greater than unity diminishes because the cyclotron orbits become much smaller then those arising solely from the lateral confinement.

The most striking difference between the two ideal spectra is the general lifting of the degeneracies of the energy levels in the same shell at 0 T that is introduced when $\delta > 1$ as a result of breaking the circular symmetry. In this situation, another more subtle difference depends on the size and precise value of δ. To see this, consider, for example, the two-level crossing between the $2p^-$ and $3d^+$ states which, when $\delta = 1$, occurs at finite B-field. As δ is increased from unity (with the constraint that the product of $\hbar\omega_x$ and $\hbar\omega_y$ is constant), the crossing between the two related states [$(n_x,n_y) = (1,0)$ and $(0,2)$] shifts progressively to lower B-field. Eventually, at $\delta = 2$, the crossing occurs at 0 T, and for $\delta > 2$ it will not take place at all. Generalizing, if δ becomes too large, level crossings will disappear, particularly in the lower part of the energy spectrum, and one would need to go to ever higher energy to encounter the level crossings. Also note that for certain 'magic' values of δ ($\delta = 2$ is one example), widespread level degeneracy will occur at 0 T between levels which cross at finite B-field when $\delta = 1$ [95,97]. For the situation most relevant for the measured spectra to be introduced next $\delta < 1.5$. In this case, the ideal circular parabolic and the elliptical parabolic single-particle spectra are quite similar in form for B > 1 T, as is clear from Fig. 4.2.

4.2 Measured Quantum Dot Energy Spectra

Using a vertical double QD device (recall the measurement setup and device geometry described in Chap. 3) and consistent with the measurement principle described in Ref. [70] (recall Sec. 2.2.3), we can use the 1s-like state of the upstream dot to probe the single-particle states of the downstream dot in the single-electron tunneling (SET) regime (recall Fig. 2.12). We will now describe some of the basic properties of the two

measured spectra shown in Fig. 4.3, deferring until Sec. 4.3 the question of precisely how the spectra are acquired.

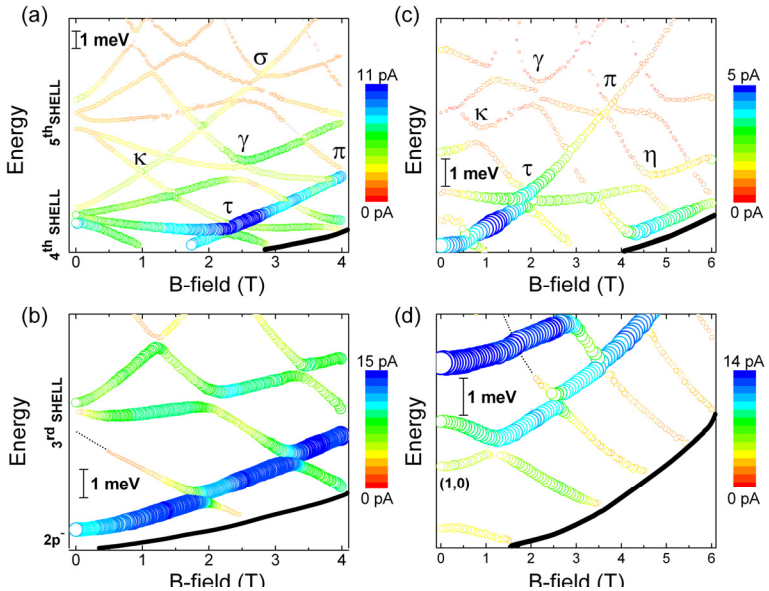

Fig. 4.3. Energy spectra of dot 2 from Device VI [(a) and (b)] and dot 2 from Device I [(c) and (d)]. Black lines indicate the edge of the measurement window in each panel (see Sec. 4.3 which also explains why each spectrum is captured in two portions). The ~pA resonant current (non-resonant background current not removed) is indicated by the colour scale and size of the symbols. Dotted black lines identify barely resolvable portions of some weak spectral features. The $2p^-$-like state and the related $(n_x,n_y) = (1,0)$-like state are marked in (b) and (d) respectively.

Appealingly, even without detailed knowledge of how it is acquired, it is apparent that the spectrum of dot 2 from Device VI shown in Figs. 4.3(a) and (b) closely resembles a FD spectrum [note the nearly degenerate levels within shells at 0 T and see Fig. 4.2(a)]. Meanwhile, the spectrum of dot 2 from Device I shown in Figs. 4.3(c) and (d) closely resembles the spectrum for elliptical parabolic confinement [note the levels are well separated at 0 T and see Fig. 4.2(b)]. Furthermore, by comparing the measured spectra in Fig. 4.3 to the ideal spectra in Fig. 4.2, we see that there are no additional features in the

measured spectra and so we are confident that these spectra are single-particle in nature (see also discussion in Sec. 4.3).

Two key observations are readily apparent on examination of the measured spectra. Firstly, an attractive attribute of acquiring energy spectra in the way we do with a vertical double QD device is that we can easily access the single-particle states over a large energy window, limited only by the onset of longitudinal-optic phonon emission at ~37 meV [98]. This window is much larger than that possible with 'current stripe' measurements on a single vertical QD, as described in Sec. 2.1.5, where excited states of the one-electron system can only be clearly observed if they lie within a ~5 meV window (limited approximately by the confinement energy, $\hbar\omega_0$) [78]. Secondly, and crucial for Chap. 5, the naive expectation from the ideal spectra of Fig. 4.2 that all the level crossings should be exact is manifestly incorrect as we observe widespread anti-crossing behaviour in Fig. 4.3 when two or more single-particle energy levels approach each other. In particular, the three lowest energy three-level crossings labelled τ, γ and π show pronounced anti-crossing behaviour (which will be discussed in Sec. 5.1), as do many of the visible two-level crossings (see discussion on the crossings labelled κ and η in Sec. 5.2.3). Interestingly, also visible in Fig. 4.3(a) is a four-level crossing, labelled σ, which exhibits clear anti-crossing behaviour (see Sec. 5.2.4).

While some crossings in the spectra of Fig. 4.3 may appear to be exact crossings, anti-crossings smaller than the spectral resolution of ~50 μeV are not resolvable. The observed energy splitting is typically several hundred meV ($\gg k_BT \approx 25$ μeV) and can be as large as ~1 meV. This is much larger than other sources of splitting which come to mind, namely Δ_{SAS}, Zeeman splitting (<100 μeV up to 4 T [99]), and spin-orbit splitting

(<50 μeV [99]). Furthermore, since the spectra are single-particle in nature, splitting due to Coulomb interactions can also be discounted [50]. Therefore, we will argue in Sec. 4.5 that the observed anti-crossing behaviour can arise from natural perturbations in the confinement potentials of real QDs caused by local randomness and imperfections. Furthermore, in Sec. 5.3 we will show how by including appropriate symmetry breaking terms in the confinement potential of the downstream dot, we can explain the experimental observations at specific crossings.

The strength of the spectral features in Fig. 4.3 reflects the resonant current and this too can provide valuable information about the nature of transport through the QDs. For instance, as we will discuss in detail in Sec. 4.4, if the two dots are assumed to be both *ideal* and *identical*, in the framework of a simple coherent tunneling model one would expect that *only* the 1s-1s resonance should be observed for the measurement principle we employ due to wavefunction orthogonality, i.e., the 1s-X resonant current would be zero if X is any downstream dot state other than 1s (see also Ref. [70]). In actuality, we find that almost all 1s-X resonances carry non-zero current (of order 1-10 pA) indicating that there is a finite tunnel coupling between the upstream dot's 1s-like state and the downstream dot's probed states. We will discuss these inter-dot tunnel couplings, which are not to be confused with the bare tunnel coupling, Δ_{SAS}, in more detail in Sec. 4.4. Furthermore, we will demonstrate in Sec. 4.5 that they can be induced by symmetry breaking perturbations in the dot confinement potentials.

Evident from the spectra presented in Fig. 4.3, the resonant currents vary non-trivially from resonance-to-resonance and as a function of B-field. The general trend, namely that the currents are smaller at higher energy, is likely the result of an enhanced

tunnel barrier between the source contact and the upstream dot when a more negative V_G is applied in order to access the higher energy states (see the discussion in Sec. 4.3 of how the measurements are performed). In the original work of Ref. [70] (recall Sec. 2.2.3), two possible pictures to explain the resonant currents were put forward, namely coherent tunneling and (incoherent) sequential tunneling. As we will discuss in Sec. 4.5, within the framework of coherent tunneling, we can successfully explain the general properties of a measured dot energy spectrum, namely non-zero currents for almost all resonances, and widespread anti-crossings and level mixing behaviour, by including higher order terms into the dot confinement potential as perturbations. However, while this approach can also reproduce the pronounced mixing at specific crossings (see Sec. 5.3), to date a full microscopic model that can explain a sizeable portion of the spectrum (energy and current) does not exist.

Neglecting the mixing of levels in the regions where the levels are anticipated to cross exactly, *overall* the measured energy spectrum of dot 2 from Device VI shown in Figs. 4.3(a) and (b) is well reproduced by the calculated FD spectrum shown in Fig. 4.2(a), and likewise *overall* the measured energy spectrum of dot 2 from Device I shown in Figs. 4.3(c) and (d) is well reproduced by the calculated elliptical parabolic spectrum shown in Fig. 4.2(b). That the agreement is so good justifies the subtraction of the energy of the ground state from the energy of all higher states in the calculated spectra shown in Fig. 4.2 accounting for the diamagnetic shift of the ground state, consistent with the measurement scheme (see also Sec. 4.3). Indeed, had we not done this subtraction, the agreement would be not quite as good, since the energy levels in the calculated spectra would, at any given B-field, all have larger slopes than actually observed.

It may seem curious that the spectra for these two dots have different ellipticities despite both being located in nominally circular mesas. However, it is well documented from measurements in the few-electron regime that the ellipticity of vertical QDs varies considerably from device-to-device and is never exactly unity, but rather is typically in the range of ~1.05-2 (see Refs. [11,31,100]). Natural perturbations in the confinement potentials of vertical QDs caused by local randomness and imperfections are ultimately responsible for this (as well as for the anti-crossing behaviour in the measured energy spectra, see Sec. 4.5).

In order to estimate the confinement energies of the probed dots from the measured spectra in Fig. 4.3 (required for the calculated spectra in Fig. 4.2), we note that for an ideal elliptical parabolic potential both the relative spacing of the energy levels at 0 T and the B-field position of the exact level crossing points are uniquely determined by the confinement energies $\hbar\omega_x$ and $\hbar\omega_y$. Utilizing this principle, we can take a measured spectrum and estimate the confinement energies by matching it with a calculated elliptical parabolic spectrum. This then allows us to set the energy scale bars in Fig. 4.3. What the 'energy' axis actually corresponds to in the measurements will be explained in Sec. 4.3. In the case of the energy spectrum of dot 2 from Device VI shown in Figs. 4.3(a) and (b), an estimate reveals $\delta \approx 1.05$, which is sufficiently close to unity that we will continue to treat this dot as being circular in the following discussions. This is quite reasonable since the splitting of the levels in the shells at 0 T is small compared to the energy separation between the shells [see for example the nearly degenerate four (five) levels in the fourth (fifth) shell in Fig. 4.3(a)]. In contrast, for dot 2 from Device I δ is estimated from Figs. 4.3(c) and (d) to be ~1.3-1.5 (see confinement energies quoted

below) so this probed dot evidently can not be treated as being approximately circular.

In practice there is one complication in determining the confinement energies of the probed dots from the measured spectra that can not be neglected. Recalling from Sec. 4.1 that the energy level crossings in the ideal spectra calculated for fixed confinement occur in 'families' of crossings at certain distinct B-fields, close inspection of the measured spectra reveals that higher energy crossings in any given 'family' are in fact systematically shifted to higher B-field. For instance, in Fig. 4.3(c), we see that the (centers of the) τ and γ crossings occur respectively at ~1.9 T and ~2.2 T. The reason for this, which will also become clearer in Sec. 4.3, is that in the measurement scheme we employ, in order to capture a spectrum at higher energy, more negative V_G is required, and hence the dots are 'squeezed' more (see Ref. [76]). Thus, the effective confinement of the probed dot actually increases along the 'energy' axis of a spectrum which explains why the members of a 'family' of crossings are not all observed at the same B-field as naively expected from the ideal calculated spectra of Fig. 4.2. Consequently, we chose to determine what are essentially *average* confinement energies separately for each panel in Fig. 4.3. To do this we selected a low-energy crossing point and a high-energy crossing point in each panel, which would both occur at the same B-field if the confinement were constant, took the average of their actual B-field positions, and then used this to generate the appropriate calculated spectrum. The choice of confinement energies in Fig. 4.2 is now clear. In Fig. 4.2(a), we show a FD spectrum calculated with a confinement energy of $\hbar\omega_0 = 6.1$ meV, which is appropriate for the upper part of the spectrum of dot 2 from Device VI [Fig. 4.3(a)], while the lower part of this dot's spectrum [Fig. 4.3(b)] is best modeled by a FD spectrum calculated with $\hbar\omega_0 = 4.8$ meV (not shown). As a useful rule-

of-thumb, the confinement energy can be estimated from a FD spectrum by noting the B-field (in Tesla) at which the lowest energy two-level crossing (between the $2p^-$ and $3d^+$ states) occurs and multiplying this by 2.47 to obtain the confinement energy in meV. In Fig. 4.2(b), we show an elliptical parabolic spectrum calculated with confinement energies $\hbar\omega_x$ = 6.1 meV and $\hbar\omega_y$ = 4.6 meV, i.e., $\delta \approx 1.33$, which is appropriate for the upper part of the spectrum of dot 2 from Device I [Fig. 4.3(c)], while the lower part of this dot's spectrum [Fig. 4.3(d)] is best modeled by an elliptical parabolic spectrum calculated with $\hbar\omega_x$ = 5.4 meV and $\hbar\omega_y$ = 3.5 meV, i.e., $\delta \approx 1.54$ (not shown).

4.3 Details of Spectral Measurement Technique

Having demonstrated in Sec. 4.2 that the spectra of dot 2 from Device I and dot 2 from Device VI are well modelled by elliptical parabolic spectra, we will now describe in detail how the measured spectra were actually acquired. In Sec. 2.2.3 we introduced the basic measurement principle, namely to use the 1s-like state of the upstream dot to probe the single-particle states of the downstream dot in the single-electron tunneling regime (see also Ref. [70]). Additionally, Sec. 2.2.3 described some limitations which were apparent in the original work of Ref. [70], most notably the limited B-field resolution and energy range of the measured spectrum [recall Fig. 2.13(b)]. Compared to the results of Ref. [70], the measured spectra presented in Fig. 4.3 have a higher B-field resolution and cover a wider energy range. These two improvements are both critical in order to investigate multi-level mixing as will be described extensively in Chap. 5.

While both the results in Sec. 4.2 and the original work of Ref. [70] arise from applying the same measurement principle, the precise measurement strategy differs.

Henceforth, we refer to the strategy used for the measurements of Sec. 4.2 as strategy A, and the original strategy employed in Ref. [70] as strategy B. In Sec. 4.3.1 we will describe strategy A and explain how it differs from strategy B, while Sec. 4.3.2 will provide some additional details about the measured spectra shown in Fig. 4.3. We note that a demonstration that the choice of measurement strategy does not affect the multi-level mixing physics of interest will be given in Sec. 5.1.4 by characterising the γ crossing in the spectrum of dot 2 from Device I using both strategies.

4.3.1 Spectral Measurement Strategies

Figure 4.4(a) shows the differential conductance in the V_{SD}-V_G plane for Device I measured at 0 T [recall Fig. 3.11(a)]. Several familiar features are visible, namely the V-shaped $N = 0$ region where the device is pinched-off and the first few Coulomb blockade diamonds where the number of electrons trapped in the double QD system is constant. Furthermore, the two regions in which sequential single-electron tunneling (SET) through the two dots occurs [recall Fig. 2.11(b)] in the absence of electrons being permanently trapped on either dot are identified in Fig. 4.4(a). Note that unlike in the calculation shown in Fig. 2.11(b), in the experimental data these regions have finite curvature and hence are referred to as being 'arc-shaped.' This shape is substantially due to increased band bending as a result of the increasingly negative V_G and large V_{SD} applied. Furthermore, recalling Figs. 2.12 and 2.13(a), each resonance line (black and white stripe) inside the SET regions of Fig. 4.4(a) corresponds to a single-particle state in the downstream dot being probed by the 1s-like (ground) state of the upstream dot. For instance, on the left side of Fig. 4.4(a), triangles mark the 1s-$2p^+$, 1s-$2p^-$, and 1s-$3d^+$

reverse bias resonances. Note as well that these resonances extend outside of the SET region (towards more positive V_G). In fact, the lower edge of the SET region marks the onset of an additional sequential tunneling cycle for which one electron is permanently trapped in the downstream dot. Furthermore, as we move towards more positive V_G additional sequential tunneling cycles involving more electrons permanently trapped on the downstream dot also become possible. Hence, below the SET region additional resonances corresponding to double-, triple-, etc. electron tunneling may also be visible.

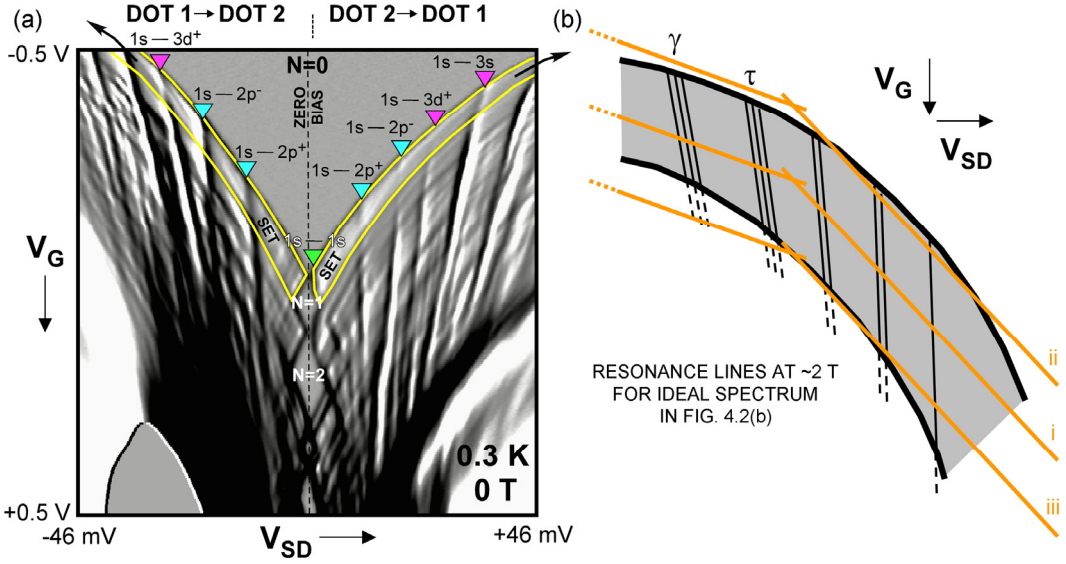

Fig. 4.4. (a) Numerically derived differential conductance, dI/dV_{SD}, in the V_{SD}-V_G plane for Device I. The current is less than 200 pA (except in the grey region in the lower left of the figure). The dot 1 (dot 2) spectrum can be measured in forward (reverse) bias. (b) Cartoon of extended reverse bias SET region (in grey) showing three possible two-part 'vector voltage' line scans numbered i, ii and iii. The situation depicted, with the spectrum of dot 2 from Device I in mind [see Figs. 4.3(c) and (d)], is of the nearly vertical resonance lines cut at ~2 T if the dot 2 spectrum were that shown in Fig. 4.2(b). For this condition, the resonance lines relevant to the τ and γ crossings are minimally separated. When the resonance lines pass below the SET region into the region where other tunneling processes can additionally occur, they are shown as dashed lines, and not all resonance lines that may appear in this region are shown.

In order to capture the energy spectrum of one of the dots in Device I, we could have proceeded in a similar fashion to Ref. [70], i.e., by strategy B. Using this strategy, to measure the spectrum of one dot we would have performed a similar measurement to that shown in Fig. 4.4(a), but for only one bias direction and then stepped the B-field [recall Fig. 2.13(a)]. Subsequently, we could then have extracted the position of the resonances in order to build-up the spectrum [recall Fig. 2.13(b)]. However, in order to produce a spectrum comparable to that shown in Figs. 4.3(c) and (d), i.e., 0 T to 6 T range in steps of 0.06 T, this would have taken ~500 hours of measurement time. Although feasible, not only would the measurement of a high resolution spectrum by strategy B be exceedingly long, it would be tedious to assemble the data sets to generate the spectrum.

Therefore, in order to minimize the time required to build-up a high resolution spectrum, we employed strategy A which we now describe fully. Using strategy A, we measure the current, at fixed B-field, by scanning along straight 'vector voltage' lines (ideally solely) within one of the arc-shaped SET regions shown in Fig. 4.4(a) and then step the B-field. With such 'vector voltage' lines we can cut across the resonance lines of interest inside the SET region in either bias direction. This leads to a series of current peaks and by extracting their positions as a function of B-field, an energy spectrum such as those shown in Fig. 4.3 is built-up. Explicitly, along the 'vector voltage' lines, which constitute the vertical energy axes in the measured spectra of Fig. 4.3, V_{SD} and V_G are altered such that $\Delta V_G/\Delta V_{SD} = \lambda$ where λ is a constant. By limiting the measurement to a single 'vector voltage' line for each B-field, as opposed to a large region of the V_{SD}-V_G plane, a high resolution spectrum can be built-up in ~15 hours.

One complication in performing a strategy A measurement is that due to the

extent and shape of the SET regions in the V_{SD}-V_G plane, which extend well beyond the highlighted regions in Fig. 4.4(a) in the direction of the black arrows, it is not possible to measure an energy spectrum over a very large energy window with a single straight 'vector voltage' line scan. Thus, we usually measure a spectrum in at least two parts, as is the case in Fig. 4.3 for both devices, i.e., one 'vector voltage' line scan captures the lower part of the spectrum at lower bias and another 'vector voltage' line scan, of different slope, captures a higher part of the spectrum at higher bias [see for example scan i in Fig. 4.4(b)]. Furthermore, while the goal when setting up a 'vector voltage' line scan is to ensure that the line always remains inside the target SET region, the resonances may not be visible if all or part of the 'vector voltage' line is above the SET region and instead cuts into the V-shaped $N = 0$ region [see for example scan ii in Fig. 4.4(b)]. Another scenario is that all or part of the 'vector voltage' line cuts into the region just below the SET region possibly resulting in extra spectral features that arise only when permanent dot charging occurs [see for example scan iii in Fig. 4.4(b)]. If this occurs it is straightforward to exclude the unwanted extra resonance lines by comparison with the calculated spectra, and so we are confident that the spectra in Fig. 4.3 are single-particle in nature.

A further complication to using strategy A is that due to the diamagnetic shift of a dot's ground state, both the SET regions systematically move down, towards more positive V_G, relative to any *fixed* 'vector voltage' line with increasing B-field. As a result of this shift, it can be challenging to set up the 'vector voltage' line scan appropriately so that it stays substantially within the target SET region over the course of an entire measurement (typically over a 4 or 6 T range). As a final comment on the 'vector voltage'

line scans, we note that for convenient reference we normally start the 'vector voltage' line scan in the V-shaped $N = 0$ region, but still close to the target SET region. This explains why the measured parts of the spectra only 'appear' above the thick black line at the bottom right of each of the panels in Fig. 4.3.

4.3.2 Extra Details Regarding the Measured Spectra

Now that we have fully explained strategy A, we return to the spectra shown in Fig. 4.3 and provide some additional details about the measurements. The initial discussion in this section focuses on Device I, in particular Fig. 4.4(a), however, many of the comments could equally apply to other devices.

As discussed in the previous section, each resonance line inside the SET regions of Fig. 4.4(a) corresponds to a single-particle state in the downstream dot being probed by the 1s-like (ground) state of the upstream dot. The spectrum shown in Figs. 4.3(c) and (d) is measured in reverse bias and actually corresponds to the spectrum of dot 2 being probed by the 1s-like state of dot 1 (recall also Fig. 2.12). The lower part of the spectrum displayed in Fig. 4.3(d) is essentially captured with a 'vector voltage' line scan through the reverse bias SET region shown in Fig. 4.4(a) (although the 1s-$2p^+$ resonance line is no longer cut by the 'vector voltage' line above ~1.5 T). The upper part of the spectrum displayed in Fig. 4.3(c) is captured with another 'vector voltage' line scan through the same reverse bias SET region but at more negative V_{SD} and V_G. Furthermore, we note that resonance lines are also visible on the forward bias side of Fig. 4.4(a), where the dot being probed (dot 1) is the dot which provided the 1s-like 'prober' state for the reverse bias spectrum in Fig. 4.3(c) and (d). Therefore, by setting up 'vector voltage' lines in the

opposite bias direction, the spectrum of dot 1 can also be measured. Depending on the nature of the perturbations in the confinement potentials of the dots, these spectra may or may not be similar in appearance. Although not shown here, the energy spectrum of dot 1 from Device I (Device VI) is overall quite similar in general appearance, but not fine detail, to that of dot 2 from the same device. In particular, the dot ellipticities are comparable (see Fig. 4.7 in Sec. 4.6 which shows a portion of the spectrum of dot 1 from Device I).

The fact that the spectral lines in Fig. 4.3 are well reproduced by the ideal calculated spectra in Fig. 4.2 (away from the immediate crossing regions) confirms their single-particle nature and the involvement of only the 1s-like state of the upstream dot. Were other higher energy states in the upstream dot available for tunneling, or electrons permanently trapped on either dot, we would expect the spectral lines shown in Fig. 4.3 to be very different. For instance, as mentioned in Sec. 4.3.1, because it can be difficult to set up the 'vector voltage' lines to capture the single-particle spectrum of one of the dots, extra features related to permanent dot charging are sometimes captured. In fact, while the data sets used to build-up the parts of the spectra shown in Figs. 4.3(a)-(c) had no extra spectral features [see for example the top panel of Fig. 4.1(a) which shows no extra features in the differential conductance for the data set related to Fig. 4.3(c)], the data set used to build-up Fig. 4.3(d) did have some extra spectral features [the most prominent of which occur at higher energy than the portion shown in the lower panel of Fig. 4.1(a)]. Thus, the 'vector voltage' lines employed were well set up for the measurements related to Figs. 4.3(a)-(c) but not quite so well set up for the measurement related to Fig. 4.3(d). Nonetheless, it was straightforward to exclude the unwanted extra lines in Fig. 4.3(d) by

comparison with the calculated spectrum in Fig. 4.2(a) and so we are confident that the spectra in Fig. 4.3 are single-particle in nature. Given the clear nature of the measured spectra, apparently the 1s-like (ground) state of the upstream dot is 'pinned' close to the Fermi-level of the source contact, even for the typically high bias applied to capture the single-particle spectra [up to ~150 mV, for example, in Fig. 4.3(a)], indicating that the electric field across the downstream dot is much larger (consistent with the results of Ref. [101] which obtained information about the voltage drop across each of the three barriers in a vertical double dot structure similar to the ones studied here). Beyond the scope of this thesis, it would be interesting if a suitably sophisticated and realistic self-consistent calculation could reproduce the empirical observations at high bias.

4.4 Influence of Inter-dot Tunnel Coupling on the Spectral Measurements

In this section, we discuss the issue of the inter-dot tunnel coupling, not only to account for why the measurements succeeded, but also as a starting point for introducing the model described in Sec. 4.5 which attempts to reproduce some features of both the energy dispersion and the resonant currents in a measured single-particle spectrum. A key ingredient of the model will be the inclusion of higher order perturbative terms to the lateral confinement potentials of the dots. The goal of this section is to demonstrate that such terms are essential in order to couple the ground state of the upstream dot to the higher energy states in the downstream dot, making it possible to capture a QD energy spectrum using the measurement principle we employ (recall Sec. 2.2.3).

In the following, we initially picture an ideal vertical double QD device consisting of two identical, circular parabolic dots and will limit the discussion to the case of B = 0 T. We begin by carefully introducing the notation used in this section to label the QD states. Initially we will explicitly consider *all* spatial components of these wavefunctions, whereas previously we focused only on the lateral component. We will assume that the wavefunctions of the electronic states in each QD can be separated into two parts, namely the lateral (*x*- and *y*-) and vertical (*z*-) components. For convenience, we refer to the two dots as the left dot and the right dot. Hence, we use the notation $\{z_{Li};A_{Lj}\}$ and $\{z_{Rp};A_{Rq}\}$ to label the states in the two *uncoupled* dots, where subscript L (R) identifies a left (right) dot state. In this notation z_{Li} and z_{Rp} label the *z*-components of the states and A_{Lj} and A_{Rq} label the lateral components. Note that the indices for both components indentify states in terms of increasing energy, i.e., $i,p = 0, 1, 2, \ldots$ and A_{Lj}, A_{Rq} = 1s, $2p^-$, $2p^+$, …, where, for compactness, we use the familiar atomic-orbital-like notation. Thus, $\{z_{L0};1s\}$ ($\{z_{R0};1s\}$) denotes the ground state in the *uncoupled* left (right) dot. The energy offset between $\{z_{L0};1s\}$ and $\{z_{R0};1s\}$, which is essentially proportional to V_{SD}, will be referred to as the detuning, with positive detuning defined such that the energy of $\{z_{L0};1s\}$ is higher than that of $\{z_{R0};1s\}$.

For the coupled vertical QD structures we study, as discussed in Sec. 3.1.3, the confinement energy in the *z*-direction (~70 meV) is much larger than the energy window over which we can probe the single-particle states. Consequently, we typically only need to consider the ground state in the *z*-direction of each of the two dots for the moderate bias we apply to capture the dot energy spectra. Hence, we are only concerned with states of the form $\{z_{L0};A_{Lj}\}$ and $\{z_{R0};A_{Rq}\}$ in this section. We stress that elsewhere in this thesis,

when referring to such states we omit the *z*-component and simply discuss the lateral component (represented by the atomic-orbital-like notation).

We now consider a pair of corresponding left and right dot states, i.e., $\{z_{L0};A_{Lk}\}$ and $\{z_{R0};A_{Rk}\}$ where $A_{Lk} = A_{Rk}$. In general, if these two states are uncoupled, then they cross exactly as a function of detuning, while for finite coupling they form two anti-crossing branches. Consider Fig. 4.5(a) which shows the crossing between the ground states of the two dots $\{z_{L0};1s\}$ and $\{z_{R0};1s\}$. At zero detuning [point i in Fig. 4.5(a)] the two states hybridize into symmetric (S) and anti-symmetric (AS) states, explicitly $\{z_{S0};1s\} = 1/\sqrt{2}\,(\{z_{L0};1s\} + \{z_{R0};1s\})$ and $\{z_{AS0};1s\} = 1/\sqrt{2}\,(\{z_{L0};1s\} - \{z_{R0};1s\})$. The energy separation between these states, which we refer to as the bare tunnel coupling, is labelled Δ_{SAS} (note that for simplicity, we take Δ_{SAS} to be the bare tunnel coupling for *all* pairs of corresponding $\{z_{S0};A_{Lk}\}$ and $\{z_{AS0};A_{Rk}\}$ states). Meanwhile, for small, but finite detuning (point ii), where the separation between $\{z_{L0};1s\}$ and $\{z_{R0};1s\}$ is still comparable to Δ_{SAS}, the states are referred to as bonding (B) ($\{z_{B0};1s\}$) and anti-bonding (AB) states ($\{z_{AB0};1s\}$). Finally, for large detuning (point iii), where the separation between $\{z_{L0};1s\}$ and $\{z_{R0};1s\}$ is much greater than Δ_{SAS}, the states are effectively uncoupled and can be regarded as left dot and right dot states.

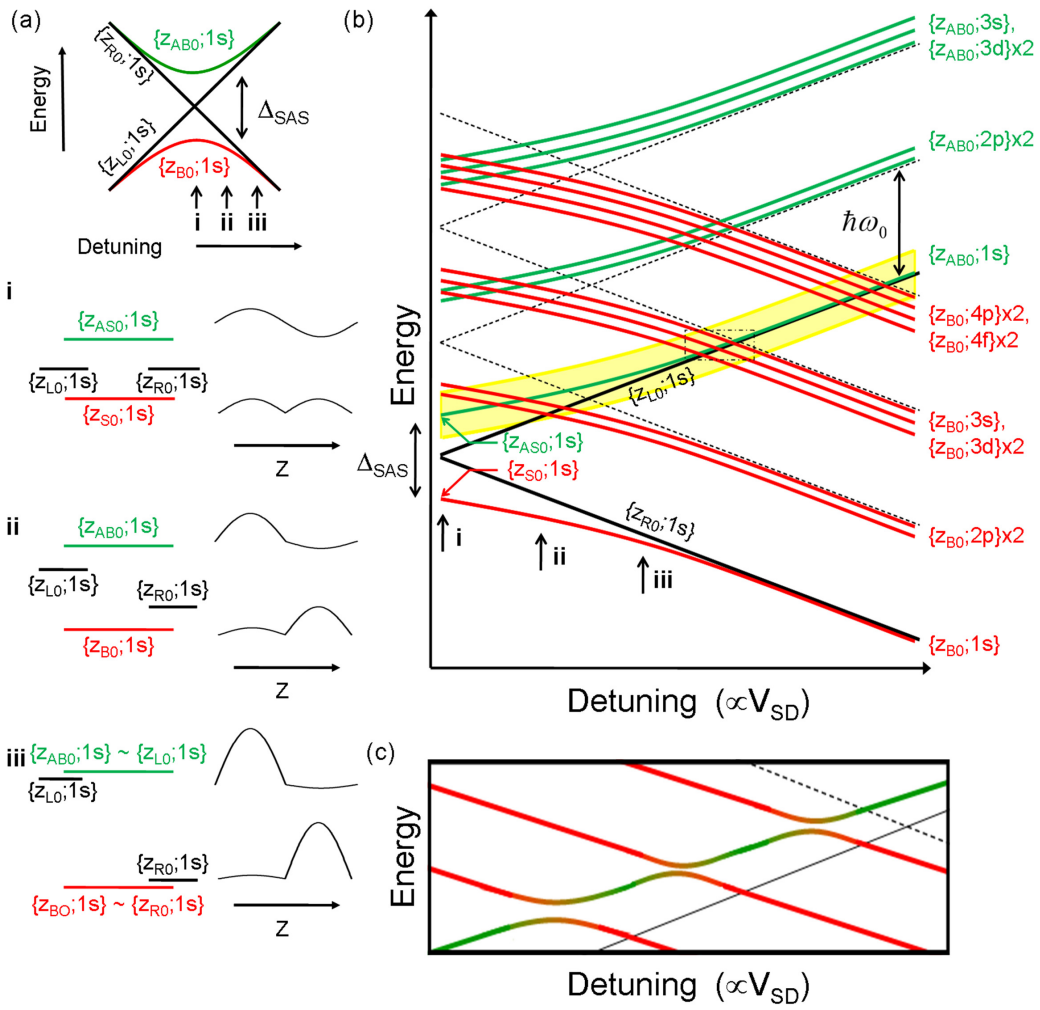

Fig. 4.5. (a) Schematic diagram representing the energies of left and right dot states $\{z_{L0};1s\}$ and $\{z_{R0};1s\}$ when coupled as a function of detuning. The *z*-component of the symmetric/anti-symmetric, bonding/anti-bonding and approximately left/right dot wavefunctions are also sketched out at respectively points i, ii and iii. (b) Schematic diagram representing the energies of the single-particle states in the first few shells of two coupled QDs as a function of detuning (states with excited *z*-components are at much higher energy). Red (green) states correspond to the coupled states $\{z_{B0};A_{Bj}\}$ ($\{z_{AB0};A_{ABj}\}$). Although the states within each shell are degenerate at 0 T for a circular parabolic lateral confinement potential, here they are vertically offset a little for clarity. The solid black lines mark the energies of the uncoupled ground states $\{z_{L0};1s\}$ and $\{z_{R0};1s\}$, while the dotted black lines provide a guide to the eye for states with higher energy lateral components. The confinement energy, $\hbar\omega_0$, assumed to be the same for both dots, is also indicated. For clarity, the figure is drawn for an overly large value of

Δ_{SAS}, comparable to $\hbar\omega_0$, although we measure weakly coupled dots where $\Delta_{SAS} \ll \hbar\omega_0$. (c) Expanded view of the boxed region in (b) showing small anti-crossings of different sizes between the up-going $\{z_{L0};1s\}$ and the down-going $\{z_{R0};A_{Rq}\}$ states (where A_{Rq} is $3d^+$, 3s and $3d^-$ for the three states shown) necessary in order for a resonant current to be observed using the measurement principle we employ.

Figure 4.5(b) shows schematically the energies of the single-particle states from the first few FD shells of the two coupled QDs as a function of detuning. The states are drawn for finite tunnel coupling, meaning that at zero detuning (point i) corresponding symmetric and anti-symmetric states are separated by Δ_{SAS} [for clarity only the lowest energy symmetric/anti-symmetric pair, $\{z_{S0};1s\}$ and $\{z_{AS0};1s\}$, is labelled in Fig. 4.5(b)]. Recall that in Sec. 3.1.3, we stated that Δ_{SAS} is <0.1 meV [87]. Although the self-consistent calculation described in Sec. 3.1.3 is for the triple-barrier double-well hetero-structure and not for the QD devices, within the framework of separable wavefunctions, it is a reasonable approximation to take Δ_{SAS} to be <0.1 meV for the QD devices as well. Therefore, as $\Delta_{SAS} \ll \hbar\omega_0 \approx 5$ meV, even at small detuning (low bias) the $\{z_{B0};A_{Bj}\}$ and $\{z_{AB0};A_{ABq}\}$ states are already well approximated by the $\{z_{L0};A_{Lj}\}$ and $\{z_{R0};A_{Rq}\}$ states.

As discussed in Sec. 4.3 (see also Sec. 2.2.3), to perform spectral measurements we use the 1s-like state of the upstream dot to probe the single-particle states of the downstream dot in the single-electron tunneling regime. For the situation pictured in this section where the left dot probes the right dot spectrum, this means we wish to use the $\{z_{L0};1s\}$ state to resonantly probe the $\{z_{R0};A_{Rq}\}$ states (elsewhere in this thesis we suppress the *z*-component and represent the resonances as 1s-A_{Rq}). For this measurement principle, we expect from an energetic point of view, ignoring any possible selection rules which may apply, that a finite resonant current through the double QD system would flow

whenever the $\{z_{L0};1s\}$ is energetically aligned with a $\{z_{R0};A_{Rq}\}$ state as the detuning is swept. In Fig. 4.5(b), such crossing points between the energetically up-going $\{z_{L0};1s\}$ state and the down-going $\{z_{R0};A_{Rq}\}$ states are all located within the region highlighted in yellow (and as a function of B-field, the states, and hence the crossing points, evolve in energy and so the right dot spectrum can be mapped out).

However, a complication immediately arises when we consider what appears to be an obvious selection rule. As mentioned in Sec. 4.2, within the framework of a simple coherent tunneling picture, if the two dots are assumed to be both *ideal* and *identical*, one would expect that *only* the $\{z_{L0};1s\}$-$\{z_{R0};1s\}$ resonance should be observed due to wavefunction orthogonality. In actuality (recall Fig. 4.3), we find that almost all $\{z_{L0};1s\}$-$\{z_{R0};A_{Rq}\}$ resonances have non-zero current (of order 1-10 pA). In order to reconcile this and account for the observed resonant currents, there *must* be finite tunnel coupling [102] between the $\{z_{L0};1s\}$ state and each of the $\{z_{R0};A_{Rq}\}$ states [see Fig. 4.5(c)]. The size of these couplings can vary from crossing to crossing and so we label them Ω_q. A rough estimate for the typical size of Ω_q can be obtained by taking the 1-10 pA resonant current and converting it to a semi-classical timescale of $\tau \approx e/I \approx$ 16-160 nsec, which corresponds to an energy scale of $E = \hbar/\tau \approx$ 4-40 neV ($\ll \Delta_{SAS}$). This emphasizes that the Ω_q are distinct from Δ_{SAS} and, as we shall see in the following section, their origin is attributed to natural symmetry breaking perturbations in the dot confinement potentials.

While the discussion in this section has been restricted to B = 0 T, we are ultimately interested in the B-field evolution of the single-particle states throughout a measured energy spectrum (recall Fig. 4.3). In particular, in Chap. 5 we will focus on anti-crossing behaviour observed at specific B-field induced level crossings. We stress

that these anti-crossings indicate that states in the right dot are themselves coupled. Such *intra*-dot couplings are distinct from the *inter*-dot couplings described in this section.

4.5 Modelling General Properties of Energy Spectra

In this section we introduce a simple model, based on a coherent tunneling picture, which can reproduce some general features of the measured single-particle QD energy spectra (recall Fig. 4.3), namely the non-zero resonant currents, and the widespread anti-crossing and level mixing behaviour. An essential ingredient is the inclusion of higher degree terms in the dot confinement potentials to account for deviations from ideal elliptical parabolic confinement in realistic dots. In particular, we will see how appropriate higher degree terms can couple the 1s-like ground ('prober') state of the upstream dot to the single-particle states in the downstream dot. As argued in Sec. 4.4, this is necessary in order to measure resonant currents and hence map out dot energy spectra using the measurement principle described in Sec. 2.2.3. Additionally, the higher degree terms introduce anti-crossings into the probed energy spectra. In this section, we focus only on the general properties of the spectra, while subsequently, in Sec. 5.3, the model will also be applied to study specific level crossings.

As *overall* the energy spectra of the QDs, *except* in the vicinity of the level crossings, can be well reproduced with a calculated spectrum for a two-dimensional elliptical parabolic potential (recall Secs. 4.1 and 4.2), we start with such a potential, namely: $V_{eff}(x,y) = \frac{1}{2}m^*\omega_y^2(\delta^2 x^2 + y^2)$ for ellipticity $\delta \geq 1$. However, recalling Fig. 4.2, the single-particle energy states calculated for such a potential show no anti-crossing behaviour. As we shall see shortly, the addition of anharmonic terms ($x^p y^q$ of degree n

where $n = p + q$) to V_{eff} as perturbations can break the symmetry and induce anti-crossings between the single-particle states. We note that for an elliptical parabolic potential in the *x*-*y* plane with uniform *B*-field along the *z*-direction, the *lowest* degree monomial term in V_{eff} that can induce direct mixing between any two single-particle eigenstates with quantum numbers (n_{x1},n_{y1}) and (n_{x2},n_{y2}) is of degree $m = |n_{x1} - n_{x2}| + |n_{y1} - n_{y2}|$ [103]. For the case of a circular parabolic dot, this condition equates to simply the difference in orbital angular momentum of the two states, i.e., $m = |\ell_1 - \ell_2|$ where ℓ_1 and ℓ_2 are the orbital angular momentum quantum numbers of the two states. As a illustrative example, consider the $2p^-$ and $3d^+$ states for which $(n,\ell) = (0,-1)$ and $(0,2)$ respectively, meaning $m = 3$ and so terms of the form x^3, x^2y, xy^2 and y^3 would be required to couple these two states. Note that as $m > 2$ for all level crossings in the single-particle spectrum of elliptical parabolic dots, only additional terms of degree three or more are of interest since they can remove the exact level crossings.

Recall from Sec. 2.2.3 that in order to measure the single-particle energy spectrum of one of the constituent dots in a double QD device, we use the upstream dot's 1s-like state to probe the single-particle states of the downstream dot. In a simple coherent tunneling picture, derived from a Fermi golden rule argument (see Sec. 4.6 for additional details), the resonant current through the *j*th probed state (I_j) is proportional to the square of the in-plane overlap integral between the wavefunction of the upstream dot's 1s-like state, $\psi^U_{n_x,n_y}(x,y) = \psi^U_{0,0}(x,y)$, and the wavefunction of the downstream dot's state, $\psi^D_j(x,y)$. Explicitly, I_j is given by Eq. 4.1,

$$I_j \sim \left|\left\langle \psi^U_{0,0} \middle| \psi^D_j \right\rangle\right|^2 = \left|\int\int \mathrm{dx\ dy} \left[\psi^U_{0,0}(x,y)\right]^* \psi^D_j(x,y)\right|^2 \qquad (4.1).$$

Note that the model implicitly assumes that we are in a situation of weak inter-dot tunnel coupling (we will comment on this assumption in Sec 4.6).

Figure 4.6 shows the single-particle energy spectra calculated numerically for three different confinement potentials. The log of the square of the overlap integral between each single-particle wavefunction ψ_j^D and $\psi_{0,0}^U$, calculated using Eq. 4.1, is also indicated in the figure. Note that in calculating the overlap integrals, we have taken an ideal elliptical parabolic confinement potential for the upstream dot's potential, explicitly $V_{eff}(x,y)/m^*\omega_y^2 = \frac{1}{2}(\delta^2 x^2 + y^2)$. This simplifying assumption is justified as the 1s-like $\psi_{0,0}^U(x,y)$ state in the upstream dot is more spatially compact in the *x*-*y* plane than the higher energy probed dot states (recall Fig. 2.3), and is thus the least sensitive to the addition of the perturbative terms. Additionally, we use $\delta = 4/3$ and a confinement energy of $\hbar\omega_y = 3.9$ meV in the calculations. The choice of these specific values will be made clear in Sec. 5.3 when we compare the results of the calculations with data from specific crossings in the measured spectra of dot 2 from Device 1 [recall Figs. 4.3(c) and (d)].

We begin with identical elliptical parabolic confinement potentials for both dots, i.e., $V_{eff}(x,y)/m^*\omega_y^2 = \frac{1}{2}(\delta^2 x^2 + y^2)$. In this case, as expected, there are no anti-crossings in the calculated spectrum [see Fig. 4.6(a)]. Furthermore, the overlap integral between $\psi_{0,0}^U(x,y)$ and any one of $\psi_{n_x,n_y}^D(x,y)$, *except* for $\psi_{0,0}^D(x,y)$, is zero due to orthogonality. This confirms the above statement that for two identical ideal dots, within a simple coherent tunneling picture, it would not be possible to measure an energy spectrum as the higher energy states in the downstream dot are not coupled to the 1s-like 'prober' state of the upstream dot. To explain the spectra we can manifestly measure (recall Fig. 4.3), we

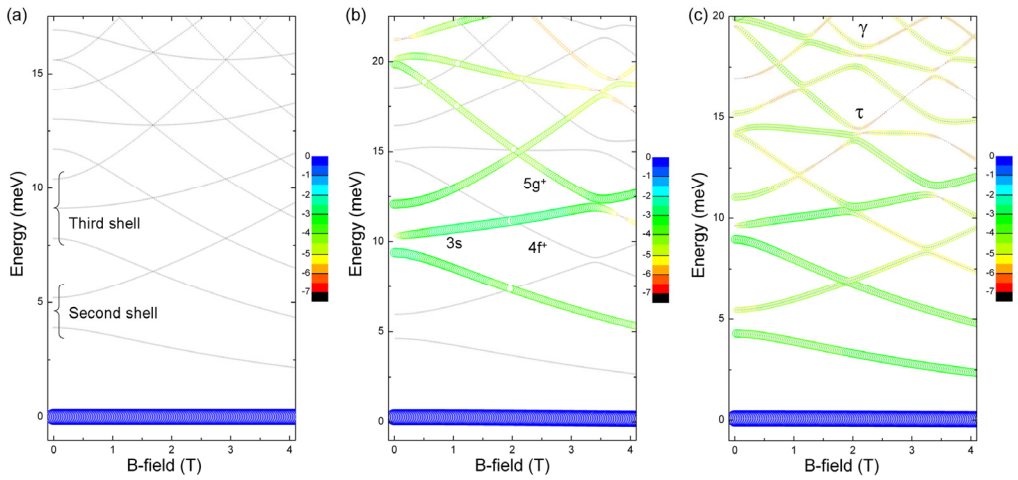

Fig. 4.6. Energy spectra calculated for three different downstream dot lateral confinement potentials (see text). The colour scale and the size of the symbols reflect the log of $\left|\left\langle \psi_{0,0}^{U} \middle| \psi_{j}^{D} \right\rangle\right|^2$ for each state. Before taking the log, the calculated values are normalized to the value of $\left|\left\langle \psi_{0,0}^{U} \middle| \psi_{0,0}^{D} \right\rangle\right|^2$ in (a). After taking the log, any value which is less than -7 is indicated by a black point.

must introduce higher degree perturbative terms into the ideal potential of the downstream dot which couple these states. The result is that the states may no longer be orthogonal to $\psi_{0,0}^{U}(x,y)$ and so the overlap integrals can be non-zero.

To demonstrate this, we examine a confinement potential for the downstream dot which, as an illustrative example, includes two fourth order terms, although no particular meaning is attached to the selected terms. Explicitly, consider the potential $V_{eff}(x,y)/m^{*}\omega_y^{2}$ = ½($\delta^2 x^2 + y^2 + 0.1(\delta^4 x^4 + y^4)$). The inclusion of the fourth order terms has two obvious effects on the dot spectrum [see Fig. 4.6(b)]. i. Consistent with the choice of fourth order terms, anti-crossings (with energy splitting up to ~0.5 meV) have appeared where two approaching states have quantum numbers such that m = 4, while, notably, other crossings where $m \neq 4$ remain exact. For example, the 3s-like state crosses both the $4f^{+}$-,

and $5g^+$-like states for the B-field range shown. At these crossing points, m = 3 and 4 respectively. Clearly, of the two crossings, only the one between the 3s- and $5g^+$-like states shows anti-crossing behaviour. ii. The overlap integral $\left|\left\langle \psi_{0,0}^{U} \middle| \psi_{j}^{D} \right\rangle\right|^2$ is non-zero for some, but certainly not all, of the downstream dot wavefunctions. Evidently this confinement potential is still sufficiently symmetric that some of the downstream dot wavefunctions remain orthogonal to $\psi_{0,0}^{U}(x,y)$. Nonetheless, even with the addition of only two higher degree terms, there is clear evidence that the overlap integrals can be induced to vary strongly in the vicinity the anti-crossings (for example, see again the crossing between the 3s- and $5g^+$-like states).

In order to generate more widespread anti-crossing and level mixing behaviour, we take the next step and include a larger number of higher degree terms of different orders. Explicitly, consider the confinement potential $V_{eff}(x,y)/m^*\omega_y^2 = \frac{1}{2}(\delta^2 x^2 + y^2 - 0.12x^2y + 0.05xy^2 + 0.05y^3 + 0.1x^4y + 0.02x^6 + 0.02y^6$. The motivation for the specific higher degree terms chosen will be made clear in Sec. 5.3. The most important point about the spectrum calculated for this potential [see Fig. 4.6(c)] is the confinement potential is now sufficiently non-elliptical that the overlap integrals of each downstream dot states' wavefunction with $\psi_{0,0}^{U}(x,y)$ are finite throughout most of the B-field range shown. In addition, significantly more of the level crossing regions now show clear anti-crossing behaviour, and pronounced mixing is visible at many of these regions (see for instance the τ and γ three-level crossings near ~2 T). In all essential aspects, the spectrum shown in Fig. 4.6(c) reproduces the general properties of a measured dot energy spectrum quite well.

Having demonstrated that the model can generate a spectrum with widespread level mixing, we could, in principle, attempt to perform a fit in order to find a suitable potential which models the energy dispersion and resonant currents of a large portion of a measured spectrum. However, this would be very challenging due to the large number of higher degree terms that would potentially need to be included. For example, if we wish to include terms up to degree six, the total number of possible higher degree terms is twenty-two and, in general, for degree m there are $\sum_{n=3}^{n=m}(n+1)$ possible terms. A further difficulty would be to account for how the confinement energies change as a function of energy throughout a measured spectrum (recall discussion in Sec. 4.2). Nonetheless, as we shall see in Sec. 5.3, by selecting appropriate terms, when we focus on a few selected crossing regions in a measured spectrum, we are able to qualitatively reproduce both the energy dispersion and the resonant currents reasonably well.

4.6 Summary and Concluding Comments

This chapter focused on the global properties of the single-particle energy spectra of two specific QDs, namely dot 2 from Device I and dot 2 from Device VI. In Sec. 4.1, as a starting point to understand the measured dot spectra, we introduced the ideal calculated spectrum for elliptical parabolic confinement and compared and contrasted it to the special case of the familiar FD spectrum for circular parabolic confinement. Subsequently, in Sec. 4.2 we described the measured spectra and showed how, *overall*, neglecting the widespread anti-crossing and level mixing behaviour, the spectrum of dot 2 from Device VI (Device I) can be well modelled by assuming circular (elliptical) parabolic confinement. Furthermore, we also explained how comparing the measured

spectra to ideal spectra allowed us to estimate the dot confinement energies and ellipticities. Section 4.3 described how the high-resolution energy spectra of the dots were measured using 'vector voltage' line scans, extending the technique of Ref. [70] to overcome some of the limitations in the original measurements. In Sec. 4.4 we discussed the role of the inter-dot tunnel coupling and explained why finite coupling between the 1s-like state in the upstream dot and the higher energy states in the downstream dot is necessary in order to measure an energy spectrum. Section 4.5 introduced a simple model, based on a coherent tunneling picture, which attempts to reproduce in general terms some features of both the energy dispersion and the resonant currents of the states in the single-particle spectrum. An essential ingredient of the model is the inclusion of higher degree terms to the confinement potential which account for anharmonicity and anisotropy and can couple the higher energy states in the downstream dot to the 1s-like 'prober' state in the upstream dot.

We now make some concluding comments about the coherent tunneling model and suggest what would need to be considered if we were to develop it further. Recall that we used Eq. 4.1 in order to compute the resonant currents within the framework of a simple coherent tunneling picture. Underlying the existing simple model is an important assumption, namely that the inter-dot tunneling rate, Γ, is the rate limiting step compared to the tunneling rates from the source contact to the upstream dot, Γ_U, and from the downstream dot to the drain contact, Γ_D, i.e., $\Gamma \ll \Gamma_U,\Gamma_D$. There are two aspects of the experimental data which favour this assumption. First, the tunneling processes of interest involve nearly orthogonal states with a small overlap induced by anharmonic perturbations. Second, the conditions of the measurement of the spectra in Fig. 4.3

involve rather high bias voltages (~50-100 mV) so that the source and drain contacts are more strongly coupled to the QDs than at equilibrium (zero bias). While the condition $\Gamma \ll \Gamma_U \approx \Gamma_D$ is true at zero bias, for high bias, one might also expect that $\Gamma_U \ll \Gamma_D$ [104]. It can be shown for this condition too that Eq. 4.1 remains valid provided $\Gamma \ll \sqrt{\Gamma_U \Gamma_D}$ [103]. While the simple analysis in Sec. 4.5 does qualitatively explain the general properties of the observed spectra, and the model can successfully reproduce both the energy dispersion and resonant current behaviour at specific level crossing regions (see Sec. 5.3), a more complete model is desired to shed more light on the microscopic tunneling processes. Such a model would need to explicitly take into account the tunneling rates Γ_U and Γ_D and specifically how they change with V_{SD} and V_G. In order to do this, a full three dimensional self-consistent calculation would be required.

Further work remains from an experimental point of view in order to evaluate more advanced models. In particular, closer examination of the measured spectra (recall Fig. 4.3) suggests that there are systematic trends in the resonant currents as a function of B-field or energy. As a specific example, consider Fig. 4.7 which shows a portion of the spectrum of dot 1 from Device I [Fig. 4.7(a)] and the measured resonant currents for both the $2p^-$- and 3s-like states [Fig. 4.7 (b)]. Neglecting all crossing regions, i.e., picturing the states as being effectively uncoupled, then over a large B-field, the currents do appear to vary systematically and fairly smoothly along each resonance. In particular, for the $2p^-$-like state the current gradually increases across the entire 0-6 T range, while for the 3s-like state the current decreases gradually until ~3 T and then increases gradually. A detailed understanding of these interesting trends is beyond the scope of this thesis.

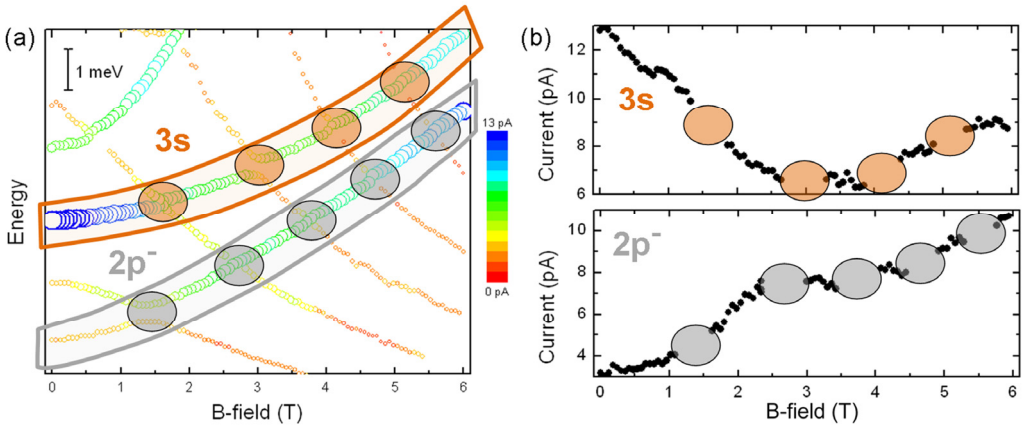

Fig. 4.7. (a) Low energy portion of the spectra of dot 1 from Device I where the ~pA resonant current is indicated by the colour scale and the size of the symbols. (b) Resonant current of the 3s-like (top panel) and $2p^-$-like (bottom panel) states showing variations in the measured current away from regions (highlighted by orange and grey circles) where the state of interest is close to (or appears to cross with) other states.

Having throughout this chapter looked at wide portions of the measured spectra, in Chap. 5 we will focus on multi-level mixing at *specific crossings*. When we come to the detailed modelling of specific crossing regions, we will certainly need to account for the current variations revealed in Fig. 4.7 by some means.

Chapter 5

Coherent Energy Level Mixing in Quantum Dot Energy Spectra

The general engineering and understanding of coupling and consequent coherent mixing between quantum levels leading to level anti-crossing and superposition of states is important in many fields of research including electronics and optics in the solid state. Anti-crossings and state superposition, although not previously observed in transport measurements in the context of purely electronic single-particle states in QD structures, are prevalent in many different types of low dimensional semiconducting nano-systems, particularly for two-level-systems as diversely exemplified in Refs. [45-53].

There have been several recent proposals to exploit coherent mixing between more than two quantum levels in transport measurements for multi-QD structures (see for example Refs. [54,55,57-59]). While inter-dot level mixing is indeed the most obvious and, in the long term, the most desirable vehicle for implementing these protocols, there remain technical limitations. In this chapter we demonstrate that we can access essentially the same physics with multiple levels in a single dot via intra-dot mixing.

From the measured single-particle spectra of two dots from two double QD devices, we demonstrated in Chap. 4 that the lateral confinement potentials of the dots are highly symmetric, and close to elliptical and parabolic in form. However, an initially unexpected, although positive, additional feature of the measured dot spectra, key to this chapter, is widespread anti-crossing behaviour and variation in the resonant currents

when two, three and even four single-particle energy levels are brought into close proximity by the applied B-field. This mixing was attributed to non-negligible anisotropy and anharmonicity in the confining potential (recall Sec. 4.5).

In this chapter, we investigate specific examples of such level crossings to learn more about the underlying physics. In particular, we will focus on crossings where we observe the suppression of an otherwise strong current resonance. We will demonstrate that this is a signature of coherent mixing leading specifically to 'dark state' formation. In particular, the mixing we observe at three-level crossings represents an all-electrical analogue of coherent population trapping from the realm of quantum and atom optics [62,63]. Figure 5.1 shows examples of two-, three- and four-level mixing leading to dark state formation as evidenced by resonant current suppression. Using a generic level mixing model based on a simple coherent tunneling picture we will attempt to explain both the pronounced anti-crossing behaviour, as well as the transfer of resonant current strengths (both enhancement and suppression) observed at such crossings [105].

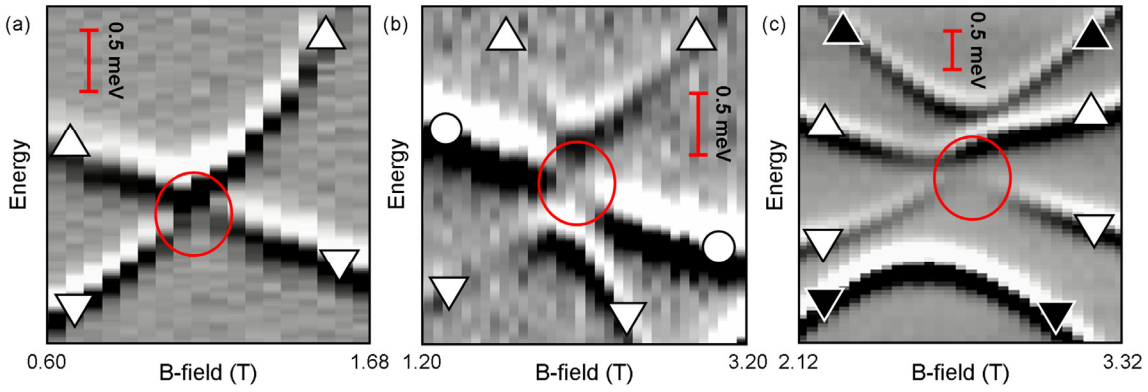

Fig. 5.1. Differential conductance [106] plots measured by strategy A (as described in Chap. 4) showing (a) two-, (b) three- and (c) four-level mixing leading to current suppression in the regions indicated by the red circles. Symbols identify distinct resonance branches in each panel.

The structure of this chapter is as follows. We begin in Sec. 5.1 with an investigation of three-level mixing. Motivated to understand the different energy dispersions at three-level crossings visible in the dot energy spectra (recall Fig. 4.3), we introduce the first part of a simple level mixing model consisting of a matrix Hamiltonian which accounts for pair-wise coupling of states. We then focus on one particularly interesting three-level crossing [see Fig. 5.1(b)] where we find clear evidence of resonant current suppression strongly suggesting that the observed mixing is in fact coherent. In order to study the resonant currents at this crossing, we begin by discussing how to correctly extract them using the two measurement strategies (A and B) introduced in Sec. 4.3.1. Next, we introduce the second part of the simple level mixing model which will allow us to compute the resonant currents within the framework of a coherent tunneling picture. Applying the model we will then fit the data at this first three-level crossing which will lead to an insightful understanding of the underlying physics. Subsequently, we will investigate a second three-level crossing where current suppression is also observed in order to demonstrate the robustness of the coherent mixing effects, namely that dark states at three-level crossings are not limited to a unique set of circumstances. We will then look deeper into the underlying level mixing physics to emphasize the link with other quantum three-level mixing phenomena.

The study of three-level crossings provides a springboard to a number of further investigations. Firstly, in Sec. 5.2, we will demonstrate that dark states can also arise at both two and four-level crossings [see Figs. 5.1(a) and (c)] and adapt the coherent level mixing model to explain these cases too. Secondly, in Sec. 5.3 we will revisit the model first encountered in Sec. 4.5 in order to demonstrate that we can reproduce the mixing

observed at specific level crossings by including appropriate higher degree terms into the dot confinement potentials as perturbations to couple the underlying basis states. Thirdly, in Sec. 5.4, employing a vertical double QD device where the single gate is patterned into four gates [88], we will demonstrate how we can influence the observed level mixing by applying different combinations of voltages to the gates in order to perturb the lateral confinement potentials of the constituent dots. Finally, in Sec. 5.5, we discuss some limitations of the data extraction techniques and of the coherent level mixing model as well as indicating some avenues for continued investigation.

5.1 Three-Level Mixing

Three-level crossings in the measured dot energy spectra (recall Fig. 4.3) are sufficiently numerous and sufficiently varied that they are a natural place to begin the investigation of coherent mixing. In particular, the portion of the spectrum presented in Fig. 4.3(c) shows three interesting examples of three-level mixing (highlighted in Fig. 5.2). We note that for each of these three-level crossings the energy dispersions are quite different and, furthermore, they display significant variations in the spectral strength of the resonances. For example, at the γ crossing (middle panel of Fig. 5.2) the strong resonant current of the center branch is completely suppressed near the center of the crossing region, strongly suggesting destructive interference (leading to dark state formation, i.e., a state which is not visible).

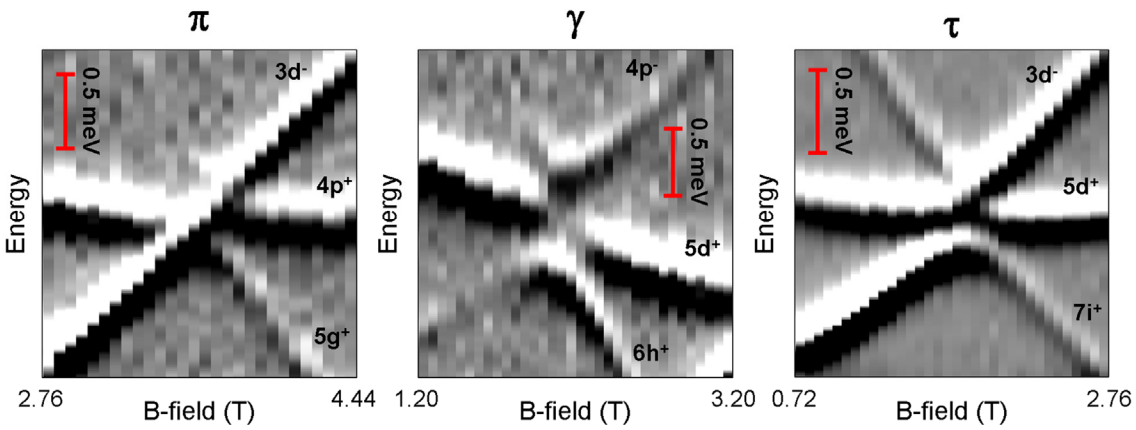

Fig. 5.2. Differential conductance [106] plots for the π, γ and τ three-level crossings measured in dot 2 from Device I [see the spectrum in Fig. 4.3(c)]. States are labelled using the atomic orbital-like notation.

As additional motivation for exploring three-level crossings, we note that coherent phenomena in quantum transport involving three levels are of interest for advanced quantum information protocols (see for example Refs. [54-56]). By studying intra-dot mixing at the observed three-level crossings, we can address the same underlying physics envisioned in these inter-dot mixing schemes. We also note that while two-level anti-crossings are commonly encountered in a diverse range of experimental fields, instances of anti-crossings involving three or more levels are much rarer (we know of only one example from the realm of superconductivity [107]).

In order to quantitatively discuss the mixing which we observe at three-level crossings, we have developed a simple model, based on a coherent tunneling picture, with which we can compute and fit both the energy level position and the resonant current for each of the three branches throughout any three-level crossing region. In the following section we initially focus on the energy dispersions, delaying discussion of the currents until Sec. 5.1.4.

5.1.1 Three-Level Mixing Model: Energy Dispersion

Motivated to understand the varied energy dispersions at three-level crossings we developed a 3x3 matrix Hamiltonian model which allows us to study mixing at a generic crossing between three approaching and initially uncoupled basis levels, each assumed to have a linear dispersion with B-field. We note that in general, the single-particle energy levels observed in the dot spectra (recall Fig. 4.3) have non-linear B-field dispersions, but in the vicinity of a crossing, over a limited B-field range, linear dispersion is a reasonable approximation. For ease of discussion (and generality) we label these basis levels (states) 1, 2 and 3 in the sense indicated in Fig. 5.3(a). Explicitly, the Hamiltonian is given in Eq. 5.1,

$$H = \begin{pmatrix} -x & C_{12} & C_{13} \\ C_{12} & 0 & C_{23} \\ C_{13} & C_{23} & ax \end{pmatrix} + E_0(x)I \qquad (5.1)$$

where the couplings between each pair of basis levels are characterized by three off-diagonal matrix elements (coupling energy parameters), C_{12}, C_{13} and C_{23}. These coupling parameters are assumed to be real, but may be positive or negative, and independent of B-field and each other. The Hamiltonian is constructed such that all the mixing physics of interest is contained in the first term. In this term, the parameter a allows for the possibility that the slopes of basis states 1 and 3 are not equal and opposite, and the slope of basis state 2 is assumed to be zero. However, in general for the measured three-level crossings the center level has a non-zero slope (see for example the γ crossing in Fig. 5.2). To account for this, the Hamiltonian includes the term $E_0(x)I$ (where I is the 3x3 identity matrix) which effectively rotates the entire crossing described by the first term so that it can be made to match with a measured crossing as desired for the fitting process.

Note as well that the model can also be easily adapted to allow for the possibility that the three basis levels do not meet at exactly one point.

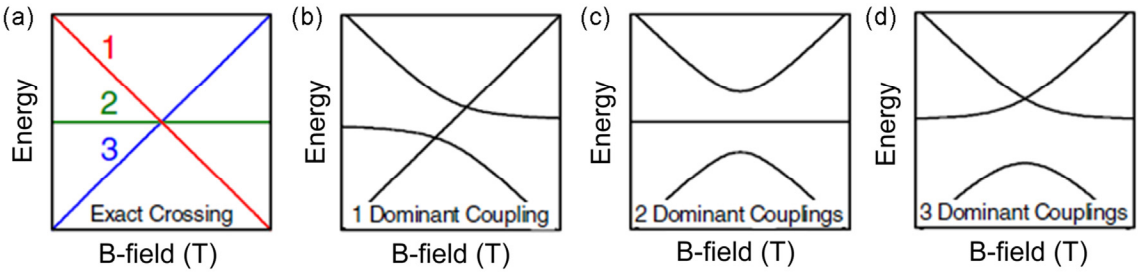

Fig. 5.3. Three-level crossing simulations performed using Eq. 5.1 with $E_0 = 0$, $a = 1$ and (a) $C_{12} = C_{13} = C_{23} = 0$, i.e., uncoupled basis states meeting at a point, (b) $C_{12} = 1$, $C_{13} = C_{23} = 0$, (c) $C_{12} = C_{23} = 1$, $C_{13} = 0$ and (d) $C_{12} = C_{13} = C_{23} = 1$.

The four basic types of three-level crossings described by the model are given in Figs. 5.3(a)-(d). In these simulations, we have taken basis level 2 to have zero slope while basis levels 1 and 3 have slopes of equal magnitude but opposite sign, i.e., in Eq. 5.1 a has been set to unity and $E_0(x)$ is zero. Candidate exact crossings [Fig. 5.3(a)] are rarely observed (see Fig. 4.3). Instead, more interesting 1-, 2-, and 3-dominant coupling-type crossings are seen [Figs. 5.3(b)-(d)]. For example, recalling Fig. 5.2, the π, γ and τ three-level crossings observed in the measured spectrum of dot 2 from Device I appear to be respectively 1-, 2- and 3-dominant coupling-type three-level crossings. Note that not all possible variants of three basic shapes are shown in Fig. 5.3(b)-(d). Furthermore, by changing the signs of certain coupling parameters, the basic shapes can be inverted in either the energy or B-field axes.

5.1.2 Extraction of Resonant Currents

Having understood the origin of the different three-level energy dispersions observed, extra information about the mixing is clearly present in the strength of the spectral features. Towards a full understanding of the mixing, we need to accurately and reliably extract the resonant currents, and ensure that the details of how the data is captured do not affect the interpretation of the underlying physics. As an example, we focus on the γ three-level crossing in the spectrum of dot 2 from Device I [recall Fig. 4.3(c)] which shows clear evidence of three-level mixing leading to current suppression. As we have two measurement strategies, A and B, available (recall Sec. 4.3.1), we will begin with the more intuitive strategy A. Note that in the next section we will also characterize the γ crossing with strategy B in order to demonstrate that the choice of measurement strategy does not influence the interpretation of the underlying coherent mixing.

Figure 5.4(a) shows the numerically derived differential conductance [106] plot for the γ crossing which is from the same data set used to build-up the spectrum in Fig. 4.3(c). Every second one of the current traces measured in the vicinity of the γ crossing are shown explicitly in Fig. 5.4(b). In both panels we clearly see three distinct branches, which we refer to as the upper, center, and lower branches (identified respectively by an up-pointing triangle, a circle and a down-pointing triangle). Starting from the left of the crossing region, the weak (‘dark’) upper and lower branch resonances approach the strong (‘bright’) center branch resonance as the B-field is increased. At the center of the crossing region (near ~2.2 T), when the branches are minimally separated, the upper and lower branch resonances have become strong (‘bright’) while the center branch resonance

has been completely suppressed (becomes 'dark'). As the B-field is increased further, the center branch resonance recovers its strength and the other two branch resonances start to weaken.

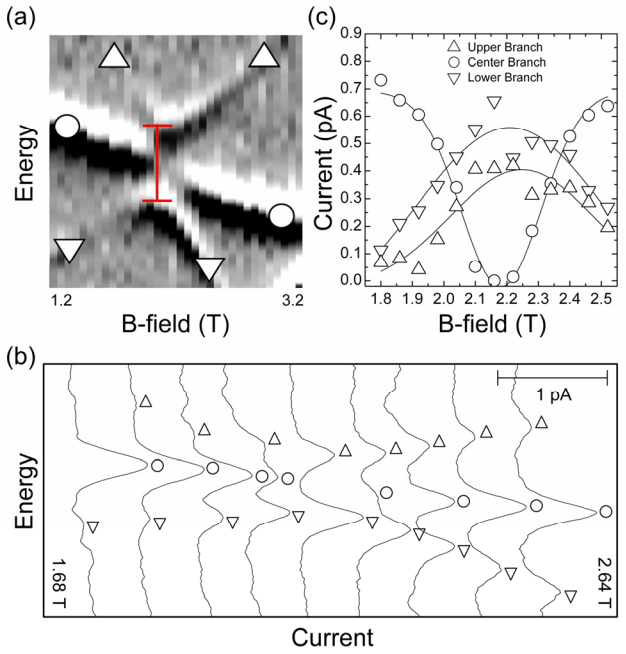

Fig. 5.4. (a) Energy level (differential conductance resonance [106]) position versus B-field measured by strategy A for the γ crossing in the spectrum of dot 2 from Device I [see Fig. 4.3(c)]. The energy scale bar corresponds to ~0.8 meV. (b) Selected current traces which when numerically differentiated form vertical sections of the plot in (a) (non-resonant background current not removed). The peaks of the three branch resonances are marked by an up-pointing triangle, a circle and a down-pointing triangle for each trace, except where the peaks are too weak to identify. Traces are horizontally offset by 0.5 pA. (c) Current values (resonant current with non-resonant background component subtracted). The black lines are a guide to the eye (and are generated by simple Gaussian fitting although no meaning is attached to the fitting procedure).

The bright resonance-to-dark resonance inter-conversion observed at the γ crossing is suggestive of strong interference. In order to confirm this and explore the

underlying coherent mixing, we will need to determine the resonant currents reliably. Two hurdles must be overcome to do this. First, we need to extract the resonant currents correctly accounting for the non-resonant background current. Second, we need to confirm that the choice of vector voltage line for the strategy A measurement (recall Sec. 4.3.1) has not unduly influenced how the mixing is manifested. Once we are confident that we have fairly determined the resonant current behaviour, we will introduce the second half of the simple coherent level mixing model so that we can proceed to fit both the energy dispersion and the resonant currents at this crossing region. An additional complication which we will have to deal with is the underlying variation in resonant currents with B-field (recall Fig. 4.7).

To obtain the B-field dependence of the branch currents shown in Fig. 5.4(c), the resonant current component *must* be extracted for each of the relevant current peaks from the 'vector voltage' line scans acquired in strategy A measurements. This is necessary because even 'on-resonance,' not all of the measured current is solely resonant current. In order to identify, fit and then correctly remove the non-negligible non-resonant background current from each of the current traces, we typically examine the current traces over a wider range in energy than shown in Fig. 5.4(b). Figure 5.5 shows two selected current traces (in black), over a wide energy range, which demonstrate the fitting procedure in detail. These two traces were selected because one [Fig. 5.5(a)] is illustrative of a straightforward case where the three resonances of interest are well separated and the other [Fig. 5.5(b)] is illustrative of a more challenging case where the fitting becomes difficult because the resonances are quite close together, and additionally one resonance is significantly weaker than the others.

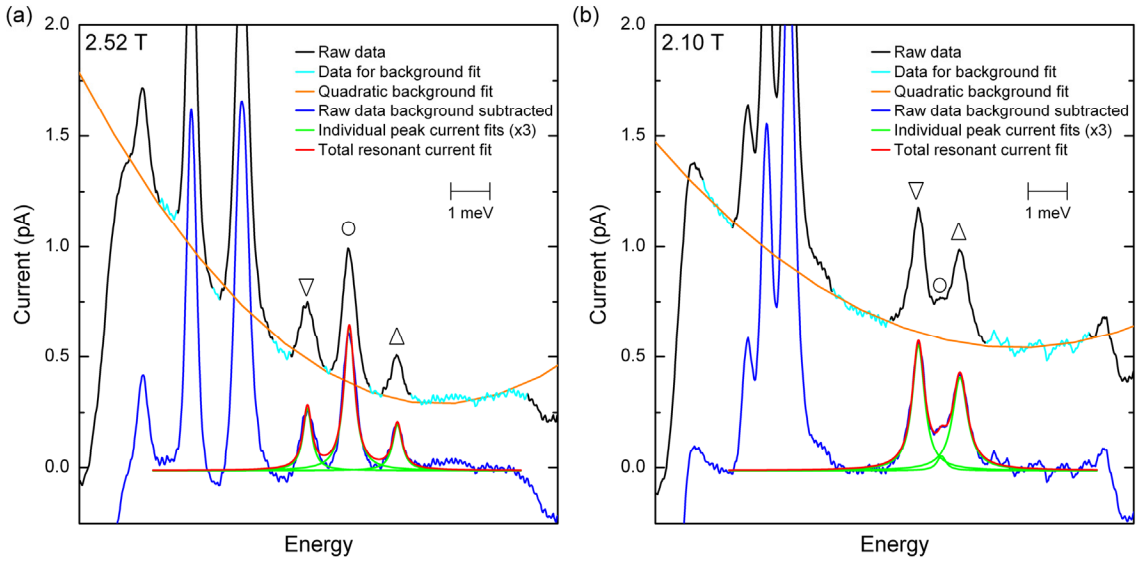

Fig. 5.5. Fitting procedure for two selected traces (measured at 2.52 and 2.10 T respectively) which make up the data for the γ crossing shown in Fig. 5.4 (the three relevant resonances are labelled by an up-pointing triangle, a circle and a down-pointing triangle). In both (a) and (b) the raw current trace is black, while the current trace with the non-resonant current component subtracted is blue. The relevant portion of the later is fitted with three unconstrained Lorentzians [individually coloured green, while their sum (the total fit) is red]. The steps in current at both low and high energy [evident in both (a) and (b)] mark the places where the vector voltage line cuts across the border of the SET and $N = 0$ regions [recall Fig. 4.4(a)], and hence define the measurement window in which we can probe single-particle resonances.

In Fig. 5.5, the non-resonant background current is identified (in teal) and, although it fluctuates a little from trace-to-trace, a quadratic fit (in orange) is found to be sufficient to account for the generally smooth variation along each trace. Once the background current is subtracted, we find that a simultaneous fit of the current peaks of interest with unconstrained Lorentzians is sufficient to extract the resonant current component for each current peak. The fitting works extremely well for cases where the resonances are well separated [as in Fig. 5.5(a)], while it can be difficult to extract the

resonant currents when a feature is very weak [such as in Fig. 5.5(b)] or if features are very close together in energy (less than the spectral resolution of ~50 μeV).

The resonant currents for the three branches of the γ crossing extracted by this fitting procedure are given in Fig. 5.4(c). Their B-field dependence is now clearly revealed and reflects well the behaviour discussed qualitatively above for Figs. 5.4(a) and (b), namely the bright resonance-to-dark resonance inter-conversion on tuning the B-field through the crossing. Note that if we did not properly remove the background current, the true nature of the coherent mixing would be obscured. Shortly, in Sec. 5.1.4, we will describe the second half of the simple coherent level mixing model introduced in Sec. 5.1.1 which will allow us to fit the γ crossing data shown in Fig. 5.4 (see Sec. 5.1.5). However, before proceeding any further, we address the question of whether or not this data, obtained using strategy A, fairly characterizes the mixing.

5.1.3 Comparison of Measurement Strategies for Characterization of Coherent Level Mixing

Recalling the practical points related to setting up a good 'vector voltage' line scan discussed in Sec. 4.3.1 [see also Fig. 4.4(b)], there are some notes of caution in using strategy A to extract information about the coherent mixing at level crossings. Foremost, each resonance is a *line* within a single-electron tunneling (SET) region [recall Fig. 4.4(a)]. Thus, even if we can ensure that the 'vector voltage' line scan always remains inside the target SET region, so excluding the possibility of picking up unwanted extra spectral features, it only cuts through each of the resonance lines of interest at one *point*, i.e., the choice of a good 'vector voltage' line is not unique. Furthermore, the

position of the point (relative to say the lower and upper edges of the SET region) where the fixed 'vector voltage' line cuts each resonance line will inevitably change during a spectral measurement as the diamagnetic shift effect causes the SET region to move towards more positive V_G with increasing B-field. Because of these factors we considered it possible that the precise position of the points where the 'vector voltage' line cuts the resonance lines could significantly alter the appearance of the crossing and, in particular, the behaviour of the branch currents, so potentially influencing any interpretation of the underlying coherent mixing. For example, would the center branch resonance of the γ crossing still 'vanish' at the center of the crossing if the 'vector voltage' line scans were set up differently? In this section we now demonstrate that the observed behaviour at the γ crossing is robust and not dependent on the details of how the scan was set up.

Figure 5.6 shows the differential conductance in the relevant region of the V_{SD}-V_G plane in the vicinity of the γ crossing at eight different B-fields. The same general behaviour evident in Fig. 5.4(a) is clearly seen again in Fig. 5.6, namely three distinct resonance lines on the low (1.8-2.0 T) and high (2.4-2.5 T) B-field side of the crossing, and when the resonance lines are minimally separated, at 2.2 T, only two resonance lines (the upper and lower branches) are visible since the center resonance line (the center branch) has been completely suppressed. Interestingly, in the 2.1 T and 2.3 T panels, only part of the center resonance line (upper part at 2.1 T and lower part at 2.3 T) is clearly visible. That all or part of the center resonance line is absent only for a narrow B-field range demonstrates that the presence of the dark state at the center of the crossing region observed in the strategy A measurement (see Fig. 5.4) is not critically sensitive to the choice of 'vector voltage' line.

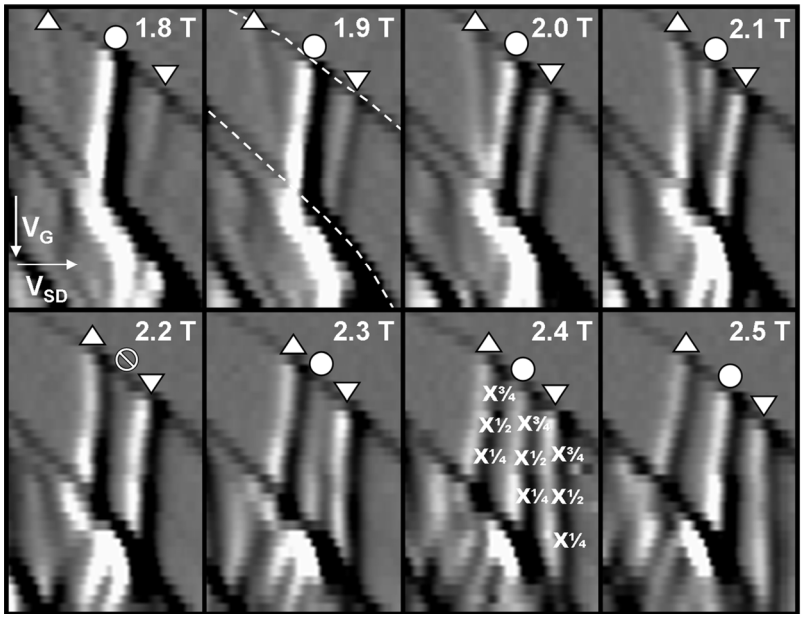

Fig. 5.6. Panels showing grey scale plots of the differential conductance, dI/dV_{SD}, in the vicinity of the γ crossing [the relevant region of the V_{SD}-V_G plane is at large reverse bias, outside of the range shown in Fig. 4.4(a)]. Dashed lines in the 1.9 T panel highlight the lower and upper edges of the region of interest in which SET dominates. The upper, center, and lower branch resonance lines respectively are labelled by an up-pointing triangle, a circle and a down-pointing triangle. Due to the extent and shape of the SET region, the time required for the measurements is minimized by capturing data from a parallelogram-shaped region in the V_{SD}-V_G plane rather than a (more conventional) rectangular-shaped region [as was done in Figs. 2.13(a) and 4.4(b)]. However, the data is displayed here in rectangular-shaped panels for which the start and end points of the V_{SD} sweep are systematically shifted together for each value of V_G [stepped from -0.55 V to -0.9 V from bottom to top] such that at the bottom (top) of each panel, V_{SD} = -47 mV (-100 mV) on the left-side and V_{SD} = -31 mV (-84 mV) on the right-side of the panel. The crosses in the 2.4 T panel are explained in the main text in connection with Fig. 5.7.

The resonance lines of interest in the panels of Fig. 5.6 lie within an extended arc-shaped region of interest in which SET dominates (highlighted by dashed lines in the 1.9 T panel). We note that the lower edge of the reverse bias SET region [recall Fig. 4.4(a)] actually weakens and eventually all but disappears at high bias (V_{SD} < -50 mV). The

reason for this is not fully understood. However, in the vicinity of the γ crossing for each panel in Fig. 5.6, this edge, if visible, would bisect the region of interest into two zones. Only the upper zone is strictly part of the reverse bias SET region. In the lower zone, double-electron tunneling can occur, but apparently the additional tunneling processes are very weak as no extra spectral features (resonance lines) are evident in contrast to the region below this zone. Thus, SET dominates inside the extended region of interest consisting of both zones (see also discussion in Sec. 6.3.6).

In the panels of Fig. 5.6, although not yet understood, we do see some small variations (short range with respect to V_G) in the strength and width of the white-black resonance lines on moving from the lower edge to the upper edge of the region of interest in which SET dominates (similar variations have recently been reported for weakly coupled vertical QDs under different experimental conditions in Ref. [101]). In order to track any systematic variation (long range with respect to V_G) along the length of the resonance lines which might influence our interpretation of the underlying mixing, we determine the value of the resonant current at points a quarter, half and three quarters of the way along each of the three resonance lines inside the region of interest (see 2.4 T panel of Fig. 5.6 for definition of these points) for different B-fields close to the crossing region. Furthermore, note that the quarter (three quarters) points lie in the lower (upper) zone where SET dominates (only SET can occur) while the half points lie close to the border between the two zones.

Figures 5.7(a)-(c) show the extracted resonant currents, with the non-resonant background current subtracted, for each of these three points. Although the background current could, in principle, depend on three parameters, namely B-field, V_G and V_{SD}, we

find that only the V_G dependence is significant, although even its dependence is comparatively weak in the vicinity of the γ crossing. In detail, the background current is examined along two series of points parallel to the resonance lines, one series to the left of the resonance line marked by an up-pointing triangle and the other series to the right of the resonance line marked by a down-pointing triangle, at two fixed B-fields (2.0 T and 2.3 T), and a quadratic fit is found to be sufficient to account for the V_G dependence. At 2.1 T the lower part of the center resonance line is not visible and so the corresponding quarter point resonant current has been set to zero in Fig. 5.7(a). Lastly, in Fig. 5.7(d) we show for each B-field the average values of the currents at the three points for each branch.

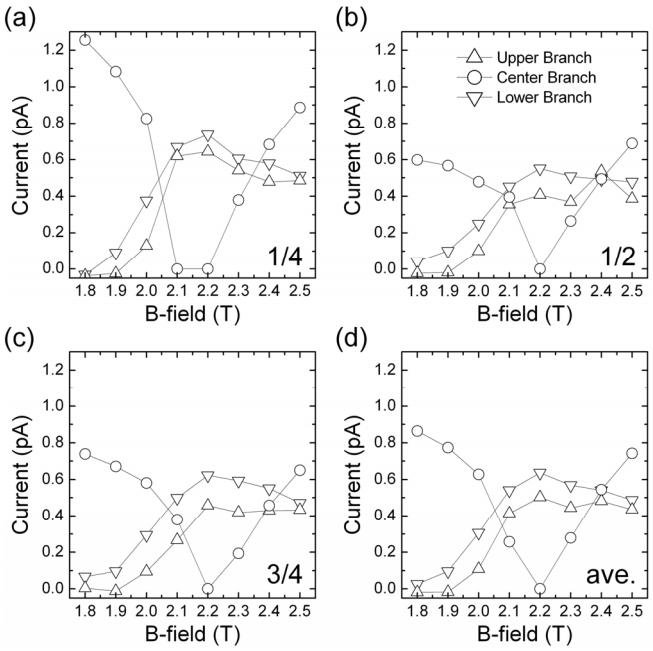

Fig. 5.7. Resonant current (with non-resonant background component subtracted) versus B-field for each branch of the γ crossing in the spectrum of dot 2 from Device I extracted by strategy B at points (a) a quarter, (b) half and (c) three quarters of the way along each of the three resonance lines inside the region of interest. The average values of the currents at these three points are shown in (d).

Figures 5.7(a)-(c) can be viewed as approximately mimicking the outcome of three reasonable 'vector voltage' line scans which could have been used in strategy A measurements, i.e., line scans which cut across all three resonance lines and have slopes appropriate for capturing a reasonably large portion of the dot's single-particle energy spectrum. Evidently, the B-field dependences of the branch currents at the three selected points along the resonance lines shown in Figs. 5.7(a)-(c) are qualitatively the same. This reveals that the overall behaviour of the branch currents is essentially independent of the detailed choice of the position of the point along each of the resonance lines at which the current is determined provided the choice is sensible, i.e., the relative position of the point should be approximately the same for all the resonance lines. Hence, this provides strong evidence that when using strategy A it does not depend critically where the (straight) 'vector voltage' line cuts the resonance lines of interest so long as they are all sensibly cut inside the region where SET dominates.

Using either measurement strategy [108], it is clear in all respects that the following is robust: to the low and high B-field side of the crossing, the upper and lower branch resonances are weak and the center branch resonance is strong, while at the center of the crossing, the upper and lower branch resonances are strong and the center branch resonance is completely suppressed. Quantitatively, the measured current values for each branch do vary in a fairly systematic fashion with position along the resonance lines [see Figs. 5.7(a)-(c)] with the current of each branch generally decreasing on moving from the lower edge to the upper edge of the region of interest. Reassuringly, when we compare the branch currents obtained using strategy A [Fig. 5.4(c)] with those obtained from strategy B (Fig. 5.7) we see that at any given B-field current values for the former lie

within the range of the current values for the latter. Most likely, the 'vector voltage' line scan used in the strategy A measurement cut the resonance lines somewhere near the half and three quarter points.

Reassured that regardless of the measurement strategy employed the dramatic suppression of the otherwise strong center branch resonance at the center γ crossing is a robust observation, in the next section we introduce the second half of the simple coherent level mixing model which addresses the current.

5.1.4 Three-Level Mixing Model: Current

As discussed in Sec. 4.5, in a simple coherent tunneling picture derived from a Fermi Golden Rule argument applicable for weak tunnel coupling, the resonant current in the j = (upper, center, lower) branch can be computed as $I_j = c\left|\langle g|\psi_j\rangle\right|^2$. This overlap integral approach attributes the source of all mixing (inter- and intra-dot) to natural anharmonicity in realistic dot confinement potentials (see Secs. 4.5 and 5.3). However, it is challenging to make any interpretation of the underlying physics at a specific level crossing using this approach.

Within the same coherent tunneling picture, there is a second approach for computing the resonant currents which we now describe. In the matrix Hamiltonian model introduced in Sec. 5.1.1 for a generic three-level crossing we have three basis levels which are coupled together pair-wise by *C*-parameters. We now introduce *current amplitude* (*s*-) parameters which essentially represent the tunneling amplitudes through the relevant uncoupled basis states. When squared they give approximately the branch currents far to the left and right of a crossing where the states are essentially uncoupled.

We can now compute the resonant current for each branch of a generic three-level crossing as the square of the sum of eigenvector components (v) multiplied by the s-parameters. Explicitly, $I_j = \left| \sum_m v_m^j s_m \right|^2$ where m = 1, 2, 3 is the basis state index. While the two approaches are ultimately equivalent, they emphasize different aspects. In particular, the matrix Hamiltonian model simply assumes that the basis states are coupled and that finite current flows through them, assigning no importance to the microscopic origin of the C- and s-parameters. Nonetheless, this picture can provide a more insightful understanding of the underlying mixing physics (as we shall see shortly).

Before proceeding to apply the model to fit the data for the γ crossing, we note that, for simplicity, one could assume that the s-parameters are independent of B-field. However, typically this does not reproduce the experimental data well because the resonant currents vary even away from the immediate crossing regions (recall Fig. 4.7 which showed how the total current for two sample states varied smoothly throughout an entire measured spectrum). Consequently, when fitting crossings we find that we have to employ an interpolation scheme for the s-parameters.

5.1.5 Coherent Mixing at the γ Three-Level Crossing

We now have all the ingredients in place to apply the coherent level mixing model and attempt to fit the measured energy level position and resonant currents at the γ crossing. Figure 5.8(a) and (b) show the energy level position and extracted resonant currents for each branch determined by strategy A. In addition, Fig. 5.8(c) shows the resonant currents extracted by strategy B. After examining the fit of the energy level

positions, we will discuss the fit of the resonant currents from both strategies in order to demonstrate again that the choice of measurement strategy does not influence the underlying physics.

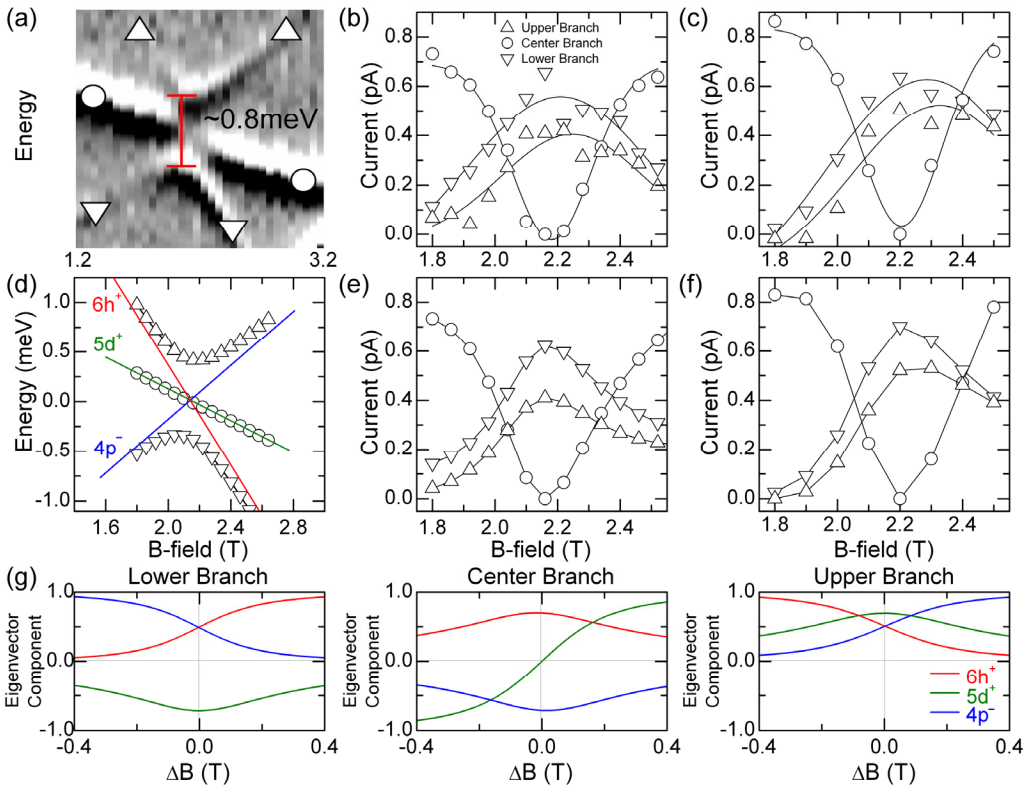

Fig. 5.8. γ three-level crossing. (a) Energy level (differential conductance resonance [106]) positions. (b) [(c)] Extracted branch currents (resonant current with non-resonant component subtracted) for strategy A (B) measurements. The black lines in both (b) and (c) are a guide to the eye (and are generated by simple Gaussian fitting although no meaning is attached to the fitting procedure). (d) Fit of energy level positions. Lines estimating the positions of the uncoupled basis levels provide a guide to the eye. The energy of the point where the three uncoupled basis levels cross is set to zero energy. (e) [(f)] Fit of currents for strategy A [B] measurements. The fitted *current amplitude* parameters are, in $pA^{1/2}$, s_1 = -0.176, s_2 = 0.941, and s_3 = -0.042 at 1.8 T, and s_1 = -0.233, s_2 = 1.038, and s_3 = 0.182 at 2.5 T [s_1 = -0.400, s_2 = 0.804, and s_3 = 0.219 at 1.8 T, and s_1 = -0.213, s_2 = 1.22, and s_3 = 0.209 at 2.5 T]. (g) Reconstructed eigenvectors. ΔB = 0 T is at ~2.12 T.

The fit to the measured energy level position [see Fig. 5.8(d)] reveals that the couplings are, in meV, $C_{12} = 0.30$, $C_{23} = 0.29$, and $C_{13} = 0.03$, or in terms of magnitude $C_{12} \approx C_{23} \gg C_{13}$. This result demonstrates that the distinctive shape of the γ crossing is due to two dominant and approximately equal couplings between the $6h^+$- and $5d^+$-like states (C_{12}), and between the $5d^+$- and $4p^-$-like states (C_{23}), whereas the coupling between the $6h^+$and $4p^-$-like states (C_{13}) is very weak [recall also Fig. 5.3(c)].

In terms of the resonant currents, the fit is able to reproduce the experimental data from both measurement strategies quite well, as shown in Figs. 5.8(e) and (f). In order to fit the data, we found that a simple linear variation of the *s*-parameters with B-field is adequate (true for all crossings in this thesis where a fit was attempted). Thus, there are six *s*-parameters, three each representing current *amplitudes* to the left (low B-field side) and right (high B-field side) of the crossing. Though qualitatively quite similar, the values of the branch currents extracted by the two measurement strategies are quantitatively slightly different. Consequently, the current amplitude parameters determined from the data in Figs. 5.8(b) and (c) are also slightly different [109]. In both cases it remains true that at both 1.8 and 2.5 T, in terms of magnitude, $s_2 > s_1, s_3$, i.e., the center branch current is the strongest.

To understand precisely how mixing gives rise to the observed branch currents, we reconstruct in Fig. 5.8(g) the eigenvectors for the three branches giving the components of the uncoupled basis states. Well to the left and right of the crossing the expected behaviour is apparent. For each branch one of the three components tends to ±1 and the remaining two tend to zero meaning the branch current simply tends to the square of the relevant current *amplitude*. Meanwhile, for the condition $C_{12} = C_{23} > 0$ and $C_{13} = 0$,

which is close to the fitted parameters, the currents at the crossing point of the uncoupled basis levels (ΔB = 0 T) are given by the following expressions: $I_{upper} = \frac{1}{4}\left(s_1 + \sqrt{2}s_2 + s_3\right)^2$, $I_{center} = \frac{1}{2}\left(s_1 - s_3\right)^2$, and $I_{lower} = \frac{1}{4}\left(s_1 - \sqrt{2}s_2 + s_3\right)^2$. Since s_2 » $s_1 \approx s_3$, $I_{upper} \approx I_{lower} \approx \frac{1}{2}(s_2)^2$ and I_{center} is greatly reduced from its uncoupled value of $\sim(s_2)^2$. Thus, the upper and lower branch resonances are dominated by the large contribution of the uncoupled center branch current *amplitude*, s_2, and appear bright. Furthermore, the center branch resonance appears dark when the influence of s_2 is zero. I_{center} will vanish *precisely* at ΔB = 0 T if s_1 and s_3 are equal in magnitude and of the same sign. The position of the current suppression can be shifted slightly from ΔB = 0 T if certain values of C and s are not the same. For the γ crossing, s_1 and s_3 are of similar magnitude but opposite sign at ΔB = 0 T, so a small contribution of s_2 is required to attain zero center branch current. This occurs a little to the right of ΔB = 0 T. The current suppression is thus a genuine and robust effect arising as a consequence of coherent mixing leading to destructive interference. Before discussing the deeper physical significance of this finding (see Sec. 5.1.7), we first discuss a second example of three-level mixing.

5.1.6 A Second Example of Current Suppression at a Three-Level Crossing

Having discussed an otherwise bright resonance becoming dark at the γ crossing in the spectrum of dot 2 from Device I (recall Fig. 5.8), we now address the question of whether this result is unique, i.e., can the suppression of an otherwise strong resonance

arise at other three-level crossings, and if so, are the conditions of the underlying coherent mixing the same? In order to address this, we now turn to the τ crossing between the $3d^-$-, $4p^+$- and $5g^+$-like single-particle states in the spectrum of dot 1 from Device VI [the bias direction is opposite to that of the measured spectrum in Figs. 4.3(a) and (b)]. Note that having demonstrated explicitly for the γ crossing that the observed effects were not influenced by the choice of measurement strategy, for the remainder of Chap. 5 we focus solely on strategy A measurements for simplicity.

Figures 5.9(a) and (b) show the behaviour at the τ crossing. Like the γ crossing in the spectrum of dot 2 from Device I discussed in Sec. 5.1.5, this crossing also has three distinct branches. Furthermore, the center branch resonance is also strongly suppressed near the center of the crossing region when the branches are minimally separated. Although at first sight the behaviour at the τ crossing appears quite similar to that at the γ crossing in Fig. 5.8, the τ crossing does exhibit some subtle differences as compared to the γ crossing. For instance, the center of the τ crossing occurs at ~2.68 T [see Fig. 5.9(c)], while the center branch current is most strongly suppressed at ~2.86 T [as shown in Fig. 5.9(b)], i.e., the suppression minimum is shifted to the right of the center of the crossing region. Additionally, there is also a pronounced 'wiggle' in the energy level position of the center branch evident in Fig. 5.9(a). Furthermore, although there is enhancement of the resonant current, the upper and lower branch currents are nonetheless dissimilar with the former (latter only) showing a monotonic increase (a maximum) close to the center of the crossing [see Fig. 5.9(b)].

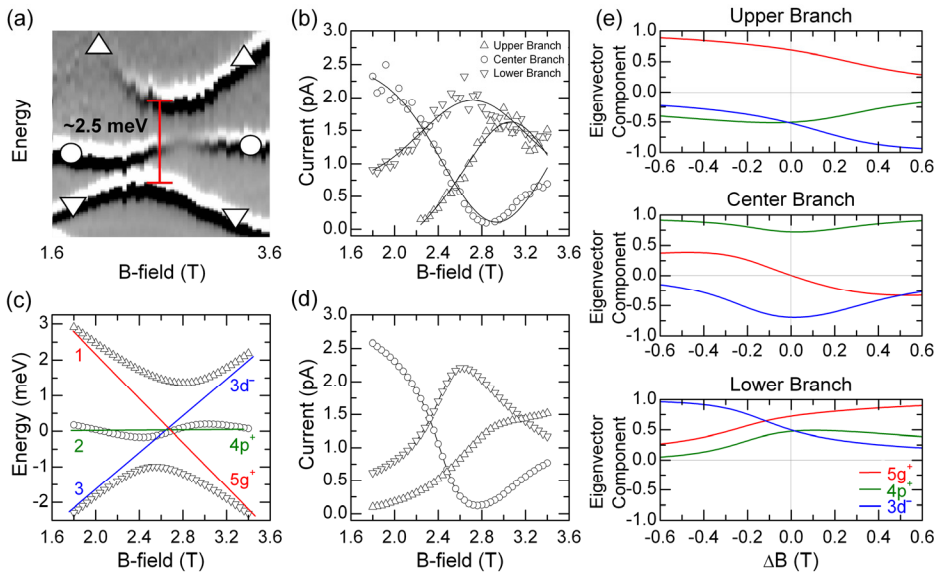

Fig. 5.9. τ three-level crossing. (a) Energy level (differential conductance resonance [106]) positions. The upper, center, and lower branches respectively are labelled by an up-pointing triangle, a circle and a down-pointing triangle. (b) Extracted resonance branch currents (non-resonant background component removed). The upper branch current to the left of ~2.2 T is too small to determine. The black lines are a guide to the eye (and are generated by simple Gaussian fitting although no meaning is attached to the fitting procedure). (c) Fit of energy level positions [110]. (d) Fit of branch currents. The fitted *current amplitude* parameters are, in $pA^{1/2}$, s_1 = 0.391, s_2 = 1.55, and s_3 = 0.844 at 2.24 T, and s_1 = 0.418, s_2 = 1.37, and s_3 = 1.19 at 3.4 T, with the values in between linearly interpolated. (e) Reconstructed eigenvectors of the three branches showing the components of the uncoupled basis states on passing through the crossing region. ΔB = 0 T is at ~2.68 T.

In order to quantitatively discuss the mixing, we now apply the simple coherent level mixing model to the τ crossing to interpret the energy level position and branch current behaviour shown in Figs. 5.9(a) and (b). The results of the fitting are shown in Figs. 5.9(c) and (d). The fact that the fit is quite reasonable overall for both the energy dispersion and the resonant currents at a second three-level crossing suggests that the model is robust. The fitted coupling energy parameters are, in meV, C_{13} = -0.88, C_{12} = -

0.85, and C_{23} = 0.13, or in terms of magnitude $C_{13} \approx C_{12} \gg C_{23}$. Thus, the fitting has revealed that the anti-crossing behaviour at this crossing is determined by two dominant and approximately equal couplings between the $5g^+$- and $3d^-$-like states (C_{13}), and between the $5g^+$- and $4p^+$-like states (C_{12}), whereas the coupling between the $4p^+$and $3d^-$-like states (C_{23}) is very weak. Interestingly, the result for the τ crossing, namely that $C_{13} \approx C_{12} \gg C_{23}$, differs from the situation for the γ crossing in Fig. 5.8 where we found that $C_{12} \approx C_{23} \gg C_{13}$.

The eigenvectors for the τ crossing presented in Fig. 5.9(e) are also quite different compared to those for the γ crossing [see Fig. 5.8(g)]. Nonetheless, the clear suppression of the center branch current still arises as a consequence of coherent mixing leading to destructive interference. To understand this, consider the following. For the condition $C_{12} = C_{13} < 0$, $C_{23} = 0$, which is close to that for the fitted parameters, the currents at ΔB = 0 T are given by the following expressions: $I_{upper} = \frac{1}{4}\left(\sqrt{2}s_1 - s_2 - s_3\right)^2$, $I_{center} = \frac{1}{2}\left(s_2 - s_3\right)^2$, and $I_{lower} = \frac{1}{4}\left(\sqrt{2}s_1 + s_2 + s_3\right)^2$. Thus the dark center branch resonance at ΔB = 0 T occurs when the influence of s_1 is zero, and the current will vanish there if s_2 and s_3 are equal and of the same sign. For the τ crossing, although of the same sign, s_2 and s_3 do not quite have the same magnitude and so some small contribution of s_1 is required to 'trim' the current close to zero. This occurs a little to the right of ΔB = 0 T.

Summarizing the key findings of the fitting, the model has revealed that along with the γ crossing of Fig. 5.8, the τ crossing of Fig. 5.9 has two dominant couplings. Nonetheless, the dark center branch resonance near the center of these two three-level crossings actually arises through destructive interference from *different* conditions, i.e.,

dark states formed by three-level mixing do not arise from a unique set of circumstances and are not specific to QDs of a certain ellipticity (as is well demonstrated in Fig. 5.8 and 5.9 for two quite different QDs from two different devices). Clearly, strong suppression of the resonant current in one branch is a genuine and robust effect originating from three-level mixing. In the next section, we address the deeper physical significance of the preceding findings for the γ and τ crossings.

5.1.7 A Deeper Look at the Underlying Coherent Mixing Physics

We now draw attention to the link between the three-level mixing we observe and other quantum phenomena which involve three-level mixing. In particular, we will consider the situation of coherent population trapping well established in a three-level-system of quantum and atom optics [62,63], as well as two all-electrical single-electron tunneling schemes, one for coherent population trapping and one for the related coherent tunneling by adiabatic passage, which have recently been proposed for systems of three triangularly or linearly arranged QDs [54,55]. We will focus specifically on the origin of the dark state we observe at the γ crossing in the spectrum of dot 2 from Device I however, the comments we make could easily be adapted to apply to the τ crossing in the spectrum of dot 2 from Device VI as well.

As shown schematically in Fig. 5.10(a), optical coherent population trapping involves three states, which we label $|1\rangle$, $|2\rangle$ and $|3\rangle$, arranged in a Λ-configuration. States $|1\rangle$ and $|2\rangle$ are coupled by one laser, and states $|2\rangle$ and $|3\rangle$ are coupled by a second laser, while states $|1\rangle$ and $|3\rangle$ are uncoupled. The level coupling parameters may

thus be taken as $C_{12} = C_{23} = 1$ and $C_{13} = 0$. In general, a coherent mixture of the three states can be written as $\Psi = a|1\rangle + b|2\rangle + c|3\rangle$, but for the aforementioned (ideal) coupling parameters, a = -c, and b = 0. The state, $|\mathrm{D}\rangle = (|1\rangle - |3\rangle)/\sqrt{2}$ appears dark because b = 0 and thus the spontaneous emission from state $|2\rangle$ to some auxiliary (Aux) level vanishes (this emission provides a means to monitor the population of state $|2\rangle$). Provided the C-parameters are real, $|\mathrm{D}\rangle$ may be pictured as follows. Consider a unit sphere where basis states $|1\rangle$, $|2\rangle$ and $|3\rangle$ are represented by unit vectors $\vec{V}_1$, $\vec{V}_2$ and $\vec{V}_3$ parallel to the x, y, and z axes respectively [see Fig. 5.10(b)]. $|\mathrm{D}\rangle$ is then represented by a point that lies on the surface of the sphere in the x-z plane inclined 45° below the x-axis. We will see shortly that $|\mathrm{D}\rangle$ is equivalent to the dark state we observe at the center of the γ crossing due to three-level mixing in the double QD device.

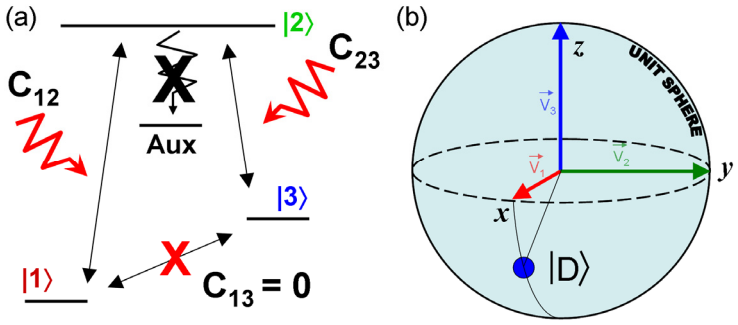

Fig. 5.10. (a) Familiar three-level mixing scheme encountered for a Λ-system of quantum and atom optics leading to coherent population trapping. (b) Graphical representation of dark state $|\mathrm{D}\rangle$ for $C_{12} = C_{23} = 1$ and $C_{13} = 0$.

Using the simple coherent tunneling model we developed, we now consider an ideal three-level crossing which is very close to the situation actually encountered at the γ

crossing. Specifically, we take $C_{12} = C_{23} = 1$ and $C_{13} = 0$, and $s_1 = s_3 = 0$ and $s_2 = 1$, and assume that the *s*-parameters are independent of B-field. For this ideal 2-dominant coupling-type crossing, the distinct upper, center and lower branches are present in the energy dispersion [see Fig. 5.11(a)] and the resonant current through the otherwise strong center branch is completely suppressed at the center of the crossing region ($\Delta B = 0$ T) marking the formation of a dark state [see Fig. 5.11(b)]. Note that throughout the crossing region, the resonant current through the upper and lower branches are identical.

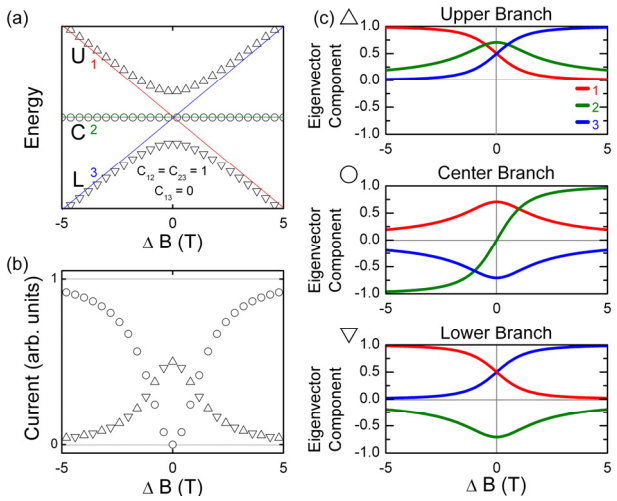

Fig. 5.11. Calculation of (a) energy level position (b) resonant current and (c) eigenvector components for ideal three-level mixing. The upper, center, and lower branches are labelled respectively by an up-pointing triangle, a circle and a down-pointing triangle.

In order to understand the link between the dark state we observe and coherent population trapping, we use the simple geometrical picture introduced in Fig. 5.10(b). We begin by describing how the branch eigenvectors for the ideal case [see Fig. 5.11(c)] traverse the unit sphere. In Fig. 5.12 we plot the eigenvectors for each of the three branch states (a) to the left, (b) at the center and (c) to the right of the crossing region. As we move from left to right, the upper branch eigenvector ($\vec{U}$) is originally pointing parallel

to the *x*-axis and ends up pointing parallel to the *z*-axis having moved out of the *x*-*z* plane in between. Meanwhile, the lower branch eigenvector ($\vec{L}$) begins pointing parallel to the *z*-axis and finishes parallel to the *x*-axis having also moved out of the *x*-*z* plane in between. Finally, the center branch eigenvector ($\vec{C}$) starts by pointing anti-parallel to the *y*-axis and ends up pointing parallel to the *y*-axis having passed through a point in the *x*-*z* plane (located 45° below the *x*-axis). The position of the center branch eigenvector in Fig. 5.12(b) (at the center of the crossing) is exactly equivalent to the graphical representation of the dark state due to coherent population trapping [see Fig. 5.10(b)].

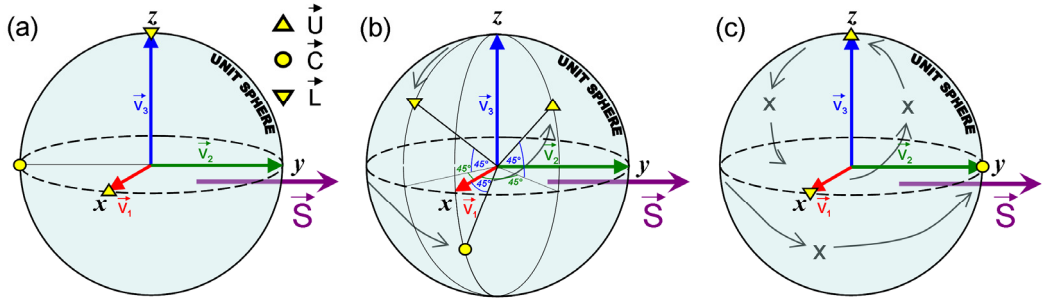

Fig. 5.12. Graphical representation of the eigenvectors for the three branches of the γ crossing [see Fig. 5.8(g)] and current 'read-out' scheme through $\vec{S}$ (a) well to the left, (b) at the center (ΔB = 0), and (c) well to the right of the crossing.

In our simple coherent tunneling model, the branch currents can be expressed as $I_k = \left|\sum_m v_m^k s_m\right|^2 = \left|\vec{k}\cdot\vec{S}\right|^2$, where $\vec{k}$ is the eigenvector for the k = (upper, center, lower) branch and $\vec{S} = s_1\vec{V}_1 + s_2\vec{V}_2 + s_3\vec{V}_3$ represents the uncoupled current amplitude parameters. For the ideal three-level mixing case under focus, $\vec{S}$ points parallel to the *y*-axis. Hence, regarding the center branch, the current is strong well to the left and right because $\vec{C}$ is respectively anti-parallel and parallel to $\vec{S}$ ($|\vec{C}\cdot\vec{S}|^2 = 1$). At the center of

the crossing, $\vec{C}$ is in the *x*-*z* plane, i.e., perpendicular to the *y*-axis, so the center branch current will be completely suppressed ($|\vec{C}\cdot\vec{S}|^2 = 0$). This situation is exactly equivalent to the dark state $|\mathrm{D}\rangle$ graphically represented in Fig. 5.10(b) (note that any point on the sphere within the *x*-*z* plane would be a dark state when $\vec{S}$ is parallel to the *y*-axis and hence dark states can arise when $C_{12} \neq C_{23}$, provided $C_{13} = 0$). Regarding the upper and lower branches, the current is zero well to the left and right because both $\vec{U}$ and $\vec{L}$ are in the *x*-*z* plane and hence are perpendicular to $\vec{S}$ ($|\vec{U}\cdot\vec{S}|^2 = |\vec{L}\cdot\vec{S}|^2 = 0$). On moving to the center of the crossing, both $\vec{U}$ and $\vec{L}$ have relocated out (and to either side) of the *x*-*z* plane, i.e., they have finite components parallel or anti-parallel to the *y*-axis and so the branch currents are non-zero ($|\vec{U}\cdot\vec{S}|^2 = |\vec{L}\cdot\vec{S}|^2 = ½$).

There are a few interesting differences between the coherent three-level mixing we observe and familiar coherent population trapping in quantum and atom optics. Usually, the coupling parameters are adjustable (by tuning the power of the lasers for example) while the energies of the states involved are essentially fixed, whereas in our transport scheme, the coupling parameters are fixed while the energies of the levels can be adjusted (by changing the B-field). Furthermore, in the optical case, the population of $|1\rangle$, $|2\rangle$ and $|3\rangle$ can be monitored directly via decay to auxiliary levels, while in our case the projection of the eigenvectors onto $\vec{S}$ constitutes the 'read-out' scheme.

From a quantum electronics perspective, two relevant all-electrical single-electron tunneling schemes have recently been proposed. The first scheme, from Ref. [55], considers three QDs arranged in a triangle [see Fig. 5.13(a)] each with a single available

state (labelled $|1\rangle$, $|2\rangle$ and $|3\rangle$. In this scheme, during a DC measurement, an electron can become trapped in a coherent superposition of states in different dots when the couplings between $|1\rangle$ and $|2\rangle$, and $|3\rangle$ and $|2\rangle$ are non-zero, while the coupling between $|1\rangle$ and $|3\rangle$ is zero. Once this 'dark' state is occupied no further transport is possible. Explicitly, the dark state has exactly the same form, namely $|D\rangle = (|1\rangle - |3\rangle)/\sqrt{2}$, as those described above. Meanwhile, the second scheme, from Ref. [54] pictures three linearly arranged QDs [see Fig. 5.13(b)] each with a single available state (again labelled $|1\rangle$, $|2\rangle$ and $|3\rangle$). A protocol is envisaged to coherently transfer an electron from $|1\rangle$ to $|3\rangle$ 'without going through $|2\rangle$,' i.e., without any population in $|2\rangle$. To do this, the couplings between the states are controlled as a function of time in a counter-intuitive manner. Specifically, C_{23} is turned on before C_{13}. Throughout the procedure, the system occupies a dark state, and, notably, at the halfway point this state has the form $|D\rangle = (|1\rangle - |3\rangle)/\sqrt{2}$. Clearly, the dark state we observe at the γ crossing where three levels mix *intra*-dot is equivalent to that in these *inter*-dot mixing schemes. We also note that, motivated by the work we have performed, recently Emary et. al. [59] have taken a deeper look at the all-electrical analogue of coherent population trapping.

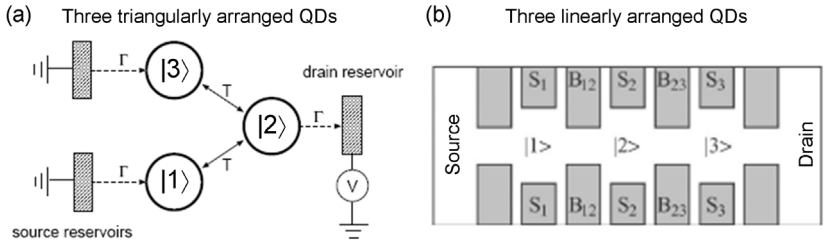

Fig. 5.13. Electronic schemes for realizing (a) coherent population trapping and (b) coherent tunneling by adiabatic passage (images adapted from Refs. [54,55] respectively).

5.2 Two- and Four-Level Mixing

Having explored dark state formation at two three-level crossings, namely, the γ crossing in the spectrum of dot 2 from Device I and the τ crossing in the spectrum of dot 2 from Device VI, we now investigate the suppression of an otherwise strong resonance at level crossings involving two or four levels (recall Fig. 5.1). In order to study the coherent mixing at such crossings, we will need to adapt the simple coherent three-level mixing model introduced in Sec. 5.1 to cope with two- and four-level crossings.

5.2.1 Introduction to Two-Level Anti-Crossings

Two-level mixing has been widely encountered in many different semiconductor nano-systems (see for instance Refs. [45-53]). When thinking of two-level mixing, naturally one pictures two anti-crossing branches where the mixing of levels or excitations leads to monotonic exchange of resonance character as a function of an external parameter, a situation we will refer to as the familiar case. An illustrative example involving electric-field induced mixing of direct (bright) and indirect (dark) exciton states in coupled QDs can be found in Refs. [47,51].

While we observe such familiar two-level anti-crossings (see for example left side of Fig. 5.14), we also observe current suppression near the center of the crossing (see right side of Fig. 5.14). This is a rather uncommon situation and in fact we know of only a few examples (from the realm of superconductivity) of anti-crossings where the resonance character of one branch is suppressed (see Refs. [111,112]). We will refer to this situation as the ideal case. The sense in which we mean ideal will be made clear in

Sec. 5.2.2. In what follows we will attempt to explain both the familiar and ideal anti-crossing behaviour within the framework of a single coherent level mixing model.

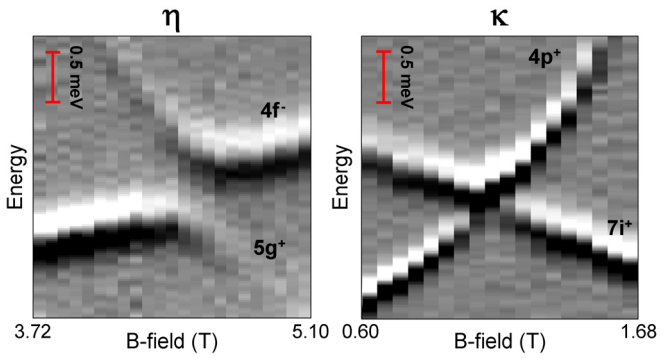

Fig. 5.14. Differential conductance [106] plot for the η (κ) two-level crossing measured in dot 2 (1) from Device I [recall the dot spectra in Figs. 4.3(c) and 4.7]. States are labelled using the atomic orbital-like notation.

5.2.2 Modelling Two-Level Anti-Crossings

In order to study two-level anti-crossings we trivially adapt the 3x3 matrix Hamiltonian model (recall Eqn. 5.1). For a two-level crossing there are only two basis states, which we label $|1\rangle$ and $|2\rangle$, and so a 2x2 matrix is sufficient. In the model these basis states are still assumed to have linear dispersions and the coupling between them is characterized by a single off-diagonal coupling parameter, C_{12}. As expected, when there is no coupling between the two basis states ($C_{12} = 0$) they cross exactly [see Fig. 5.15(a)], but for finite coupling the states hybridize and there is an anti-crossing [see Fig. 5.15(b)] where the upper and lower branches are separated by $2C_{12}$. The upper and lower branch states (labelled $|U\rangle$ and $|L\rangle$) are now linear combinations of the two uncoupled basis states.

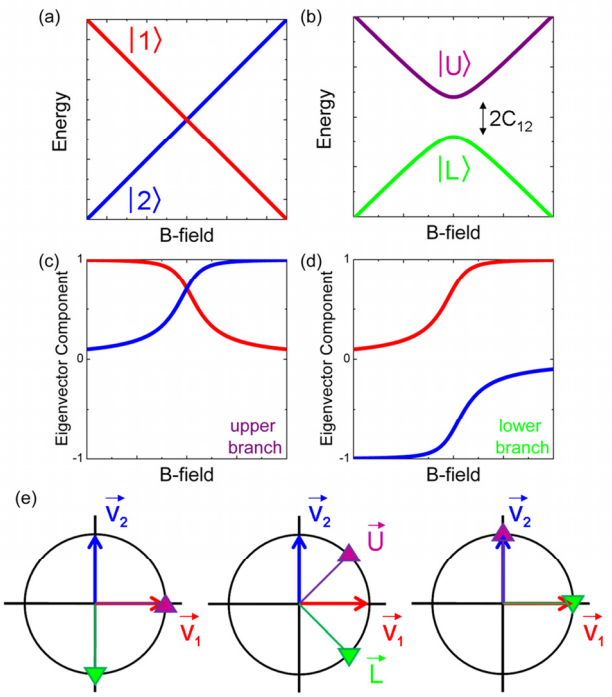

Fig. 5.15. (a) Uncoupled basis states $|1\rangle$ (red) and $|2\rangle$ (blue). Note that in this section we use the notation $|1\rangle$ and $|2\rangle$ rather than the more compact 1 and 2 because we explicitly discuss linear combinations of the basis states. (b) Finite coupling of the basis states results in an anti-crossing. (c) and (d) Eigenvector components of the two states as a function of B-field. (e) Simple geometric aid showing how the eigenvector components change as a function of B-field throughout a two-level crossing region. Left, center and right panels are respectively for far to the left (low B-field), at the center and far to the right (high B-field) of the crossing region.

We now adapt the simple geometrical aid introduced in Sec. 5.1.7 to help understand how the eigenvectors change throughout a two-level crossing region. Rather than the unit sphere we used in relation to a three-level crossing, for a two-level crossing we now picture a unit circle (in the *x*-*y* plane). Once again, the two basis states are represented by unit vectors $\vec{V}_1$ and $\vec{V}_2$ along the *x* and *y* axes and the vectors $\vec{U}$ and $\vec{L}$ represent the eigenvectors for the upper and lower states. The eigenvector components

[see Fig. 5.15(c) and (d)] reveal that (strictly infinitely) far to the left of the crossing region, where the basis states are uncoupled, $|U\rangle = |1\rangle$, and $|L\rangle = -|2\rangle$, at the center of the crossing region, where we have symmetric and anti-symmetric states, $|U\rangle = {}^{1}\!/_{\sqrt{2}}|1\rangle + {}^{1}\!/_{\sqrt{2}}|2\rangle$ and $|L\rangle = {}^{1}\!/_{\sqrt{2}}|1\rangle - {}^{1}\!/_{\sqrt{2}}|2\rangle$ and (strictly infinitely) far to the right of the crossing region, where the basis states are again uncoupled, $|U\rangle = |2\rangle$, and $|L\rangle = |1\rangle$. Correspondingly, in the geometrical aid, as the B-field is tuned from far to the left of the crossing through to far to the right, $\vec{U}$ and $\vec{L}$ rotate around the origin by ninety degrees as shown in Fig. 5.15(e).

In order to include current we again adapt the simple coherent tunneling model for the case of a two-level crossing. Explicitly, the resonant current of the k = (upper, lower) branch, I_k, is computed as $I_k = \left|\sum_m v_m^k s_m\right|^2 = \left|\vec{k}\cdot\vec{S}\right|^2$, where m = 1, 2 is the basis state index and $\vec{S} = s_1\vec{V}_1 + s_2\vec{V}_2$ is a vector representing the s-parameters. Note that, in this section, we will assume that $\vec{S}$ is fixed when we compute the resonant currents throughout a crossing region although this need not be the case in practice.

We can now understand the origin of *both* the familiar and ideal behaviour at two-level crossings. For the familiar case, where the current through one basis state is much larger than the other, $\vec{S}$ is parallel to (or very close to parallel to) one axis, here chosen to be the x-axis, i.e., we take $s_1 = 1$, $s_2 = 0$ meaning $\vec{S} = \vec{V}_1$ (see the top left panel of 5.16). For this situation the currents evolve in the familiar way, namely that to the far left of the crossing, the upper branch current is strong ($|\vec{U}\cdot\vec{S}|^2 = 1$), while the lower branch current

is weak ($|\vec{L}\cdot\vec{S}|^2 = 0$), at the center of the crossing the two currents are equal ($|\vec{U}\cdot\vec{S}|^2 = |\vec{L}\cdot\vec{S}|^2 = ½$) and to the far right of the crossing the lower branch current is strong ($|\vec{L}\cdot\vec{S}|^2 = 1$), while the upper branch current is weak ($|\vec{U}\cdot\vec{S}|^2 = 0$).

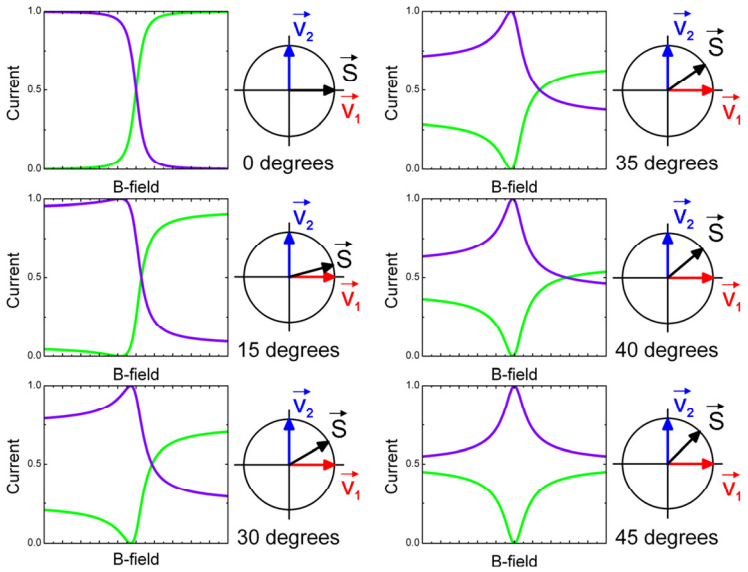

Fig. 5.16. Simulations explaining the transition from familiar to ideal behaviour as s_1 and s_2 are altered from $s_1 = 1$, $s_2 = 0$ (top left panel) to $s_1 = s_2 = 1/\sqrt{2}$ (bottom right panel).

Now suppose we repeat the exercise, but rotate $\vec{S}$ anti-clockwise in steps (keeping the length, $\sqrt{s_1^2 + s_2^2}$, equal to unity). The simulations in Fig. 5.16 reveal that a peak (dip) in the upper (lower) branch current develops on the low B-field side of the crossing and the point where the two branch currents cross, which is initially in the center of the crossing region, shifts towards higher B-field. In particular, for the case where $s_1 = s_2$, i.e., $\vec{S} = {}^{1}\!/_{\sqrt{2}}\vec{V}_1 + {}^{1}\!/_{\sqrt{2}}\vec{V}_2$, shown in the lower right panel of Fig. 5.16, we now observe two equal resonant currents far to the left and right of the crossing region ($|\vec{U}\cdot\vec{S}|^2 = |\vec{L}\cdot\vec{S}|^2 = ½$) and exactly at the center of the crossing region, the upper branch

current is doubled ($|\vec{U} \cdot \vec{S}|^2 = 1$), while the lower branch current is completely suppressed ($|\vec{L} \cdot \vec{S}|^2 = 0$). This suppression marks the formation of a dark state. We refer to this behaviour as ideal because the dark state forms only at the center of the crossing region provided the currents through the two underlying basis states are equal. Note that continuing to rotate $\vec{S}$ anti-clockwise will result in the peak and the corresponding dip in the branch currents shifting toward higher B-field, eventually returning to the familiar case when $\vec{S}$ is parallel to the *y*-axis ($s_2 \gg s_1$).

The geometric aid has provided a simple and intuitive picture for understanding how two-level mixing can lead to both the familiar behaviour and dark state formation in the ideal case. In the next section, we will now characterize the measured η and κ two-level crossings (recall Fig. 5.14) in order to verify whether the behaviour observed at both these crossings can indeed be understood within the framework of the simple coherent level mixing model just proposed.

5.2.3 Fitting Familiar and Ideal Two-Level Anti-Crossings

We begin with the η two-level crossing between the $4p^+$- and $7i^+$-like states from the spectrum of dot 2 from Device I [recall Fig. 4.3(c)]. Figures 5.17(a)-(c) show the relevant data and clearly evident is the familiar behaviour for a two-level anti-crossing, namely the monotonic exchange of resonance character on passing through the crossing region. Explicitly, to the left of the crossing region, the lower (upper) branch resonance [identified by an up- (down-) pointing triangle] is strong (weak), while at the center of the crossing region the two branches have roughly equal strength and to the right of the

crossing the lower (upper) branch is weak (strong). To extract the resonant current [Fig. 5.17(c)] we have removed the non-resonant background current and fit each current trace to two Lorentzians (recall the similar fitting procedure discussed in Sec. 5.1.2 for the γ crossing in the spectrum of dot 2 from Device I).

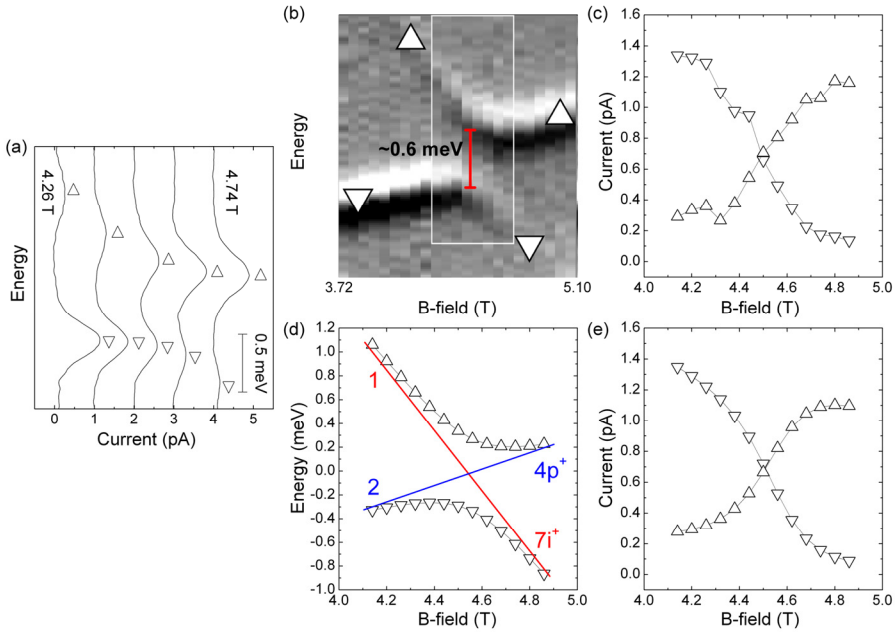

Fig. 5.17. η two-level crossing. (a) Every second current trace near the center of the crossing region (non-resonant background current removed). Traces are horizontally offset by 1 pA. (b) Energy level (differential conductance resonance [106]) position. When numerically differentiated the traces in (a) form vertical sections of the region indicated by the white box. (c) Extracted resonance branch currents (non-resonant component removed). (d) [(e)] Fit of energy level positions (resonant currents) [110]. The fitted *current amplitude* parameters are, in $pA^{1/2}$, s_1 = -0.256 and s_2 = 1.24 at 4.14 T, and s_1 = -0.02, and s_2 = 1.09 at 4.86 T, with the values in between linearly interpolated.

Figures 5.17(d) and (e) show the results of fitting the energy dispersion and resonant currents of the η crossing to the simple coherent level mixing model. Evidently the model does a good job of reproducing both the energy dispersions and the resonant

currents. The value of C_{12} is -0.312 meV, so the energy splitting between the upper and lower branches is ~0.6 meV, consistent with the experimental observations. Notably in terms of the *s*-parameters, $s_2 \gg s_1$ both to the left and right of the crossing region, as expected for the familiar behaviour discussed in Sec. 5.2.2.

Turning now to the κ two-level crossing between the $4f^-$- and $5d^+$-like states from the spectrum of dot 1 from Device I, Figs. 5.18(a)-(c) show the relevant data. Clearly evident in all three panels is the ideal behaviour for a two-level anti-crossing, namely two branches of approximately equal strength to both the left and right of the crossing region and at the center of the crossing region, the upper branch [identified by an up-pointing triangle] strength is approximately doubled while the lower branch [identified a down-pointing triangle] strength is strongly suppressed.

Figures 5.17(d) and (e) show the results of fitting the energy dispersion and resonant currents of the κ crossing to the simple coherent level mixing model. Once again, the model successfully reproduces both the energy dispersions and the resonant currents. The observed energy splitting between the upper and lower branches is ~0.2 meV and the value of C_{12} (0.12 meV) is consistent with this. Furthermore, the fit reveals that $s_1 \approx s_2$ both to the left and right of the crossing region, as expected for the ideal behaviour discussed in Sec. 5.2.2.

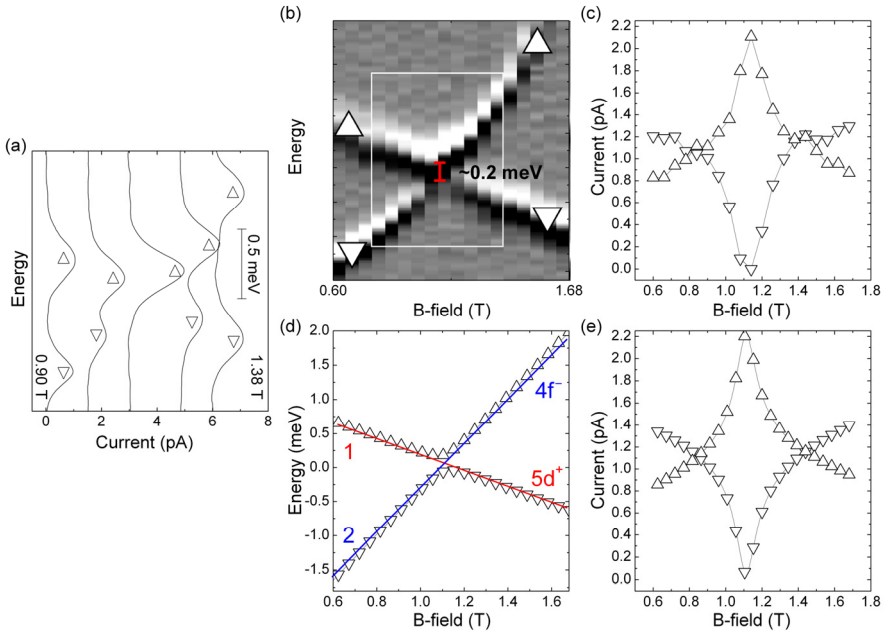

Fig. 5.18. κ two-level crossing. (a) Every second current trace near the center of the crossing region (non-resonant background current removed). Traces are horizontally offset by 1.5 pA. (b) Energy level (differential conductance resonance [106]) position. When numerically differentiated the traces in (a) form vertical sections of the region indicated by the white box. (c) Extracted resonance branch currents (non-resonant component removed). (d) [(e)] Fit of energy level positions (resonant currents) [110]. The fitted *current amplitude* parameters are, in $pA^{1/2}$, $s_1 = 0.85$ and $s_2 = 1.21$ at 0.60 T, and $s_1 = 1.23$, and $s_2 = 0.92$ at 1.68 T, with the values in between linearly interpolated.

As a final comment on the κ crossing, we note that for the ideal case discussed in Sec. 5.2.3 (recall the lower right panel of Fig. 5.16), it is only far to the left (low B-field) and right (high B-field) of the crossing where the branch currents approach each other and become equal, i.e., the branch currents never cross. However, for the κ crossing, although the branch currents are certainly approximately equal to the left and right of the center of the crossing region, the branch currents cross at ~0.8 T and ~1.4 T, i.e., to the left of 0.8 T and to the right of 1.4 T the resonant current of the lower branch is slightly larger than that of the upper branch [see Fig. 5.18(c)]. Given this difference, why then do

we still see the near ideal concurrent enhancement and suppression at the κ crossing? For the ideal case shown in the lower right panel of Fig. 5.16, we note that the *s*-parameters are equal and constant throughout the entire crossing region. For the κ crossing, fitting reveals that although the s-parameters are not equal at low and high B-fields, their interpolated values at the center of the crossing are nonetheless practically the same (s_1 = 1.03 and s_2 = 1.08 at 1.14 T). Furthermore the sum of s_1 and s_2 is approximately conserved throughout the crossing region. Consequently, the current suppression in one branch and the current enhancement in the other branch still occurs at the center of the crossing and the crossing is manifestly still ideal-like.

Summarizing this section, we have demonstrated that both the familiar and ideal two-level mixing observed at the η and κ crossings can be understood within the same coherent tunneling picture. In the next section, we move on to study an example of four-level mixing.

5.2.4 Four-Level Mixing

Our initial investigation of the multi-level crossings focused on the interesting three-level crossings in the measured spectra (recall Fig. 4.3) not least because instances of three-level crossings are less common than two-level crossings in the literature. Additionally, they are sufficiently numerous and varied in the measured spectra that we can reasonably expect to gain a fairly complete picture of the physics of a three-level crossing. As we do see some four-level crossings in the measured spectra, one may wonder what we can learn about coherent level mixing at these crossings too, i.e., how far we can extend our understanding as the number of levels increases. However, since

the four level crossings occur quite high up in energy, approaching the longitudinal-optical phonon emission limited edge of the available energy range, we only observe a few examples of them. Consequently, we expect that we will only observe a few of the many possible varieties of behaviour. Nonetheless, we will examine one example, namely the σ crossing between the $4f^-$-, 5s-, $6f^+$- and $7i^+$-like single-particle states in the spectrum of dot 1 from Device VI [recall Fig. 5.1(c)], where coherent level mixing is still found to lead to current suppression of an otherwise strong resonance. In order to do so, we extend the simple matrix Hamiltonian model to cover the case of a four-level crossing, although, as we shall see, we start to approach the limit of applicability of the current model and also encounter challenges in fitting the data.

Figure 5.19(a) shows the energy dispersion at the σ crossing measured using strategy A. Clearly visible at this crossing are four distinct branches, which we refer to as the upper, upper middle, lower middle and lower branches (identified by black up-pointing, white up-pointing, white down-pointing and black down-pointing triangles). When we examine the resonant currents shown in Fig. 5.19(b), we observe strong variations in all the branch currents. However, the most interesting feature is the suppression of the lower middle branch current near the center of the crossing region. Explicitly, the center of the σ crossing occurs at ~2.70 T [see Fig. 5.19(c)], and the lower middle branch current is most strongly suppressed at ~2.76 T [as shown in Fig. 5.19(b)]. Close examination of the other resonant currents also reveals that the upper middle branch current is suppressed, although not completely, near ~2.56 T, while the lower branch current is enhanced a little at ~2.70 T and the upper branch current, which decreases from left to right of the crossing region, also shows enhancement near ~2.50 T.

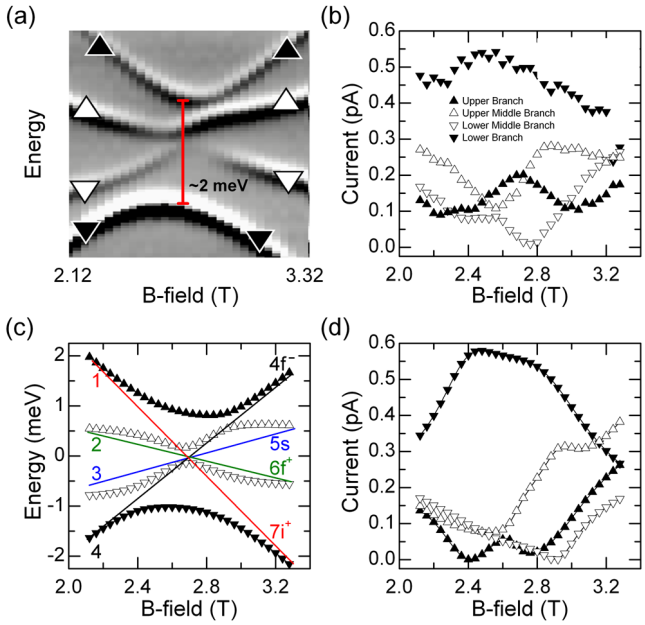

Fig. 5.19. (a) Energy level (differential conductance resonance [106]) position versus B-field for the four-level σ crossing in the spectrum of dot 1 from Device VI. (b) Extracted resonance branch currents (non-resonant background component removed). (c) [(d)] Fit of energy level positions (resonant currents) [110]. The fitted *current amplitude* parameters are, in $pA^{1/2}$, $s_1 = 1.87$, $s_2 = -1.31$, $s_3 = 0.78$ and $s_4 = 1.47$ at 2.12 T, and $s_1 = 1.35$, $s_2 = -1.72$, $s_3 = -1.65$ and $s_4 = 1.81$ at 3.32 T, with the values in between linearly interpolated.

In order to fit the experimental data shown in Figs. 5.19(a) and (b) we extend the matrix Hamiltonian model to include four basis levels which we label 1, 2, 3 and 4 in the sense indicated in Fig. 5.19(c). As a consequence, in order to pair-wise couple the basis states we now require six coupling parameters, C_{12}, C_{13}, C_{14}, C_{23}, C_{24} and C_{34}. Even ideally restricting the coupling parameters to be either 0 or 1, having six *C*-parameters means that there are now 64 (2^6) different possible (basic) combinations, as opposed to only 8 (2^3) for the three level case with three coupling parameters. Consequently, in practical terms, it is not straightforward to categorize the possible four-level crossing types by shape as was done for the three-level crossings (recall Fig. 5.3) and since only a

few examples of four-level crossings are observed, it is unlikely we would observe all possible basic shapes in any case. Furthermore, there are also an increased number of *s*-parameters (eight), basis state slopes (four) and possibilities for basis states not meeting at a single point (up to six). Therefore we expect that fitting a four-level crossing will be significantly more challenging than a three-level crossing.

Nonetheless, we still attempt to fit the data for the σ crossing. The fitted energies of the branches are shown in Fig. 5.19(c) and the fit is actually quite good. The coupling parameters we extract are, in meV, $C_{12} = 0.47$, $C_{13} = -0.40$, $C_{24} = 0.26$, $C_{34} = 0.17$ $C_{14} = -0.06$ and $C_{23} = 0.01$, or in terms of magnitude $C_{12} \approx C_{13} > C_{24} \approx C_{34} > C_{14} \approx C_{23}$. Note that these values are comparable to those determined for the two- and three-level crossings examined previously (recall Secs. 5.1.5, 5.1.6 and 5.2.3).

However, when we attempt to fit the resonant currents, the result shown in Fig. 5.19(d) is not particularly good quantitatively, though it is qualitatively reasonable in many respects. For the lower middle branch, most importantly, the suppressed region of current at the center of the crossing is reproduced, however the fitted current to the left and right of the crossing are too weak. Concerning the upper middle branch, the general shape agrees quite well with the experimental data, although the fitted current to the right of the crossing is slightly too strong. For the lower branch, the increased current near the center of the crossing region is reproduced qualitatively however, the general decrease in current from left to right of the crossing region is absent and the fitted current is too weak to both the left and right of the crossing. Finally, for the upper branch the increased current near the center of the crossing region is reproduced qualitatively although, to both the left and right of this feature the fitted current suppression is too strong.

Although the fit results may not be very good quantitatively, we have nonetheless demonstrated that coherent mixing at four-level crossings can lead to a dark state evidenced by current suppression of an otherwise strong resonance. Furthermore, the coupling parameters we extract at the σ four-level crossing are comparable to those determined for other two- and three-level crossings. However, clearly the fit of the resonant current data at the σ crossing is poor, in large part due to the increased parameter space inherent to a four-level crossing. This suggests that a more sophisticated model or an improved strategy for fitting the data may be required to understand four-level crossings further (see discussion in Sec. 5.5).

5.3 Modelling Modified Confinement Potentials

In Sec. 4.5 we introduced a simple model, based on a coherent tunneling picture, which explained the general properties of measured QD single-particle energy spectra by including higher degree terms in the dot confinement potentials to account for anharmonicity and anisotropy. We now return to this model and attempt to reproduce the experimental observations at specific crossings. In this section, we present detailed calculations for a case study of two crossings in the spectrum of dot 2 from Device I, namely the η two-level crossing between the $4p^+$- and $7i^+$-like states (recall Fig. 5.17) and the γ three-level crossing between the $4p^-$-, $5d^+$- and $6h^+$-like states (recall Fig. 5.8). In particular, we select the γ crossing to see if the model can reproduce the suppression of the otherwise strong center branch resonance attributed to coherent mixing. Furthermore, although it may have been simpler to study only the γ crossing, we additionally select a second crossing as a first step towards trying to model a larger part of an entire spectrum

(for example one of the panels in Fig. 4.3).

In Sec. 4.5 we demonstrated that to induce anti-crossings between the single-particle states in the model we should add anharmonic terms ($x^p y^q$ of degree n where $n = p + q$) to an ideal two-dimensional elliptical parabolic potential, namely $V_{eff}(x,y) = \frac{1}{2}m^*\omega_y^2(\delta^2 x^2 + y^2)$. Specifically, terms of degree $m = |n_{x1} - n_{x2}| + |n_{y1} - n_{y2}|$ are required to mix two single-particle states with quantum numbers (n_{x1},n_{y1}) and (n_{x2},n_{y2}) [103]. Thus, for the η crossing, 5th degree terms are required to mix the $4p^+$- and $7i^+$-like states since $(n_x,n_y) = (1,2)$ and $(0,6)$, meaning $m = 5$. Likewise, for the γ crossing, 3rd degree terms are needed to mix $4p^-$ (2,1) with $5d^+$ (1,3), and $5d^+$ with $6h^+$ (0,5), since $m = 3$ in both cases, and 6th degree terms to mix $4p^-$ with $6h^+$, since $m = 6$.

The calculations presented in Fig. 4.6(c) took the downstream dot's potential to be $V_{eff}(x,y)/m^*\omega_y^2 = \frac{1}{2}(\delta^2 x^2 + y^2 - 0.12x^2y + 0.05xy^2 + 0.05y^3 + 0.1x^4y + 0.02x^6 + 0.02y^6$, and used parameters $\delta = 4/3$ and $\hbar\omega_y = 3.9$ meV to produce an example of a spectrum with both widespread anti-crossing behaviour and variations in the resonant currents. However, the terms in this potential were actually selected to reproduce the *B*-field dependence of *both* the energy levels and resonant currents at the η *and* γ crossings (see Fig. 5.20), i.e., the extra terms are essentially restricted to only those which could mix directly the states relevant to the η *and* γ crossings. Explicitly, the potential includes one 5th degree term of strength ~10% that mixes the $4p^+$- and $7i^+$-like states at the η crossing, and three 3rd degree terms of strength up to ~12% that mix the $4p^-$- and $5d^+$-like states and the $5d^+$- and $6h^+$-like states at the γ crossing. The weaker (~2%) 6th degree terms allow for a small coupling between the $4p^-$- and $6h^+$-like states at the γ crossing and also ensure that the potential does not become negative at larger values of x and y, which would be

unphysical. The results of the independent fit of this crossing with the matrix Hamiltonian model influenced the choice for the strengths of the higher degree terms in V_{eff}. In particular, although the matrix Hamiltonian model does not provide any information about the origin of the couplings between states, it does allow us to extract their strengths. Hence, as the mixing at the γ crossing can be well explained by two dominant and approximately equal couplings between the $4p^-$- and $5d^+$-like states and the $5d^+$- and $6h^+$-like states, and one much weaker coupling between the $4p^-$- and $6h^+$-like states, we took the 3rd degree terms to be stronger than the 6th degree terms. Nonetheless, it remains true that we did not attempt an exhaustive fit of all possible higher degree terms, i.e., the specific terms selected were chosen in an ad-hoc manner. For instance, why a fifth order term of the form x^4y, but none of the other possible fifth order terms, appears necessary to reproduce the experimental data (principally the η crossing) is not yet understood.

With the selected confinement potential, the calculations reproduce well the experimental data for the energy dispersions, Fig. 5.20(b) [Fig. 5.20(c)], and the branch currents, Fig. 5.20(d) [Fig. 5.20(e)], of the η (γ) crossing (thus taking a first step along the road towards modelling an entire measured spectrum). As seen in Fig. 5.20(b) [Fig. 5.20(c)], the selected V_{eff} gives an energy splitting of ~0.2 (~1.0) meV between the upper and lower branches of the η (γ) crossing. We emphasise that the most important feature of the experimental data for the γ crossing, the vanishing center branch current (marking dark state formation), is clearly visible in Fig. 5.20(e) when the branches are minimally separated in energy. In the model, this occurs when the downstream dot's state becomes nearly orthogonal to the upstream dot's 1s-like state.

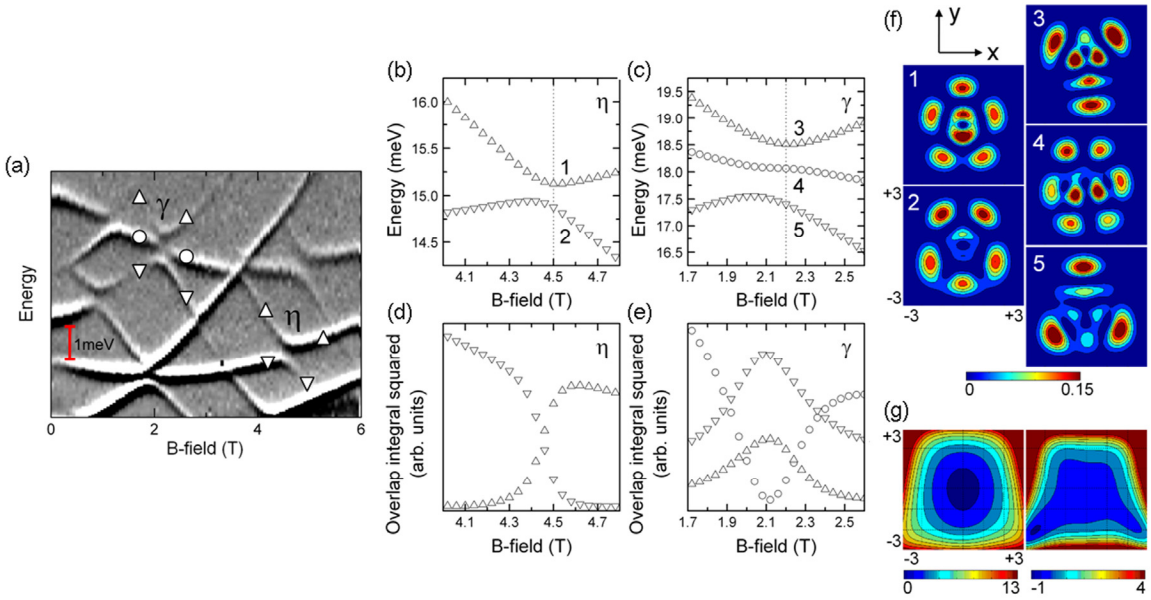

Fig. 5.20. (a) Differential conductance greyscale plot [106] showing the energy spectrum of dot 2 from Device I measured by strategy A [see also Fig. 4.3(c)]. (b), (c) [(d), (e)] Calculated energy level position (overlap integral squared) for each branch in the vicinity of the η and γ crossings using the potential given in the text. Note that the additional perturbation terms in V_{eff} themselves shift features in the spectrum to higher B-field, and thus tend to increase the effective confinement which explains why the confinement strength used in the calculations, $\hbar\omega_y$ = 3.9 meV, is slightly less than the value of 4.6 meV for the ideal elliptical parabolic spectrum [recall Fig. 4.2(b)] which reproduces well the measured spectrum (except in the vicinity of the crossings). (f) Normalized density plots in x-y plane of the downstream dot's states for the branches of the η (γ) crossing at 4.5 T (2.2 T) [marked 1 and 2 in (b) and 3, 4, and 5 in (c)]. The x and y length unit is $\ell_0 = \sqrt{\hbar / m^* \omega_y}$. Colourbar numbers should be multiplied by $1/\ell_0^2$. (g) Representation of the effective in-plane potential used in the calculation over same area as density plots (left plot) which consists of the sum of an ideal elliptical parabolic potential with a small perturbative potential (represented on its own on the right). Colourbar numbers should be multiplied by $\hbar\omega_y$.

Figure 5.20(f) displays selected density plots calculated for the two states of the η crossing at 4.5 T [positions labelled 1 and 2 in Fig. 5.20(b)] and for the three states of the

γ crossing at 2.2 T [positions labelled 3, 4 and 5 in Fig. 5.20(c)]. These plots clearly reveal geometric asymmetry consistent with the inclusion of higher degree terms in V_{eff}. Figure 5.20(g) also gives pictorial representations of the effective potential. Interestingly, we can see that the effective potential is still approximately elliptical near the dot center, but the deviations become more apparent on moving radially outwards from the center (left plot). By excluding the quadratic terms from the potential it is easier to see the presence of the other terms (right plot).

To summarize this section, we have presented a numerical study of a symmetry breaking potential that can explain mixing, and, for instance, reproduce dark state formation, at specific anti-crossings in a measured QD single-particle energy spectrum. Inclusion of higher degree terms in dot confining potentials appears essential to understand realistic QDs. Although the approach has explained well the mixing observed at two specific crossings with higher degree terms appropriate *just* for these crossings, we have not attempted an exhaustive fit. It would also be interesting, but challenging, to see if one effective potential could be found which explains the mixing over a larger part of a measured spectrum containing many anti-crossing regions (like the spectra in Fig. 4.3). However, while the general characteristics of a measured spectrum, namely widespread anti-crossings and current mixing behaviour can easily be reproduced [recall Fig. 4.6(c)], modelling the specific behaviour of an entire spectrum would likely be quite challenging due to the rapid increase in the number of higher degree terms needed to model multiple level crossings simultaneously. Nonetheless, the energy dispersion at the crossings and especially the overlap integrals are evidently very sensitive to the exact shape of the confining potential, and thus the measurement principle can provide very detailed

information about realistic dots. Finally, we note that there may be other schemes or strategies for including symmetry breaking which work equally well. For example, one could simulate the presence of impurities in the contacts by including randomly positioned delta function potentials in the dot confinement potential [113].

5.4 Modifying Level Mixing in a Device with Four Gates

In the work described so far, it has not been possible to alter the effective QD confinement potentials in-situ and so the mixing could not be changed, i.e., the *C*-parameters were fixed. In this section, we now demonstrate how, by using a vertical double QD device in which the side gate is split into four separate gates [30], we are able to perturb the effective QD confinement potentials and hence influence the level mixing to some degree. After introducing the device concept, we will focus on one particular three-level crossing, and describe how the energy dispersion with B-field and the resonant currents are altered when different combinations of voltages are applied to the four gates.

5.4.1 Device Structure and Gate Operation Principle

Figure 5.21(a) shows a SEM image of a four-gated double QD device similar to the one measured. This device, which was fabricated and measured at ICORP by S. Amaha, is essentially very similar to Device VI except it has four thin line mesas radiating out from the center mesa rather than one (note also that the starting material is the same as for Devices I-VI). These line mesas now pattern the gate metal into four parts [30]. The single-particle energy spectra of the constituent dots can be captured using the

measurement principle described in Sec. 2.2.3 (see also Sec. 4.3.1 and Ref. [70]) in a similar manner as for the single-gated devices. However, the additional capability is that now the lateral confinement can be changed by applying different combinations of voltages to the four side gates around the mesa.

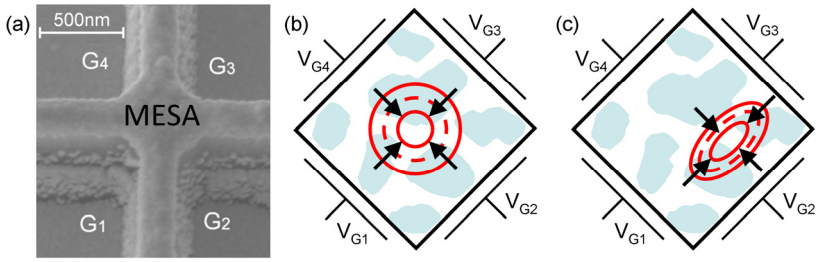

Fig. 5.21. (a) SEM image of a four-gated device mesa with the gates identified as $G_{1\text{-}4}$. (b) Plan view cartoon showing an approximately circular QD (realized by applying equal voltages to all four gates) and how it can be 'squeezed' (in the direction of the arrows) by changing the gate voltages. (c) Cartoon illustrating how application of different voltages to the four gates can change the shape and position of the QD. The way the QD is 'squeezed' is also different from that in (b). Faint blue irregular shapes in (b) and (c) represent the anharmonicity and anisotropy present in the device which influence the effective lateral confinement potential. Although the device consists of two vertically coupled QDs, for clarity, only the top-most QD is illustrated in each of the cartoons.

In order to understand the influence of the four gates on the QDs, consider the cartoons in Figs. 5.21(b) and (c). For simplicity, we will assume that all four gates are identical and that the action of each gate on the QDs is the same. Additionally, we will initially assume the QD confinement potentials to be ideal. In Fig. 5.21(b), first imagine that all four gates are set to the same voltage ($V_{G1} = V_{G2} = V_{G3} = V_{G4}$), giving approximately circular QDs whose centers are at the center of the mesa. Then, as $V_{G1\text{-}4}$ are all simultaneously made more negative the QDs are 'squeezed' as shown. Next, in Fig. 5.21(c), suppose that the various gate voltages are initially set differently (for example, in

the figure $V_{G1} \approx V_{G4} < V_{G2} \approx V_{G3}$). This can influence the QD confinement potentials in two ways. Firstly, the center of the QD confinement potentials is shifted away from the center of the mesa. Secondly, the shape of the QD confinement potentials can be changed to be approximately elliptical. After $V_{G1\text{-}4}$ are initially set, they can also be all swept simultaneously to more negative voltages, which squeezes the QDs as shown.

Crucially, the preceding discussion neglects the influence of anharmonicity and anisotropy, due to local imperfections and randomness in the structure, on the dot confinement potentials. These perturbations, which are represented by the blue irregular shapes in Figs. 5.21(b) and (c), induce pronounced energy level mixing in the single-particle spectra of the QDs. Although the presence of these perturbations makes it hard to realize QD potentials which are nearly ideally circular or elliptical and parabolic, we can still expect that by altering how $V_{G1\text{-}4}$ are initially applied and subsequently swept, the electrons traversing the QDs will see different effective confinement potential *landscapes* which can influence the coherent level mixing that occurs in the vicinity of the crossing points in the spectra, i.e., the coupling (*C*-) and current amplitude (*s*-) parameters are now dependant to some degree on the choice of $V_{G1\text{-}4}$.

5.4.2 Energy Level Mixing in a Four-Gated Device

The single-particle energy spectrum of one of the constituent QDs in the four-gated device, measured using strategy A (recall Sec. 4.3) and with equal voltages on all four gates, is shown in Fig. 5.22(a). One can regard this spectrum as a close approximation to the spectrum which would have been measured had the device only a single gate surrounding the mesa. The general properties of the measured spectrum are

quite similar to those measured for dots in single-gated devices (recall Fig. 4.3). Explicitly, the measured spectrum can be well reproduced overall by an energy spectrum for ideal elliptical and parabolic confinement [see 5.22(b)] except in the vicinity of the level crossings where pronounced anti-crossing behaviour is again prevalent.

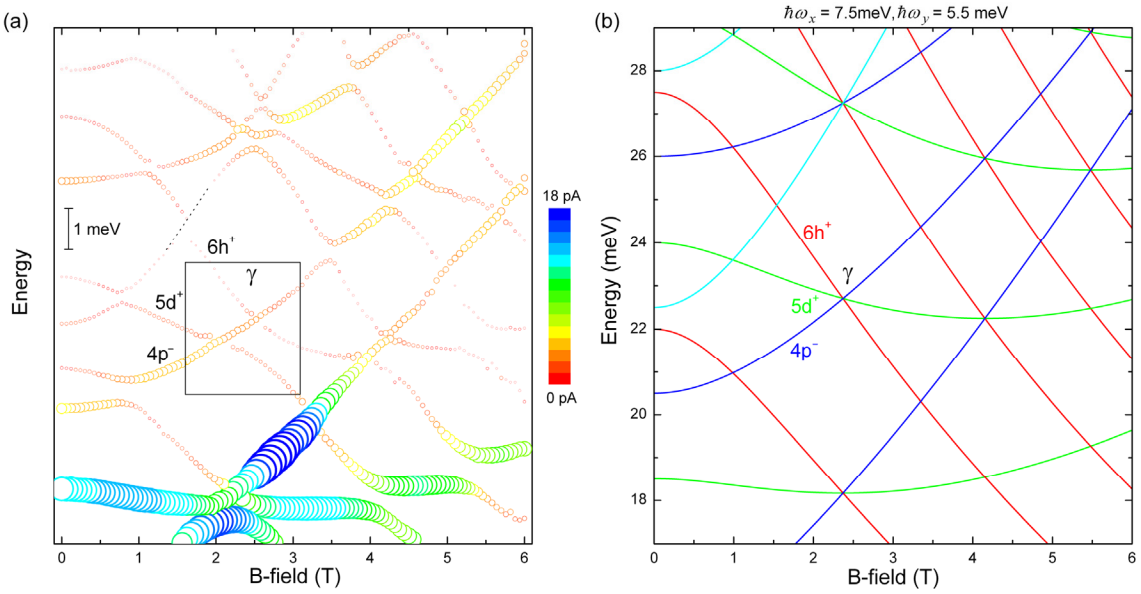

Fig. 5.22. (a) Single-particle energy spectrum of one dot from the four-gated device captured at ~1.6 K with the gate voltages scanned such that $V_{G1} = V_{G2} = V_{G3} = V_{G4}$. The ~pA resonant current (non-resonant background current not removed) is indicated by the colour scale and the size of the symbols. A dotted black line identifies one barely resolvable portion of a weak spectral feature. States relevant to the γ crossing are labelled using the atomic orbital-like notation. (b) Ideal elliptical parabolic spectrum with confinement energies $\hbar\omega_x$ = 7.5 meV and $\hbar\omega_y$ = 5.5 meV, i.e., ellipticity δ = 1.4, which reproduces the measured spectrum in (a) well overall.

Focusing now on the γ three-level crossing between the $4p^-$-, $5d^+$- and $6h^+$-like states, Figs. 5.23(a) and (b) show the energy dispersion of this crossing region for two different QD potential *landscapes* referred to as I and II. Before discussing the data further, we note that, for the first time in this thesis, we are examining in detail crossings

which are more challenging to characterize because the resonance branches are not clearly distinct, i.e., within the resolution limit of the measurement (~50 μeV) there appear to be exact crossings in both Figs. 5.23(a) and (b). As a consequence, we can no longer simply refer to the branches as upper, center and lower. Instead, we use coloured squares to identify the three branches by eye in the manner shown in Figs. 5.23(a) and (b).

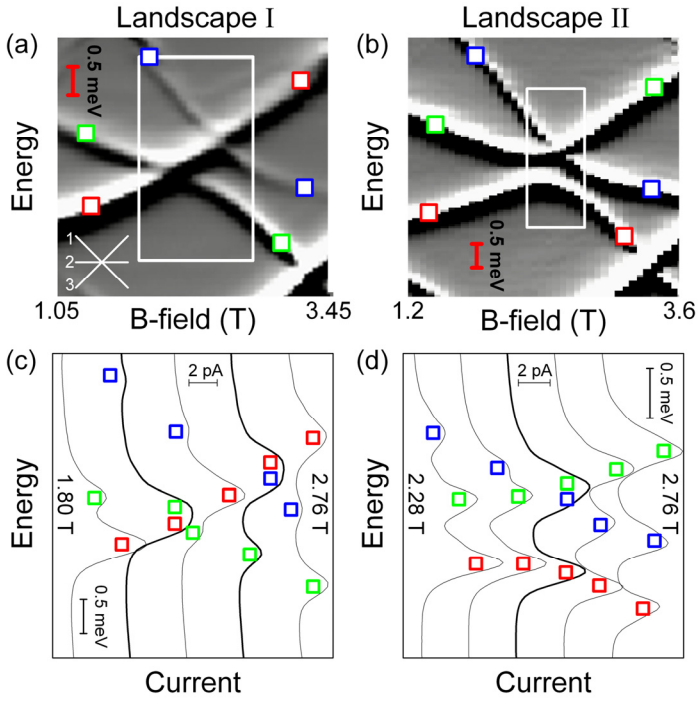

Fig. 5.23. (a) [(b)] Measured energy level (differential conductance resonance [106]) position of the γ crossing for potential *landscape* I (II). Both *landscapes* differ from the one sampled to capture the spectrum in Fig. 5.22(a). Explicitly, for *landscape* I the gate voltages are scanned such that $V_{G1} = V_{G2}$ = -34 mV (-119 mV) and $V_{G3} = V_{G4}$ = -62 mV (-105 mV) at the lowest (highest) energy in panel (a), while for *landscape* II $V_{G1} = V_{G2}$ = 86 mV (45 mV) and $V_{G3} = V_{G4}$ = -134 mV (-176 mV) at the lowest (highest) energy in panel (b). (c) [(d)] Selected current traces (non-resonant background current not subtracted) which when numerically differentiated form vertical sections of the region indicated by the white box in (a) [(b)] Traces are horizontally offset by 4 pA (2.5 pA) in (c) [(d)].

Now that the way we choose to identify the resonance branches has been made clear, we can discuss the properties of the crossing shown in Fig. 5.23. For *landscape* I, we observe a clear anti-crossing between the branches labelled by the blue and green squares, while the third branch, identified by the red squares, appears to cross exactly with the other two. Meanwhile, for *landscape* II, we see quite different behaviour. In particular, a distinct lower branch resonance is now visible, labelled by the red squares, while the other two branches, identified by blue and green squares, appear to cross exactly. Recalling the predicted forms of the basic three-level crossing shapes shown in Figs. 5.3(b) and (d), the crossings in Figs. 5.23(a) and (b) appear to be 1- and 3-dominant coupling-type crossings respectively.

We now test this expectation. Following the same procedure as in Sec. 5.1, we need to extract the energy level positions and resonant currents before attempting a fit using the simple coherent level mixing model to determine the *C*- and *s*-parameters. However, reliably extracting the energy level positions and the resonant currents in the vicinity of what appear to be exact crossings between two resonance branches now becomes quite challenging. In such situations, we are attempting to fit two unconstrained Lorentzians to what essentially appears to be a single current peak [see for example the bold traces in Figs. 5.23(c) and (d)]. This causes an even greater problem when the 'single peak' has a similar width to the two well separated peaks [like the bold for the bold trace in Fig. 5.23(d)]. As we shall see, such difficulties make it much harder to characterize a crossing and ultimately can lead to a poor result when fitting the data to the simple coherent level mixing model.

Figures 5.24(a) and (b) show the extracted energy level positions for the data

shown in Figs. 5.23(a) and (b), while the extracted resonant currents are shown in Figures 5.24(c) and (d). Despite the presence of what appear to be exact crossings in the data, the fits of the data reveal small (~0.2 meV) anti-crossings [see Figs. 5.24(a) and (b)]. Thus, we revert to the notion of distinct upper, center and lower resonance branches and use an up-pointing triangle, a circle and a down-pointing triangle to identify them as for all previous three-level crossings analyzed.

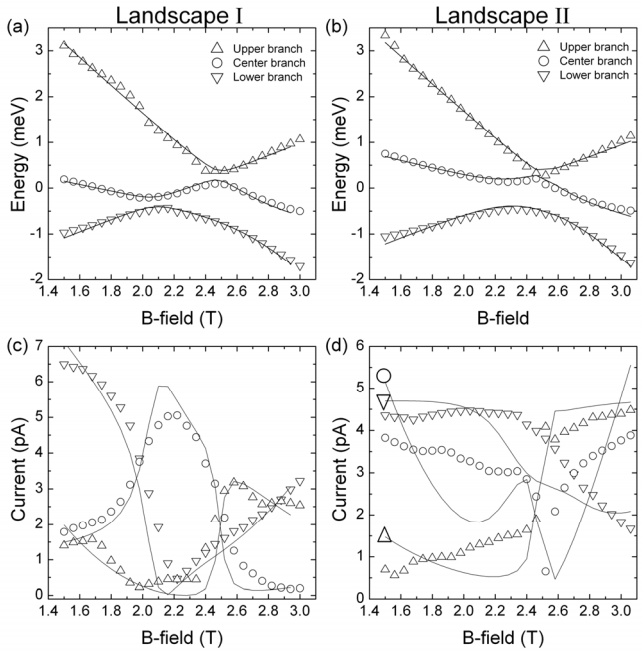

Fig. 5.24. (a) and (b) [(c) and (d)] Extracted energy level positions (resonant currents) for potential *landscapes* I and II respectively. Lines show the result of fitting the data to the model. In (d), where the fit is poor, symbols at the left edge of the panel identify which fit line corresponds to which branch. For *landscape* I (II), the fitted *current amplitude* parameters are, in $pA^{1/2}$, s_1 = 1.34, s_2 = 1.24 and s_3 = 2.70 at 1.5 T and s_1 = -1.45, s_2 = 1.23 and s_3 = 1.39 at 3.0 T (s_1 = 1.31, s_2 = 1.82 and s_3 = -2.51 at 1.5 T and s_1 = -0.58, s_2 = -2.34 and s_3 = -2.54 at 3.06 T), with the values in between linearly interpolated.

Having extracted the necessary information from the current traces, we now attempt to fit the energy dispersions and resonant currents to the simple coherent level

mixing model. Note that for these two data sets the energy dispersions were fitted first to determine the *C*-parameters which were then kept fixed while the currents were fitted to determine the *s*-parameters. This is in contrast to some of the other crossings studied (notably the easy-to-characterize ones) where the fitting was performed simultaneously. Furthermore, when fitting the data to the simple coherent level mixing model, we still refer to the three basis states as 1, 2 and 3 in the sense as before [see inset to Fig. 5.23(a)].

In the case of the energy level positions, the fitting procedure has done a reasonable job for the data from both *landscape* I [see Fig. 5.24(a)] and *landscape* II [see Fig. 5.24(b)]. For *landscape* I, the fitted coupling energy parameters are, in meV, C_{12} = 0.21, C_{13} = -0.08 and C_{23} = 0.03, revealing that the anti-crossing behaviour at this crossing is indeed determined by one dominant coupling as suspected, i.e., in terms of magnitude $C_{12} \gg C_{13} \approx C_{23}$. Meanwhile, for *landscape* II the fitted coupling energy parameters are, in meV, C_{12} = -0.12, C_{13} = -0.09 and C_{23} = -0.10, revealing that the energy dispersion is a consequence of three dominant couplings, i.e., in terms of magnitude $C_{12} \approx C_{13} \approx C_{23}$. As a result of the gate controlled change in landscape, the fitting of these two data sets has revealed that in terms of magnitude, C_{12} and C_{23} have been changed by ~0.1 meV while C_{13} has remained approximately constant. That the couplings can be influenced by applying different combinations of voltages to the four gates in order to probe different potential landscapes provides additional experimental evidence that the mixing is attributable to anharmonicity and anisotropy in the dot confinement potentials. Although not discussed in this thesis, we have also observed similar variations in the *C*-parameters at a four-level crossing.

In terms of the resonant currents, the results of the fit to the model are quite good

for the data from *landscape* I [see Fig. 5.24(c)]. However, for the data from *landscape* II [see Fig. 5.24(d)] the fit is certainly not very good quantitatively, though it is perhaps qualitatively reasonable in places (see for example the fitted currents for the upper and lower branches). Ultimately, the reason why the fit of the currents for *landscape* II is poor is that it can be challenging to reliably extract the energy level positions and resonant currents at what appears to be an exact crossing [recall Fig. 5.23(b)]. Taking the currents extracted near this apparent exact crossing at face value, they change quite abruptly in the space of one or two data points [see the upper and center branch currents in Fig. 5.24(d)]. The simple coherent level mixing model may struggle to handle such abrupt changes. Potentially, this problem could be overcome by increasing the B-field resolution of the measurement (assuming the currents can be reliably extracted).

In summary, we have demonstrated, using a vertical double QD device with four side gates, that we can alter the strength of the coupling parameters at level crossings by at least ~0.1 meV. However, the *C*-parameters still arise essentially randomly due to anharmonicity and anisotropy in the confinement potential and we do not have the ability to fine tune them independently or arbitrarily. Fine control of the couplings is required to implement advanced quantum information protocols involving three levels such as the one proposed one Ref. [54]. Furthermore, the couplings would need to be modulated in time which is beyond the current technology. Additionally, we have also encountered, for the first time, level crossings where it is difficult to extract the energy level positions and resonant currents. Consequently, fitting the data with the simple coherent level mixing model can become challenging, in particular making it difficult to extract meaningful *s*-parameters.

5.5 Summary and Concluding Comments

In this chapter we have investigated coherent level mixing observed in the vicinity of single-particle energy level crossings between two, three or four levels. Of particular interest at such level crossings is the observed suppression of an otherwise strong resonance, a hallmark of destructive interference leading to dark state formation. In order to explore the underlying physics, we developed a simple coherent level mixing model. This model explained how the three-level mixing we observe can be viewed as an all-electrical analogue of coherent population trapping, as well as how both familiar and ideal behaviour can arise at two-level crossings. We also demonstrated that the observed level mixing at specific crossings can be reproduced by including appropriate higher order terms in the dot confinement potentials as perturbations. Furthermore, we described how the coupling parameters can be altered using a four-gated device.

While the simple coherent level mixing model was applied successfully to understand several level crossings, some limitations were also apparent. In particular, we struggled to fit the data for a four-level crossing due to the increased parameter space. We also found that the model works best at easy-to-characterize crossings where the resonances are distinct so allowing the energy level positions and resonant currents to be easily extracted by fitting the resonant peaks to unconstrained Lorentzians.

To address these difficulties, a more detailed procedure will ultimately be required to extract information from numerous challenging-to-characterize crossings which are of potential interest. With this in mind, we have begun to study other spectral properties which may provide valuable information. Two examples of such properties are the resonant peak widths and the sum of the branch currents throughout a crossing region.

Figure 5.25 shows these quantities extracted for the easy-to-characterize κ, γ and σ crossings which served as motivation at the start of this chapter (recall Fig. 5.1). Initial investigations indicate that these quantities appear to be approximately conserved throughout crossing regions. This may provide a means to constrain the Lorentzian fits and successfully extract the energy level positions and resonant currents at the challenging-to-characterize crossings.

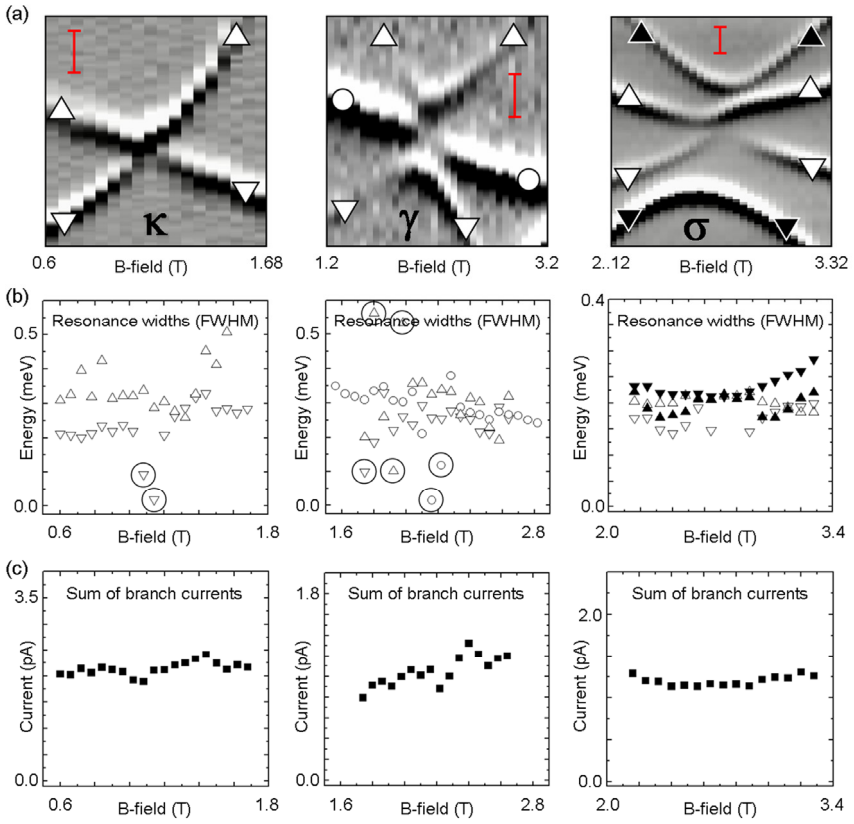

Fig. 5.25. (a) Energy dispersion, (b) resonance widths [explicitly the full-width-at-half-maximum (FWHM) extracted by Lorentzian fitting] and (c) sum of branch currents for the κ, γ and σ crossings measured in dot 1 from Device I, dot 2 from Device I and dot 2 from Device VI respectively. Scale bars in (a) all correspond to 0.5 meV. In (b) several outlying points are circled for emphasis. These points correspond to places where the related feature in (a) is very weak.

Chapter 6

Electron Spin-Nuclear Spin (Hyperfine) Interaction in Quantum Dots

Early research on transport through QDs paid little attention to how the confined electrons could be influenced by coupling to atomic nuclei. It is only relatively recently, beginning with the pioneering work on coupled vertical QDs of Ref. [33] that clear evidence of electron spin-nuclear spin (hyperfine) interaction was found in transport measurements (see Sec. 6.1). After this initial discovery, much new experimental and theoretical work has focused on this area. There has also been parallel work exploring the influence of the hyperfine interaction on the optical properties of QDs (for illustrative examples see work on interface fluctuation QDs [114] and self-assembled QDs [115]).

One of the main reasons for the interest in the role of the hyperfine interaction in QD transport is that if one strives to use the spin of an electron trapped in a III-V semiconductor QD as a qubit (recall Sec. 1.3 and see Ref. [41]), hyperfine coupling to the nuclear spins in the host material is now recognized as a major cause of electron spin qubit decoherence (see review articles in Refs. [8,116]). Therefore, despite a number of proposals to exploit nuclear spin by using it for quantum memory (see for example Ref. [117]), and efforts to perform arbitrary spin rotations using hyperfine-mediated electron dipole spin resonance [67], much work is still focused on attempts to characterise the hyperfine interaction and understand it in detail at a fundamental level.

One goal of work in this area is to mitigate the effects of the nuclei on the electrons in order to extend the electron spin coherence time. In order to do this, several techniques have been proposed (see for example Refs. [118,119]) and even implemented

(see for example Refs. [43,120-122]). Additionally, several groups are now working with materials where nuclear spin plays less of a role (see for example recent work on carbon nanotube QDs [69] and SiGe QDs [123]).

The experimental work described in this chapter will attempt to shed further light on the specifics of the hyperfine interaction in QD transport. Section 6.1 will serve as an introduction, focusing on experiments performed in vertical QDs, in preparation for the work to follow. As a starting point, in Sec. 6.1.1 we will outline the measurements of Ref. [33] where effects such as B-field induced switching and hysteresis, as well as oscillations on a timescale of tens of seconds, were observed in the leakage current in the two-electron ($N = 2$) spin blockade regime (recall Secs. 2.2.4 and 2.2.5). Such features are now recognized as hallmarks of the hyperfine interaction (see also Refs. [26,64,65,69,124]). Subsequently, in Sec. 6.1.2, we will introduce a toy model which explains how the hyperfine interaction can lift the spin blockade for a two-electron double QD system. Furthermore, in Sec. 6.1.3, we will discuss the work of Refs. [66,84] which describes how to dynamically polarize the nuclei by manipulating the two-electron spin states using a bias voltage pulsing procedure with coupled vertical QDs. The experiments in Refs. [33,66,84] provide the principle motivation for some of the experimental work described in subsequent sections.

The rest of this chapter will focus on experimental work on two main topics:

i. In Sec. 6.2, we will focus on measurements which can provide additional information about the hyperfine interaction *inside* the familiar $N = 2$ spin blockade regime. In particular, we will uncover a previously unreported intricate V_G dependence of hysteretic features in the leakage current over a wide (0 to 2.75 T) B-field range in one device.

Subsequently, we will reveal strong device-to-device variations in how the hyperfine interaction manifests itself by studying another device at low B-field (< |45| mT) where we observe a funnel-like structure which bears some similarity to those recently reported in other weakly coupled QD systems [26,43,64,67-69]. Furthermore, by adapting the technique of Ref. [66], we employ multiple-sweep mHz bias voltage pulsing procedures to program the leakage current response via the hyperfine interaction [see Fig. 6.1(a)].

ii. In Sec. 6.3, we will address the question of whether or not nuclear spin related effects can occur *outside* the familiar $N = 2$ spin blockade region. As a starting point, we focus on a large portion of the V_{SD}-V_G plane, *at high bias*, well outside the spin blockade region, where we unexpectedly observe B-field induced current switching and hysteresis [see Fig. 6.1(b)]. In this region few-electron tunneling processes occur, so it is challenging to identify the electronic states involved. Subsequently, we will describe a funnel-like structure [see Fig. 6.1(c)], also observed at high bias, but in a regime close to pinch-off where we can identify the electronic states involved allowing us to propose a mechanism for this funnel which involves the hyperfine interaction.

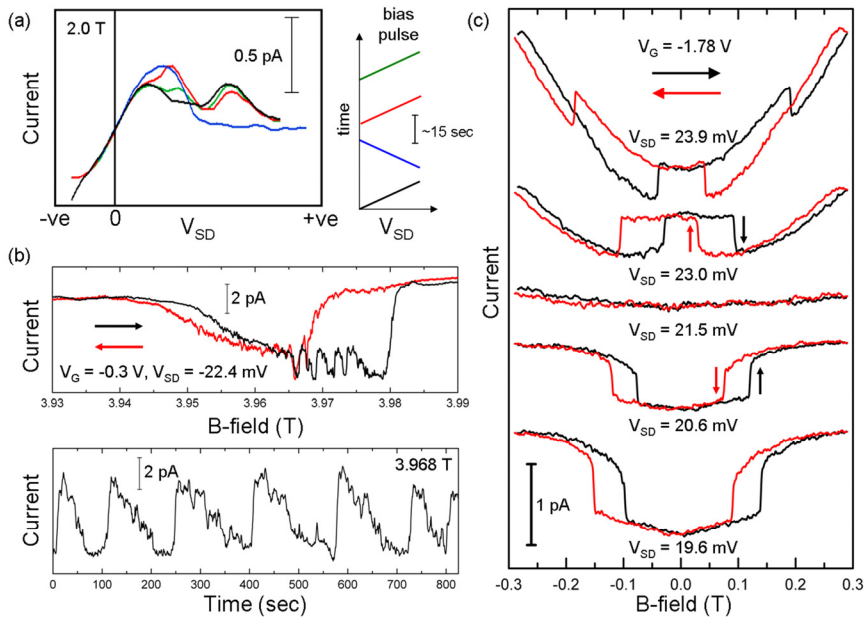

Fig. 6.1. (a) Current response in the vicinity of the $N = 2$ spin blockade region to a mHz V_{SD} pulse. (b) Hysteretic feature observed at high bias as the B-field is swept-up (black) and swept-down (red) exhibiting strong current fluctuations (top panel) and quasi-periodic current oscillations in time at fixed B-field (bottom panel). (c) Hysteretic funnel-like structure observed at high bias as the B-field is swept-up (black) and swept-down (red) displaying intriguing inversion of hysteresis as V_{SD} is changed.

6.1 Introduction to Hyperfine Interaction Effects in Vertical Quantum Dots

In this section we describe two key experiments performed in the familiar $N = 2$ spin blockade region which serve to introduce the hallmarks of the hyperfine interaction. These experiments demonstrate that there are two simple approaches for probing the hyperfine interaction, namely sweeping the B-field at fixed V_{SD} and sweeping V_{SD} at fixed B-field. We will also introduce a toy model which provides a starting point to understand how the hyperfine interaction can play a role in the $N = 2$ spin blockade region.

6.1.1. Hyperfine Interaction in the Two-Electron Spin Blockade Region

In Chap. 2 we described the original spin blockade measurements [32], and emphasized that the current suppression is nonetheless *not* complete. The ~2 pA leakage current was originally attributed to either co-tunneling processes or the spin-orbit interaction, however, as we now discuss, the hyperfine interaction can also play a role.

The pioneering experiments of Ono and Tarucha [33] focus on the leakage current in the $N = 2$ spin blockade region in a weakly coupled vertical double QD. Figure 6.2(a) shows an example of the measured leakage current as the in-dot-plane B-field is swept-up and swept-down. Considering the up-sweep, the current is initially nearly constant however, a sharp step-like increase of ~0.3 pA is observed at ~0.5 T and then the current stays 'high' until a sharp decrease back to the original level at ~0.8 T. Furthermore, in the range of ~0.5 T to ~0.8 T fluctuations in the current are observed, which appear to get stronger towards the high side of this range. The down-sweep shows similar characteristics but shifted to lower B-field, i.e., a sharp step-like increase at ~0.75 T and a sharp decrease at ~0.35 T. Intriguingly, fixing the B-field at points inside the hysteretic feature reveals the current fluctuations to be slow periodic oscillations in time [see Fig. 6.2(b)]. Furthermore, both the oscillation amplitude and the period increase systematically as the B-field is stepped-up.

In Ref. [33], nuclear magnetic resonance (NMR) measurements were also performed by placing a small coil above the device in order to generate a small oscillating B-field perpendicular to the static B-field. Figure 6.2(c) shows how the period of the oscillations is influenced by the application of the oscillating B-field. Notably, the

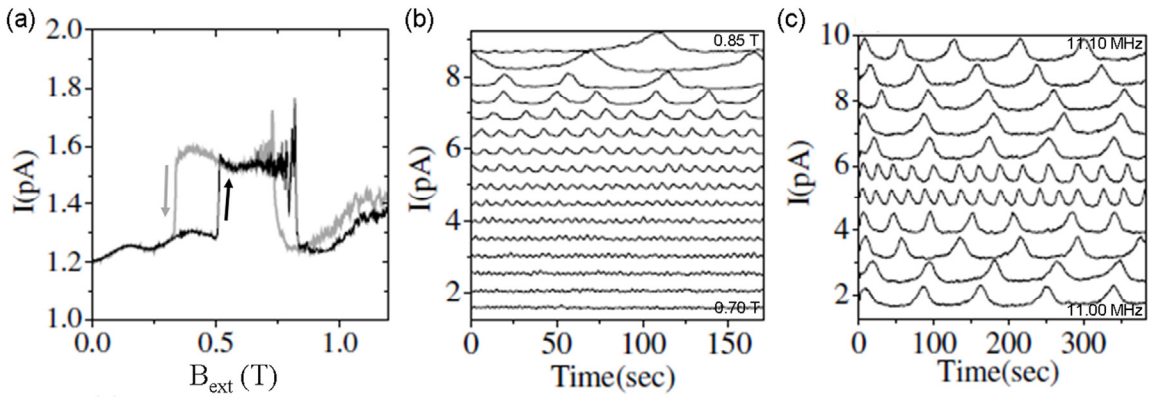

Fig. 6.2. (a) Leakage current measured at fixed V_G and V_{SD} in the $N = 2$ spin blockade region as a function of B-field swept-up (black) and swept-down (grey) at sweep rate of 0.5 T/min. An in-dot-plane B-field is applied meaning the orbital response of the single-particle states is suppressed and only the Zeeman effect can play a role. (b) Time evolution of the leakage current measured for B = 0.70 T to B = 0.85 T (steps of 0.01 T). (c) Time evolution of the leakage current measured with a small oscillating B-field applied perpendicular to the static B-field (fixed at 0.85 T). Frequency of the oscillating B-field is changed from 11.00 MHz to 11.10 MHz (0.01 MHz step). Traces are vertically offset by 0.5 (0.75) pA in (b) [(c)] (figure adapted from Ref. [33]).

oscillation period is markedly reduced when the frequency of the oscillating B-field corresponds to the ^{71}Ga nuclear spin resonance (Ref. [33] also demonstrated that the resonance frequency depended linearly on the static B-field, a key signature of NMR). This provided the primary evidence that nuclei are ultimately responsible for the observed current features.

6.1.2 Hyperfine Interaction Toy Model

We now discuss a toy model developed after the pioneering work of Ref. [33] in order to understand, in simple terms, the influence of the hyperfine interaction in the $N =$

2 spin blockade region (for additional details about the hyperfine interaction in nanostructures see Ref. [116] as well as Ref. [8]).

In an atom, the hyperfine interaction between a single electron spin $\vec{S}$ and a nucleus of spin $\vec{I}$ is described by a Hamiltonian which has the form $H_{HF} = A\vec{I}\cdot\vec{S}$, where A characterizes the coupling strength. However, an electron trapped on a QD interacts with many nuclear spins. Assuming that the host material has an s-type conduction band, the Fermi contact Hamiltonian describes the interaction between an electron with spin $\vec{S}$ and N nuclei each with spin $\vec{I_i}$, where i indexes the nuclear spin position. This Hamiltonian has the form $H = \sum_i H_{HF}^i$ and can be written out explicitly as in Eq. 6.1,

$$H = \sum_i A_i \vec{I_i}\cdot\vec{S} = \sum_i A_i\left(I_z^i S_z + \frac{I_+^i S_- + I_-^i S_+}{2}\right) \qquad (6.1),$$

where A_i is the hyperfine coupling strength which varies for each nucleus and $S_\pm$ ($I_\pm$) are the electron (nuclear) spin raising and lowering operators.

The Hamiltonian given in Eq. 6.1 contains two parts. The first is known as the Overhauser term [125], while the second is known as the flip-flop term. The Overhauser term results in the electron experiencing an effective nuclear B-field, B_n, given by $\vec{B_n} \sim \frac{1}{g\mu_B}\sum_i A_i\vec{I_i}$, where g is the electron g-factor. In GaAs, considering the relative abundance of the isotopes ^{69}Ga, ^{71}Ga and ^{75}As, the appropriately weighted average value of the hyperfine coupling constant is ~90 μeV [126]. Hence, for fully polarized nuclear spins $B_{n,max}$ is ~5 T. For unpolarized nuclei, temporal fluctuations of the nuclear spins give rise to a randomly orientated effective B-field of root-mean-square magnitude

$B_{n,\max}/\sqrt{N}$ [127]. This corresponds to B_n ~5 mT in a typical GaAs QD where $N \approx 10^6$. Meanwhile, the flip-flop term in Eq. 6.1 allows for the possibility of the electron and a nucleus to exchange their spin. However, for a single electron spin trapped in a single QD, such a mechanism is suppressed at finite B-field due to the fact that the electron Zeeman energy is roughly one thousand times larger than the nuclear Zeeman energy, i.e., there is a large energy mismatch.

Although, electron spin-nuclear spin flip-flops are suppressed at finite B-field for one electron, for two electrons in a double dot, this need not be the case as the energy mismatch limitation can be overcome. We now explain how the hyperfine interaction can potentially lift the $N = 2$ spin blockade resulting in an increased leakage current. Recall from Sec. 2.2.4, that spin blockade occurs in a double QD when the T(1,1) state becomes occupied and transport can not proceed because the $T^*(0,2)$ state is energetically inaccessible. In order to lift the spin blockade, a mechanism is required which allows the blockaded T(1,1) state to transition to another (current carrying) state. There are several possible mechanisms, including co-tunneling, spin-orbit coupling and hyperfine coupling, which could accomplish this. Although all three of these mechanisms may contribute to the leakage current in the spin blockade region, only the hyperfine interaction involves the nuclei and only the hyperfine interaction can explain the observed hysteresis as well as the abrupt increase in leakage current.

We now return to the two-electron description of spin blockade introduced in Sec. 2.2.5 in order to see how the hyperfine interaction can lift the spin blockade. Specifically, we extend Fig. 2.16(b) and show a schematic energy diagram for the relevant two-electron singlet and triplet states as a function of detuning which includes a small external

in-dot-plane B-field [see Fig. 6.3(a)]. Recall that, for an appropriate offset at zero bias, spin blockade can be observed over a range of positive detuning values [corresponding to the pink region in Fig. 6.3(a)].

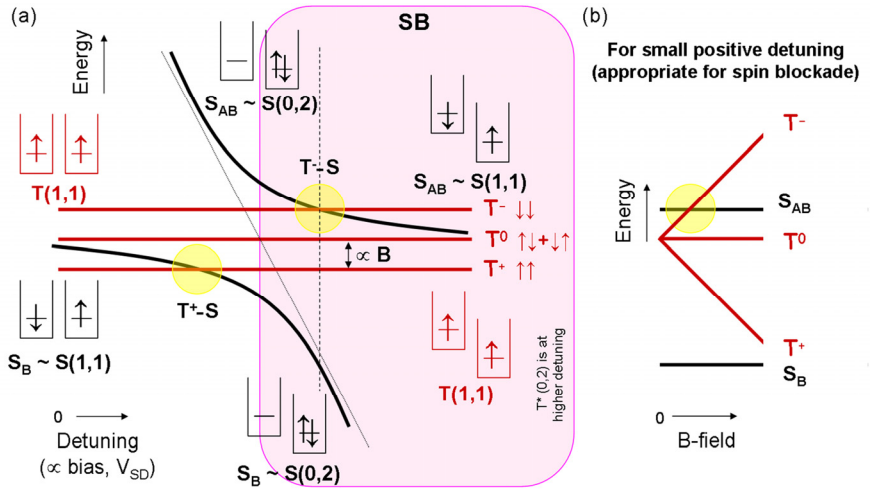

Fig. 6.3. Schematic energy diagrams for the two-electron singlet and triplet states. In (a) the S(0,2) and S(1,1) states anti-cross because of a small tunnel coupling resulting in bonding (S_B) and anti-bonding (S_{AB}) singlet branches. When the single-particle ground states of the two dots are energetically aligned (zero detuning), S_B ~ S(1,1) and S_{AB} ~ S(0,2), while for large detuning S_B ~ S(0,2) and S_{AB} ~ S(1,1). The dotted line in (a) indicates the detuning condition appropriate for (b). The diagrams are drawn in the absence of the hyperfine interaction. Note that in (a) the higher energy $T^*(0,2)$ state has been omitted for compactness. In both (a) and (b) an in-dot-plane B-field is considered, meaning orbital effects can be neglected, while the three triplet states are split by the Zeeman energy.

As a result of the finite external B-field, the T^- and T^+ states are split off from the T^0 state by the Zeeman energy $\pm g\mu_B B_{ext}$. Consequently, there is a point where the T^- (T^+) state is degenerate with S_{AB} (S_B). At these singlet-triplet crossing points [circled in yellow in Fig. 6.3(a) and labelled T^--S and T^+-S respectively] the states can be mixed by the hyperfine interaction [resulting in a small anti-crossing not shown in Fig. 6.3(a)], and

an electron spin-nuclear spin flip-flop can occur, i.e., $\downarrow\Uparrow\rightarrow\uparrow\Downarrow$ or $\uparrow\Downarrow\rightarrow\downarrow\Uparrow$, where $\uparrow$ and $\downarrow$ ($\Uparrow$ and $\Downarrow$) represent up and down electron (nuclear) spins. Crucially, if a T(1,1) state is occupied and transport can not proceed due to spin blockade, then for appropriate detuning and B-field conditions the blockade can be lifted by a flip-flop process. Explicitly, transport can then proceed through the (0,1) → T(1,1) → S(1,1) → S(0,2) → (0,1) cycle where the transition T(1,1) → S(1,1) transition is accompanied by a flip-flop process.

We now describe a notable additional consequence of lifting the spin blockade via the hyperfine interaction, namely the possibility of dynamical nuclear polarization (DNP). To understand how DNP can occur, suppose that the spin blockade has been lifted due to a flip-flop at the T^--S crossing point [we assume, as for the situation depicted in Fig. 6.3(a), that the T^+-S crossing point occurs at lower detuning, outside the spin blockade region, and so is not relevant]. After the flip-flop transport proceeds and the system returns to a (0,1) state. At this point, a new electron can enter a (1,1) state and if it populates the triplet state, once again transport will be blocked by spin blockade, requiring another electron spin-nuclear spin flip-flop in order to proceed. If electrons flow continuously in this manner, successive nuclear spins can be flipped from up spin to down spin, i.e., the nuclear spins can be pumped. This accumulation of polarized nuclei results in a finite (non-equilibrium) effective Overhauser field, B_n, which contributes to the total effective B-field, $B_{Tot} = B_{ext} + B_n$, consequently increasing the splitting of the triplet states (which is now equal to $\pm g\mu_B B_{Tot}$). We note that for appropriate external B-field and detuning conditions, it may equally be possible to pump the nuclear spins at the T^+-S crossing point. The pumping which occurs at the T^--S (T^+-S) crossing point results

in B_n which 'adds to' ('opposes') the applied B-field as a consequence of the signs of the electronic g-factor and the value of the hyperfine coupling constant in GaAs [8].

This simple picture of consecutive spin flips leading to a build-up of nuclear polarization makes several assumptions. In particular, it essentially assumes that the external B-field and detuning conditions are such that only flip-flops at one of the singlet-triplet crossing points (T^--S) are relevant in the spin blockade regime when a finite B-field is applied. This appears reasonable considering the position of the crossing points in Fig. 6.3(a), however these points move as a consequence of DNP [66]. Furthermore, the polarization process is known not to lead to 100% polarization (as we shall see in Sec. 6.1.3). In addition to potential competition between opposing spin flip processes at the two crossing points, the model also neglects the loss of the built-up nuclear polarization due to both diffusion and intrinsic decay of the polarized nuclear spins, i.e., spin-lattice relaxation of the nuclear spins (T_1 processes).

Nonetheless, the toy model offers an explanation of the observation from Ref. [33] that the leakage current abruptly increases as the B-field is swept-up [recall Fig. 6.2(a)]. Figure 6.3(b) now draws the relevant two-electron states as a function of in-dot-plane B-field for a fixed finite detuning appropriate for the measurements of Ref. [33]. As the B-field is increased the T^- state approaches the anti-bonding singlet branch. When the T^--S crossing point is reached, hyperfine mixing can lift the spin blockade, leading to the observed increase in current. While the toy model is simple and insightful, ultimately it is fairly crude. Many questions posed by the data of Ref. [33] can not be answered by the toy model or by more sophisticated models developed to date. For instance, no model can

adequately explain quantitatively the height of the current step, the extent of the observed hysteresis or the timescale of the oscillations shown in Fig. 6.2.

6.1.3 Probing Dynamical Nuclear Polarization

Whereas the original measurements in Ref. [33] where performed by sweeping the in-dot-plane B-field at fixed detuning, the same two-electron singlet-triplet mixing can also be accessed using a second technique, namely sweeping the detuning at fixed B-field. We now summarize the measurements of Baugh et. al. [66,84] performed using this technique, which will provide the main motivation for the work to be discussed in Sec. 6.2.

Figure 6.4(a) shows the leakage current measured as V_{SD} is initially swept-up. When a finite (external) B-field is applied, a ~0.5 pA step-like increase in the leakage current is observed. This feature is of similar magnitude to the feature observed in Ref. [33] [recall Fig. 6.2(a)]. In both cases the increased leakage current is attributed to the onset of hyperfine induced singlet-triplet mixing leading to nuclear polarization. Furthermore, the position of the step-like feature [labelled V_{step} in Fig. 6.4(a)] was found to shift to lower V_{SD} at higher B-field (note that no step-like feature is observed for $B < 0.1$ T). The shift of V_{step} to lower bias as the B-field is increased is precisely what would be expected for the T^--S crossing point which moves to lower detuning as the B-field is increased [recall Fig. 6.3(a)].

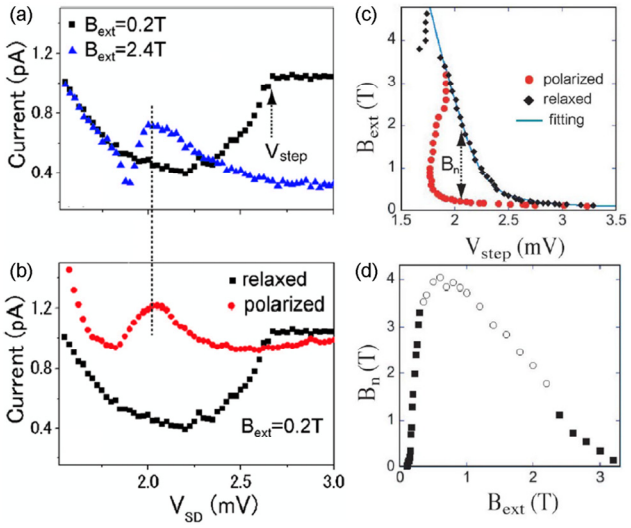

Fig. 6.4. (a) Leakage current measured in the $N = 2$ spin blockade region for V_{SD} up-sweeps at B = 0.2 and 2.4 T. (b) Leakage current in the spin blockade measured at 0.2 T for 'relaxed' and 'polarized' nuclear spin configurations. (c) The position of V_{step} extracted from both the 'relaxed' and 'polarized' traces for different applied B-fields. (d) B_n extracted for different applied B-fields. Note that the black points are determined directly from the experimental values of V_{step}, while the white points rely on the fit to the 'relaxed' data shown in (c) (figure adapted from Ref. [66]).

By implementing a simple bias pulsing procedure, Baugh et. al. [66] found that the position of the step-like feature was dependent on B_n. Starting from an unpolarized or 'relaxed' nuclear spin configuration, the leakage current is first measured by executing a bias up-sweep [see the 'relaxed' trace in Fig. 6.4(b)]. Polarization is then allowed to build-up through repeated electron spin-nuclear spin flip-flops when the bias is held fixed for ~30 s at the end of the up-sweep [corresponding to the detuning being held fixed near the T^--S crossing point]. After the polarization has built-up, the bias is quickly returned to zero and then swept back up again *at the same external B-field*. The corresponding current trace labelled 'polarized' is given in Fig. 6.4(b). Clearly, the current step seen on executing the first up-sweep has shifted to lower bias when subsequently encountered on

the second up-sweep (after 'pumping'), a result attributed to the finite B_n. Repeating such measurements over a range of external B-field allows the position of V_{step} for both the 'relaxed' and 'polarized' traces to be mapped out [see Fig. 6.4(c)]. By matching the position of V_{step} in the 'polarized' trace at a given B-field, and in a 'relaxed' trace at higher B-field, B_n can be determined from the difference in B-fields [see Fig. 6.4(d)]. The maximum value of B_n determined from Fig. 6.4(d) is ~4 T. This corresponds to ~40% nuclear polarization for a GaAs QD (taking the effective g-factor to be ~0.25).

In the original work of Ref. [66], the action of two consecutive up-sweeps was considered. Subsequently, Ref. [84] reported the effect of performing a down-sweep after the initial up-sweep [see Fig. 6.5(a)]. For both the up- and down-sweep shown in Fig 6.5(a), the current step is once again attributed to the hyperfine interaction at the T^--S crossing point leading to DNP. However, while sweeping the detuning through the T^--S crossing point in either direction will lead to DNP, there is a subtle difference between the two sweep directions. In order to understand the difference, recall from Fig. 6.3(a) that when a finite B_n is built-up by successive flip-flops, the T^--S crossing point will essentially shift to lower detuning. Crucially, for the up-sweep the period in detuning when the T^- and S_{AB} states are close together allowing DNP to build-up is limited [see inset to Fig. 6.5 (b)] because the crossing point effectively moves counter to the direction the detuning is being swept (as a consequence of DNP feedback). In contrast, for the down-sweep, further nuclear polarization drives the T^--S crossing point towards lower detuning so the T^- and S_{AB} remain close together as the detuning is swept down and potentially a larger nuclear polarization can be built-up [see Fig. 6.5(b)].

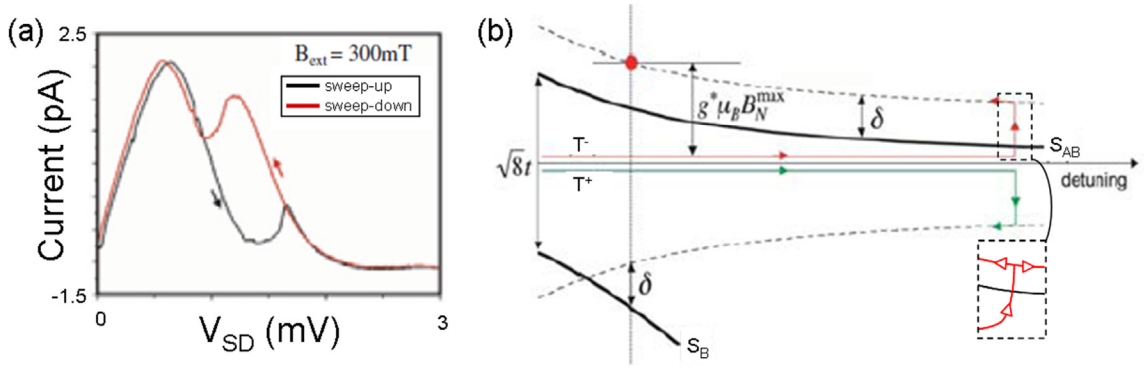

Fig. 6.5. (a) Current measured in the $N = 2$ spin blockade region in response to V_{SD} being swept-up and then immediately swept-down at fixed B = 300 mT. (b) Schematic energy diagram of the relevant two-electron singlet and triplet states which illustrates the effect of sweeping the detuning up and down (figure adapted from Ref. [84]).

6.1.4. Take Home Message

In this section, we have introduced the hallmarks of the hyperfine interaction namely, current switching, hysteresis and slow oscillations originally observed in the $N = 2$ spin blockade region. As demonstrated in the key works of Ono and Tarucha [33], and Baugh et. al. [66], there are two simple approaches to probe the influence of the hyperfine interaction in double dots, namely sweeping the B-field for fixed detuning and sweeping detuning for fixed B-field. In the following sections, we will use these observations and techniques to shed further light on, and exploit, the hyperfine interaction.

6.2 Experimental Investigation of Hyperfine Interaction Effects in the Two-Electron Spin Blockade Region

If one takes the works of Refs. [33,66,84] at face value, it would appear that the influence of the hyperfine interaction in the $N = 2$ spin blockade is reasonably well

documented for vertical double dots. However, while the toy model described in Sec. 6.1.2 is capable of qualitatively explaining some of the results of Refs. [33,66,84], neither it nor any existing (more sophisticated) model can adequately explain most of the observed features quantitatively.

Some unanswered questions remain from an experimental point of view. For instance, the experiments described in Refs. [33,66,84] did not explore the entire spin blockade region, but rather focused solely on a V_G close to where the $N = 1$ and $N = 2$ Coulomb diamonds touch at zero bias. Furthermore, the measurements reported in Ref. [33] and Refs. [66,84] were each performed on a single device fabricated from different materials. Inspection of their results, and those of Refs. [128-130] too, suggests that the appearance of the features in the spin blockade regime attributed to the hyperfine interaction varies strongly device-to-device due to a combination of factors including material parameters (such as tunnel barrier widths), and natural randomness and imperfections (leading to, for instance, different energy offset values at zero bias). Also, while Refs. [66,84] explored the influence of two possible combinations of bias voltage sweeps (namely two consecutive up-sweeps and an up-sweep followed by a down-sweep) the influence of the remaining two combinations (namely two consecutive down-sweeps and a down-sweep followed by an up-sweep) could also be explored.

In this section we will describe measurements which address the preceding points and may prove useful in developing a more complete understanding of the hyperfine interaction. In Sec. 6.2.1, we discuss measurements demonstrating intricate V_G dependence of hyperfine-induced fine features throughout the entire spin blockade region over a wide B-field range (up to ~3 T) in one device. Subsequently, in Sec. 6.2.2 we will

describe a funnel-like structure observed in the spin blockade region at low B-field (< |45| mT) in another device. Finally, although many details of the hyperfine interaction in the spin blockade region remain unclear, we will nonetheless exploit it throughout Secs. 6.2.3 and 6.2.4 to demonstrate basic memory effects using a V_{SD} pulsing scheme based on the work of Refs. [66,84].

It is important to note that throughout Sec. 6.2 the bias convention has been *reversed* for convenience and for easy comparison with the results of Refs. [66,84] presented in Sec. 6.1.3, i.e., for Device IV the spin blockade chevron now appears in forward bias, whereas in Chap. 3 it is in reverse bias [see Fig. 3.11(d)].

6.2.1 Gate Voltage Dependence of Fine Features in the Two-Electron Spin Blockade Leakage Current

We now focus on experimental results, obtained using Device IV, which reveal features in the $N = 2$ spin blockade regime similar in some respects to those attributed to the hyperfine interaction in Refs. [66,84]. Figure 3.11(d) established that this device has an appropriate energy offset at zero bias to observe the spin blockade chevron clearly at 0 T. Figure 6.6 focuses on this region in greater detail and at finite B-field.

Figure 6.6 shows a sequence of differential conductance plots in the vicinity of the $N = 2$ Coulomb blockade (CB) diamond and the chevron-shaped spin blockade (SB) region. In the absence of a B-field, the spin blockade region is featureless and there is essentially no difference between the data captured when V_{SD} is either swept-up (left side of Fig. 6.6) or swept-down (right side). However, when an out-of-dot-plane B-field is

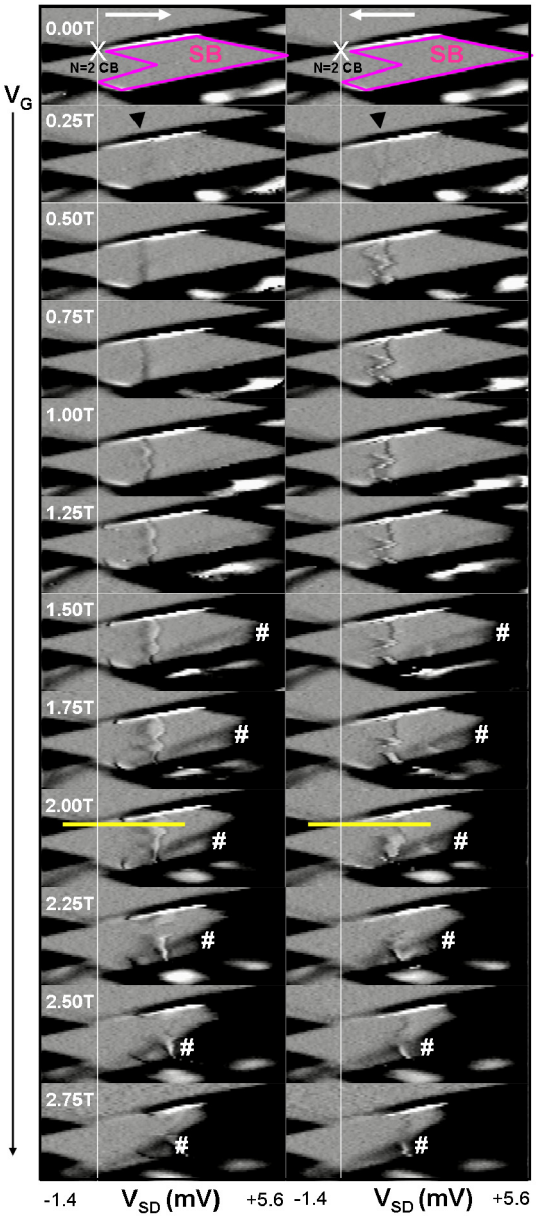

Fig. 6.6. Differential conductance, dI/dV_{SD}, in the V_{SD}-V_G plane for different B-fields between 0 T and 2.75 T (steps of 0.25 T) in the vicinity of the spin blockade regime. Panels on the left (right) are for V_{SD} up-sweeps (down-sweeps). V_{SD} sweep rate is ~0.1 mV/s. In contrast to the work of Refs. [33,66,84] discussed in Sec. 6.1, here the B-field is applied in the out-of-plane direction, meaning that now the orbital response of the single-particle states is not suppressed. Consistent with Fig. 3.11(d), the feature marked by a # symbol indicates where the spin blockade is lifted at high bias due to the energetically downshifting $2p^+$-like state in the downstream dot [see also Ref. [32] and Fig. 2.17(c)]. The yellow line in the 2.00 T panel is explained in Sec. 6.2.3.

applied, fine features (identified by the symbol ▼ in the 0.25 T panel) begin to appear within the spin blockade region by ~0.2 T. These features, which grow in strength with B-field, are ~1 pA in magnitude and depend intricately on the B-field as well as on V_G, a dependence not discussed in Refs. [33,66,84]. Furthermore, their appearance depends strongly on the V_{SD} sweep direction and so is clearly hysteretic. Based on the observations of Refs. [66,84], we attribute the hysteretic fine features observed at finite B-field to hyperfine induced singlet-triplet mixing leading to DNP.

The hysteretic nature of the fine features is easier to discern by examining I-V_{SD} traces where the up- and down-sweeps can be plotted together for easy comparison. Figure 6.7(a) demonstrates that the I-V_{SD} traces measured at 0 T are featureless in the spin blockade region and that there is no hysteresis. In contrast, Fig. 6.7(b) reveals the nature of the fine features at 2 T in detail, providing evidence of hysteresis and a strong V_G dependence. In particular, the trace measured at V_G = -1.28 V (marked by the symbol ■) appears very similar to that shown in Ref. [84] (recall Fig. 6.5). In fact, both the trace marked ■ and the trace shown in Fig. 6.5 were recorded at a V_G approximately corresponding to where the N = 1 and N = 2 Coulomb blockade diamonds touch at zero bias. The other traces can be organised into families with similar properties [labelled i-iv in Fig. 6.7(b)]. Moving from the trace labelled ■ towards more positive V_G, family i shows up to three features in either sweep direction, while family ii shows a large feature (~0.3 pA) in the up-sweep and a smaller one (< 0.1 pA) in the down-sweep. Meanwhile, going from the trace labelled ■ towards more negative V_G family iii shows signs of hysteresis on the high bias side of the main feature and in family iv this has disappeared. Again, we stress that such strong V_G dependence was not discussed in Refs. [33,66,84],

and is not accounted for within the standard toy model. We are aware of no other works which specifically explore it although Ref. [131] may provide a starting point.

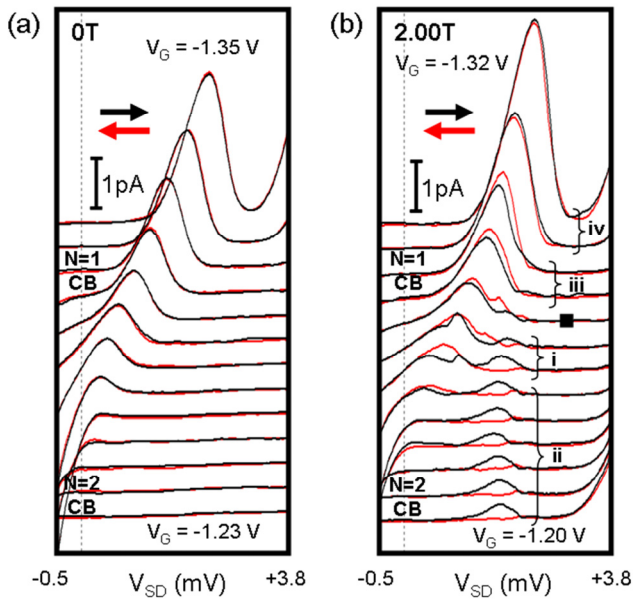

Fig. 6.7. I-V_{SD} traces measured for bias up-sweeps (black) and down-sweeps (red) at (a) 0 T and (b) 2 T showing part of the spin blockade region in positive bias. Parts of the $N = 1$ and $N = 2$ Coulomb blockade (CB) diamonds are visible. The dotted line corresponds to zero bias. Traces are vertically offset by 0.5 pA.

It is important to note that in both panels of Fig. 6.7 the I-V_{SD} traces for up-sweeps (down-sweeps) have all been shifted by -0.07 mV (+0.07 mV). This correction procedure is performed in order to account for hysteresis as a result of a short time delay due to cable and wiring capacitance and instrumentation, and the magnitude of the shift is chosen so that the traces for corresponding up- and down-sweeps are essentially aligned near zero bias. Crucially, while the correction accounts for the unwanted hysteresis, the hysteresis of interest due to the hyperfine interaction remains. To see this explicitly, consider Fig. 6.8 which shows examples of measured traces with (left side) and without (right side) the correction. Clearly, for 0 T [Fig. 6.8(a)], the correction results in two

traces which are practically identical, while for 2 T [Fig. 6.8(b)] pronounced hysteresis of interest remains. Note as well that the extent of the hysteresis arising from the hyperfine interaction is larger than that of the hysteresis due to the measurement set-up.

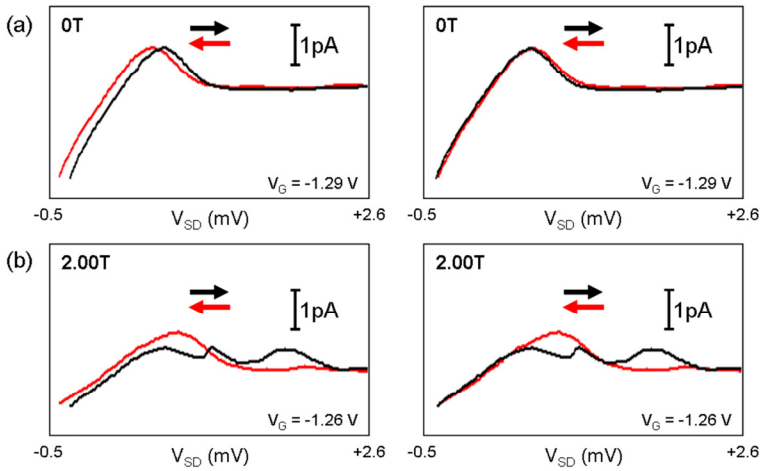

Fig. 6.8. *I*-V_{SD} traces measured for bias up-sweeps (black) and down-sweeps (red) at (a) 0 T and (b) 2 T in the spin blockade region demonstrating two types of hysteresis. The correction procedure described is applied throughout Chap. 6.

We can make several comments regarding the observed V_G dependence. Recall from Sec. 2.2.4 that spin blockade occurs when the T(1,1) state is occupied *and* the electron on the upstream dot can not easily return to the source contact [see Fig. 2.17(a)]. When V_G is adjusted the energy of the ground state of the upstream dot relative to the chemical potential of the source contact is altered. We presume that this influences the details of the hyperfine interaction mechanism leading to the observed intricate pattern of the fine features [131]. Additionally, the nearly, but not quite, vertical resonance lines observed in the V_{SD}-V_G plane [recall Fig. 3.11(d)] indicate that the gate is approximately, but not exactly, equally coupled to both dots. Consequently, changing V_G may result in a small change in detuning which also influences the appearance of the fine features. We

note that the fine features shown in Fig. 6.6 appear to shift to higher V_{SD} and increase in strength as the B-field increases. Both of these dependences are not currently understood.

6.2.2 Funnel-like Structure Observed in the Two-Electron Spin Blockade Region

While hysteretic fine features observed in the leakage current in the $N = 2$ spin blockade region can ultimately be attributed to the hyperfine interaction, the appearance of such features can vary significantly from device-to-device. In order to emphasize this, we now discuss measurements performed with Device III. Recall that Fig. 3.11(c) demonstrated that this device also has an appropriate energy offset at zero bias to observe the spin blockade chevron clearly at 0 T. In contrast to Sec. 6.2.1, we now focus on the low B-field (< |45| mT) regime. In this regime we observe a hysteretic funnel-like structure. We stress that for Device IV, which was fabricated from the same material and apparently has a similar energy offset at zero bias, at such low B-fields the spin blockade region was found to be featureless as mentioned in the previous section.

Funnel-like structures (see Fig. 6.9) in the familiar two- (or effective two-) electron spin blockade region have recently been reported in the transport properties of a number of weakly coupled QD systems including lateral GaAs dots [43,64,67,68,132], InAs dots in a nanowire [26], and ^{13}C dots in a carbon nanotube [69]. The funnel-like structures occur near 0 T and typically exhibit hysteresis on sweeping a weak B-field back and forth through 0 T [26,64,69]. Additionally, we note that recent observations from weakly coupled vertical QDs in the $N = 2$ spin blockade region close to 0 T also appear to show signatures of funnel-like structures [82,128,129]. These works described

measurements where the B-field is initially set to 0 T and subsequently swept but for only one B-field polarity rather than both. Consequently, their results essentially reveal one side of the funnel-like structure.

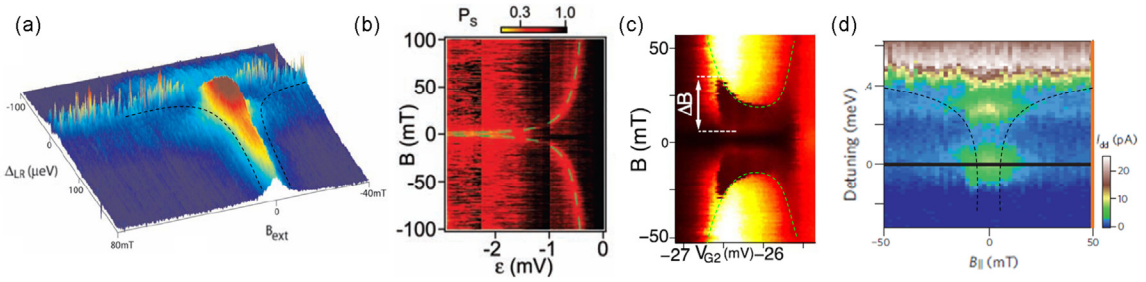

Fig. 6.9. Examples of funnel-like structures near 0 T related to the hyperfine interaction observed in double dots mostly in the $N = 2$ spin blockade region [(images in (a), (b), (c) and (d) adapted from Refs. [64], [43], [26] and [69] respectively)

All of the aforementioned funnel-like structures have been attributed two-electron singlet and triplet state mixing in the presence of the hyperfine interaction. Specifically, the funnel shape reflects the position in detuning of the singlet-triplet crossing points (recall Fig. 6.3) as a function of B-field, i.e., essentially, near the anti-crossing between the S(1,1) and S(0,2) states the funnel-like structure maps out the curvature of the singlet branches.

We now focus on the measurements performed in the low B-field regime with Device III. Figure 6.10(a) shows the current measured in the spin blockade region as V_{SD} is swept-up and swept-down for different B-fields. Specifically, these measurements are performed with $V_G = -0.2$ V which corresponds to a point close to where the $N = 2$ and $N = 3$ Coulomb diamonds touch at zero bias. The I-V_{SD} traces in Fig. 6.10(a) show a step-up (step-down) in the current on the up-sweep (down-sweep). The differential conductance greyscale plots shown in Fig. 6.10(b) reveal that the step-like features form

a funnel-like structure located symmetrically around 0 T similar to those in Fig. 6.9. Consistent with observations from the references discussed above, we attribute the funnel-like structure to singlet-triplet mixing and DNP.

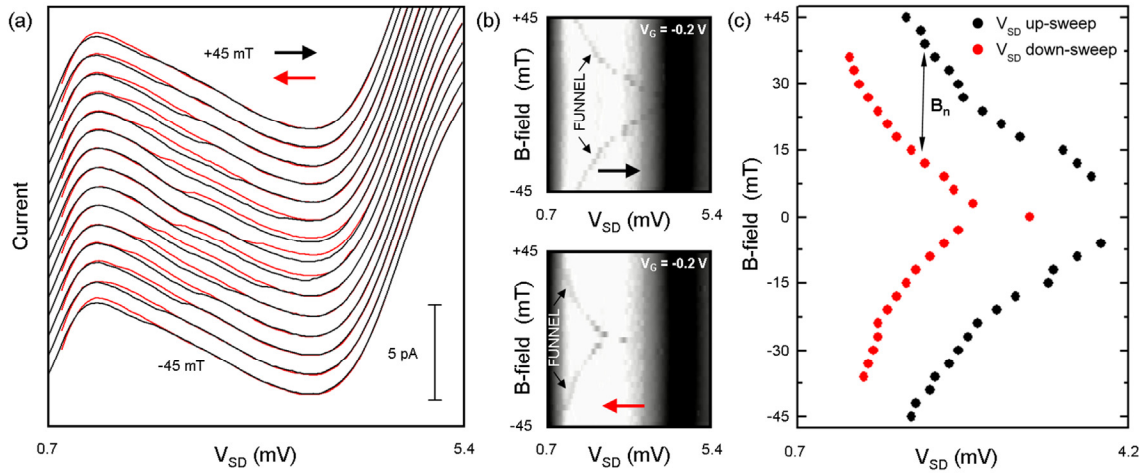

Fig. 6.10. (a) I-V_{SD} traces which cut through the spin blockade region near to where the N = 2 and N = 3 Coulomb blockade diamonds touch at zero bias for different values of B-field (-45 mT to +45 mT in steps of 6 mT). Black (red) traces correspond to V_{SD} up-sweeps (down-sweeps). The correction procedure (recall Fig. 6.8) has been applied by uniformly shifting the up- and down-sweeps by ±0.14 mV. Traces are vertically offset by 1 pA. (b) The funnel-like structure is clearly evident in numerically derived differential conductance plots for the bias up-sweeps (top) and down-sweeps (bottom). (c) By matching the position of the step-down feature in the down-sweep (red points) with the position of the step-up feature in the up-sweep (black points) at higher B-field, a value of B_n can be estimated.

In more detail, the up-sweep traces in Fig. 6.10(a) are reminiscent of those in Ref. [66] [recall Fig. 6.4(b)] for higher (in-dot-plane) B-fields (>100 mT). The step-up in current is ~0.3 pA and the position of the step is in the range of 1.5 to 4 mV. These values are comparable to those in Ref. [66]. Adapting the technique described in Ref. [66] [recall Fig. 6.4(c)], we estimate the nuclear field is ~25 mT for an applied B-field of

15 mT, i.e., the V_{SD} position of the step-down in the down-sweep at B = 15 mT coincides with the V_{SD} position of the step-up in the up-sweep at B = 40 mT. That we see the funnel at comparatively low B-field may reflect the weaker tunnel coupling in the double QD structure we study. We also note that the funnel-like structure can be observed for other values of V_G that cut through the $N = 2$ spin blockade region, although we do not discuss its V_G dependence here.

This section has focused on a funnel-like structure observed at low B-field in the $N = 2$ spin blockade region of one device. The fact that we have seen it in Device III and not in another similar device (recall discussion of Device IV in Sec. 6.2.1) is clear evidence that the influence of the hyperfine interaction can vary dramatically from device-to-device. Additionally, we note that even the appearance of the spin blockade region itself varies significantly from device-to-device. In particular, by comparing the I-V_{SD} traces in Fig. 6.7(a) for Device IV with those in Fig. 6.10 for Device III, we see that the shape of the traces is quite different. Specifically, in Device IV, the region of suppressed current in the I-V_{SD} traces is approximately flat, while in Device III, the current decreases gradually to a minimum, but does not become flat. Furthermore, the leakage current in Device III is ~1 pA, while in Device IV it is ~7 pA at the minimum. We note that the leakage current in other vertical double QDs is typically ~1 pA, but that it is known to vary (see for example Refs. [33,66]). Evidently, the value of the energy offset between the two dots at zero bias, as well as the choice of V_G, i.e., where precisely the spin blockade is cut, influences both the shape of the I-V_{SD} trace and the magnitude of the leakage current.

Finally, we note a funnel-like structure which maps out the curvature of the singlet branches [reflecting the position in detuning of the singlet-triplet crossing points (recall Fig. 6.3) as a function of B-field] itself can be considered a hallmark of the hyperfine interaction. Intriguingly, in Sec. 6.3.6 we will encounter another funnel-like structure in a different regime, i.e., outside the familiar $N = 2$ spin blockade region.

6.2.3 Programming the Current Response in the Two-Electron Spin Blockade Region

Based on the data presented in the previous two sections, manifestly many questions remain about the details of the hyperfine interaction mechanism in the familiar $N = 2$ spin blockade regime. Nonetheless, measurement protocols utilizing hyperfine related effects can still be exploited for performing basic memory and even logic operations. Motivated by the work of Refs. [66,84] outlined in Sec. 6.1.3, we now examine the effects of performing mHz bias voltage pulsing sequences on the leakage current in the $N = 2$ spin blockade region in the presence of the hyperfine interaction. We will begin in this section by looking at the current response to combinations of two consecutive V_{SD} sweeps. Subsequently, in Sec. 6.2.4 we will extend the pulsing sequences to include four parts in order to gain additional insight into how the current response can be influenced by different combinations of up- and down-sweeps. In both Secs. 6.2.3 and 6.2.4 all measurements reported were performed on Device IV with an out-of-dot-plane B-field fixed at 2 T.

Whereas Ref. [66] ([84]) reported the influence of two consecutive up-sweeps (an up-sweep followed by a down-sweep), we now focus on the current response to each of

the four possible combinations of two V_{SD} sweeps composed of up- and down-sweeps. We will we refer to these combinations as up-up, down-down, up-down and down-up. For each V_{SD} sweep we perform, the bias is swept, at a rate of 0.24 mV/s, through the $N = 2$ spin blockade region with V_G fixed close to where the $N = 1$ and $N = 2$ Coulomb diamonds touch (see yellow line in 2 T panel of Fig. 6.6). Furthermore, each sweep (up or down) takes ~13.5 s, the time between consecutive sweeps is ~6.5 s and any adjustment of bias between consecutive sweeps is done rapidly within ~2.5 s.

The current measured in response to each of the four possible combinations of two V_{SD} sweeps is shown in Fig. 6.11. Clearly the total outcome is distinctly different in each case, i.e., it is strongly V_{SD} history dependent. We stress that for V_G values away from where the $N = 1$ and $N = 2$ Coulomb diamonds met, but still within the spin blockade chevron, either there is essentially no difference between up- and down-sweeps or there is a difference but there is no history dependence (so the up-sweeps are the same and the down-sweeps are the same).

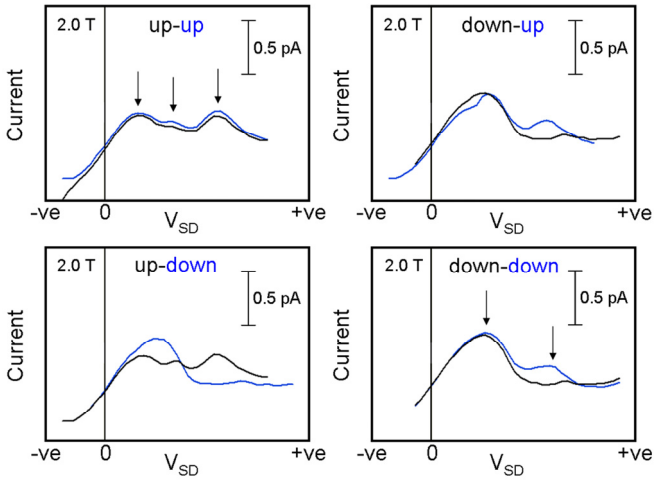

Fig. 6.11. Current response to two consecutive V_{SD} sweeps, where the first (second) sweep in each panel is coloured black (blue). The correction procedure (recall Fig. 6.8) has been applied by uniformly shifting the up- and down-sweeps by ±0.2 mV.

Several interesting observations can be made about the data shown in Fig. 6.11. Firstly, the current trace measured for an up-sweep is always different than that measured for a down-sweep. In particular, the up-sweeps all show three features (see arrows in upper left panel of Fig. 6.11), while the down-sweeps show only two (see arrows in lower right panel of Fig. 6.11). Secondly, it appears that a down-sweep has a more pronounced effect on subsequent sweeps than an up-sweep. To see this, consider the up-up combination which shows that the second up-sweep is almost unchanged. On the other hand, for the down-down combination the magnitude of the rightmost feature increases in the second down-sweep. Furthermore, the up-down combination shows that the down-sweep is effectively unchanged if it is preceded by an up-sweep (compare with the first down-sweep in either the down-up or down-down combination) while the down-up combination shows that the up-sweep is strongly influenced by the preceding down-sweep (compare with the first up-sweep in either the up-down or up-up combination).

As a tentative explanation of the results of Fig. 6.11, it appears that down-sweeps influence (polarize) the nuclei more than up-sweeps, and the effects can be seen in the subsequent sweeps. Although the details remain unclear, this appears consistent with the picture put forth by Ref. [84] which suggests the a down-sweep may lead to larger nuclear polarization [see Fig. 6.5(b)]. Nonetheless, by extending the pulsing sequences, we may expect to gain some additional insight to help interpret the data and even extract a timescale for the nuclear relaxation.

6.2.4 Four-part mHz Bias Voltage Programming

To further investigate the influence of up- and down-sweeps on subsequent sweeps, we now adapt the simple V_{SD} pulsing sequences described in the previous section to include four parts [133]. The measurements described in this section are performed under the same conditions (B-field, V_G, V_{SD} range and sweep rate) as those in the previous section. Furthermore, the main components of each V_{SD} pulse, i.e., the up- and down-sweeps and the pauses between them, are of the same duration as before.

In order to capture the data, we apply a bias waveform consisting of four four-part V_{SD} pulsing sequences, two of which are shown in Fig. 6.12. We choose to label each up-sweep (down-sweep) by a 0 (1) and so each four-part V_{SD} pulse can be identified by a four digit binary number. For example, the four-part V_{SD} pulse consisting of three consecutive up-sweeps followed by a down-sweep is labelled 0001. It is desired that each four-part V_{SD} pulse within the waveform begins with no built-up nuclear polarization, and so an 'erase' operation is included between each four-part pulse (purple points Fig. 6.12). We found that an ~8 s excursion several mV to either the left or right of the spin blockade region, i.e., to relatively high bias where the current is comparatively high, appeared sufficient to 'erase' any built-up memory of the preceding waveform. However, we made no attempt to determine the efficiency of the 'erase' operations or to identify other possible 'erase' operations. Furthermore, we did not attempt to identify the mechanism by which the 'erase' operation actually works, but simply presume that the increased current (several tens of pA compared to ~1 pA in the spin blockade) through the system can help nuclear spins relax through appropriate coupling mechanisms [134].

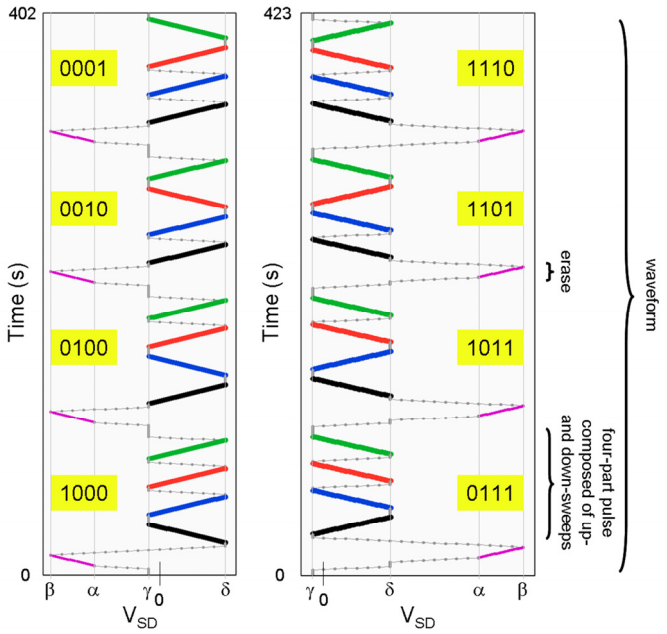

Fig. 6.12. Two examples of bias waveforms each consisting of four four-part V_{SD} pulses. For the waveform on the left (right) points α, β, γ and δ correspond to -2.80 (6.54), -4.67 (8.41), -0.47 and +2.8 mV. The first, second, third and fourth component of each four-part pulse are black, blue, red and green respectively, while the 'erase' operation is purple. The data points are acquired at a rate of 2.67 Hz. The waveforms both last ~400 s, meaning the duration of each four-part V_{SD} pulse is ~100 s, i.e., the pulse repetition rate is ~10 mHz, and within each pulse the time interval between the start of neighbouring sweeps is ~20 s, i.e., the sweep repetition rate is ~50 mHz.

Of the sixteen possible four-part V_{SD} pulsing sequences, the eight selected in the two bias waveforms shown in Fig. 6.12 are of particular interest because the current response to each of them clearly illustrates the differences between up- and down-sweeps as well as the differences between neighbouring sweeps. In particular, the waveform on the left (right) side of Fig. 6.12 demonstrates the operation of shifting a single 'minority' down-sweep (up-sweep) through three 'majority' up-sweeps (down-sweeps).

Figure 6.13 shows the current response to the bias waveform portrayed in the left panel of Fig. 6.12. An important observation is that the 'erase' operation of the pulsing

sequence has been successful at eliminating any built-up nuclear polarization. To see this, consider the first up-sweep in the 0100, 0010 and 0001 pulses which are all very similar (black trace for each of the indicated pulses). We can make several other observations consistent with the trends observed for the combinations of two V_{SD} sweeps. Firstly, careful inspection of these I-V_{SD} traces reveals that the total outcome is distinctly different in each case, i.e., the total current response is strongly V_{SD} history dependent. Secondly, the appearance of a down-sweep is always quite different from an up-sweep (particularly in the vicinity of the first feature to the right of zero bias) and it does not depend strongly on the number of preceding up-sweeps (see each of the down-sweeps in Fig. 6.13). Thirdly, while consecutive up-sweeps after an 'erase' operation are almost identical, up-sweeps after a down-sweep are not only strongly perturbed but, interestingly, they slowly relax back to their unperturbed state. For example, in the 1000 pulse the fine features in the vicinity of the first main feature to the right of zero bias slowly change (relax) in each subsequent up-sweep. We will return to this observation shortly in order to extract a retention time, but first, for comparison, we consider the complementary waveform on the right of Fig. 6.12.

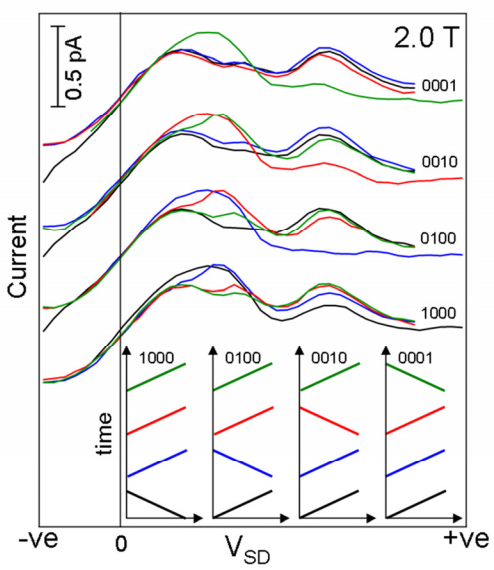

Fig. 6.13. Current response to the bias waveform shown in the left panel of Fig. 6.12. The measured currents corresponding to each four-part pulse are grouped together and each group is vertically offset by 0.5 pA. The correction procedure (recall Fig. 6.8) has been applied by uniformly shifting the up- and down-sweeps by ±0.2 mV. The first, second, third and fourth component of each four-part pulse are coloured black, blue, red and green respectively.

The current response to the bias waveform shown in the right panel of Fig. 6.12 is shown in Fig. 6.14. The relevant observations made for Fig. 6.13 about the success of the 'erase' operation, the appearance of the up- and down-sweeps, and the total current response also apply to the data in Fig. 6.14. Additionally, we can make two further observations. Firstly, for consecutive down-sweeps beginning after an 'erase' operation, all subsequent down-sweeps are perturbed relative to the first even if there is an intervening up-sweep. However, for the 1110 pulse it worth noting that the third consecutive down-sweep appears quite similar to the second, i.e., its appearance has 'saturated' and changes no further. Secondly, all the up-sweeps preceded by a down-sweep look the same, but are distinct from an up-sweep which follows the 'erase'.

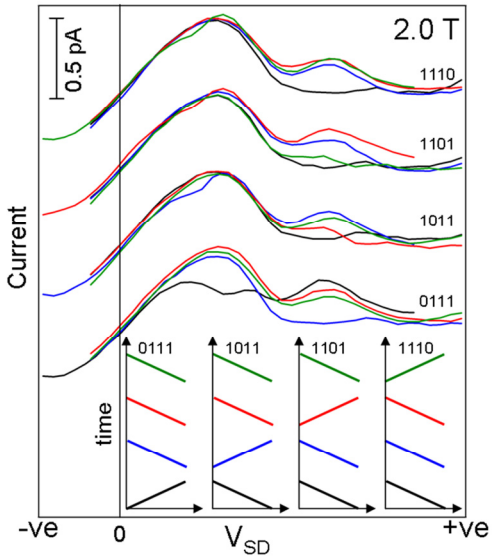

Fig. 6.14. Current response to the bias waveform shown in the right panel of Fig. 6.12. The details given in the caption of Fig. 6.13 apply for this figure as well.

Treating the double QD device somewhat as a 'black-box,' we now consider explicitly the question of how long the memory of a single perturbing minority sweep is retained. In order to extract a retention time scale, we will examine how long the majority sweeps take to 'recover' after a perturbing sweep. Figure 6.15(a)[(b)] plots the current response to the 0100 (1011) four-part V_{SD} pulse, where the second part of the pulse is the perturbing minority sweep. For reference, we also plot the 'saturated' current response (labelled Ref.) after a sequence of three majority sweeps in grey in both Figs. 6.15(a) and (b). Examining the current response to the third part of the 0100 or 1011 V_{SD} pulse, we see that it is strongly perturbed relative to the 'saturated' majority sweep. However, the current response to the fourth part of each of these V_{SD} pulses is practically identical to the 'saturated' majority sweep. As the time interval between neighbouring parts is ~20 s, we therefore deduce a recovery time ~40 s. A recovery (or relaxation) time of several tens of seconds appears consistent with the observations described in Refs. [66,84].

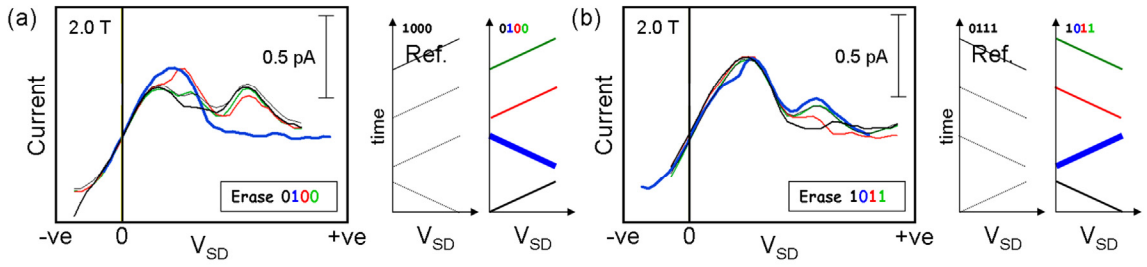

Fig. 6.15. Current response to four-part V_{SD} pulses consisting of three majority sweeps and a minority sweep as the second component of the pulse, i.e., 0100 and 1011. In (a) [(b)] the majority sweeps are up-sweeps (down-sweeps). The meaning of the reference pulses (Ref.) is discussed in the text. The relevant details given in the caption of Fig. 6.13 apply for this figure as well.

Finally, we note that for a four-part V_{SD} pulse sequence there are sixteen possible combinations of up- and down-sweeps. For completeness, Fig. 6.16 shows the measured current response for *all* sixteen possibilities. While we focused on half of these, specifically those where a minority sweep is shifted through three majority sweeps, a detailed examination of all sixteen possibilities together confirms that the current response to each of the four-part V_{SD} pulse sequences is still unique.

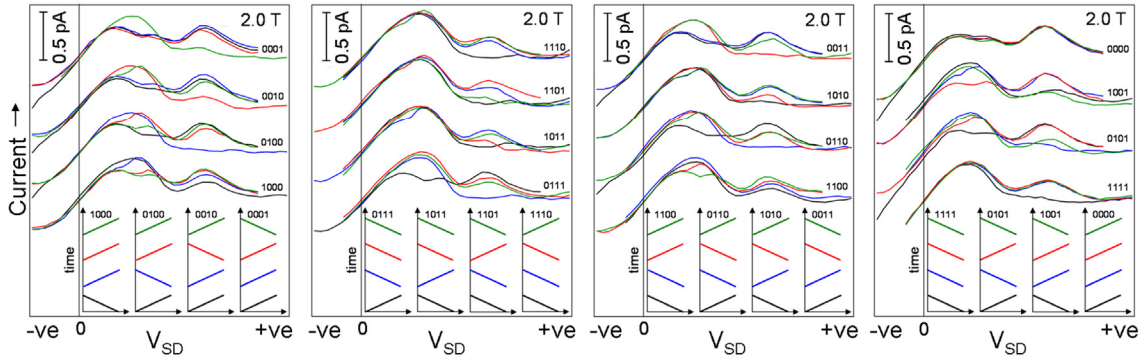

Fig. 6.16. Current response to all possible four-part V_{SD} pulses. The details given in the caption of Fig. 6.13 apply for this figure as well.

6.2.5 Summary

In this section we have reported how for finite out-of-dot-plane B-field, fine features attributed to the hyperfine interaction manifest themselves throughout the $N = 2$ spin blockade region. These features are hysteretic with V_{SD} sweep direction and exhibit intricate B-field and V_G dependence. Furthermore, the appearance of such features varies strongly device-to-device. Aspects of these features are consistent with related features representative of a wide range of double QD systems. Although a full understanding of these observations will require more advanced models, the simple picture put forth in Refs. [66,84] appears to be a good starting point. Despite an incomplete understanding of the fine features, we can nonetheless exploit the hyperfine interaction to demonstrate basic memory effects. In particular, by applying appropriate multi-part V_{SD} pulses, we can effectively program fine features in the current in the spin blockade region. Notably, we were able to extract a retention time of ~40 s, consistent with the observations of Refs. [66,84].

6.3 Hyperfine Interaction Beyond the Two-Electron Spin Blockade Region

It is now well established that current switching, hysteresis and even slow oscillations in the $N = 2$ spin blockade region are signatures of the hyperfine interaction. Unexpectedly, we observe similar features at high bias *outside* of the $N = 2$ spin blockade region.

At the start of this section, we extensively characterize these features and will

argue that they are still likely due to the hyperfine interaction. In this new regime, we find such features are widespread and robust, however no detailed model exists to account for them. Although few-electron states are involved, they are difficult to identify, which presents a significant obstacle to developing a model. We end this section by discussing a funnel-like structure, also observed at high bias, which is sufficiently close to pinch-off that the relevant few-electron states can be identified, allowing us to propose a specific mechanism for this funnel.

It is important to note that throughout this section we return to the original bias voltage convention of Chap. 3 and in all cases where we explicitly show reverse bias current, we take the *absolute value of the current* for clarity.

6.3.1 Introductory Observations

The 0 T differential conductance plot for Device V [Fig. 6.17(a)] shows many characteristic traits of vertical double QDs, namely the familiar $N = 2$ spin blockade chevron and numerous vertical-running resonances at higher bias. Surprisingly, in addition, numerous unusual looking fine features appear throughout a wide region of the V_{SD}-V_G plane when an out-of-dot-plane B-field is applied as exemplified by Figs. 6.17(b) and (c). Specifically, these features are generally evident at large negative bias, well beyond the $N = 2$ spin blockade region. They are quite clear at ~5 mV and persist to at least ~20 mV. This bias range corresponds to an energy range of roughly one to several times the charging energy indicating that we are in a regime beyond that of simple SET. Furthermore, while the features appear to peter out close to pinch-off, they are present at more positive V_G and persist until at least ~-0.7 V. Additionally, as we now demonstrate,

upon sweeping the B-field numerous reproducible and robust features are encountered which exhibit current switching, hysteresis and even slow oscillations in time. These are strong signatures of the hyperfine interaction.

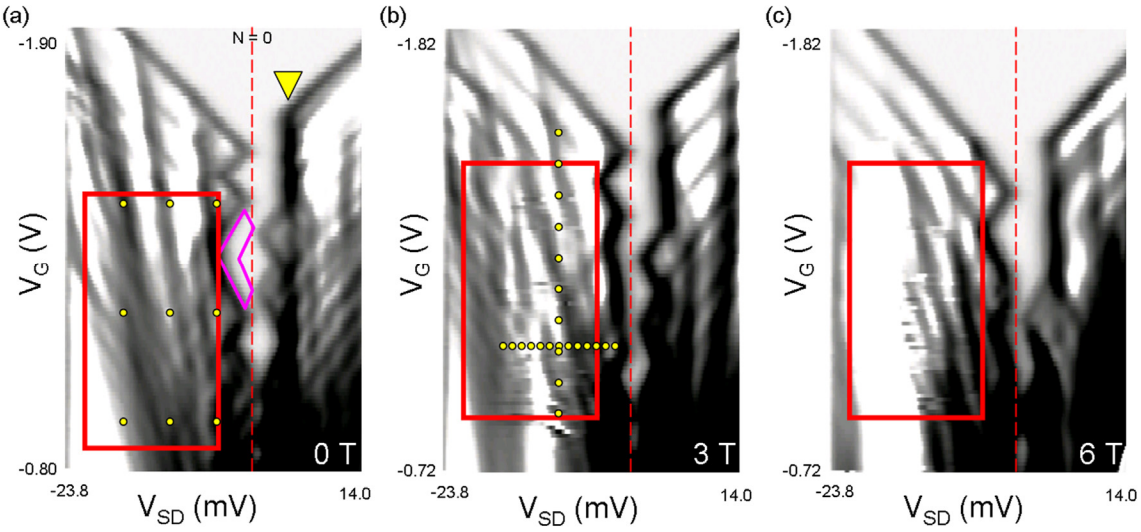

Fig. 6.17. Differential conductance, dI/dV_{SD}, measured in Device V at (a) 0 T, (b) 3 T and (c) 6 T. The red dashed line indicates zero bias. In (a) the $N = 2$ spin blockade region is highlighted in pink and the 1s-1s resonance is identified by a yellow triangle. The features of interest in reverse bias are located primarily in the region highlighted by red boxes (see also Figs. 6.18 and 6.19). Note that, due to the diamagnetic shift, the V_G axes are different in (b) and (c) as compared to (a).

For a clear demonstration of the widespread nature of the fine features in the V_{SD}-V_G plane, consider Fig. 6.18 which shows a series of current traces measured as the B-field is swept-up and swept-down. The V_{SD} and V_G conditions for these traces correspond to the widely dispersed yellow points in Fig. 6.17(a). In the measured current numerous clearly hysteretic features can be observed on sweeping the B-field, even at low B-fields, although they typically become more prominent above ~1.5 T and are visible up to at least 6 T. Notably, the features are visible at all three values of V_G considered and they

are strongest in the mid V_{SD} range (~10 mV), although they are still visible for lower (~5 mV) and higher (~15 mV) V_{SD} as well.

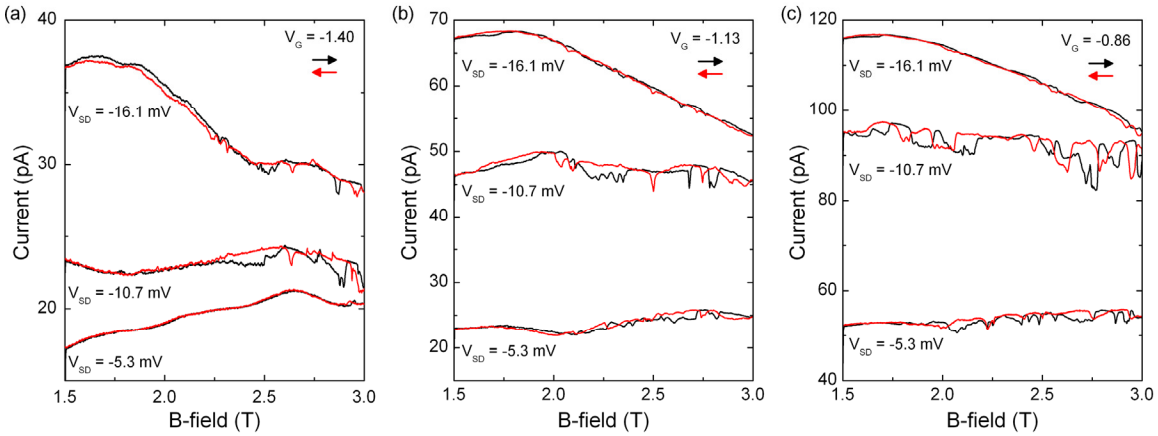

Fig. 6.18 Current measured in Device V as the B-field is swept-up (black) and swept-down (red) at a rate of 0.125 T/min (each up-down sweep takes 25 min). V_G is set to (a) -1.40 V, (b) -1.13 V and (c) -0.86 V. At each V_G up-down sweeps are recorded for three values of V_{SD} (-5.3 mV, -10.7 mV and -16.1 mV).

In order to examine the hysteretic features in more detail and to reveal any systematic trends as a function of V_G or V_{SD}, Fig. 6.19 shows two sequences of current traces measured as the B-field is swept-up and swept-down. The traces in Fig. 6.19(a) were measured at fixed V_G while stepping V_{SD}, and those in Fig. 6.19(b) were measured at fixed V_{SD} while stepping V_G. Both sequences are within the target area as identified by the yellow points in Fig. 6.17(b). Clearly most of the features appear as sharp 'dips' in the current with magnitude, ΔI, of up to ~10 pA. The relative strength of typical features compared to the background current, $\Delta I/I$, is 5-10%. For comparison, the size of step-like increase in the current seen in the $N = 2$ spin blockade region in Ref. [33] is ~0.3 pA and its relative size is ~30% (recall Fig. 6.2). Furthermore, most, if not all, of the features in both Figs. 6.19(a) and (b) appear to show systematic trends as V_{SD} or V_G is changed (see

dotted guidelines for some examples). For instance, in 6.19(b) features in both the up- and down-sweeps tend to move to higher B-field as V_G is made more negative.

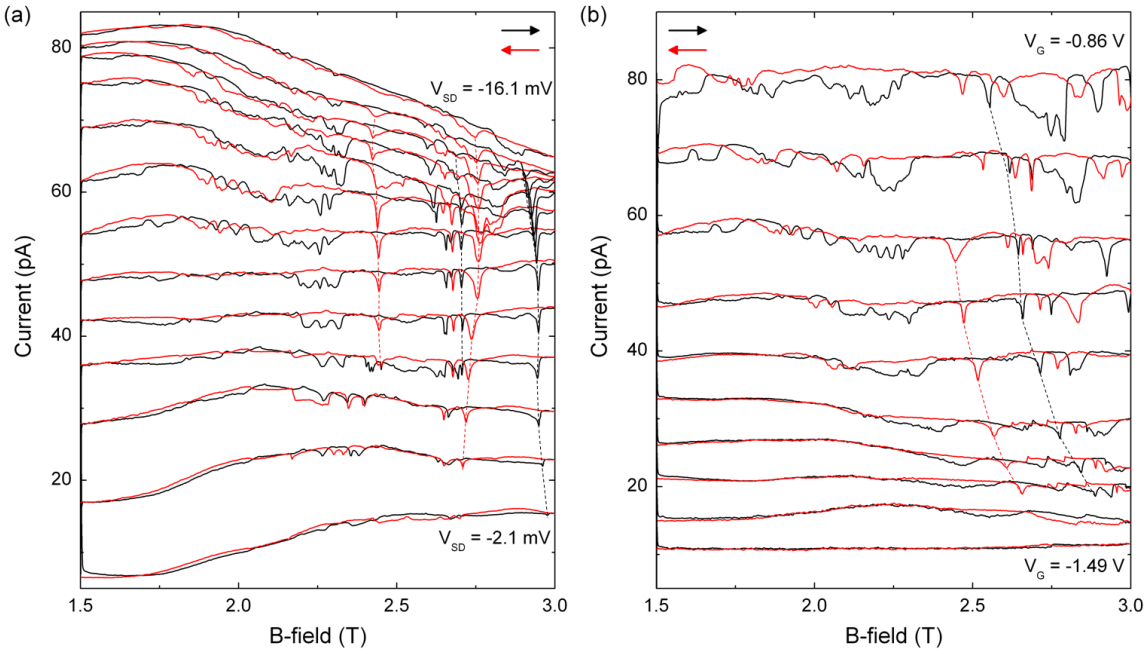

Fig. 6.19. Current measured in Device V as the B-field is swept-up (black) and swept-down (red) at a rate of 0.125 T/min (each up-down sweep takes 25 min). In (a) V_G = -1.04 V and V_{SD} is stepped from -2.1 mV to -16.1 mV, while in (b) V_{SD} = -9.1 mV and V_G is stepped from -0.86 V to -1.49 V. Dotted lines provide a guide to the eye.

While the preceding discussion focuses only on reverse bias, numerous B-field induced hysteretic features also appear in the current throughout an equally wide portion of the V_{SD}-V_G plane at high forward bias (outside the V_{SD} range of the plots in Fig. 6.17). Figure 6.20 shows the current measured as a function of B-field for several different values of V_G all measured with V_{SD} = 16.1 mV. The current traces again show current 'dips' (ΔI is up to ~3 pA) which display clear hysteresis as the B-field is swept-up and swept-down. As in Fig. 6.19(b), most of the features shift systematically towards higher B-fields as V_G is made more negative.

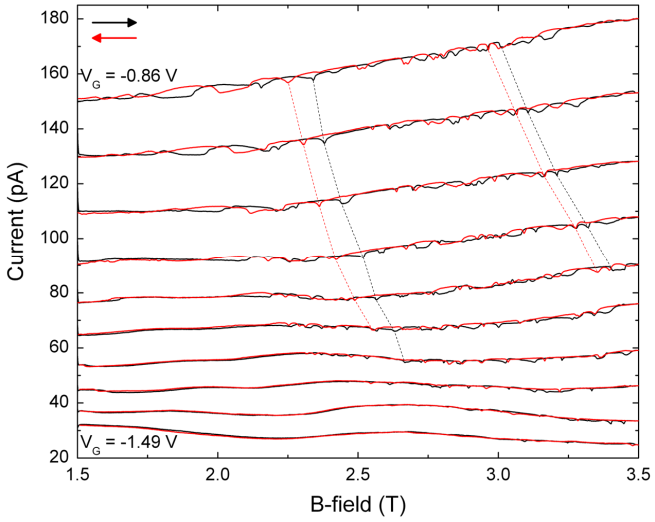

Fig. 6.20. Current measured in Device V as the B-field is swept-up (black) and swept-down (red) at a rate of 0.125 T/min. V_{SD} = 16.1 mV and V_G is stepped from -0.86 V to -1.49 V.

6.3.2 Reproducibility and Robustness of Observed Features

Given the unexpected location of the hysteretic fine features, several questions immediately come to mind with respect to the reproducibility and robustness. The most obvious question is: i. Are the hysteretic features spurious? If not, one could additionally ask: ii. If a measurement is repeated under the same conditions, are the features reproducible? iii. Do other devices show similar behaviour? iv. If so, do the hysteretic features of interest appear only in devices where the $N = 2$ spin blockade is observed? v. Is the hysteresis still clear at higher temperature?

We now address these questions in turn. To do so, we introduce a specific set of high bias measurements where the current is measured as the B-field is swept-up and swept-down (see Fig. 6.21). Examining the traces recorded for a 'fast' B-field sweep rate of 0.300 T/min, a number of clearly hysteretic step-like features are visible. In order to

demonstrate that these features are not spurious, we reduce the sweep rate to an intermediate value of 0.150 T/min and a 'slow' value of 0.015 T/min. By reducing the sweep rate the step-like features are captured by an increased number of data points. For the slow sweep rate traces the narrowest step-like feature (circled in blue in Fig. 6.21) extends over ~200 data points (corresponding to approximately one minute). In contrast, one extremely sharp spurious noise spike (highlighted by the blue arrow) is visible where the current jumps abruptly (~40 pA between two data points) before settling back down after ~10 points (corresponding to a few seconds). Thus, the answer to question i is no, the features are not spurious, and since even 0.3 T/min is not an excessively fast sweep rate, nor do they reflect any change that could arise by sweeping the B-field too quickly, i.e., heating effects or performing the measurement too quickly.

Concerning question ii, the data in Fig. 6.21 demonstrates that for each of the B-field sweep rates selected, when the up- and down-sweeps are repeated for the same conditions, the measured current is practically unchanged. This reproducibility provides further evidence that the observed features are not due to random events like noise. Addressing the questions iii-v, we note that the current traces in Fig. 6.21 were measured for Device II *not* Device V, demonstrating that the hysteretic features are visible in other devices as well. In fact, hysteretic features are observed in all four devices studied in detail (Devices II-V) irrespective of whether or not the $N = 2$ spin blockade is observed in a given device. Recall from the differential conductance greyscale plot in Fig. 3.11(b) that the spin blockade chevron is not visible in Device II in contrast to Device V. Lastly,

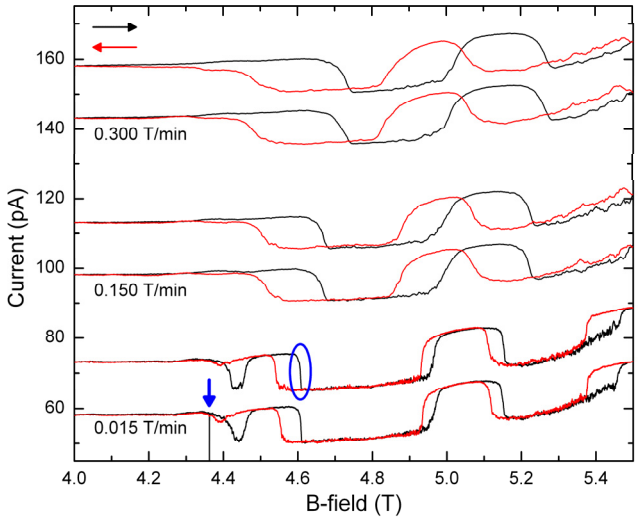

Fig. 6.21. Current measured in Device II as the B-field is swept-up (black) and swept-down (red) at ~4K with V_{SD} = -22.4 mV and V_G = -0.3 V for three different B-field sweep rates. Traces recorded for the same sweep rate are vertically offset by 15 pA and each group of traces is vertically offset by 40 pA. For the 0.300 T/min, 0.150 T/min and 0.015 T/min sweep rates the total time taken for an up-down sweep is 10, 20 and 200 min respectively.

the data in Fig. 6.21 was captured at ~4 K indicating that the hysteretic features are robust up to at least this temperature. Note as well that hyperfine induced hysteretic features in regions of spin blockade have been previously observed at ~1.6 K [33,66,130].

Having demonstrated that the hysteretic features we observe are numerous in B-field, widespread in V_G and V_{SD}, reproducible, and robust, we now characterize them further, focusing on the effects of changing the B-field sweep rate in Sec. 6.3.3 and their temporal properties in Sec. 6.3.4, before discussing possible underlying mechanisms in general terms in Sec. 6.3.5.

6.3.3 Influence of B-field Sweep Rate on Hysteretic Features

We begin by focusing on the influence of the B-field sweep rate because it is a convenient and simple means to influence the features of interest. Additionally, the hyperfine interaction, and DNP in particular, are time dependant so varying the sweep rate has the potential to offer insight into the underlying mechanism.

To examine the influence of adjusting the B-field sweep rate, we return to Device V and fix V_G = -1.04 V and V_{SD} = -6.77 mV. The result of measuring the current as the B-field is swept-up and swept-down for five different sweep rates is shown in Fig. 6.22. The current shows many sharp dips with magnitude of up to ~10 pA in both up- and down-sweeps and these features are clearly hysteretic [see Fig. 6.22(a)]. To ensure that the clarity of the features in Fig. 6.22(a) is not obscured we plot the up- and down-sweeps separately in Figs. 6.22(b) and (c).

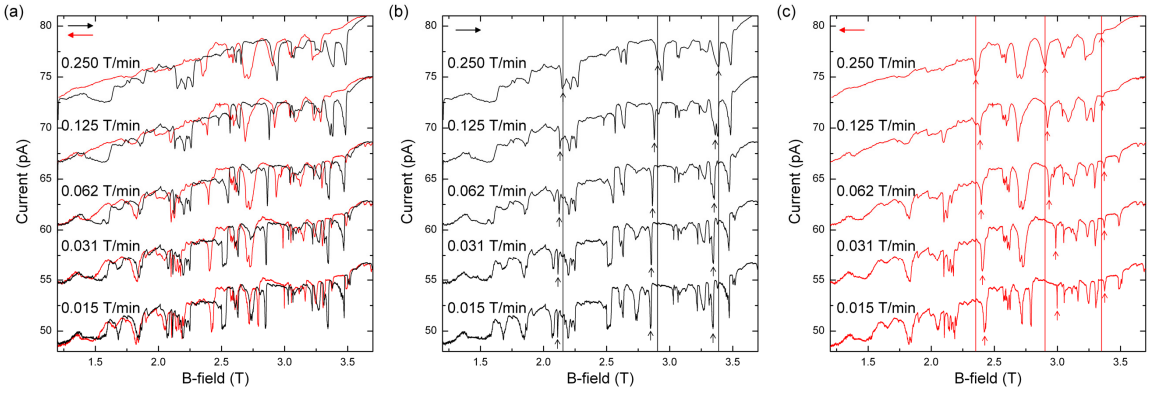

Fig. 6.22. Current measured in Device V as the B-field is swept-up (black) and swept-down (red) for five different sweep rates. In (a) the up- and down-sweeps are shown together, while (b) [(c)] shows the up-sweeps (down-sweeps) separately. For the fastest (slowest) sweep rate, an up-down sweep takes 20 mins (~330 mins). Arrows identify corresponding features in each trace. As a guide to the eye, vertical lines identify the position of the selected features in the trace measured at the fastest sweep rate. Traces are vertically offset by 6 pA.

The B-field sweep rate has two main effects on the hysteretic features. First, the position of the dips is influenced by the sweep rate. In particular, as the sweep rate is reduced, the features typically shift to lower (higher) B-field when the B-field is swept-up (swept-down). Second, when the sweep rate is reduced, the features generally sharpen considerably. We now examine both of these effects in more detail.

Figure 6.23(a) focuses on two neighbouring pairs of corresponding features (labelled 1 and 2) in the current measured for up- and down-sweeps at high B-field in Device II. These features are selected as they are both sharp and isolated, and so their B-field positions are easy to locate. Consistent with the trends suggested by Fig. 6.22, clearly features in the up-sweep shift to lower B-field as the sweep rate is decreased and in the down-sweep the corresponding features shift to higher B-field. The combined effect is that corresponding features in the up- and down-sweeps appear closer together when the sweep rate is reduced. Interestingly, the features do not coincide even at the slowest sweep rate.

Figures 6.23(b) and (c) plot the B-field position of the corresponding features in pairs 1 and 2 in the up- and down-sweeps. For 'fast' sweep-rates the corresponding features are separated by as much as ~200 mT, while for 'slow' sweep rates the separation is reduced to a few tens of mT. The magnitude of the separation in the positions of features in the up- and down-sweeps for 'slow' and 'fast' sweep rates is consistent with the extent of the hysteresis observed in the familiar $N = 2$ spin blockade region of Ref. [33] (recall Fig. 6.2) and Ref. [135]. Furthermore, the sense of the hysteresis is also consistent with these works. Explicitly, features in the up-sweep (down-sweep) appear at higher (lower) B-field, i.e., the hysteresis is retarded. Furthermore, the

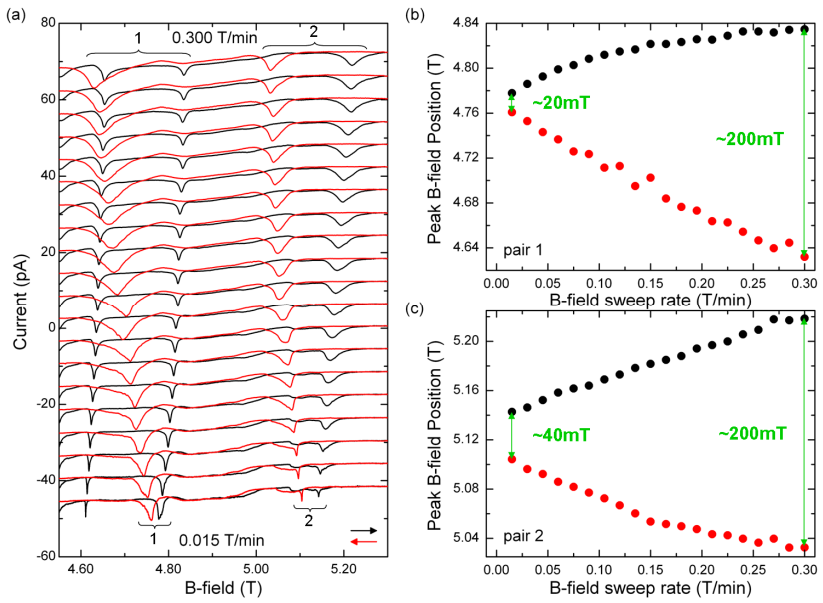

Fig. 6.23. (a) Current measured in Device II as the B-field is swept-up (black) and swept-down (red) for different sweep rates changed from 'fast' (0.300 T/min) to 'slow' (0.015 T/min) in steps of 0.015 T/min. Traces are vertically offset by 6 pA. (b) [(c)] B-field position of the corresponding features in pair 1 (2) as a function of B-field sweep rate.

extent of the hysteresis observed in Device II is comparable to that observed for Device V [see Fig. 6.22(a), although due to the increased number of features, it is more difficult to identify corresponding features in the up- and down-sweeps].

Turning briefly to the shape of the observed current features and its dependence on B-field sweep rate, we focus on pair 2 as an example. Fig. 6.24 shows the corresponding features of pair 2 measured for five selected B-field sweep rates. Evident in the traces for both the B-field up- and down-sweeps is the sharpening of the current dip as the sweep rate is reduced. For the faster sweep rates, the features appear to be roughly Lorentzian shaped, although the shape seems to be more complicated for the slower sweeps. Explicitly, the full width at half maximum of the feature in both the up- and down-sweep is ~30 mT for the fast sweep rate and ~3 mT for the slow sweep rate.

Intriguingly, the slow sweep rate width is similar to the root-mean-square magnitude of the fluctuating effective B-field due to the nuclei ($B_n \approx 5$ mT), although without a detailed model, we do not know if this fact is significant or not. Furthermore, note that even for faster sweep rates not all the hysteretic features observed appear to be Lorentzian shaped.

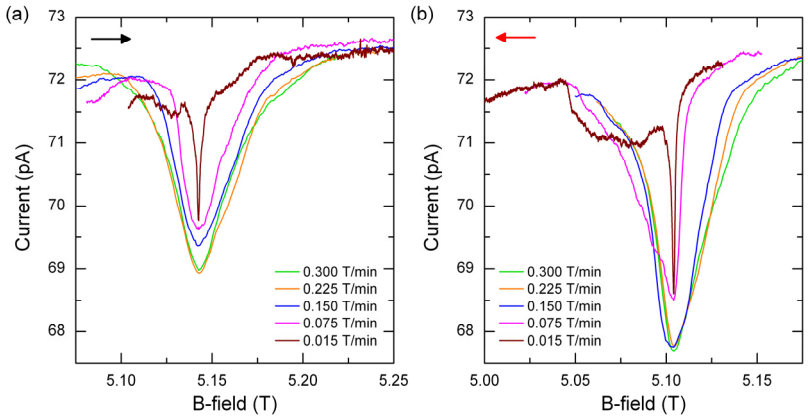

Fig. 6.24. Line shape of features in pair 2 as a function of B-field sweep rate for (a) up-sweeps and (b) down-sweeps. Taking the 0.015 T/min trace as a reference, each of the other traces has been adjusted such that the position of minimum of the current dip is aligned in all traces.

6.3.4 Temporal Properties of Hysteretic Features

We now switch to a description of the temporal properties observed for two particular hysteretic features. Figure 6.25(a) shows a selected portion of the current captured for one very slow B-field up- and down-sweep measurement focusing on a particular (~25 mT wide) hysteretic feature. In the up-sweep the current appears to show an oscillatory behaviour near the high B-field side of the feature which motivated us to investigate the temporal properties of the measured current in more detail. To do so, we step the B-field through the feature and measure the current at each point [indicated by

arrows in Fig. 6.25(a)] as the system evolved for periods of ~40 min [see Fig. 6.25(b)].

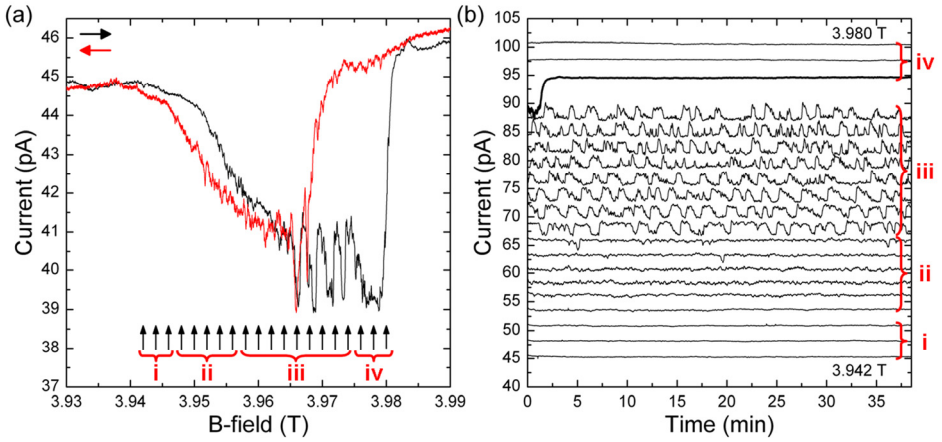

Fig. 6.25. (a) Current measured in Device V with V_{SD} = -22.4 mV and V_G = -0.3 V as the B-field is swept: up-sweep (black) and down-sweep (red). The full trace covers the range of 2.9-4.1 T. The B-field sweep rate is 2 mT/min. The extent of the hysteresis is 5-10 mT. (b) Current measured as a function of time at fixed B-field. The B-field is stepped between 3.942 and 3.980 T (in steps of 2 mT). Traces are vertically offset by 3 pA.

For ease of description, it is convenient to group the traces in Fig. 6.25(b) into four families. For the traces which are recorded at low B-field, just to the left of the feature (family i), the measured current as a function of time is essentially constant (limited by noise of a few tens of fA). Moving to the traces which correspond to the left side of the feature (family ii), the current becomes 'choppy' with time and fluctuations of up to several hundred fA are observed [see for example the 3.952 T trace in Fig. 6.26(a)]. Most intriguingly, traces towards the right side of the feature (family iii) reveal that as a function of time the current executes quasi-periodic multi-frequency oscillations [see for example the 3.960, 3.964, 3.968 and 3.974 T traces in Fig. 6.26(a)]. Collectively, the traces in family iii were recorded over ~300 min indicating that the oscillations persist on a time scale of at least several hours. The oscillations have a strong (~2.5 pA amplitude)

long period component (~150 sec) and weaker (several hundred fA amplitude) shorter period components (few tens of seconds). These shorter period components appear somewhat similar to the 'choppy' current in the traces of family ii [for example compare the traces in Fig. 6.26(b) and (c)], however since the individual fluctuations contain many tens of data points they are not attributable to intrinsic noise. Another intriguing aspect of the traces in family iii is that as we move towards higher B-field the character of the oscillations subtly changes. Explicitly, for lower B-fields [see for example the 3.960 T trace in Fig. 6.26(a)] for the majority of the time the current is 'high,' while for higher B-fields [see for example the 3.972 T trace in Fig. 6.26(a)] the current is 'low' for the majority of the time. We will comment on this further in Sec. 6.4. Finally, the traces which are recorded at high B-field, just to the right of the feature (family iv) are constant again as is the case for the traces in family i. The bold trace in Fig. 6.25(b), which marks the border between families iii and iv (see also 3.974 T trace in Fig. 6.26 for an expanded view), shows fluctuations at the start of the trace. Intriguingly though, in this trace the fluctuations end abruptly after ~100 sec and then the current rises approximately exponentially over a period of ~20 seconds before becoming flat.

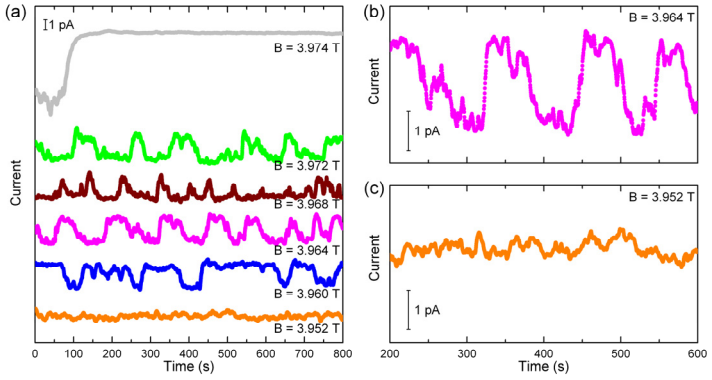

Fig. 6.26. (a) Expanded portion of selected current traces from Fig. 6.25(b). (b) [(c)] Magnified view of a portion of one trace in group iii (ii).

The oscillations observed for family iii bear some similarity to those encountered by Ono and Tarucha in Ref. [33] [recall Fig. 6.2(b)] within the hysteretic feature found in the familiar $N = 2$ spin blockade region and so deserve further comment. First, the oscillations we observe do not appear as regular as those of Ref. [33] which seem to have only one dominant frequency (for each fixed B-field). Second, while the oscillations described in Ref. [33] have a fairly symmetric (sinusoidal-like) shape, the dominant shape of the oscillations we report is more complex, appearing to be saw-tooth-like or square-like. Third, the oscillation amplitude, ΔI, and the relative strength of the oscillations, $\Delta I/I$, were ~0.4 pA and ~30% respectively in Ref. [33] whereas for the oscillations we observe ΔI is ~2.5 pA and $\Delta I/I$ is ~5%. Fourth, neither the magnitude nor the (dominant) period of the oscillations we report appear to vary significantly as a function of in-dot-plane B-field, unlike the oscillations observed in Ref. [33] where both magnitude and period increased as a function of out-of-dot-plane B-field. However, note that the feature we study occurs over a much narrower B-field range (~25 mT compared to ~300 mT).

Having observed striking quasi-periodic temporal oscillations by fixing the B-field within one particular feature observed in a selected portion of a current trace it is a legitimate question to ask if such oscillations are seen in other features. We will therefore examine a second selected feature (in a different device).

The current near this second (~10 mT wide) hysteretic feature is shown in Fig.6.27(a) and the results of measuring the current as a function of time for periods of ~14 min as the B-field is stepped through the feature are shown in Fig. 6.27(b). We can group the traces in Fig. 6.27(b) into three families. For families i and iii, which are to the

left and right of the feature respectively, the current is approximately constant to within the intrinsic noise level. Meanwhile, within the feature (family ii) we do observe strong fluctuations (up to ~2.5 pA in amplitude) in the current as a function of time however, the fluctuations appear 'random' [at least compared to those in family iii traces in Fig. 6.25(b)]. Intriguingly, in the bold trace in Fig. 6.27(b), which corresponds to the border between families i and ii, the current is approximately constant for ~5 min before decreasing approximately exponentially by ~10 pA over ~100 seconds, after which the fluctuations start. This behaviour bears some similarity to that seen in the trace at the border between families iii and iv in Fig. 6.25. Curiously though, for Fig. 6.27 (Fig. 6.25) the trace at the border of families i and ii (iii and iv) shows an approximately exponential decrease (increase) in the current. Note also that the decrease (increase) occurs at the low (high) B-field side of the feature examined. This difference is not fully understood.

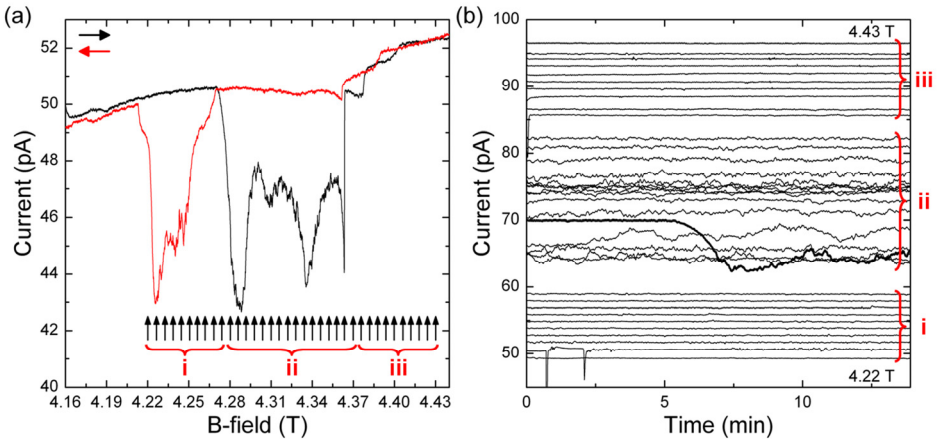

Fig. 6.27. (a) Current measured in Device III as the B-field is swept-up (black) and swept-down (red) with V_{SD} = -18.7 mV and V_G = -0.36 V (the full trace covers the range of 3.8-5.3 T). The B-field sweep rate is 6 mT/min. The extent of the hysteresis is 5-10 mT. (b) Current as a function of time at fixed B-field. The B-field is stepped between 4.22 and 4.43 T (in steps of 6 mT). Traces are vertically offset by 1 pA and family ii is offset by an additional 10 pA from family i.

6.3.5 Further Arguments for the Involvement of the Hyperfine Interaction

In Sec. 6.3.2, we demonstrated that the unexpected current switching and hysteresis encountered at high bias as the B-field is swept is reproducible and robust having been observed in four devices, over a wide portion of the V_{SD}-V_G plane, and at temperatures up to ~4 K. Given the nature of the observed features and their similarities to those previously encountered in the $N = 2$ spin blockade regime which have been attributed to the hyperfine interaction, we now argue that the origin of the high bias features is most likely related the hyperfine interaction. However, before doing so, we examine whether other possible explanations are plausible.

Faced with the unexpected observations described in Secs. 6.3.1-6.3.4, one could reasonably ask if the hysteretic features arose from some unforeseen issues with the measurement equipment. However, the fact that the features we observe are reproducible and do not occur, for example, only at specific values of either B-field, V_G or V_{SD} (reflecting glitches due to internal circuitry switching) suggests that spurious effects due to the cryostat, magnet and measurement electronics can be dismissed. Equally, we have no evidence that they could be device-related due to some characteristic of the chip carriers, or growth of the hetero-structure material, nor steps in the processing.

Perhaps the features observed arose from an overlooked measurement set-up condition? For instance, it is well known that circuit oscillations can lead to current switching and hysteresis in regions of negative differential resistance (NDR) when the resistance is comparable to that of the leads and contacts. In particular, it is a well documented issue for large area (~100 μm diameter) resonant tunneling structures. We

encounter this situation as well when we test new materials. However, for the QD devices composed of sub-micron mesas, a conservative lower bound on the resistance is ~125 MΩ [see the V_G = +0.5 V trace in Fig. 3.9 and equally note that there is no evidence of switching in this trace]. This value is many orders of magnitude larger than the resistance of the leads and contacts, so it is an unlikely explanation. Additionally, even if one still suspected that circuit oscillations were somehow responsible, the data in Fig. 6.7(b) do not fit with this picture. Specifically, although we observe current switching and hysteresis in the vicinity of the region of NDR in the traces of family iii, these features are not visible in family iv where the resonance nearest to zero bias is larger and the magnitude of the NDR is smaller. This is counter to what we would expect if circuit oscillations were responsible.

Now that we are confident that the hysteretic features of interest are not related to the measurement equipment, the device, or the measurement set-up, we now ask the question of whether a physical mechanism intrinsic to the QDs other than the hyperfine interaction could explain the observations. For instance, hysteresis attributed to eddy currents was recently observed in lateral QD devices at B-fields corresponding to Landau level filling factors [136]. However, the hysteresis we observe is not associated with filling factors in any obvious way, nor is the nature of the hysteresis the same. Random switching (telegraph noise) due to, for example, charge traps can also be discounted because, as mentioned in Chap. 3, the devices we measure are very stable in the experimental environment during ~24 hour measurements (recall Fig. 3.11) exhibiting no signatures of random switching. Furthermore, the hysteretic features of interest are essentially reproducible for identical conditions (recall Fig. 6.21) and they evolve

systematically as a function of different control parameters (V_{SD}, V_G and B-field sweep rate).

Having so far failed to find an alternate explanation for the observed hysteretic features, we now return to the hyperfine interaction. Given that the majority of transport experiments to date which focus on the influence of the hyperfine interaction in double QDs have been performed in the familiar $N = 2$ spin blockade region, one might presume that the hyperfine interaction *only* plays a role in this regime. We now argue why this is not the case.

As a starting point, we first note that spin blockade itself is not a unique property of a double QD with two electrons, but in fact can be observed for even values of N other than two when electrons in full 'core' levels can be neglected. For example, Ref. [137] reported spin blockade with four electrons and Ref. [138] described current suppression due to spin blockade in an effective two-electron double QD where the exact number of electrons could not be determined. Furthermore, signatures of the hyperfine interaction were in fact reported in Ref. [138] and, very recently, similar signatures have been observed in vertical double QDs for regions of spin blockade involving five [139] and six [130] electrons. Clearly, these results confirm that the influence of the hyperfine interaction in the spin blockade region is not limited to the $N = 2$ case.

That signatures of the hyperfine interaction have been widely reported for measurements in the spin blockade region largely reflects the fact that spin blockade itself provides a convenient 'readout' through the leakage current. However, what really matters is that any two states can be induced to couple through the hyperfine interaction if they have the right spin properties. In the standard toy model commonly invoked to

explain spin blockade, the hyperfine interaction can couple two- (or effective two-) electron singlet and triplet states under appropriate (B-field and detuning) conditions. In particular, the $T^-(1,1)$ [$T^+(1,1)$] state can be brought into alignment with the S_{AB} (S_B) branch [recall Fig. 6.3(a)]. At both of these singlet-triplet crossing points, the states can be mixed by the hyperfine interaction leading to an electron spin-nuclear spin flip-flop and potentially DNP if repeated. When a flip-flop process occurs at these points, the change in the total spin quantum number, S, is one and the change in the z-component of the spin, S_z, is also one. Note these requirements are also satisfied for the hyperfine induced mixing of five and six electron singlet and triplet states in the spin blockade regions reported by Refs. [130,140].

The above two requirements concerning S and S_z are clearly not satisfied only by two-electron singlet-triplet crossing points. In fact, out-of-dot-plane B-field induced crossings between few- (many-) electron states with different spin are common in QDs [78]. For instance, they have been observed in current 'stripe' measurements (recall Sec. 2.1.5) on vertical double QDs at finite bias [141], and notably the number of such crossings increases dramatically as the number of electrons involved increases. See also Ref. [142] which theoretically investigates transitions between N-electron states as a function of inter-dot distance and B-field.

We now generalize the requirements necessary for the hyperfine interaction to couple two few-electron states and lead to a flip-flop at a generic crossing. Consider two double dot states each with charge configuration (N_L,N_R). For these states, we take (S,S_z) = (M,m) and (N,n) and further suppose that the energies of these two states are such that they can be made degenerate by an external control parameter (see Fig. 6.28). Given the

nature of the measurements reported in this section, the external control parameter we have in mind is B-field, but equally it could be detuning. At such a crossing, the requirements for the hyperfine interaction to couple the two states leading to a flip-flop and DNP are $|M - N| = 1$ and $|m - n| = 1$.

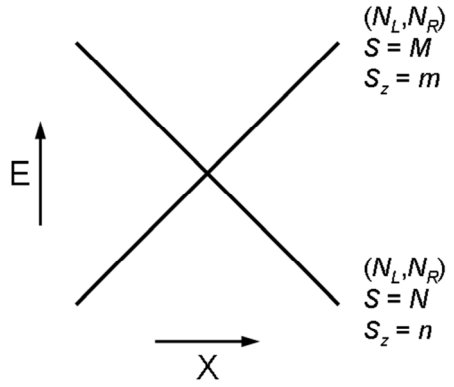

Fig. 6.28. Schematic energy diagram of two few-electron states which are induced to cross by applying an external control parameter X.

In the high bias regime we study, many few-electron states can participate in the transport processes and numerous crossings between few-electron states can be induced by applying an out-of-dot-plane B-field. In this situation there are many opportunities for the hyperfine interaction to play a role and leave signatures in the current. Specifically, at high bias many sequential tunneling cycles involving transitions between few electron configurations contribute to the measured current, i.e., the measured current is essentially a sum over all energetically allowed cycles. The transitions between configurations can be assigned tunneling rates which amongst other factors may depend on the spin of the allowed states for each configuration. DNP through flip-flops, accompanied by signatures like current switching and hysteresis, can then arise if the hyperfine interaction preferentially takes a configuration from one spin state to another (assuming the spin

states met the necessary requirements). This general description covers precisely what occurs in the familiar two-electron spin blockade region when the tunneling rates for the $T^-(1,1)$ and $T^+(1,1)$ states are suppressed in the absence of hyperfine induced mixing with the S(1,1) state. Ultimately, we believe the outlined scenario explains why we can observe the hallmarks of the hyperfine interaction in numerous features in the measured current at high bias outside the $N = 2$ spin blockade region.

Nonetheless, the serious challenge is that for all the high bias measurements we have described so far, it is very difficult to identify the configurations or states involved. In the final section, we will overcome this hurdle and study a high bias region close to pinch off where we observe a hysteretic funnel-like structure. In this instance the states involved *can* be identified and this will allow us to postulate a mechanism involving the hyperfine interaction.

6.3.6 Hysteretic Funnel Structure Observed Outside of the Two-Electron Spin Blockade Region

So far Sec. 6.3 has focused on current switching, hysteresis and slow oscillations or fluctuations at high bias outside of the familiar $N = 2$ spin blockade region. Intriguingly, the features observed bear striking similarity to those which have been reported in the $N = 2$ spin blockade region and attributed to the hyperfine interaction. We take this as evidence that the high bias features we see are also due to the hyperfine interaction. However, the features described in Sec. 6.3 occur in an extensive region of the V_{SD}-V_G plane where there are numerous possible tunneling processes and the few-electron states involved can not easily be identified. Consequently, at a microscopic level,

the origin of the features is currently too complicated to determine and, with regards to a better understanding, the situation appears hopeless. However, we also observed a hysteretic funnel-like structure *located at high bias* in one device bearing all the hallmarks of the hyperfine interaction. The key difference is, based on the location of the funnel-like structure, we can identify the relevant electronic states, allowing us to propose a specific mechanism involving the hyperfine interaction. This funnel-like structure is the subject of this section.

We start with the differential conductance greyscale plot in Fig. 6.29(a) for Device IV. Several familiar features are readily identifiable including the V-shaped $N = 0$ region where the device is pinched-off, the 1s-1s resonance in forward bias and the $N = 2$ spin blockade (SB) chevron in reverse bias (recall that in Sec. 6.2.1 we described intricate fine features attributable to the hyperfine interaction in this region for B > ~0.2 T). An expanded view of the region identified by the red box in Fig. 6.29(a) is shown in Fig. 6.29(b). The plot has been rotated counter-clockwise by ninety degrees for convenience. In Fig. 6.29(b) the $N = 0$ region is now the grey triangular region on the left of the plot, and the first black line identified by the green triangles indicates the onset of sequential electron tunneling through the double dot. A second black line, identified by blue triangles, runs parallel to the first. Visible within the arc-shaped region bound by these two lines are two clear resonances (the approximately horizontal white-black stripes). These two resonances split apart as an out-of-dot-plane B-field is increased (not shown). Consistent with the discussion in Chap. 4, we can straightforwardly identify them as the 1s-2p$^+$ and 1s-2p$^-$ resonances. Also located between the lines indentified by the green and blue triangles is a third parallel line (identified by orange triangles). This third line

appears strong below the two 1s-2p resonances, but weakens (and eventually disappears) above them. We will refer to this line as the bisecting line because it divides the arc-shaped region into two zones (labelled I and II). Note that in Sec. 5.1.3 we encountered these two zones at high bias, referring to them there as the upper and lower zones, in the vicinity of the γ three-level crossing in the spectrum of dot 2 from Device I. Within zone I sequential single-electron tunneling (SET) occurs through the (0,0) → (1,0) → (0,1) → (0,0) cycle, where (N_1,N_2) indicates the number of electrons in the upstream and downstream dots. Meanwhile, within zone II, double-electron tunneling (DET) occurs where transport may *in addition* proceed through a cycle with an electron permanently trapped on the downstream dot, specifically, through the (0,1) → (1,1) → (0,2) → (0,1) cycle. These assignments will later be confirmed by an electrochemical potential map.

Now that we have identified two key features in Fig. 6.29(b), namely the two 1s-2p resonances, and the bisecting line, we proceed to introduce the feature of primary interest in this section: the funnel-like structure. The slices in the bottom right corner of Fig. 6.29(b) each correspond to the derivatives of a series of I-V_{SD} traces (bias up-sweeps only) measured while the B-field is stepped from -450 mT to +450 mT (in steps of 15 mT), i.e., B-field at the left (right) of each slice is -450 mT (+450 mT), at a fixed V_G (-1.70 V to -1.58 V in steps of 0.02 V). Intriguingly, these slices reveal a funnel-like structure near the bisecting line at the bottom right of Fig. 6.29(b). The funnel-like structure is located to the right of the bisecting line (on the more positive V_G side) and below the two 1s-2p resonances (low bias side). The fact that the funnel-like structure is located close to not only the $N = 0$ region, but also to features such as the two 1s-2p resonances and the bisecting line suggests that we have a good chance to identify the

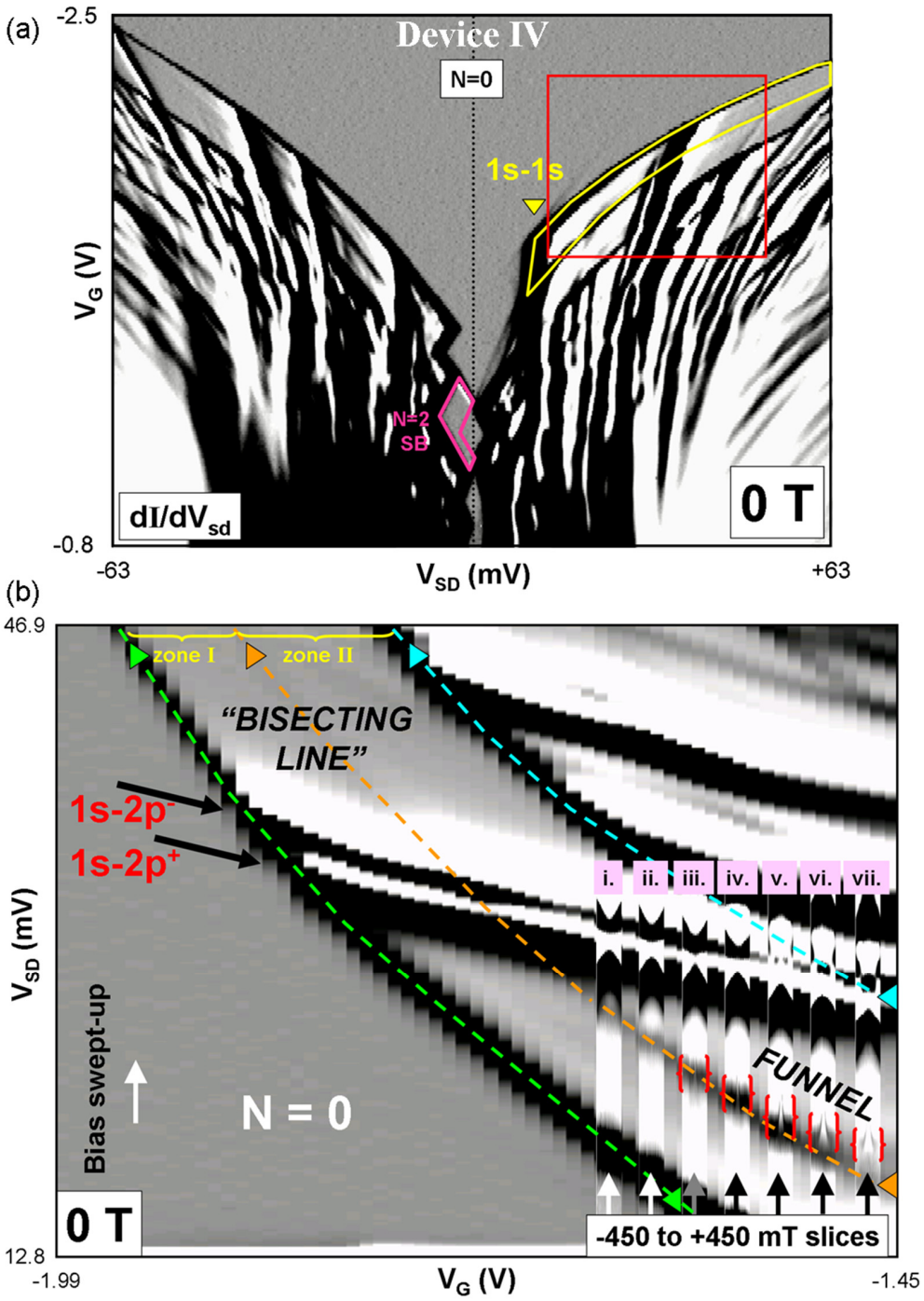

Fig. 6.29. (a) Differential conductance, dI/dV_{SD}, greyscale plot covering a wide portion of the V_{SD}-V_G plane at 0 T. The forward bias SET region is highlighted in yellow. (b) Plot which focuses on the region in the red box in (a) rotated counter-clockwise by ninety degrees. Note that the data used to generate the plot in (a) and (b) are from separate measurements. The slices on the right side of (b) are discussed in the main text (see also Fig. 6.30).

electronic states and tunneling processes relevant to the underlying mechanism. We will consider the location of the funnel-like structure in detail shortly, but first we describe its basic properties.

The top row of greyscale plots in Fig. 6.30 (labelled i-vii) show the same slices as in Fig. 6.29(b) but expanded horizontally. The white-black stripes corresponding to the two 1s-2p resonances are visible at the top of each panel. As expected, as the B-field is increased, these features split apart. Several additional features can be identified in the panels. In particular, in panel i, the grey region towards lower bias effectively corresponds to the $N = 0$ region. Furthermore, the black lines labelled with green and orange triangles correspond respectively to the onset of sequential tunneling and the bisecting line. As expected, as V_G is made progressively more positive both these lines move down systematically towards lower V_{SD}, while the two 1s-2p resonances are much less influenced. Starting with panel i, as the bisecting line moves down the funnel-like structure is 'scanned out' like a photo-copier [labelled funnel(1) in Fig. 6.30]. Apparently, the funnel-like structure is never visible below the bisecting line (low V_{SD} side). Furthermore, it appears that the funnel-like structure itself occurs approximately at fixed bias, irrespective of V_G, and the part of it which is clearest (strongest) is generally that closest to the bisecting line. We also note that at its 'mouth' (widest part) the funnel-like structure is ~300 mT wide while at its 'stem' (narrowest part) it is ~75 mT wide.

The bottom row of greyscale plots in Fig. 6.30 are measured for more positive V_G. At the bottom of these plots, the bisecting line moves out of range *however*, another line, labelled with a blue triangle, emerges near the two 1s-2p resonances. This line corresponds to the right edge of zone II (more positive V_G side) also identified by blue

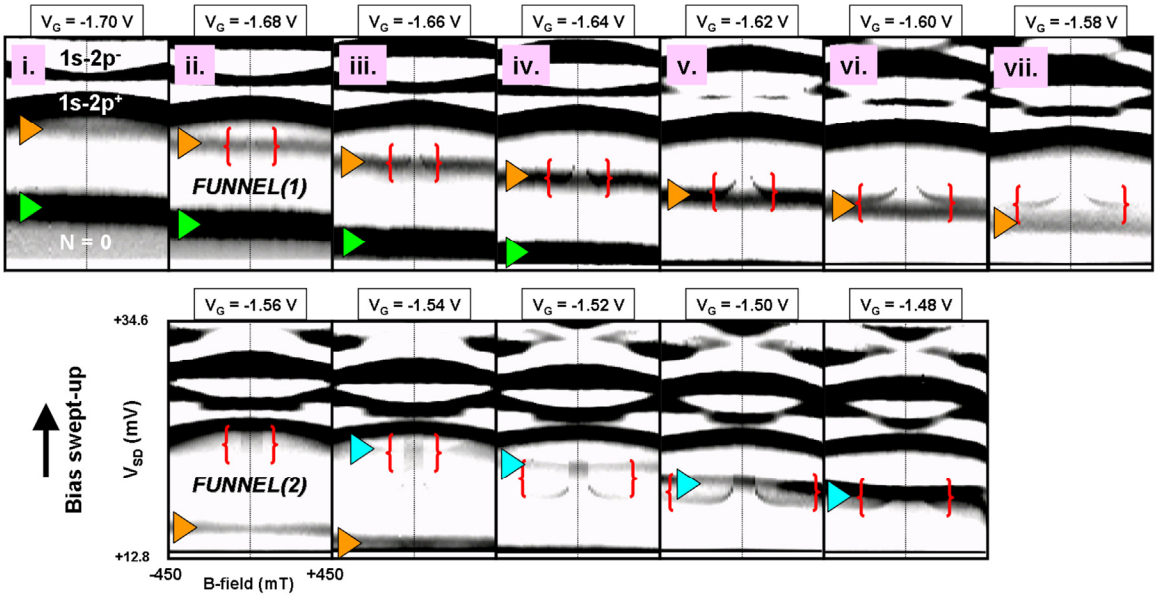

Fig. 6.30. Differential conductance, dI/dV_{SD}, greyscale plots in the vicinity of the funnel-like structure showing bias up-sweeps only as a function of B-field for different values of V_G. The funnel(1), funnel(2) notation refers to the fact that beginning from panel i the funnel-like structure is 'scanned out' twice as V_G is made more positive, once by the line labelled by an orange triangle and once by the line labelled by a blue triangle.

triangles in Fig. 6.29(b). As expected, it also shifts down systematically tracking the movement of the bisecting line. When this line is in close proximity, the funnel-like structure is 'scanned out' again [labelled funnel(2) in Fig. 6.30]. Although in Fig. 6.30 it seems that the funnel-like structure is not visible above the line (see V_G = -1.52, -1.50, and -1.48 V plots), as we shall see shortly, in fact there are features present in this region.

The shape of the high bias funnel-like structure is quite reminiscent of funnel-like structures observed in the familiar $N = 2$ spin blockade, such as the one we discussed in Sec. 6.2.2 and those described in Refs. [26,43,64,67-69,132], which have been attributed to hyperfine induced mixing. If the structure we observe at high bias is related to the hyperfine interaction, one might expect it to show hysteretic behaviour. We now investigate this using the two simple techniques introduced at the start of Chap. 6, namely

sweeping the bias for fixed B-field and sweeping the B-field for fixed bias.

Consider first Fig. 6.31 which shows greyscale plots for both V_{SD} up-sweeps (bottom panels) *and* down-sweeps (top panels) at different values of V_G. As V_G is made progressively more negative the funnel-like structure is again 'scanned out' twice, when either the bisecting line (orange triangles) or the right edge (more positive V_G side) of zone II (blue triangles) are in close proximately to it. Quite clearly the funnel-like structure is hysteretic with respect to bias sweep direction. For instance, in the up-sweeps (down-sweeps) at its 'stem' the funnel-like structure is ~75 mT (~140 mT) wide. Importantly, the appearance of the rest of the greyscale plots are unaffected by the direction of the bias sweep. Intriguingly, in this sequence of plots the funnel-like structure is visible above the line labelled by the blue triangle (see V_G = -1.80, -1.78, -1.76 and -1.748 V plots). It is also worth pointing out that the measurements presented in Fig. 6.31 were acquired during a different cool-down than those in Fig. 6.30 indicating the robustness of the observed funnel-like structure.

Figure 6.32(a) demonstrates that we can also observe the funnel-like structure by sweeping the B-field. Evident in the current traces are hysteretic step-like features. As a function of B-field these step-like features collectively form the funnel-like structure which is symmetric about 0 T. The current traces can be divided into five families with similar properties [see 6.32(a)]. Beginning at low V_{SD} (family i), the traces are initially flat (featureless) and show no hysteresis. However, moving towards larger V_{SD} (family ii) step-like features begin to develop in both the up- and down-sweeps which are clearly hysteretic. For traces in family ii the extent of the hysteresis appears to be roughly

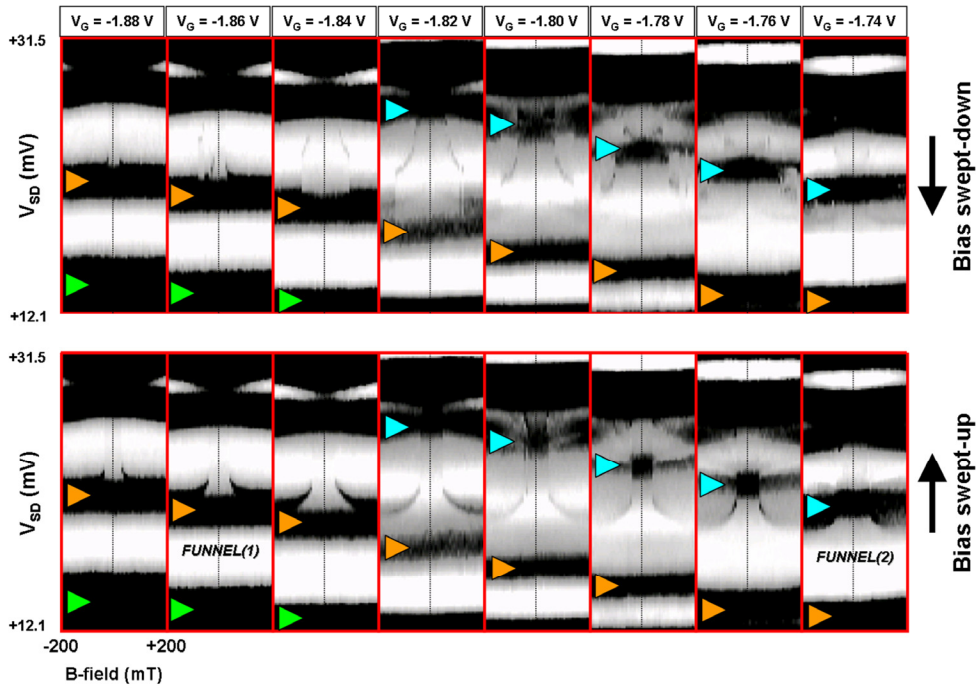

Fig. 6.31. Differential conductance, dI/dV_{SD}, greyscale plots in the vicinity of the funnel-like structure showing V_{SD} up- *and* down-sweeps over a range of -200 mT to + 200 mT (steps of 8 mT) for different values of V_G. Note that the up- and down-sweep panels have been aligned in V_{SD} using the correction procedure described in connection to Fig. 6.8.

constant at ~50 mT. When the step-like features are most pronounced their height, ΔI, is ~0.5 pA and $\Delta I/I$ is ~4%. Notably, for traces in family ii, after passing through 0 T there is a step-like *increase* in the current. These traces are somewhat similar to those reported in the spin blockade regime in Refs. [26,64]. In particular, the traces reported in those works also show a step-like increase in the current after sweeping the B-field through 0 T and the extent of the observed hysteresis is also ~50 mT. As V_{SD} is increased further, the step-like features observed in the traces of family ii begin to weaken and, in fact, there is one trace (family iii) which is almost flat, i.e., there are no hysteretic step-like features. V_{SD} for this trace likely coincides with a point on the right edge of zone II (see the line labelled by the blue triangle in the V_G = -1.78 V panel of Fig. 6.31). Continuing to

increase V_{SD} still further (family iv), curiously the hysteretic step-like features reappear. In family iv (unlike family ii) the extent of the hysteresis increases with V_{SD} (from ~75 mT to at least ~200 mT). Most intriguingly, while ΔI and $\Delta I/I$ are comparable to the traces in group iv, the sense of the hysteresis is inverted, i.e., after passing through 0 T there is a step-like *decrease* in the current. These traces are quite different than those reported in Refs. [26,64]. Furthermore, they are also different from those described in Ref. [69] which showed a step-like increase in the leakage current prior to sweeping through 0 T. Finally, the step-like features disappear as we move to even larger V_{SD} (family v).

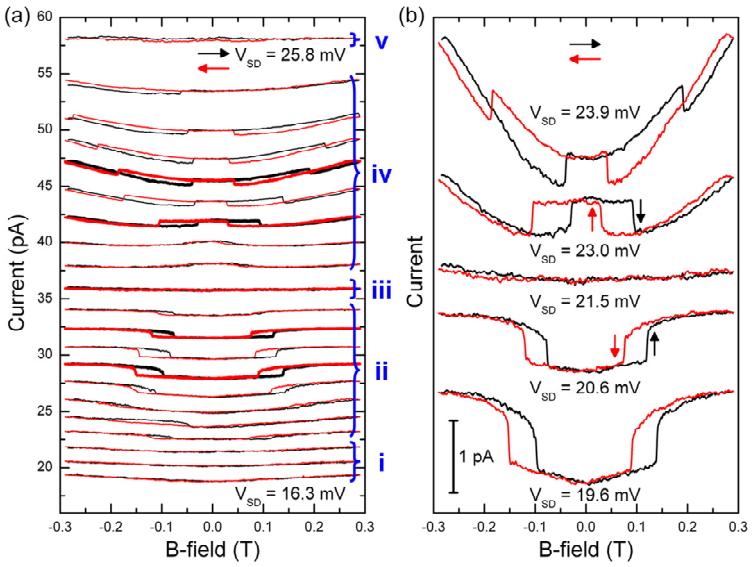

6.32. (a) Current measured as the B-field is swept-up (black) from -290 mT to + 290 mT and immediately swept-back down (red) at rate of 0.085 T/min. V_G is fixed at -1.78 V, while V_{SD} is stepped from 16.3 mV to 25.8 mV (in steps of 0.475 mV). Traces are vertically offset by 2 pA. (b) The five traces in bold in (a) are expanded for clarity. Note that the 'inversion of hysteresis' behaviour has been observed for other values of V_G (in the range of -1.75 V to -1.81 V) as well as for different sweep rates.

The funnel-like structure we have described bears strong similarity to those observed in the familiar $N = 2$ spin blockade region [26,43,64,67-69,132]. However, the

region where we observe the funnel-like structure is at high bias, and well away from the familiar $N = 2$ spin blockade region. Can we now understand the origin of the funnel-like structure in terms of the hyperfine interaction based on its location in the V_{SD}-V_G plane? Figure 6.33 shows the location of the funnel-like structure (circled in red). We can make four important observations about its location based on aspects of Fig. 6.33 (labelled points 1-4). First (point 1), it is to the low bias side of the 1s-2p$^+$ and 1s-2p$^-$ resonances (indicated by red triangles) and to the low V_G side of the bisecting line (identified by an orange triangle). Second (point 2), it is located to the right of the midpoint between the 1s-1s resonance (identified by a yellow triangle) and the two 1s-2p resonances. Third (point 3), the funnel-like structure in forward bias and the $N = 2$ spin blockade chevron (outlined in pink) in reverse bias appear to be approximately equidistant from the 1s-1s resonance. Fourth (point 4), the upper and lower edges of the region of interest (the bisecting line and the lower edge of zone II), when extrapolated through zero bias, seem to map onto the upper part of the spin blockade chevron (see dotted white lines in Fig. 6.33). In what follows, we argue that the observed funnel-like structure, particularly given its precise location, strongly suggests the involvement of hyperfine induced two-electron singlet-triplet mixing, i.e., the physics at play is two-electron spin-blockade-like, *but at high bias*.

To proceed further, we now need to understand the specific tunneling processes involved that lead to the appearance of parts of the differential conductance plot in Fig. 6.33. To do so, we construct an electrochemical potential map for appropriate conditions. The differential conductance greyscale plot for Device IV is similar in general

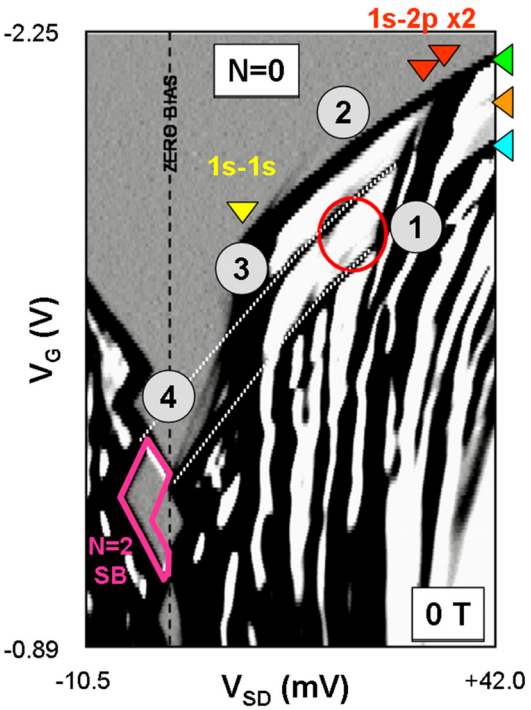

Fig. 6.33. Differential conductance, dI/dV_{SD}, greyscale plot at 0 T which identifies features relevant to understanding the location of the funnel-like structure (see text).

appearance to the corresponding plot for the device studied in Ref. [32] [recall Fig. 2.15(b)] suggesting that the relevant conditions are similar. We can therefore extend the simple model outlined in Ref. [32], keeping all essential input parameters the same, and produce the electrochemical potential map shown in Fig. 6.34(a). The conditions assumed are $E_{C1} = E_{C2} = 2E_{CM} = 2E_{off}$ where E_{C1} and E_{C2} are the charging energies of the two dots, E_{CM} is the inter-dot coupling energy, and E_{off} is the energy offset between the 1s single-particle states of the two dots at zero bias (recall Sec. 2.2). Although the model does not explicitly include confinement, the position of the two 1s-2p resonances in the forward bias SET region can easily be added. To do so we have assumed that the confinement energies of the two dots are equal and that $\hbar\omega_0 = E_{C1} = E_{C2}$.

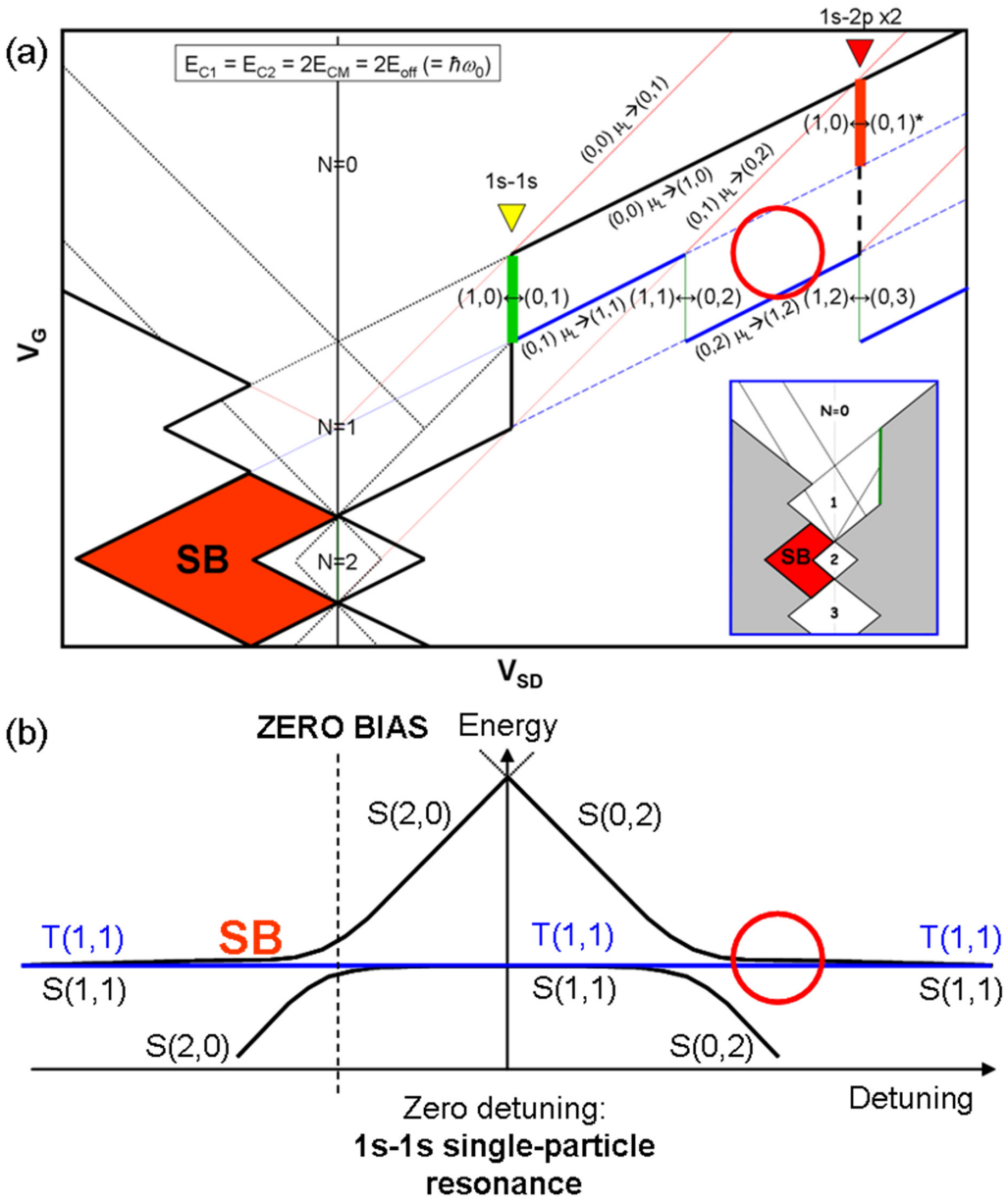

Fig. 6.34. (a) Calculated electrochemical potential map in the V_{SD}-V_G plane at 0 T. The map is essentially an extension of that derived from the simple model of Ref. [32] shown in the lower right inset [see also Fig. 2.15(c)]. Not all possible electrochemical potential lines are shown, and for clarity we only label those which are most relevant for discussing the funnel-like structure of interest (see text). (b) Schematic energy diagram at B = 0 T for the two-electron singlet (S) and triplet (T) states showing both positive and negative detuning. The $T^*(0,2)$ [$T^*(2,0)$] state occurring at more positive (negative) detuning is omitted (diagram adapted from Ref. [8]).

Overall, the electrochemical potential map in Fig. 6.34(a) reproduces several key features of the greyscale plot in Fig. 6.33 demonstrating the choice of parameters is reasonable. In particular, the 'unzipped' $N = 1$ and the well formed $N = 2$ Coulomb diamonds are visible just below the region where the device is pinched-off ($N = 0$) and the 1s-1s resonance is located in forward bias. Furthermore, the spin blockade chevron can easily be included and its position and shape are consistent with the data in Fig. 6.33. In what follows, by examining carefully the electrochemical potential lines in forward bias, we will be able to identify relevant electronic transitions in the region where the funnel-like structure is located (circled in red).

Each of the non-vertical lines present in the electrochemical potential map [Fig. 6.34(a)] at high forward bias indicate a condition when it is energetically allowed to add additional electrons to one of the dots in the double dot system. We begin by discussing the two lines which are most relevant for single-electron tunneling in forward bias, namely the lines labelled $(0,0)\mu_L \rightarrow (1,0)$ and $(0,0)\mu_L \rightarrow (0,1)$ where (N_L,N_R) indicates the number of electrons on the left (upstream) and right (downstream) dots. The $(0,0)\mu_L \rightarrow (1,0)$ notation indicates the condition that the one-electron ground state of the left dot is energetically aligned with the Fermi level of the left (source) contact so that an electron can be added to the left dot assuming the double dot system is initially in the (0,0) configuration. Above this line (toward more negative V_G) this process can not occur energetically, whereas on or below this line (toward more positive V_G) it can. Similarly, the line labelled $(0,0)\mu_L \rightarrow (0,1)$ indicates when the one-electron ground state of the right dot is energetically aligned with the Fermi level of the left contact so that an electron can be added to the right dot from the left contact (by a cotunneling process), provided the

system is initially empty. Note that these two lines have different slopes reflecting the 'lever arm' effect.

Having identified the $(0,0)\mu_L \rightarrow (0,1)$ and $(0,0)\mu_L \rightarrow (1,0)$ lines, we now discuss what these two lines together tell us about single-electron tunneling through the double dot system at high forward bias when the $(0,0)\mu_L \rightarrow (0,1)$ line is above the $(0,0)\mu_L \rightarrow (1,0)$ line. Specifically, above the $(0,0)\mu_L \rightarrow (0,1)$ line no current flows. Between the $(0,0)\mu_L \rightarrow (0,1)$ and $(0,0)\mu_L \rightarrow (1,0)$ lines a weak cotunneling current is expected. In fact, in the experimental data for this region, the cotunneling current is finite, but is generally too weak (<1 pA) too see, although a weak signature of the $(0,0)\mu_L \rightarrow (0,1)$ line is visible in Fig. 6.33 close to the 1s-1s resonance. In the region below the $(0,0)\mu_L \rightarrow (1,0)$ line SET is possible via the $(0,0) \rightarrow (1,0) \rightarrow (0,1) \rightarrow (0,0)$ cycle. When the two lines do not coincide a non-resonant tunneling process involving phonon emission can occur. However, at the point where the $(0,0)\mu_L \rightarrow (0,1)$ and $(0,0)\mu_L \rightarrow (1,0)$ lines meet resonant tunneling through the ground states of the two dots is possible. This condition fixes the V_{SD} position of the vertical 1s-1s resonance line [labelled $(1,0) \leftrightarrow (0,1)$ in Fig. 6.34(a)]. From the position of the 1s-1s resonance, we can then easily locate the two 1s-2p resonances. For B = 0 T, they occur at an energy $\hbar\omega_0$ ($= E_{C1} = E_{C2}$) above (to the right of) the 1s-1s resonance.

Continuing, we next examine conditions for tunneling processes when the dots are initially not empty. Two further lines in Fig. 6.34(a) are particularly important, namely those labelled $(0,1)\mu_L \rightarrow (1,1)$ and $(0,1)\mu_L \rightarrow (0,2)$. The $(0,1)\mu_L \rightarrow (1,1)$ line, corresponding to the bisecting line in Fig. 6.29(a), indicates when an electron can be added to an empty left dot from the left contact when an electron already occupies the right dot. Meanwhile, the $(0,1)\mu_L \rightarrow (0,2)$ line indicates when an electron can be added to the right dot from the

left contact (by a cotunneling process) assuming one electron already occupies this dot. The point where these two lines meet allows us to identify the resonance condition (1,1)↔(0,2) in Fig. 6.34(a) (a weak signature of this line is also visible in Fig. 6.33). To the right of this vertical line and below the $(0,1)\mu_L \rightarrow (1,1)$ line, in addition to the (0,0) → (1,0) → (0,1) → (0,0) cycle, the (0,1) → (1,1) → (0,2) → (0,1) cycle is also energetically allowed, i.e., DET is possible here. *It is in this region* where the funnel-like structure is located. The latter cycle is already familiar from $N = 2$ spin blockade physics. Since the hyperfine interaction can influence this cycle when spin states are considered, perhaps it can do so in the high bias setting?

Two further features in Fig. 6.34(a) are worth mentioning as they help determine the location of the funnel-like structure in the experimental data. Specifically, we are referring to the aforementioned two 1s-2p resonances, and the line labelled $(0,2)\mu_L \rightarrow (1,2)$. Notably, as the two 1s-2p resonances are easily identifiable in the experimental data (recall Fig. 6.33), they help locate the position of the weak (1,1)↔(0,2) line which, as indicated in the electrochemical potential map, occurs midway between the 1s-1s resonance and the two 1s-2p resonances (recall point 2 in connection to Fig. 6.33). Meanwhile, the $(0,2)\mu_L \rightarrow (1,2)$ line corresponds to the lower edge of zone II. Note this line and the $(0,1)\mu_L \rightarrow (1,1)$ line together when extrapolated to reverse bias do map onto the upper portion of the spin blockade chevron consistent with what is seen in the experimental data (recall point 4 in connection to Fig. 6.33). Furthermore, it is these two lines which 'scan out' the funnel-like structure in both Figs. 6.30 and 6.31.

With the aid of the electrochemical potential map we have now established that the region in which the funnel-like structure is observed is certainly below the

(0,1)μ_L→(1,1) line and on or to the right of the vertical (1,1)↔(0,2) line. It also appears to be located near the (0,2)μ_L→(1,2) line and to the left of the two 1s-2p resonances (recall point 1 in connection to Fig. 6.33). In this region the (0,1) → (1,1) → (0,2) → (0,1) cycle familiar in the context of the $N = 2$ spin blockade region is also energetically allowed. Therefore, we now return to the two-electron physics described in Sec. 6.1.2.

In the energy versus detuning diagram encountered to explain the familiar $N = 2$ spin blockade [recall Fig. 2.16(b)], only one detuning polarity is typically considered, and the spin blockade is often presumed to occur at positive detuning (in the forward bias direction). However, detuning initially aligned 1s single-particle states in both dots either way can lead to crossings of the singlet and triplet states. To see this, we draw a schematic diagram of the relevant two-electron states for both positive and negative detuning in Fig. 6.34(b).

The first thing to note is that the positive and negative detuning sides of this diagram are obviously mirror images of each other. Importantly, in this diagram zero detuning corresponds to alignment of the single-particle 1s states in the two dots. In Device IV zero detuning occurs in forward bias, as evidenced by the location of the 1s-1s resonance in Fig. 6.33, due to a finite energy offset between the two dots at zero bias. Consequently, in Device IV, the spin blockade chevron is located in reverse bias, corresponding to negative detuning. Therefore, in Fig. 6.34(b) we can attribute the $N = 2$ spin blockade region to a consequence of detuning to the left of the crossing between the S(1,1) and S(2,0) states. However, on the positive detuning side of Fig. 6.34(b) there is a similar crossing between the S(1,1) and S(0,2) states. The funnel-like structure observed in forward bias therefore appears in the region just to the right of this crossing [circled in

red in Fig. 6.34(b)]. Note this region and the equivalent region in reverse bias giving rise to spin blockade are equidistant from zero detuning (recall point 3 in connection to Fig. 6.33). If signatures of hyperfine induced singlet-triplet mixing can be observed in the spin blockade region at negative detuning, we have grounds to expect they should be observed in this positive detuning regime too. However, manifestly there is a difference between these two regimes from an experimental point of view. Namely, current is strongly suppressed in the spin blockade region at negative detuning, but the current is ~20 pA in the corresponding region at positive detuning.

Having established from an energetic point of view that there is a link between the $N = 2$ spin blockade region in reverse bias and the location of the funnel-like structure in forward bias, we now wish to understand what determines the current. To do so, we must consider the relevant sequential tunneling cycles for both regions. Figure 6.35 tabulates all possible charge configurations for a double dot containing up to three electrons. Charge configurations with the same total number of electrons are located in the same row. Possible sequential tunneling cycles are identified by triangular arrangements of charge configurations. We make a distinction between two types of sequential tunneling cycles, namely electron and hole cycles. So far, all of the cycles we have discussed are cycles of the form $(N_1,N_2) \rightarrow (N_1 + 1,N_2) \rightarrow (N_1,N_2 + 1) \rightarrow (N_1,N_2)$ which can easily be interpreted as an electron tunneling from the left contact through the two dots in series and to the right contact. Such a cycle is referred to as an electron cycle. However, sequential tunneling cycles of the form $(N_1,N_2) \rightarrow (N_1,N_2 - 1) \rightarrow (N_1 - 1,N_2) \rightarrow (N_1,N_2)$ are also possible. These cycles are referred to as hole cycles because they can be interpreted as a hole tunneling from the right contact to the left contact. In Fig. 6.35

electron, e^-, (hole, h^+) cycles appear as down-pointing (up-pointing) triangles. In forward (reverse) bias, the electron cycles are traversed clockwise (counter-clockwise) around the triangle, while the opposite is true for the hole cycles.

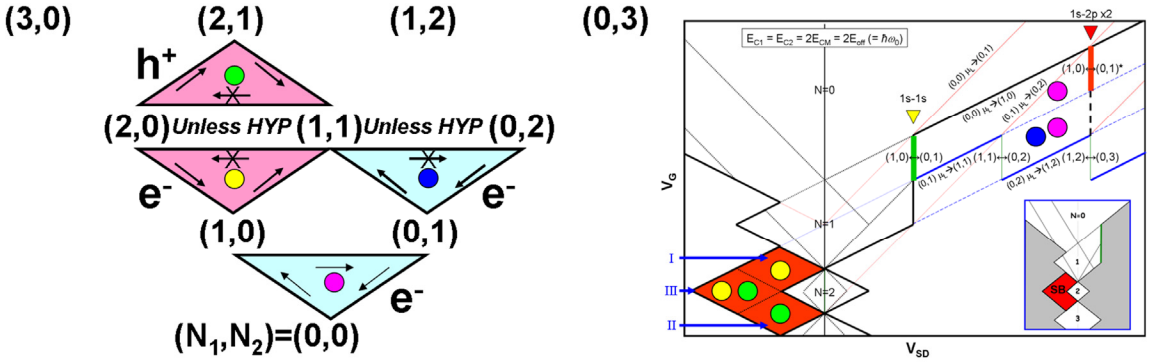

Fig. 6.35. Diagram showing all possible charge configurations for up to three electrons in a double QD system. Cycles of interest in forward (reverse) bias are indicated by blue (red) triangles. Regions in the electrochemical potential map where these cycles are relevant to the discussion are identified by coloured circles.

For the familiar $N = 2$ spin blockade region in *reverse bias*, two sequential tunneling cycles can play a role. To emphasize the nature of the reverse bias cycles we use the symbol ← to indicate electrons moving from right to left. Initially neglecting spin, in the upper portion of the spin blockade chevron (labelled I in Fig. 6.35) *only* the (1,0) ← (1,1) ← (2,0) ← (1,0) electron cycle is operative (yellow circle), while in the lower portion of the spin blockade chevron (region II) *only* the (2,1) ← (2,0) ← (1,1) ← (2,1) hole cycle is operative (green circle) (note that the measurements of Ono and Tarucha [33], and Baugh et. al. [66,84] were performed in the upper portion of the spin blockade chevron). Meanwhile, in the central portion of the spin blockade chevron (region III) *both* of the (1,0) ← (1,1) ← (2,0) ← (1,0) and (2,1) ← (2,0) ← (1,1) ← (2,1) cycles are operative. This means that in the upper and lower portions of the spin blockade chevron

SET occurs while in the central portion DET occurs. Now we must factor in spin, and irrespective of whether just one or both of these cycles is operative, if in the (1,1) charge configuration a triplet state is occupied spin blockade occurs and current is suppressed in the absence of a spin flip mechanism. In this situation though, as we have seen, the hyperfine interaction can mix the (1,1) singlet and triplet states. This lifts the spin blockade leading in the process to an electron spin-nuclear spin flip-flop.

Turning now to the region where the forward bias funnel-like structure is located, the electrochemical map indicates that two current cycles can play a role, namely the (0,0) → (1,0) → (0,1) → (0,0) and (0,1) → (1,1) → (0,2) → (0,1) electron cycles (pink and blue circles in Fig. 6.35). We stress that both these cycles are operative, meaning that DET occurs. Concerning the (0,0) → (1,0) → (0,1) → (0,0) cycle, the transition (1,0) → (0,1) is never spin blockaded (the one-electron system has only one possible spin) and a hyperfine induced flip-flop is strongly suppressed due to energy mismatch at finite B-field. If the (0,1) configuration is occupied, the system may transition to the (0,0) configuration *or* to the (1,1) configuration. The probability of (0,1) → (0,0) versus (0,1) → (1,1) depends principally on the tunneling rates (and is beyond the electrochemical potential model). Should (0,1) → (1,1) occur, neglecting spin, transport can proceed via the (0,1) → (1,1) → (0,2) → (0,1) cycle. However, considering spin, if a T(1,1) state is occupied, the transition to the (0,2) configuration is spin blockaded, provided the T^*(0,2) state is energetically inaccessible.

As the tunneling processes which occur in the forward bias region of interest can lead to a (1,1) spin blockaded triplet, it seems reasonable to expect to observe signatures of the hyperfine interaction. Specifically, we believe that the observed forward bias

funnel-like structure essentially maps out the position of the singlet-triplet crossing points at positive detuning (at least the T^--S point) as a function of either detuning or B-field, mirroring the situation for funnel-like structures observed in the familiar $N = 2$ spin blockade region (recall Sec. 6.2.2).

We now stress a crucial difference between the familiar $N = 2$ spin blockade region and the forward bias region in which the funnel-like structure is located. In terms of the familiar spin blockade region, regardless of whether one or the other or both of the relevant cycles are operative, spin blockade (leading to current suppression) is unavoidable as the (1,1) → (0,2) transition is always involved. We stress that it is this transition that matters since if a T(1,1) state is occupied the hyperfine interaction can mix it with S(1,1) so allowing S(0,2) to be populated. However, the situation is different in the region where the funnel-like structure is located. Here both the (0,0) → (1,0) → (0,1) → (0,0) cycle *and* the (0,1) → (1,1) → (0,2) → (0,1) cycle are energetically allowed and they are always in competition with each other. However, the hyperfine interaction can not influence the (0,0) → (1,0) → (0,1) → (0,0) cycle, but it can influence the (0,1) → (1,1) → (0,2) → (0,1) cycle. The degree to which the hyperfine interaction plays a role in the DET region where the funnel is located will reflect the relative probably of transport proceeding via these two cycles, i.e., the role of the hyperfine interaction will be minimized (maximized) if the former (latter) cycle is dominant. Note as well that in the region below the (0,2)μ_L→(1,2) line the (1,2) → (1,1) → (0,2) → (1,2) cycle is also operative, i.e., triple-electron tunneling occurs. That the character of the funnel-like structure changes in this region (recall the inversion of the hysteresis seen in Fig. 6.32)

presumably reflects the fact that there are now three competing cycles. This deserves further investigation.

6.4 Summary and Concluding Comments

This chapter has focused on the electron spin-nuclear spin (hyperfine) interaction in transport measurements on coupled QDs. The established hallmarks of the hyperfine interaction are current switching, hysteresis, funnel-like structures and even slow oscillations in the leakage current in the $N = 2$ spin blockade regime. We observed such features in two quite different electronic regimes. In the familiar $N = 2$ spin blockade regime, in the presence of an out-of-dot-plane B-field, we brought to light a strong V_G dependence, significant device-to-device variations and an intricate V_{SD} history dependence of the fine features observed in the leakage current. These observations collectively demonstrate that there remain many unanswered questions about the details of the hyperfine interaction in this regime. Despite this, we can still exploit the hyperfine interaction by using a bias voltage pulsing procedure to effectively program fine features in the leakage current toward basic memory operations. Unexpectedly, we also observed the hallmarks of the hyperfine interaction at high bias well outside the $N = 2$ spin blockade region. We demonstrated that these features are numerous in B-field, widespread in the V_{SD}-V_G plane, and reproducible and robust. We also examined in detail the B-field sweep rate dependence and temporal properties of these features. Intriguingly, the latter revealed instances of current fluctuations and even quasi-periodic oscillations. Although it appears the hyperfine interaction plays a role in this regime, the few-electron states involved are too numerous to easily identify. Consequently, we can not offer any

interpretation of the underlying physics at specific features in this regime. In order to address this, we focused on a hysteretic funnel-like structure also observed at high bias, but close to pinch-off. With the aid of an electrochemical potential map, and readily identifiable features in the differential conductance plot, we determined the precise location of the funnel-like structure, and identified the states involved as two-electron states. This allowed us to suggest a mechanism for how the hyperfine interaction may play a role in this regime.

The pioneering work of Ono and Tarucha [33] first revealed the hallmarks of the hyperfine interaction in the familiar $N = 2$ spin blockade region. An NMR measurement was additionally performed to confirm that nuclei were involved. Nonetheless, the technique provides little in the way of further information and, in particular, did not offer any explanation of, for instance, the height of the current step, the extent of the hysteresis, or the period of the oscillations observed in Ref. [33] (recall Fig. 6.2). Current switching, hysteresis and slow oscillations in the spin blockade region are now widely accepted as sufficient evidence for the involvement of the hyperfine interaction in QD transport measurements to the extent that NMR is not often performed or reported. For instance, several recent landmark papers on the hyperfine interaction do not report NMR [26,64,69]. That said, although we presented plausible arguments for the involvement of the hyperfine interaction at high bias (and even could formulate a specific mechanism in the case of the funnel-like structure) one could legitimately argue that an NMR measurement would be desirable to confirm definitively the involvement of nuclei in this new regime. However, the features we observe are induced by an out-of-dot-plane B-field. In fact, this orientation seems crucial to generate the numerous features seen at high bias).

In order to perform NMR when the static B-field is in the out-of-dot-plane direction, a coil would have to be wrapped around the chip carrier to apply the in-dot-plane oscillating B-field. This configuration is different to that employed in Ref. [33] where the static B-field was applied in the in-dot-plane direction, so NMR was performed by placing a small coil immediately above the chip carrier. Even if successful, as was the case in Ref. [33], we would not expect an NMR measurement to provide much else in the way of useful information which could help explain the details of our observations at high bias.

Lastly, one of the most intriguing observations from Ref. [33] was the slow oscillations [recall Fig. 6.2(b)]. To date, these oscillations have defied many attempts to explain their origin (for example see Ref. [143]). Although they may not be as regular, we too observe similar oscillations within one particular hysteretic feature (recall Fig. 6.25). As outlined in Sec. 6.3.4, the current within this feature appears to oscillate between 'high' and 'low' as a function of time and, notably, the amount of time the current is 'low' or 'high' varies systematically as the B-field is stepped through the feature. Figure 6.36 plots this dependence explicitly. For $B < 3.960$ T the quasi-periodic oscillations have not started and so the percentage of time that the current is 'low' is found to be close to zero. At the onset of the oscillations ($B = 3.960$ T) the current is 'low' for ~30% of the time and the percentage gradually increases before levelling off at ~75% at the high B-field edge of the range where the oscillations are observed. It is presumed the oscillations are a result of DNP. However, the reason for the form of the dependence shown in Fig. 6.36 or why the percentage of time in the 'low' state saturates at a value other than unity is currently unknown.

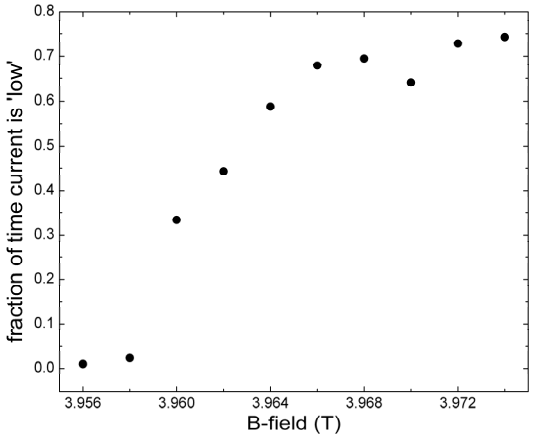

Fig. 6.36. Fraction of time current is ‘low’ as a function of B-field. With reference to the feature shown in Fig. 6.25(a), the first two points on the low B-field side are in family ii (left side of the feature), while the remaining points are in family iii (right side of the feature). ‘High’ and ‘low’ refer to when the current is above or below the average value.

Chapter 7

Conclusion and Future Directions

We have performed transport measurements on weakly coupled vertical double QD devices to investigate two major topics.

We began by describing how to measure a high resolution single-particle energy spectrum of one of the constituent dots over a wide energy range. The measured spectra are well modelled *overall* by ideal spectra for elliptical, parabolic confinement allowing us to extract global properties such as confinement energies and ellipticities. However, an initially unexpected property of the measured spectra is widespread energy level mixing and resonant current variations at two-, three- and four-level crossings. These features can be understood within a simple coherent tunneling picture by including higher order symmetry breaking terms in the dot confinement potentials (to account for natural anharmonicity and anisotropy) in order to provide the necessary inter- and intra-dot couplings. Subsequently, we focused on specific examples of two-, three- and four-level mixing where we observed the suppression of an otherwise strong resonance, a signature of destructive interference. By using a generic level mixing model, we were able to explore the underlying physics by fitting the energy level positions and resonant currents in order to extract coupling and current amplitude parameters. In particular, we demonstrated that the mixing we observed at two three-level crossings represents an all-electrical analogue of coherent population trapping. Furthermore, we demonstrated that the model can explain different instances of two-level crossings (including both familiar and ideal two-level mixing) within one unified picture. Additionally, we also examined

examples of level mixing which approach the limit of what we can reliably fit (both challenging-to-characterize crossings and one example of a four-level crossing). Preliminary measurements towards controllably altering the coupling parameters at level crossings using a device with four gates were also performed.

We further explored the hyperfine interaction. We started in the familiar two-electron spin blockade regime where it is known that the hyperfine interaction can lead to hysteretic fine features in the leakage current. We discussed the strong gate voltage dependence, device-to-device variations and bias voltage history dependence of such hysteretic features, none of which can be explained by any existing model, demonstrating that there remain many unanswered questions in this regime. Nonetheless, by using multiple-sweep mHz bias voltage waveforms we were able to program the total current response in this regime and extract a recovery time of ~40 sec. Unexpectedly, we also observed widespread signatures of the hyperfine interaction, namely current switching and hysteresis, at high bias, well outside the spin blockade region. Although we suggested how the hyperfine interaction may play a role here too, any detailed modeling of these features is hampered by the fact that we can not easily identify the electronic states involved. As a first step towards a better understanding of the features observed at high bias, we described a funnel-like structure observed at high bias close to pinch-off where the relevant electronic states were indentified as two-electron states. This allowed us to attribute the funnel-like structure to two-electron spin-blockade-like physics in the presence of the hyperfine interaction. We hope that these observations will stimulate the development of models to understand how the hyperfine interaction can influence few-(many-) electron states.

We now suggest several areas for further investigation, beginning with the single-particle energy level spectroscopy and level mixing. i. Understanding the numerous interesting examples of challenging-to-characterize level crossings where resonances appear to cross exactly or become very weak will require improved techniques for extracting the relevant energies and resonant currents. Initial investigations suggest that the resonant peak widths and the sum of the branch currents appear to be approximately conserved throughout crossing regions possibly providing an avenue toward improved data extraction techniques. ii. In terms of the symmetry breaking potentials, so far the modelling of specific crossings has proceeded by including appropriate terms in an ad-hoc manner. It would be interesting, although challenging, to attempt to fit the experimental data of an entire spectrum (both energy and resonant currents). iii. Other schemes for inducing level mixing, such as incorporating delta function impurity potentials in the contacts, could also be explored. iv. A full three dimensional self-consistent calculation would likely provide some insight into the details of the microscopic tunneling processes involved by explicitly shedding light on how the tunneling rates from the dots to the source and drain contacts change as a function of V_{SD} (and V_G). This could potentially offer some clues to explain the systematic trends observed in the resonant currents independent of the level mixing at the crossings. v. It would be interesting to measure energy spectra in regimes other than the single-electron tunneling regime. For example, one could probe dot energy spectra when electrons are permanently trapped in the double dot system, i.e., in the presence of Coulomb interactions. Furthermore, one could measure a spectrum at higher energies where phonon-assisted tunneling is possible. Energy level mixing in both of these regimes

would also be of interest.

We now turn to the hyperfine interaction. i. A model which examines the influence of the tunneling rates from the dots to the source and drain contacts on the details of the hyperfine interaction could offer some insight into the strong V_G dependence of the hysteretic features observed in the familiar two-electron spin blockade region. ii. The bias pulsing schemes we employed could be applied to spin blockade regions other than the familiar two-electron regime where the hyperfine interaction plays a role. iii. In order to further probe the hysteretic current features, rather than being limited to simple up-down B-field sweeps at a uniform sweep rate, one could implement advanced B-field sweep programming along the lines demonstrated for mHz bias voltage programming, i.e., multi-part waveforms where each part can have a different start point, end point and sweep rate. iv. In order to demonstrate explicitly (and independently) that the hysteretic features observed in the high bias current are due to the hyperfine interaction, it would be useful to perform an NMR experiment in this regime. However, the required measurement geometry is non-trivial. v. Further analysis could be performed on the quasi-periodic temporal current oscillations (recorded for a particular feature observed at high bias and high B-field). Specifically, Fourier analysis may help reveal the dominant frequencies in the oscillations, and more detailed analysis of the time spent in the 'up' and 'down' states could be of interest. This may help shed light on the as yet poorly understood slow oscillations originally observed in the $N = 2$ spin blockade region more than five years ago by Ono and Tarucha [33]. vi. In terms of the forward bias funnel-like structure, a model which examines the occupation probabilities and tunneling rates for the different charge configurations or cycles involved could offer some insight.

The extent of the observed hysteresis, both as a function of V_{SD} and B-field, deserves further investigation too.

References

1. L. Jacak, P. Hawrylak, and A. Wojs, *Quantum Dots* (Springer, Germany, 1998).

2. D. Bimberg, M. Grundmann, and N. N. Ledentsov, *Quantum Dot Heterostructures* (John Wiley & Sons, Chichester, 1999).

3. T. Chakraborty, *Quantum Dots* (Elsevier Science, The Netherlands, 1999).

4. L. P. Kouwenhoven, C. M. Marcus, P. L. McEuen, S. Tarucha, R. M. Westervelt, and N. S. Wingreen, in *Mesoscopic Electron Transport, Vol. 345 NATO Advanced Studies Institute, Series E: Applied Sciences*, Edited by L. L. Sohn, L. P. Kouwenhoven, and G. Schon (Kluwer Academic, Dordrecht, 1997), p. 16.

5. L. P. Kouwenhoven, D. G. Austing, and S. Tarucha, Rep. Prog. Phys. **64,** 701 (2001).

6. S. M. Reimann and M. Manninen, Rev. Mod. Phys. **74,** 1283 (2002).

7. W. G. Van der Wiel, S. De Franceschi, J. M. Elzerman, T. Fujisawa, S. Tarucha, and L. P. Kouwenhoven, Rev. Mod. Phys. **75,** 1 (2003).

8. R. Hanson, L. P. Kouwenhoven, J. R. Petta, S. Tarucha, and L. M. K. Vandersypen, Rev. Mod. Phys. **79,** 1217 (2007).

9. M. A. Kastner, Physics Today **46,** 24 (1993).

10. R. C. Ashoori, Nature **379,** 413 (1996).

11. T. Fujisawa, D. G. Austing, Y. Tokura, Y. Hirayama, and S. Tarucha, Nature **419,** 278 (2002).

12. J. Lambe and R. C. Jaklevic, Phys. Rev. Lett. **22,** 1371 (1969).

13. H. R. Zeller and I. Giaever, Phys. Rev. **181,** 789 (1969).

14. T. A. Fulton and G. J. Dolan, Phys. Rev. Lett. **59,** 109 (1987).

15. M. A. Reed, J. N. Randall, R. J. Aggarwal, R. J. Matyi, T. M. Moore, and A. E. Wetsel, Phys. Rev. Lett. **60,** 535 (1988).

16. B. Su, V. J. Goldman, and J. E. Cunningham, Science **255,** 5042 (1992).

17. M. Tewordt, L. Marti¦n-Moreno, J. T. Nicholls, M. Pepper, M. J. Kelly, V. J. Law, D. A. Ritchie, J. E. F. Frost, and G. A. C. Jones, Phys. Rev. B **45,** 14407 (1992).

18. R. C. Ashoori, H. L. Stormer, J. S. Weiner, L. N. Pfeiffer, S. J. Pearton, K. W. Baldwin, and K. W. West, Phys. Rev. Lett. **68,** 3088 (1992).

19. J. M. Elzerman, R. Hanson, J. S. Greidanus, L. H. W. van Beveren, S. De Franceschi, L. M. K. Vandersypen, S. Tarucha, and L. P. Kouwenhoven, Phys. Rev. B **67,** 161308 (2003).

20. F. H. L. Koppens, C. Buizert, K. J. Tielrooij, I. T. Vink, K. C. Nowack, T. Meunier, L. P. Kouwenhoven, and L. M. K. Vandersypen, Nature **442,** 766 (2006).

21. M. Pioro-Ladriere, T. Obata, Y. Tokura, Y. S. Shin, T. Kubo, K. Yoshida, T. Taniyama, and S. Tarucha, Nature Physics **4,** 776 (2008).

22. M. Ciorga, A. S. Sachrajda, P. Hawrylak, C. Gould, P. Zawadzki, S. Jullian, Y. Feng, and Z. Wasilewski, Phys. Rev. B **61,** R16315 (2000).

23. N. C. van der Vaart, S. F. Godijn, Y. V. Nazarov, C. J. P. M. Harmans, J. E. Mooij, L. W. Molenkamp, and C. T. Foxon, Phys. Rev. Lett. **74,** 4702 (1995).

24. T. Hatano, M. Stopa, and S. Tarucha, Science **309,** 268 (2005).

25. K. Shibata, M. Jung, K. M. Cha, M. Sotome, and K. Hirakawa, Appl. Phys. Lett. **94,** 162107 (2009).

26. A. Pfund, I. Shorubalko, K. Ensslin, and R. Leturcq, Phys. Rev. Lett. **99,** 036801 (2007).

27. S. J. Tans, M. H. Devoret, H. Dai, A. Thess, R. E. Smalley, L. J. Geerligs, and C. Dekker, Nature **386,** 474 (1997).

28. L. A. Ponomarenko, F. Schedin, M. I. Katsnelson, R. Yang, E. W. Hill, K. S. Novoselov, and A. K. Geim, Science **320,** 356 (2008).

29. D. G. Austing, T. Honda, Y. Tokura, and S. Tarucha, Jpn. J. Appl. Phys. **34,** 1320 (1995).

30. D. G. Austing and T. Honda, Semicond. Sci. Technol. **11,** 388 (1996).

31. S. Tarucha, D. G. Austing, T. Honda, R. J. van der Hage, and L. P. Kouwenhoven, Phys. Rev. Lett. **77,** 3613 (1996).

32. K. Ono, D. G. Austing, Y. Tokura, and S. Tarucha, Science **297,** 1313 (2002).

33. K. Ono and S. Tarucha, Phys. Rev. Lett. **92,** 256803 (2004).

34. J. Salfi, S. Roddaro, D. Ercolani, L. Sorba, I. Savelyev, M. Blumin, H. E. Ruda, and F. Beltram, Semicond. Sci. Technol. **25,** 024007 (2010).

35. P. Recher and B. Trauzettel, Nanotechnology **21,** 302001 (2010).

36. G. E. Moore, Electronics **38** (1965).

37. P. W. Shor, in *Proc. 35th Ann. Symp. on Found. of Comp. Sci.*, (IEEE Comp. Soc. Press, Los Alamitos, California, USA, 1994), p. 124.

38. S. Lloyd, Science **273,** 1073 (1996).

39. M. A. Nielsen and I. L. Chuang, *Quantum Computation and Quantum Information* (Cambridge University Press, Cambridge, 2000).

40. Quantum Information Science and Technology Roadmap, online at http://qist.lanl.gov

41. D. Loss and D. P. DiVincenzo, Phys. Rev. A **57,** 120 (1998).

42. J. M. Elzerman, R. Hanson, L. H. W. van Beveren, B. Witkamp, L. M. K. Vandersypen, and L. P. Kouwenhoven, Nature **430,** 431 (2004).

43. J. R. Petta, A. C. Johnson, J. M. Taylor, E. A. Laird, A. Yacoby, M. D. Lukin, C. M. Marcus, M. P. Hanson, and A. C. Gossard, Science **309,** 2180 (2005).

44. K. C. Nowack, F. H. L. Koppens, Y. Nazarov, and L. M. K. Vandersypen, Science **318,** 1430 (2007).

45. T. H. Oosterkamp, S. F. Godijn, M. J. Uilenreef, Y. V. Nazarov, and N. C. van der Vaart, Phys. Rev. Lett. **80,** 4951 (1998).

46. L. Zimin and S. V. Nair, Phys. Rev. Lett. **80,** 3105 (1998).

47. H. J. Krenner, M. Sabathil, E. C. Clark, A. Kress, D. Schuh, M. Bichler, G. Abstreiter, and J. J. Finley, Phys. Rev. Lett. **94,** 057402 (2005).

48. S. F. Fischer, G. Apetrii, U. Kunze, D. Schuh, and G. Abstreiter, Nature Physics **2,** 91 (2006).

49. B. A. Carpenter, E. A. Zibik, M. L. Sadowski, L. R. Wilson, D. M. Whittaker, J. W. Cockburn, M. S. Skolnick, M. Potemski, and M. J. Steer, Phys. Rev. B **74,** 161302 (2006).

50. C. Ellenberger, T. Ihn, C. Yannouleas, U. Landman, K. Ensslin, and D. Driscoll, Phys. Rev. Lett. **96,** 126806 (2006).

51. E. A. Stinaff, M. Scheibner, A. S. Bracker, I. V. Ponomarev, V. L. Korenev, M. E. Ware, M. F. Doty, T. L. Reinecke, and D. Gammon, Science **311,** 636 (2006).

52. K. Hennessy, A. Badolato, M. Winger, D. Gerace, M. Atature, S. Gulde, S. Falt, E. L. Hu, and A. Imamoglu, Nature **445,** 896 (2007).

53. M. Scheibner, M. Yakes, A. S. Bracker, I. V. Ponomarev, M. F. Doty, C. S. Hellberg, L. J. Whitman, T. L. Reinecke, and D. Gammon, Nature Physics **4,** 291 (2008).

54. A. D. Greentree, J. H. Cole, and A. R. Hamilton, Phys. Rev. B **70,** 235317 (2004).

55. B. Michaelis, C. Emary, and C. W. J. Beenakker, Europhys. Lett. **73,** 677 (2006).

56. M. Korkusinski, I. P. Gimenez, P. Hawrylak, L. Gaudreau, S. A. Studenikin, and A. S. Sachrajda, Phys. Rev. B **75,** 115301 (2007).

57. T. Brandes, Phys. Rep. **408,** 315 (2005).

58. E. del Valle, F. P. Laussey, and C. Tejedor, Europhys. Lett. **80,** 57001 (2007).

59. C. Emary, C. Pöltl, and T. Brandes, Phys. Rev. B **80,** 235321 (2009).

60. L. Gaudreau, S. A. Studenikin, A. S. Sachrajda, P. Zawadzki, A. Kam, J. Lapointe, M. Korkusinski, and P. Hawrylak, Phys. Rev. Lett. **97,** 036807 (2006).

61. L. Gaudreau, A. Kam, G. Granger, S. A. Studenikin, P. Zawadzki, and A. S. Sachrajda, Appl. Phys. Lett. **95,** 193101 (2009).

62. K. Bergmann and H. Theuer, Rev. Mod. Phys. **70,** 1003 (1998).

63. M. O. Scully and M. S. Zubairy, *Quantum Optics* (Cambridge University Press, Cambridge, 1997).

64. F. H. L. Koppens, J. A. Folk, J. M. Elzerman, R. Hanson, L. H. W. van Beveren, I. T. Vink, H. P. Tranitz, W. Wegscheider, L. P. Kouwenhoven, and L. M. K. Vandersypen, Science **309,** 1346 (2005).

65. A. C. Johnson, J. R. Petta, J. M. Taylor, A. Yacoby, M. D. Lukin, C. M. Marcus, M. P. Hanson, and A. C. Gossard, Nature **435,** 925 (2005).

66. J. Baugh, Y. Kitamura, K. Ono, and S. Tarucha, Phys. Rev. Lett. **99,** 096804 (2007).

67. E. A. Laird, C. Barthel, E. I. Rashba, C. M. Marcus, M. P. Hanson, and A. C. Gossard, Phys. Rev. Lett. **99,** 246601 (2007).

68. J. R. Petta, J. M. Taylor, A. C. Johnson, A. Yacoby, M. D. Lukin, C. M. Marcus, M. P. Hanson, and A. C. Gossard, Phys. Rev. Lett. **100,** 067601 (2008).

69. H. O. H. Churchill, A. J. Bestwick, J. W. Harlow, F. Kuemmeth, D. Marcos, C. H. Stwertka, S. K. Watson, and C. M. Marcus, Nature Physics **5,** 321 (2009).

70. K. Ono, D. G. Austing, Y. Tokura, and S. Tarucha, Physica B **314,** 450 (2002).

71. D. V. Averin and K. K. Likharev, J. Low Temp. Phys. **62,** 345 (1986).

72. D. V. Averin and K. K. Likharev, in *Mesoscopic Phenomena in Solids*, Edited by B. I. Altshuler, P. A. Lee, and R. A. Webb (Elsevier, Amsterdam, 1991), p. 167.

73. D. V. Averin and Y. V. Nazarov, in *Single Charge Tunneling: Coulomb Blockade Phenomena in Nanostructures*, Edited by H. Grabert and M. H. Devoret (Plenum Press and NATO Scientific Affairs Division, New York/London, 1992), p. 217.

74. V. Fock, Z. Phys. **47,** 446 (1928).

75. C. G. Darwin, Proc. Cambridge Philos. Soc. **27,** 86 (1931).

76. D. V. Melnikov and J. P. Leburton, Phys. Rev. B **73,** 085320 (2006).

77. S. Tarucha, D. G. Austing, Y. Tokura, W. G. Van der Wiel, and L. P. Kouwenhoven, Phys. Rev. Lett. **84,** 2485 (2000).

78. L. P. Kouwenhoven, T. H. Oosterkamp, M. W. Danoesastro, M. Eto, D. G. Austing, T. Honda, and S. Tarucha, Science **278,** 1788 (1997).

79. A. Pfund, I. Shorubalko, R. Leturcq, and K. Ensslin, Appl. Phys. Lett. **89,** 252106 (2006).

80. Labview simultator courtesy of S. Amaha and K. Ono.

81. S. Amaha, C. Payette, J. A. Gupta, T. Hatano, K. Ono, T. Kodera, Y. Tokura, D. G. Austing, and S. Tarucha, Phys. Stat. Sol. (c) **5,** 174 (2008).

82. T. Kodera, K. Ono, Y. Kitamura, Y. Tokura, Y. Arakawa, and S. Tarucha, Phys. Rev. Lett. **102,** 146802 (2009).

83. T. Fujisawa, T. H. Oosterkamp, W. G. Van der Wiel, B. W. Broer, R. Aguado, S. Tarucha, and L. P. Kouwenhoven, Science **282,** 932 (1998).

84. J. Baugh, Y. Kitamura, K. Ono, and S. Tarucha, Phys. Stat. Sol. (c) **5,** 302 (2008).

85. D. G. Austing, T. Honda, K. Muraki, Y. Tokura, and S. Tarucha, Physica B **249-251,** 206 (1998).

86. M. Pi, A. Emperador, M. Barranco, F. Garcias, K. Muraki, S. Tarucha, and D. G. Austing, Phys. Rev. Lett. **87,** 066801 (2001).

87. G.C. Aers, private communication.

88. D. G. Austing and T. Honda, Jpn. J. Appl. Phys. **36,** 4151 (1997).

89. D. G. Austing and T. Honda, Semicond. Sci. Technol. **12,** 631 (1997).

90. D. G. Austing, S. Sasaki, K. Muraki, Y. Tokura, K. Ono, S. Tarucha, M. Barranco, A. Emperador, and M. Pi, in *Advanced Luminescent Materials and Quantum Confinement II*, Edited by M. Cahay, J. P. Leburton, D. J. Lockwood, D. Bandyopadhyay, N. Koshida, and M. Zacharias (The Electrochemical Society, Pennington, 2002), p. 13.

91. M. Pi, D. G. Austing, R. Mayol, K. Muraki, S. Sasaki, H. Tamura, and S. Tarucha, in *Quantum Dots: New Research*, Edited by P. A. Ling (Nova Science Publishers, Inc., New York, 2005), p. 1.

92. S. Raymond, S. Studenikin, A. Sachrajda, Z. Wasilewski, S. J. Cheng, W. Sheng, P. Hawrylak, A. Babinski, M. Potemski, G. Ortner, and M. Bayer, Phys. Rev. Lett. **92,** 187402 (2004).

93. O. Makarovsky, O. Thomas, A. G. Balanov, L. Eaves, A. Patane, R. P. Campion, C. T. Foxon, E. E. Vdovin, D. K. Maude, G. Kiesslich, and R. J. Airey, Phys. Rev. Lett. **101,** 226807 (2008).

94. T. K. Rebane, Teoreticheskaya i Eksperimental'naya Khimiya **5,** 3 (1969).

95. A. V. Madhav and T. Chakraborty, Phys. Rev. B **49,** 8163 (1994).

96. Maksym.P.A., Physica B **249-251,** 233 (1998).

97. D. G. Austing, S. Sasaki, S. Tarucha, S. M. Reimann, M. Koskinen, and M. Manninen, Phys. Rev. B **60,** 11514 (1999).

98. K. Ono et. at., unpublished.

99. J. Konemann, R. J. Haug, D. K. Maude, and V. I. ko, Phys. Rev. Lett. **94,** 226404 (2005).

100. P. Matagne, J. P. Leburton, D. G. Austing, and S. Tarucha, Phys. Rev. B **65,** 085325 (2002).

101. S. M. Huang, Y. Tokura, H. Akimoto, K. Kono, J. J. Lin, S. Tarucha, and K. Ono, Phys. Rev. Lett. **104,** 136801 (2010).

102. In Chap. 5, when we introduce a model to study generic B-field induced level crossings, these inter-dot tunnel couplings will be accounted for by *s*-parameters.

103. S.V. Nair, private communication.

104. The tunneling rate through a potential barrier is influenced by its height and width. A bias voltage applied across a potential barrier also affects its shape. In the context of the measurements performed on the vertical double dot structures at high bias, the height of the barrier between the downstream dot and the drain contact will be significantly reduced relative to energy of the injected electrons

(more so than the other two barriers). Also see discussion in Ref. [101] and Ref. [9] therein.

105. Ultimately, we are interested in the influence of the level mixing on the resonant currents in order to explain features such as dark state formation. While the simple coherent tunneling picture we use in this chapter, based on a Fermi's golden rule argument, appears to work well, an alternative scheme, namely sequential (incoherent) tunneling was originally considered in Ref. [70], but not in the context of level mixing (recall discussion in Sec. 2.2.3). Whether this scheme could explain our observations to some degree is not known, nor is it currently clear how to incorporate level mixing into this scheme.

106. Note that when we use the term differential conductance in connection with strategy A measurements in Chaps. 4 and 5, strictly speaking we are referring to dI/dE, where E is the energy axis, but this is simply proportional to dI/dV_{SD} (recall Sec. 4.3.1). Furthermore, all strategy A greyscale plots use the convention that black, gray, and white respectively correspond to positive, zero, and negative conductance.

107. J. B. Majer, F. G. Paauw, A. C. J. ter Haar, C. J. P. M. Harmans, and J. E. Mooij, Phys. Rev. Lett. **94,** 090501 (2005).

108. One could justifiably ask if it is possible to attempt to measure only a specific crossing, by either strategy, with the goal of increasing the resolution in mind [the γ crossing data actually shown in Figs. 5.4(a) and 5.6 is only a small fraction of the full data sets measured]. However, attempting to measure only one particular crossing would certainly be impossible without having first examined at least one extensive V_{SD}-V_G differential conductance plot at 0 T [like that shown in Fig. 4.4(a)] to gain the necessary information in order to set up sensible 'vector voltage' line scans. Next, the single-particle spectrum of one of the dots must be measured over a sufficiently large energy and B-field range, like that shown in Figs. 4.3(c) and (d), in order to locate the target crossing. Furthermore, even then, a high-resolution measurement of only a specific crossing would still be challenging as without a larger measurement window identifying-features may be difficult to locate, and determining the non-resonant background current accurately may prove impossible in the case of strategy A (recall Fig. 5.5). The main advantage of strategy B is that it provides significantly more information by measuring whole resonance lines in the SET region (or the extended region in which SET dominates), although it will also provide extensive information about the area outside the region of interest. However, due to the additional time required to capture large data sets from an extensive region in the V_{SD}-V_G plane for each B-field, the B-field resolution of the strategy B measurements is in practice reduced compared with the strategy A measurements [for instance the B-field step size in Fig. 5.7 is 0.1 T, while it is 0.06 T for Fig. 5.4(a)].

109. In addition to the fact that the currents determined by strategy A and strategy B are slightly different, there is another possible explanation for why the *s*-

parameters are slightly different. Namely, the numerical fitting procedure used on the two data sets was not identical.

110. As for the fit of the energy level positions for the γ three-level crossing from the spectrum of dot 2 from Device I [recall Fig. 5.8(d)], lines estimating the positions of uncoupled basis levels provide guide to the eye and the energy of the point where the three uncoupled basis levels cross is set to zero energy.

111. T. Hime, P. A. Reichardt, B. L. T. Plourde, T. L. Robertson, C.-E. Wu, A. V. Ustinov, and J. Clarke, Science **314,** 1427 (2006).

112. J. Majer, J. M. Chow, J. M. Gambetta, J. Koch, B. R. Johnson, J. A. Schreier, L. Frunzio, D. I. Schuster, A. A. Houck, A. Wallraff, A. Blais, M. H. Devoret, S. M. Girvin, and R. J. Schoelkopf, Nature **449,** 443 (2007).

113. M. Hilke, private communication.

114. A. S. Bracker, E. A. Stinaff, D. Gammon, M. E. Ware, J. G. Tischler, A. Shabaev, A. Efros, D. Park, D. Gershoni, V. L. Korenev, and I. A. Merkulov, Phys. Rev. Lett. **94,** 047402 (2005).

115. C. Latta, A. Hogele, Y. Zhao, A. N. Vamivakas, P. Maletinsky, M. Kroner, J. Dreiser, I. Carusotto, A. Badolato, D. Schuh, W. Wegscheider, M. Atature, and A. Imamoglu, Nature Physics **5,** 758 (2009).

116. W. A. Coish and J. Baugh, Phys. Stat. Sol. (b) **246,** 2203 (2009).

117. J. M. Taylor, C. M. Marcus, and M. D. Lukin, Phys. Rev. Lett. **90,** 206803 (2003).

118. M. S. Rudner and L. S. Levitov, arXiv:0705.2177 (2007).

119. D. Klauser, W. A. Coish, and D. Loss, Phys. Rev. B **73,** 205302 (2006).

120. I. T. Vink, K. C. Nowack, F. H. L. Koppens, J. Danon, Y. V. Nazarov, and L. M. K. Vandersypen, Nature Physics **5,** 764 (2009).

121. H. Bluhm, S. Foletti, I. Neder, M. S. Rudner, D. Mahalu, V. Umansky, and A. Yacoby, arXiv:1005.2995 (2010).

122. H. Bluhm, S. Foletti, D. Mahalu, V. Umansky, and A. Yacoby, Phys. Rev. Lett. **105,** 216803 (2010).

123. N. Shaji, C. B. Simmons, M. Thalakulam, L. J. Klein, H. Qin, H. Luo, D. E. Savage, M. G. Lagally, A. J. Rimberg, R. Joynt, M. Friesen, R. H. Blick, S. N. Coppersmith, and M. A. Eriksson, Nature Physics **4,** 540 (2008).

124. D. J. Reilly, J. M. Taylor, E. A. Laird, J. R. Petta, C. M. Marcus, M. P. Hanson, and A. C. Gossard, Phys. Rev. Lett. **101,** 236803 (2008).

125. A. W. Overhauser, Phys. Rev. **92,** 411 (1953).

126. D. Paget, G. Lampel, B. Sapoval, and V. I. Safarov, Phys. Rev. B **15,** 5780 (1977).

127. I. A. Merkulov, A. Efros, and M. Rosen, Phys. Rev. B **65,** 205309 (2002).

128. S. Tarucha, Y. Kitamura, T. Kodera, and K. Ono, Phys. Stat. Sol. (b) **243,** 3673 (2006).

129. T. Kodera, K. Ono, S. Amaha, Y. Tokura, Y. Arakawa, and S. Tarucha, Physica E **40,** 1139 (2008).

130. S. Amaha, T. Kodera, T. Hatano, K. Ono, Y. Tokura, S. Tarucha, J. A. Gupta, and D. G. Austing, J. Phys. : Conf. Ser. submitted (2010).

131. F. Qassemi, W. A. Coish, and F. K. Wilhelm, Phys. Rev. Lett. **102,** 176806 (2009).

132. S. Foletti, H. Bluhm, D. Mahalu, V. Umansky, and A. Yacoby, Nature Physics **5,** 903 (2009).

133. In fact, the data shown in Fig. 6.11 for combinations of two V_{SD} sweeps was actually recorded as part of four-part pulses, but the third and forth sweeps were omitted in order to simplify the initial discussion.

134. An example of a mechanism which could assist the diffusion of nuclear spin to dissipate built-up nuclear polarization is a virtual process involving two consecutive electron spin-nuclear spin flip-flops, i.e., an electron exchanges its spin with one nucleus and then again with another (distant) nucleus (see Ref. [8]). The probability of such processes occurring is likely enhanced in the many-electron tunneling regime at high bias relevant for the erase operation.

135. S. Yamaguchi, Masters Thesis, University of Tokyo (2004).

136. M. Pioro-Ladriere, A. Usher, A. S. Sachrajda, J. Lapointe, J. Gupta, Z. Wasilewski, S. Studenikin, and M. Elliott, Phys. Rev. B **73,** 075309 (2006).

137. A. C. Johnson, J. R. Petta, C. M. Marcus, M. P. Hanson, and A. C. Gossard, Phys. Rev. B **72,** 165308 (2005).

138. A. Pfund, I. Shorubalko, K. Ensslin, and R. Leturcq, Phys. Rev. B **76,** 161308 (2007).

139. That spin blockade can be observed for $N = 5$ is a consequence of Hund's first rule filling. See T. Kodera, K. Ono, S. Amaha, Y. Arakawa, and S. Tarucha, J. Phys. : Conf. Ser. **150,** 022043 (2009) for details.

140. T. Kodera, K. Ono, S. Amaha, Y. Arakawa, and S. Tarucha, J. Phys. : Conf. Ser. **150,** 022043 (2009).

141. M. Rontani, S. Amaha, K. Muraki, F. Manghi, E. Molinari, S. Tarucha, and D. G. Austing, Phys. Rev. B **69,** 085327 (2004).

142. B. Partoens and F. M. Peeters, Euro. Phys. Lett. **56,** 86 (2001).

143. S. I. Erlingsson, O. N. Jouravlev, and Y. V. Nazarov, Phys. Rev. B **72,** 033301 (2005).